Studying the direct effects of forces on embryonic stem cell behaviour

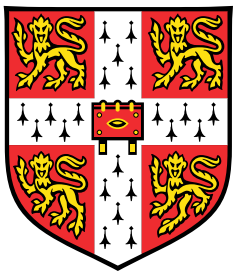

Christophe V. C. M. Verstreken

Department of Physics
University of Cambridge

This dissertation is submitted for the degree of
Doctor of Philosophy

Christ's College

August 2018

Footfalls echo in the memory,
down the passage we did not take,
towards the door we never opened.
– T. S. Eliot

Declaration

I hereby declare that except where specific reference is made to the work of others, the contents of this dissertation are original and have not been submitted in whole or in part for consideration for any other degree or qualification in this, or any other university. This dissertation is my own work and contains nothing which is the outcome of work done in collaboration with others, except as specified in the text and Acknowledgements. This dissertation contains fewer than 60,000 words including abstract, tables, footnotes and appendices but excluding table of contents, figure captions, bibliography and acknowledgements.

Christophe V. C. M. Verstreken
August 2018

Studying the direct effects of forces on embryonic stem cell behaviour

Christophe Verstreken

Abstract

Cells experience different mechanical cues from their local environment, including shear flow, forces applied by neighbouring cells, and substrate stiffness. These external signals influence cell behaviour, also in embryonic stem (ES) cells, where they could potentially affect pluripotency or differentiation. The precise effects of external forces on ES cells are confounded by forces inducing secondary changes to attachment or cell-cell signalling, which themselves can also influence cell behaviour.

In this study we developed a set-up to attach cells to elastic membranes using a novel functionalisation technique, and exposed them to single or cyclic stretch. We used this method to study the mechanosensitive response of ES cells. We found that stretching caused an immediate increase in the concentration of intracellular calcium, followed by a rapid decrease in some cells. On timescales of 1 - 2 h, stretching induced an increase in the expression of the immediate and early genes, but then cells became temporarily insensitive to subsequent mechanical signals. Stretching did not have a substantial impact on pluripotency and differentiation, as we showed using gene expression studies and a Rex1 reporter.

To study how ES cells' susceptibility to mechanical signals depended on media condition, stretch duration and stretch type, we performed RNA sequencing and used gene ontology techniques to investigate the involvement of specific pathways. We found that forces have a broad impact on the overall transcriptome that is highly culture media-dependent. However, a core transcriptional response, including the biosynthesis of membrane components and stress pathways, was largely preserved across the different conditions.

We supplemented our experimental findings with a conceptual model of force propagation in disordered environments, such as the nucleus of a cell. Using computational simulations, we studied how the large-scale behaviour of a disordered system depends on the microscopic structure. Contrary to common wisdom, we showed that disordered systems exhibit both positive and negative Poisson's ratios with equal probability.

Overall, on short timescales, stretching affected ES cells' calcium concentration and transcription. On longer timescales, ES cells' response was small in magnitude but broad in scope, with limited effects on pluripotency. As such, our results suggest that mechanosensitivity in ES cells is mediated primarily by tissue-wide changes to morphology and attachment.

Contents

List of Figures

List of Abbreviations and Symbols

Biological abbreviations

2i	N2B27 medium supplemented with Chiron and PD03
2iL	N2B27 medium supplemented with Chiron, PD03 and LIF
ABS	Acrylonitrile butadiene styrene
BS^3	bis(sulfosuccinimidyl)suberate, an amine-to-amine crosslinker
CH	CHIR99021, a small molecule inhibitor of GSK3
ECM	Extracellular matrix
GO	Gene ontology
GUI	Graphical user interface
IEGs	Immediate and early genes, including Egr-1, Jun and Fos
LIF	Leukemia inhibitory factor, binding the LIF receptor to promote pluripotency
LINC	Protein complex in the nuclear envelope linking the nucleus with the cytoskeleton
mES/ES cells	(Mouse) embryonic stem cells
MSC	Mesenchymal stem cells
N2B27	ES cell differentiation media containing the components N2 and B27
PD03	PD0325901, a small molecule inhibitor of MEK
PDMS	Polydimethylsiloxane, a silicon-based elastomer
PLA	Polylactic acid
qPCR	Quantitative real-time Polymerase Chain Reaction
RGD	Amino acid motif consisting of Arg-Gly-Asp, a sequence within fibronectin and recognised by it
SL	Culture media consisting of Serum supplemented with LIF

Physical symbols (Chapter 6)

$\delta\vec{\rho}_i$	Displacement of an individual vertex i of a triangle
$\delta\vec{R}_t$	Displacement of the centroid of triangle t
ΔL_α	The change in the length of the system in the direction α
ε_t	Strain of triangle t
ε_t^{exp}	Expansive strain of triangle t
ε_t^{rot}	Rotational strain of triangle t
ε_t^{trans}	Translational strain of triangle t
ν_{sys}	The global Poisson's ratio
ν_t	The Poisson's ratio of triangle t
σ_t	The stress of triangle t
θ_t	The rotation of triangle t, calculated as the average rotation of its vertices
$\vec{l}_c$	Loop force of cell c
$\vec{R}_{ct}$	Vector from the centre of triangle c to the centre of cell c
$\vec{r}_{ct}$	Vector along the side of a triangle t on the edge of cell c
A_t	The sum of the area of the three quadrons corresponding to triangle t
C_t	The structure tensor corresponding to triangle t
N	Number of grains in a system
N_b	Number of boundary elements in the graph
N_c	Number of cells in the graph
N_e	Number of edges in the graph
N_f	Number of faces in the graph
Q_t	The symmetric part of the structure tensor
S_t	The compliance matrix of triangle t
z	Coordination number, i.e. number of contacts per element

Preface

It is an exciting time for biophysics in stem cell biology. Increasingly the abstract approach of physics makes a valuable contribution to a field which is characterised by highly complex networks, phase transitions and apparent stochasticity. Biophysics contributes through influencing quantitative experimental design, through physical modelling of protein interactions, or through the study of the role of physics in driving biological changes.

The work presented in this thesis spans across these different applications. It includes the development of a technology to stretch cells, its application to a biological system, and the bioinformatics analysis of the results. And it contains a computational model to analyse force propagation in granular system, with the aim of, in the future, predicting and describing our experimental results physically.

The breadth of this thesis is a consequence of the choice to be involved in both the technological development and the biological application. This was necessary to develop a system that is adequately versatile and robust to be used throughout the many aspects of a biological study. And while in some instances this meant we lacked the time to explore the biological questions in more detail, it made this PhD a much more interesting and creative journey.

This text is composed as follows. Chapter 1 contains the scientific background and context of our investigation. Based on this earlier work, I formulate in Chapter 2 a number of hypotheses and objectives, while the materials and methods used in our study are described in detail in Chapter 3. The results can be found in Chapters 4 - 6. Chapter 4 discusses the development of a device that can be used to stretch the substrate of embryonic stem cells. Its application, to study the biological response of cells to forces, is described in Chapter 5. I present the development of a theoretical framework and computational model to predict the propagation of forces in granular systems in Chapter 6, which will form the basis of a model to explain how forces affect nuclear organisation. Finally, Chapter 7 concludes and outlines plans for future experiments. The appendix includes a paper published during this project, which was somewhat tangential to the main project and therefore has not been included in the main text.

Chapter 1

Background & related work

1.1 Embryonic stem cells, differentiation and pluripotency

The timeline of mouse embryo development starts at fertilisation, when a single cell (the zygote) incorporates all developmental information and potential to create the future organism [Nichols, 2001]. The time between the subsequent cell divisions gradually shortens until, by 3.5 days after fertilisation (E3.5), the embryo is a sphere of cells with an outer layer (the *trophoblast*) surrounding an inner cavity and an internal mass of cells (the *inner cell mass*), as shown in Fig 1.1 [Niakan et al., 2013].

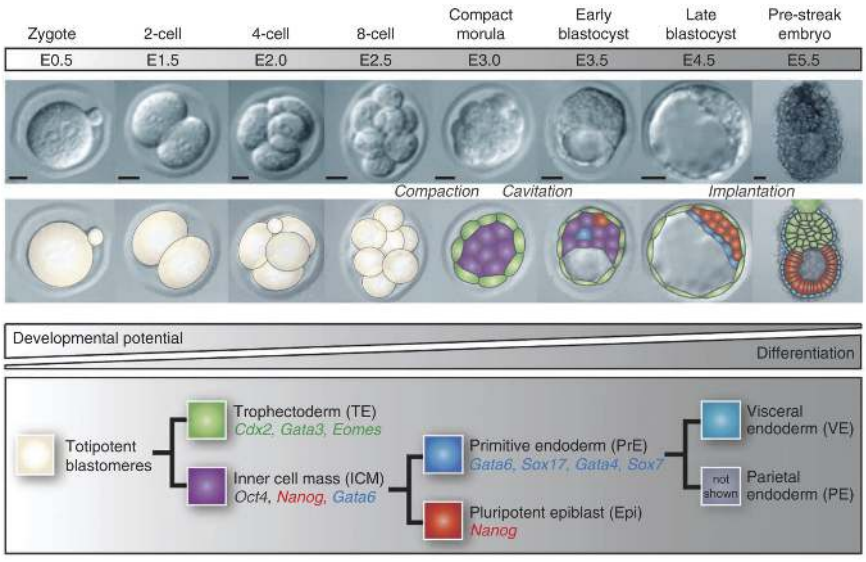

Figure 1.1 Mouse embryonic development from fertilisation to E5.5. Embryonic Stem (ES) cells are extracted from the epiblast, indicated in red, around day 4.5 after fertilisation. Figure adapted from [Niakan et al., 2013].

Cells from the inner cell mass will later produce the entire organism (although not all extra-embryonic tissues such as the trophectoderm), but at stage E4.5 cells can be extracted from the epiblast, within the inner cell mass, and cultured in vitro. Because their developmental potential remains preserved (in the form of their capability to become all cell types in the organism), they are referred to as pluripotent Embryonic Stem (ES) cells [Evans and Kaufman, 1981; Martin, 1981].

The in vitro culture of ES cells is of particular biological and medical interest, particularly the study of the maintenance of pluripotency and the regulation of differentiation into other cell types [Nagy et al., 1993; Nichols and Smith, 2009]. In addition, as they are able to self-renew indefinitely, a better understanding could allow us, in the future, to provide a theoretically unlimited supply of patient-specific cells that are able to withstand high passage numbers in vitro, and without a reduction in division rate [Chambers and Smith, 2004].

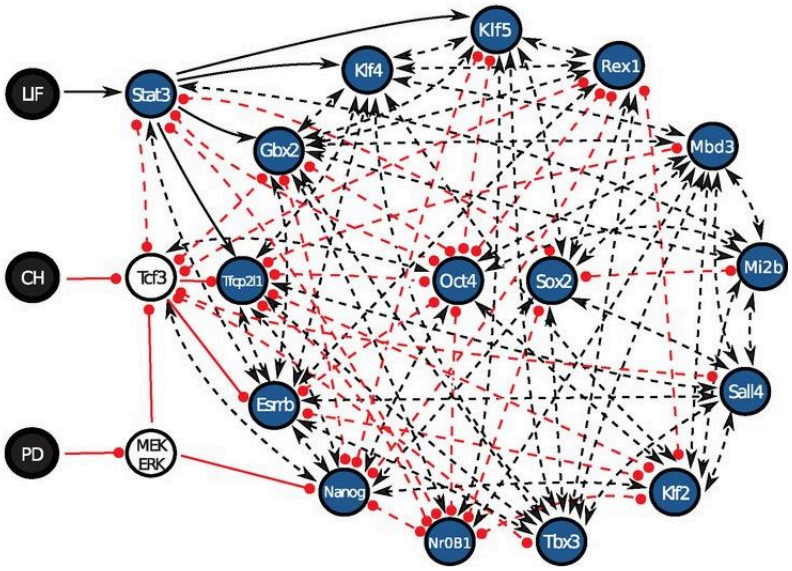

Figure 1.2 The putative programme of the pluripotency network in mice, as predicted from a computational model developed using gene expression in 2i+LIF and N2B27. The network contains definite (solid lines), potential (dashed), positive (black) and inhibitory (red) interactions between proteins (blue and white circles) and chemical inhibitors (LIF, CH, PD in black). Figure adapted from [Dunn et al., 2014].

While pluripotency in the embryo is only a temporary state in a dynamic process, its regulation involves a complex and robust set of factors controlling transcription, protein-protein interactions and epigenetic modifications [Loh and Lim, 2011]. Its inherent complexity is illustrated in Fig. 1.2, with transcription factors Oct4, Sox2 and Nanog at the heart of the

network. Further contributing to the complexity is the fact that the overexpression of these genes can both inhibit (e.g. Nanog) or facilitate (e.g. Oct4) differentiation [Chambers et al., 2003; Niwa et al., 2000; Silva et al., 2009]. As such, ES cells are cultured in an environment that balances pluripotency-maintaining factors with those promoting differentiation. For experimental purposes the actual expression of specific pluripotency genes can be mapped to their typical expression during differentiation, as discussed below, hence providing a readout of the pluripotent state of ES cells [Vallier et al., 2009].

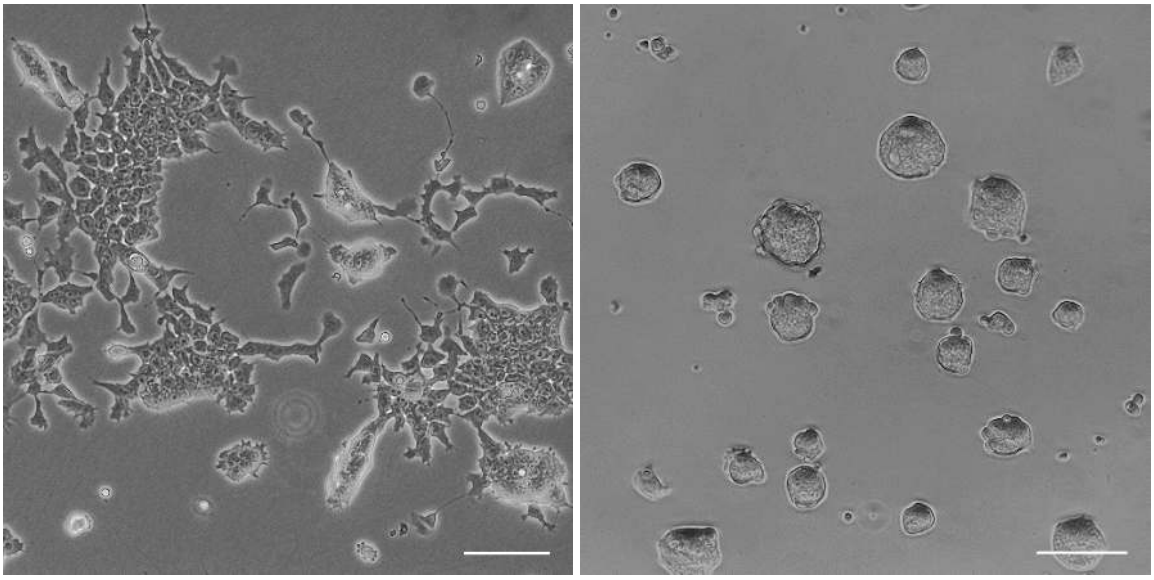

(a) Serum+LIF **(b)** 2i+LIF

Figure 1.3 Comparison of the morphology of wild-type ES cells in (a) Serum+LIF and (b) 2i+LIF medium. On tissue culture plastic, Serum+LIF causes cells to adopt a more flattened conformation, with some spherical colonies throughout. 2i+LIF is characterised by very homogeneous spherical colonies. Scale bar is 100 μm.

Recent culture systems act in a mostly chemical manner to retain ES cells in vitro in a fully pluripotent state, by inhibiting or inducing the expression of particular proteins in the pluripotency network [Williams et al., 1988]. Culturing ES cells in a medium (further referred to as *Serum+LIF*) containing GMEM, serum and LIF, which activates the Stat-3 pathway, produces a heterogeneous population of ES cells in the naive ('fully pluripotent') state combined with cells whose transcriptional profile is closer to early differentiation (for example with a reduced expression of Nanog) [Kalmar et al., 2009; Nichols et al., 1990; Niwa et al., 1998]. The morphology of ES cell culture in Serum+LIF medium is characterised by flattened cells interspersed by spherical colonies, as shown in Fig. 1.3a.

Two other types of medium, *2i* and *2i+LIF*, both used in this study, maintain cells in a more homogeneous state, both in terms of gene expression and morphology, as shown in

Fig. 1.3b [Ying et al., 2008]. 2i contains neuronal differentiation medium supplemented with PD03, which is an inhibitor of the ERK pathway, and CH, which inhibits GSK3 [Bain et al., 2007; Nichols et al., 2009; Wray et al., 2011]. Also adding LIF, to produce 2i+LIF, provides an environment that is more robust and resistant to the noise induced by the day-to-day culture. ES cells in 2i or 2i+LIF are fully naive in their transcriptional profile, and are most similar to cells in the inner cell mass [Boroviak et al., 2014]. Morphologically they are characterised by round spherical colonies that are more easily detached from the substrate.

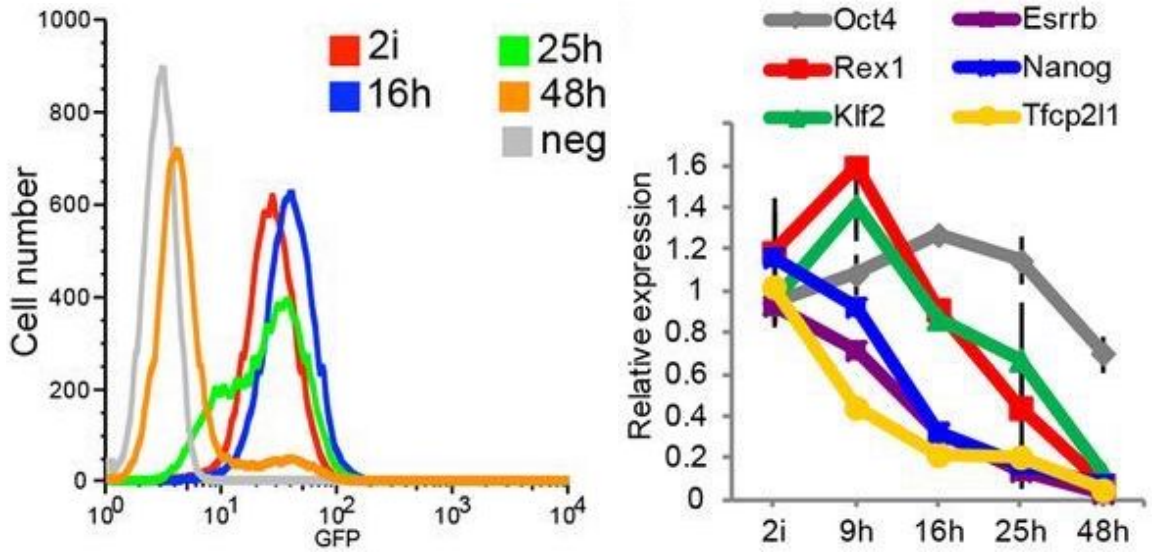

Figure 1.4 (a) Flow profile of Rex1-GFP. The left shift of the distribution accompanies the downregulation of Rex1-GFP between 16 h and 48 h. (b) Expression of pluripotency markers is downregulated at specific times in N2B27 after 2i withdrawal. Figures adapted from [Kalkan et al., 2017].

Differentiation can be induced in both types of medium by removing the inhibitors, either LIF (for Serum+LIF), PD03 and CH (for 2i), or LIF, PD03 and CH (for 2i+LIF). This sets in motion a gradual reduction in the expression of the pluripotency factors [Kalkan et al., 2017]. 24 h after withdrawal of PD03 and CH from 2i, ES cells occupy a transition state, with Nanog having been downregulated and the global distribution of the expression of Rex1, another pluripotency marker, being partially downregulated, as shown in Fig. 1.4a [Wray et al., 2011]. Within the spectrum of pluripotent states, cells in this transition state possess a high potential energy, still capable of reversing to the pluripotent state when the inhibitors are re-introduced, or moving irreversibly towards lineage specification. Indeed, other pluripotency factors such as Oct4 (corresponding to later stages of differentiation) are

downregulated at later timepoints, as shown in Fig. 1.4b. Simultaneously, the expression of markers indicating differentiation increases [Kalkan et al., 2017].

1.2 The mechanisms underlying mechanotransduction

The constant interplay between intracellular processes and the external environment occurs in first instance through the detection and release of biochemical signals. In addition, cells interact with the physical environment, in the form of stress, substrate stiffness, fluid flow and direct forces. This physical influence, which is sometimes attributed a secondary role in biological studies, can be an influential parameter in determining cell shape, spreading, proximity to neighbours, in some situations superseding biochemical cues in driving cell state [Chen et al., 2004; Nonaka et al., 2002; Yamamoto et al., 2004].

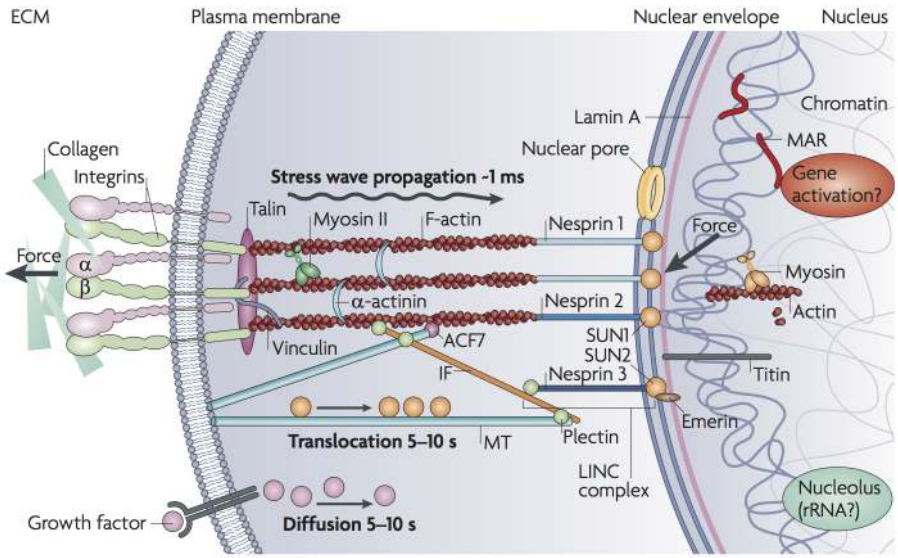

Figure 1.5 The protein networks and mechanisms transmitting forces within the cell, and their links with the nucleus. Figure adapted from [Wang et al., 2009].

In the mouse embryo, the cavity in the blastocyst exerts large-scale forces on the outer layers of the embryo [Mammoto et al., 2012; Wozniak and Chen, 2009]. These play a crucial role in breaking the symmetry in the post-implantation embryo [Shirayoshi et al., 1983]. In the pre-implantation blastocyst also, the physical interactions between the two cell types in the inner cell mass could contribute to the formation of the Primitive Endoderm layer lining the cavity (see Fig. 1.1) [Chowdhury et al., 2010b; Honda et al., 2008; Keller, 2005; Srinivas, 2004]. It is practically impossible to study these mechanisms elegantly in vivo without

secondary undesired experimental effects on cell density and development [D'Angelo et al., 2011]. ES cells in vitro can provide a useful alternative, but it is difficult to replicate the combination of different biophysical and biochemical factors in current systems. For example, substrate stiffness changes cells' preference for cell-cell versus cell-substrate adhesion, which cannot occur in the blastocyst [Wells, 2008]. In this study, we propose a technique to probe mechanotransduction pathways directly, specifically avoiding secondary effects. To assess potential targets for mechanical manipulation and evaluate potential downstream components, in this section I present an overview of the mechanisms involved in mechanotransduction.

An outline of the cellular machinery implicated in the processing of mechanical signals is shown in Fig. 1.5. In the plasma membrane, at the interface with the external environment, extracellular matrix proteins are connected to the integrins, while cadherins allow the formation of cell-cell contacts. These proteins are connected to actin fibres, which provide, together with myosin, tracks for protein motility, allow the build-up of tension in the cytoskeleton, and facilitate cellular movement. As discussed below, since the actin network is connected to the nucleus through the LINC complex, this allows the almost-direct propagation of external forces to the nucleus, and even to DNA (through chromatin domains). However, for this study, the predominant question is at which levels, and how, changes in tension and local stresses induced by the external environment are translated into biochemical signals.

1.2.1 The cytoskeleton

At the heart of cellular systems involved in mechanotransduction, the cytoskeleton connects the cell with the external environment, positions the nucleus and allows the reshuffling of internal cellular components. While both F-actin and the microtubules are involved in the response to physical stress (microtubules mainly at large strains), the ability to rapidly reorganise makes actin the most important component in modulating the cell's global response [Goldyn et al., 2009; Kubitschke et al., 2017]. In addition, actin activity is also influenced by stretch-activated intracellular calcium signalling, connecting it to an important mechanism that translates biophysical into biochemical signals [Glogauer et al., 1997].

Structurally, the persistence length of actin is 9 - 15 µm, increasing to 18 µm when stabilised by phalloidin and decreasing to 2.2 µm when bound by cofilin [Isambert et al., 1995; McCullough et al., 2008]. In addition, while a single filament of longer than 1 µm can withstand a force of several hundreds of pN, a force of only several pN is sufficient to buckle it [Howard, 2001; Kishino and Yanagida, 1988]. Because of these reasons, filamentous actin with a structural role in the cell tends to be either short or bundled, and the actin network consists of arcs, bundles (with a diameter of 7 nm [Gittes et al., 1993]) and local networks of actin fibres [Romet-Lemonne and Jégou, 2013]. This is in contrast to microtubules, which

occur mainly as single filaments, and have a much higher rigidity, derived from their larger cross-section.

Multiple roles and characteristics of the cytoskeleton rely on its existing pre-stress, which is cell-generated cytoskeletal tension. Among others, pre-stress plays a role in the tensegrity model, in maintaining cellular and nuclear shape, in expanding focal adhesions in response to additional stresses, and adjusting the cell's stiffness to that of its substrate [Katsumi et al., 2002; Lee et al., 2015; Park et al., 2010a]. An important role in this process is played by the myosin family of molecular motors, which are also involved in the local transport of proteins [Versaevel et al., 2017]. As such, treatment with Blebbistatin, an inhibitor of myosin II activity, abrogates the translation of substrate stiffness into the chemical signals that influence differentiation [Engler et al., 2006]. As discussed in Section 1.4, the effect of substrate stiffness is partly driven by cell flattening and difficulty in maintaining cytoskeletal tension, which is strongly affected by the inhibition of myosin II. But the loss of non-muscle myosin II also causes the lack of localisation of cytoskeleton components such as E-cadherin, β-catenin and actin to the cell membrane, resulting in negative effects to cell adhesion [Conti et al., 2004].

In ES cells, non-muscle myosin II consists of a bipolar dimer, with head domains on either side, and creates cortical tension in actin filaments by pulling on the filaments in a stepping motion, driven by ATP hydrolysis and the phosphorylation of the light chain [Clark et al., 2007].[1]

1.2.2 Integrins, focal adhesions and mechanotransduction

The actomyosin skeleton is connected to the extracellular matrix (ECM) and the outside world through focal adhesions, which maintain contact with the substrate, even in elastic conditions, and allow the build-up of tension in the cytoskeleton [Wang, 2017]. At the heart of the focal adhesions is a dimer of two integrin subunits that cross the plasma membrane and bind to a range of ECM proteins such as fibronectin, laminin and collagen, as shown in Fig. 1.6 [Zamir et al., 1999]. They are supplemented by, among others, zyxin, talin, vinculin and paxillin, which connect the integrins to actin fibres [Critchley, 2000].

An initial set of proteins forms early ECM connections in focal adhesions, including paxillin and β-integrins, which are supplemented by other proteins such as zyxin in a later, more stable, phase [Zaidel-Bar, 2003]. Interestingly, applying forces (e.g. through a ligand-

[1] In fact, particularly the non-muscle myosin IIB isoform is well suited to the task of inducing cortical tensions. Its specific conformation results in a slower release of ADP after conversion from ATP, which makes this a slower but more-energy efficient isoform, and therefore better suited to inducing tension [Vicente-Manzanares et al., 2009].

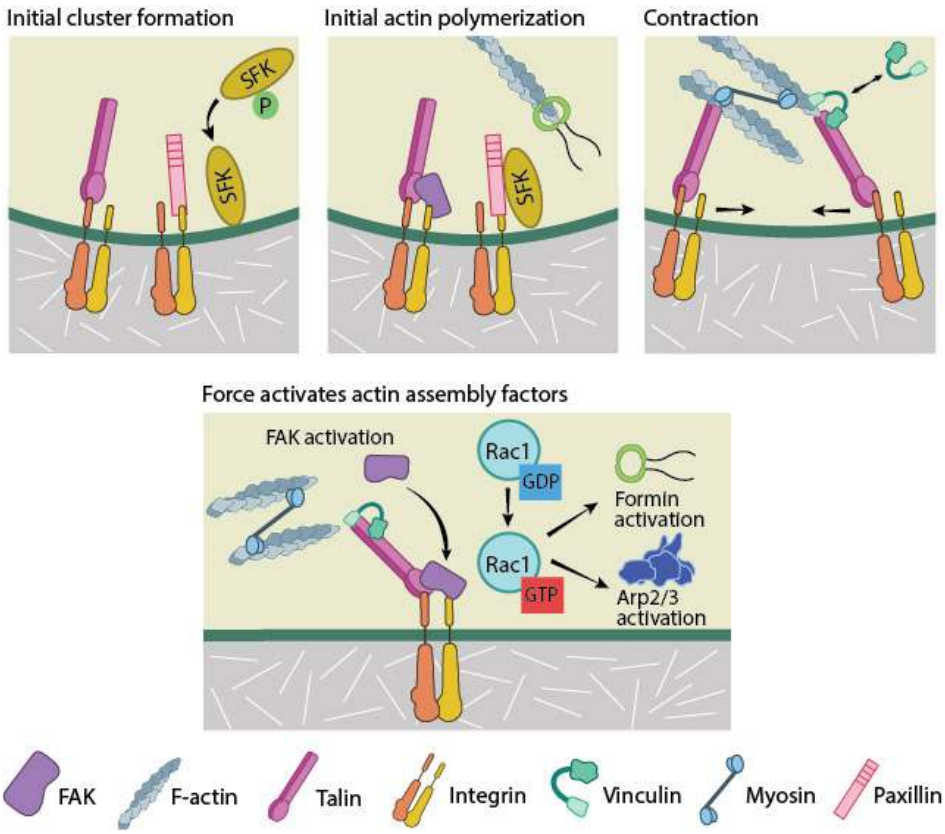

Figure 1.6 The focal adhesions connect the actin cytoskeleton to the external environment of the cell. Multiple proteins regulate and adapt the focal adhesions and the integrins to external mechanical signals. Figure adapted from [Vicente-Manzanares et al., 2009].

coated magnetic bead) to the integrins results in the recruitment of vinculin and zyxin within 30 s, and the assembly and growth of the focal adhesion, including the phosphorylation of paxillin [Bershadsky et al., 2003; Humphries et al., 2007; Wang et al., 1993]. On longer timescales of several minutes, additional integrins are recruited, followed by the activation of biochemical pathways such as JNK and c-src [Katsumi et al., 2005; Schwartz and DeSimone, 2008]. As such, the focal adhesions are a key mechanotransduction site heavily involved in translating mechanical into biochemical cues and subsequently responding to them [Janoštiak et al., 2014].

Indeed, the integrins have already been connected to mechanotransduction-related cellular activity in a variety of mechanisms. Setting off the signalling cascade activated by mechanical signals to the integrins, are the phosphorylation of FAK and the binding of Src and other proteins to FAK, followed by the interaction with Rac1 [Bass et al., 2008]. RhoA, an antagonist of Rac1, is directly involved of the regulation of the cytoskeleton. Rho and

Rac interact with the formins, which produce straight unbranched actin fibres, with WAVE proteins, which activate the actin-bindin Arp2/3 complex, and with cofilin, which severs existing actin fibres [Matsui et al., 1996; Suetsugu et al., 1999; Yang et al., 1998]. The overall cascade also causes the phosphorylation of myosin, increasing contractility, which in turn, promotes the formation of stress fibres and focal adhesions [Chrzanowska-Wodnicka and Burridge, 1996; Dovas et al., 2006]. Also, crosslinking of $\beta 1$ and $\beta 2$ integrins during fibronectin adhesion in monocytes and fibroblasts, affects the MAPK pathway [Schlaepfer et al., 1994] and induces the activation (through phosphorylation) of Erk and the activation of PI-3K [Reyes-Reyes et al., 2002]. Overall, Erk activation through the integrins at least involves FAK, Ras, Sos, Grb2 and Shc [Yee et al., 2008].

The strength of the cell's attachment to the ECM is determined by the weakest link in the focal adhesion network or by the longest lifetime of the bonds in the network (which is in the range of seconds) [Boettiger, 2007; Fuhrmann and Engler, 2015]. Estimates are in the 10 - 100 pN range per integrin-fibronectin pair (this explains why cells easily resist washes, as this only applies a total force per cell around 100 pN) [Hsieh et al., 2006; Litvinov et al., 2002]. A weaker link is formed by the intracellular connections of the integrins to the cytoskeleton. A retrograde flow of actin of more than 2 pN can already break the bond between actin and an integrin protein [Grashoff et al., 2010; Jiang et al., 2003]. Interestingly, however, externally applying a force to the integrins strengthens the integrin-cytoskeleton bond, allowing it to resist much larger forces of up to 20 pN [Choquet et al., 1997]. In addition, the size of the focal adhesions increases as a larger force is applied to them or with increasing matrix stiffness [Yeh et al., 2017]. These two examples illustrate an essential feature of the focal adhesions (and of the entire cytoskeleton), namely the possibility to adapt to external forces, mediated (among others) by the proteins talin and vinculin. Talin is a large cytoskeletal protein that can bind both actin, vinculin and integrin. As a tensile force is applied to the protein, more of its vinculin binding sites open up [Hirata et al., 2014]. Considering vinculin is another actin-binding molecule that strengthens talin, this causes the accumulation of vinculin and an increase in the tensile strength of the focal adhesions [Dumbauld et al., 2010]. Another protein, zyxin also acts as a stress sensor, translocating to locations on stress fibres that are experiencing high tension, and contributing to strengthening them [Hoffman et al., 2012; Yoshigi et al., 2005].

This mechanism thus partially explains the importance of cytoskeletal prestress to allow cells to adapt to changes in external stiffnesses and force, since it allows an increase in actin tension to be propagated to talin and zyxin, triggering the next stage of mechanosensitive signals and cytoskeletal adjustment. As such, increased force resistance of the ECM-cytoskeletal links occurs both through the clustering and increase in number of integrins, and the enlarging

of the focal adhesions and the strengthening of the constituent components, such as talin and vinculin [Gallant, 2005].

1.2.3 Binding to the extracellular matrix

Different types of integrins have a specific binding preference for the different ECM proteins, and at least ten out of a minimum of 22 can bind to fibronectin, conveying substrate specificity to mechanotransduction [Humphries, 1996; Johansson et al., 1997]. Integrin $\alpha_5\beta_1$, the most common integrin and which specifically binds to fibronectin, relieves cytoskeletal tension, thereby causing cell flattening [Bass et al., 2008; Dalton et al., 1992; Danen et al., 2002].

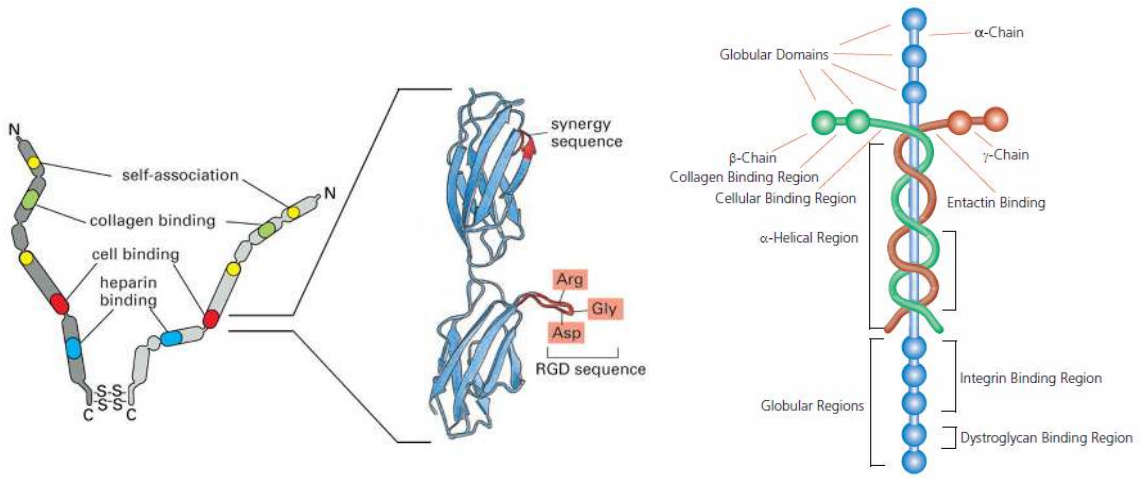

(a) Fibronectin **(b)** Laminin

Figure 1.7 Diagrams of the structure of the ECM proteins (a) fibronectin and (b) laminin. Figures adapted from (a) [Alberts et al., 2002] and (b) [Sitterley, 2008].

Fibronectin contains four types of modules, as shown in Fig 1.7a, which interact with cellular components, other types of ECM, and fibronectin itself [Kadler et al., 2008]. Through one of the modules, fibronectin forms dimers connected by disulfide bridges. A consensus site, which includes the RGD (Arg-Gly-Asp) motif, binds to the integrins, although the binding affinity for the whole protein is multitudes higher than for synthetics containing only the RGD motif [Akiyama and Yamada, 1985]. Fibronectin's ECM binding sites also allow ECM network formation with other ECM proteins, usually only after integrin binding causes a conformational change that exposes the relevant sites [Wu et al., 1993]. For example, some types of collagen, another type of ECM protein, require the presence of fibronectin to assemble.

Laminin is bound by a smaller subset of integrins, particularly $\alpha_3\beta_1$ which binds only weakly to fibronectin, and $\alpha_6\beta_1$ [Burridge and Chrzanowska-Wodnicka, 1996; Nishiuchi et al., 2006]. Laminin comprises three different domains in a tree structure, as shown in Fig 1.7b, with the stem formed by a helix of the three domains which are exposed near the top [Durbeej, 2010]. Although fibronectin is more common in vivo, laminin plays a particularly important role in the embryo, where it appears from at the 16-cell stage and remains present during the formation of the inner cell mass. Also different to fibronectin, laminin can bind to the dystroglycan complex, an alternative to integrin binding, which is required for the deposition of laminin by ES cells on their substrate. Although less is known about this complex than about integrins, they also bind to the actin cytoskeleton, constituting another direct link between the cytoskeleton and the outside world [Henry and Campbell, 1998].

Some types of collagen automatically self-assemble into fibres. Gelatin, in contrast, is a disordered form of collagen which both cheaper and easier to handle, and is often used in ES cell culture. Particularly in 2i+LIF culture, good cell adhesion requires coating of plastic dishes with ECM proteins. Interestingly, there are significant differences in the behaviour of cells grown on different ECM proteins. For example, ES cells in 2i+LIF usually form round colonies on gelatin, but flatten on fibronectin. Initial differentiation from 2i+LIF into N2B27 is possible on gelatin, fibronectin or laminin, but should ideally be performed on a laminin coating beyond 36 hours, as cell death can be significantly higher otherwise. Since different types of integrins are involved in the binding of these different types of ECM protein, the effects on differentiation are likely a reflection of how the differences in signalling propagated by the integrins affect pluripotency pathways, with a particular emphasis on the MAPK pathway, which is an important source of overlap between the mechanosensing and pluripotency networks.

1.2.4 The nucleus as mechanosensor

The nucleus, at the other end of the cytoskeletal network, is connected to actin fibres through the nesprins, a part of the LINC complex. Anchored within the nuclear membrane, the LINC complex provides a direct link between the external physical environment and chromatin architecture [Crisp et al., 2006]. In most cell types a viscoelastic network of intermediate filaments, called lamins, provide structural support to the nucleus and chromatin [Gruenbaum et al., 2005; Tee et al., 2011]. In ES cells, interestingly, a key element in this network, Lamin A/C, which forms a stable mesh, is absent (or at the least very lowly expressed). Instead only lamin B and lamin B-receptor (LBR) are expressed in ES cells [Constantinescu et al., 2006]. While the absence of lamin A/C does not prevent the bulk of lamina-gene interactions, it strongly reduces the structural role of the nuclear lamina [Pajerowski et al., 2007]. Possibly

as a result of this, embryonic stem cells do not adapt to the stiffness of the substrate to the same extent as most other cell types [Poh et al., 2010].

The putative role played by the nucleus in mechanosensing partially depends on the stiffness of the nucleus itself. While estimates vary widely (partly due to difficulties of extracting the nucleus while maintaining its structural properties), evidence indicates that the stiffness of the nucleus is higher than that of the cytoplasm, and is established by the nuclear lamina [Caille et al., 2002; Dahl et al., 2008]. Due to the absence of Lamin A/C, ES cell nuclei are extremely soft, and undergo a five-fold stiffening during differentiation. Therefore, a rearrangement of chromatin in ES cells, for example induced through a change in the ratio of euchromatin to heterochromatin, could affect the stiffness and therefore also the mechanosensitivity of the nucleus [Pajerowski et al., 2007]. Indeed, as discussed below, the effects of substrate stiffness on pluripotency, which enters the cell as physical inputs, could be translated either by the integrins or at a later stage, by the mechanical links anchoring the nucleus to the external environment.

Interestingly, it has recently been shown that local stresses applied to the surface of a cell can deform chromatin in the nucleus and induce transcription of a transgene, demonstrating that local forces are directly propagated to the nucleus and influence transcription [Tajik et al., 2016]. Applying forces directly to isolated nuclei causes stiffening of the nucleus and is dependent on emerin, another component of the LINC complex [Guilluy et al., 2014]. In addition, regions of genes can be tethered to the nuclear lamina (at locations called lamina-associated domains or LADs) [Kind et al., 2015]. Evidence indicates that moving genes to the nuclear lamina has a repressive effect [Reddy et al., 2008]. The combination of the two elements above, i.e. the physical links between the nucleus and the external environment on one hand, and indications of direct lamina-chromatin interactions on the other, points towards a direct effect of mechanotransduction pathways on gene expression, and a larger-scale impact on differentiation. In this study, we aim to develop and apply tools to investigate these effects further.

1.3 Techniques to probe cells' mechanosensitivity

On the whole, three (overlapping) types of experiments exist. First, mechanical experiments can be used to gain insight into the material characteristics of the cell, such as their stiffness or elastic response. Second, the targeted application of external forces can provide insight into the transduction of forces and their translation into biochemical signals. A third approach comprises studying the overall effects of changing cells' global biophysical mechanical environment, including on spreading and alignment, proliferation and cell state

(e.g. differentiation). This project focuses on a combination of the second and third of these elements.

1.3.1 Modifying substrate stiffness and the effects on morphology and behaviour

Culture plastic, used in most biological experiments, has a stiffness that is positioned at the upper end of the physiological range, with an elastic modulus of 2-4 GPa, as shown in Fig. 1.8. Work during the last two decades has indicated the importance of substrate stiffness in driving cell morphology and behaviour. Since plastic does not accurately replicate most in vivo environments, these findings have relied on the development on substrates whose stiffnesses can be controlled [Cox and Erler, 2011].

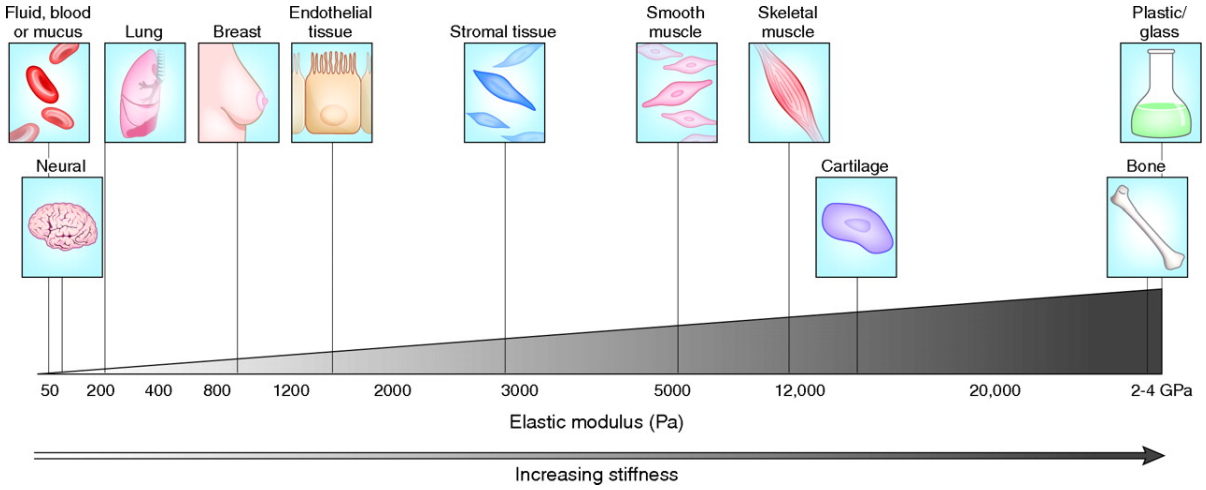

Figure 1.8 In vivo tissues span a range of stiffnesses from 50 Pa to 2 GPa, while plastic in vitro culture systems have an elastic modulus of around 2 GPa. Figure adapted from [Cox and Erler, 2011].

The importance of substrate stiffness in tissue culture was first described through the effects on cell migration, called *durotaxis*, which is the enhancement of cells' migration on stiff compared to soft substrates (even in 3D culture) [Lo et al., 2000; Zaman et al., 2006]. Focal adhesions and myosin play an important role in this feature, with an increased stability and shape on stiff substrates compared to soft substrates, cytoskeletal stiffening and increased PI3K (a protein involved in cell-cycle regulation) activation [Pelham and Wang, 1997].

The morphology of cells on stiff substrates is remarkably different compared to soft substrates, as shown in Fig. 1.9. ES cell colonies in Serum+LIF, which on plastic and stiff substrates of 30 kPa exhibit a flattened morphology similar to the one shown in Fig. 1.9a,

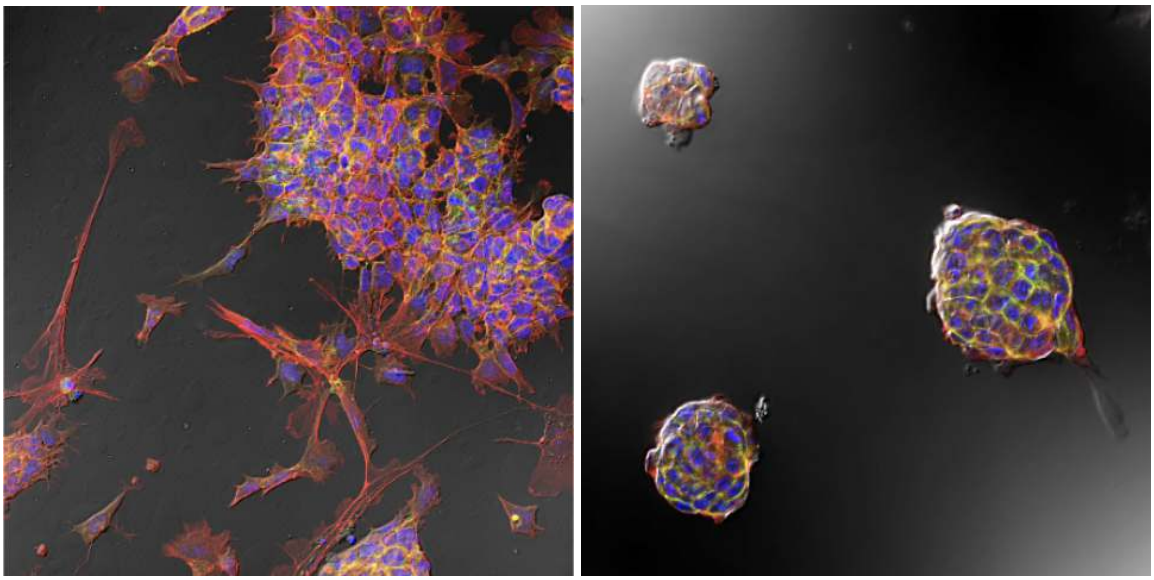

(a) 30 kPa **(b)** 0.3 kPa

Figure 1.9 Comparison of the morphology of ES cells in Serum+LIF on hydrogels with a stiffness of (a) 30 kPa and (b) 0.3 kPa. Cells on stiff substrates are characterised by a flattened and spread morphology, while cells on soft substrate maintain a rounded morphology. Actin in red, E-Cadherin in green, Hoechst in blue. Image courtesy of Chibeza Agley.

form spherical colonies when cultured on soft gels with a stiffness of 0.3 kPa. This difference is reflected in the cytoskeleton, with fewer actin stress fibres and lower integrin expression in cells on soft substrates, and in the difference in cellular contractility [Tee et al., 2011; Yeung et al., 2005]. Overall, cells appear to adapt to stiff substrates by increasing the organisation of the cytoskeleton and enhancing the stability of matrix adhesions [Discher et al., 2005].

The nucleus again appears to play a role in this process. In fibroblasts, the nucleus is flattened on stiff substrates and almost spherical on soft substrates, which corresponds to what our lab observed in ES cells on soft hydrogels (cf. Fig. 1.9) [Lovett et al., 2013]. Structurally, tissue stiffness and expression levels of lamin A are directly correlated across most cell types that possess lamin A/C, and this interplay between external stiffness and internal structure likely involves their active regulation [Swift et al., 2013]. Furthermore, a change in cytoskeletal tension induced by substrate stiffness is associated with differences in the phosphorylation of the lamins, with high nuclear tension being associated with lamin A dephosphorylation, which in turn affects nuclear stiffness [Buxboim et al., 2014]. It is currently not well understood to which extent these structural changes are reflected in differential gene expression. However, one of the areas most heavily influenced by substrate stiffness is pluripotency and differentiation, as discussed in the next section.

Compared to targeted forces, large-scale techniques lack specificity in the effects they induce [Discher et al., 2005]. As a consequence, the downstream result of changes to substrate stiffness are often difficult to distinguish from any secondary effects. For instance, as discussed, a change in substrate stiffness influences cell attachment, leading to a shift in the balance between cell-cell versus cell-substrate assessment. As such, this is a clear effect of mechanical signalling on cell morphology. However, any subsequent changes in cell behaviour or state could be the result of either this change in morphology (the primary effect), or of a shift in biochemical cell-to-cell signalling (paracrine signalling) caused by increased (or decreased) cell-cell contact (a secondary effect). As such, when analysing cell behaviour, it is often difficult to distinguish the direct mechanical effects from any additional, secondary effects.

1.3.2 Applying cell-wide deformations through cell stretching

To distinguish mechanical forces from secondary biochemical effects, devices have been designed to apply cell-wide deformations without influencing any additional environmental parameters. This study contributes to this field by presenting a novel type of cell substrate stretcher and applying it to study the mechanosensitivity of stem cells. Therefore, in this section I present a review of past development efforts.

Although rubber was first used as a substrate, most recent methods to apply cell-scale deformations rely on polydimethylsiloxane (PDMS), a transparent elastomer that is biocompatible, easy to manufacture, and can be functionalised with extracellular matrix proteins. Several different approaches can be used to attach a range of standard ECM proteins to the membrane, including fibronectin, collagen, laminin and other artificial proteins such as RGD. As PDMS is very hydrophobic, the first step involves the hydrophilization, for example using plasma treatment. One commonly used approach involves the use of the sulfo-SANPAH UV-activated crosslinker to connect the hydroxyl groups thus created to extracellular matrix proteins [Li et al., 2006; Trappmann et al., 2012]. The strength of these bonds is not always sufficient to prevent cell detachment for some cell types at high densities [Brown et al., 2005; Cunningham et al., 2002]. We present a novel alternative technique, discussed further in Section 4.2.3, which relies on the salinisation of the PDMS surface, followed by the binding of an amine crosslinker. Since ECM proteins are bound covalently, this method results in improved attachment [Wipff et al., 2009].

The specific ECM protein used to functionalise the substrate plays an important role, both from a biophysical and biochemical point of view. It was reported that in vascular muscle cells, two important markers of stretching, Egr-1 and Jun (discussed below), were upregulated when these cells were grown on collagen or fibronectin, but not on laminin

[Morawietz et al., 1999]. In fibroblast, a single biaxial stretch of 4% activated Erk, but only when grown on fibronectin, while JNK was activated on fibronectin or laminin (but not collagen) [MacKenna et al., 1998]. As discussed, this is likely due to the specific response to binding of particular integrins to different ECM proteins. In addition, the measured stiffness of the membrane can deviate by at least one magnitude depending on which ECM protein is bound [Bartalena et al., 2012].

After cells are attached to the substrates, cell-wide deformations can be applied by stretching the membrane along a single axis (uniaxially) or in all directions outwards from the centre (biaxially). The advantage of the former is its experimental and scientific elegance; cells can be stretched by simply pulling the membrane in one direction. Among others, a device for this purpose was presented by Fink et al. [2011] to exert deformations with the aim of altering spindle positioning during mitosis. Alternatively, biaxial stretch can be applied to a circular membrane by changing the pressure below it, causing it to bulge out or in [Gorfien et al., 1989; Schaffer et al., 1994; Winston et al., 1989]. Other more complex devices have also been developed, for example relying on microfluidics [Kamble et al., 2016; Tremblay et al., 2014].

In most cell types, single continuous stretch suffices to induce initial downstream signalling (as discussed in the next section), but stronger effects can be achieved with cyclic stretching [Morawietz et al., 1999]. In particular, stretching of cells and their substrate is particularly relevant for cardiac and muscle cells, cell types which are continuously exposed to stretch and compression in vivo, and these cells have been the main area of focus of cell stretching. To better replicate the conditions experienced by these cell types, some studies have relied on cyclic stretching, typically at frequencies around 1 Hz. Neidlinger Wilke et al. [1994] used this type of approach, i.e. stretching at 1 Hz for 15 min per day to find that low magnitudes of stretching (below 2%) increased the proliferation of osteoblasts in response to cyclic stretching. Interestingly, endothelial cells have been observed to align in the direction perpendicular to the direction of stretching, as shown in Fig. 1.10, when they are stretched cyclically, but to align parallel to the direction of stretch when stretched statically [De et al., 2007; Hsu et al., 2010; Moretti et al., 2004; Wang et al., 2001]. In contrast, the opposite behaviour was observed in vascular muscle cells, neurites and fibroblasts, which were observed to orient or grow in the direction of stretching and shrink in the direction perpendicular to stretching [Haston et al., 1983; Katsumi et al., 2002]. Also in smooth muscle cells, low levels of stretch (10%) decreased proliferation, while higher levels increased it [Kona et al., 2009].

As illustrated using the examples above, while most studies use comparable approaches, the particular biological results are highly dependent on the cell type and the specifics of the

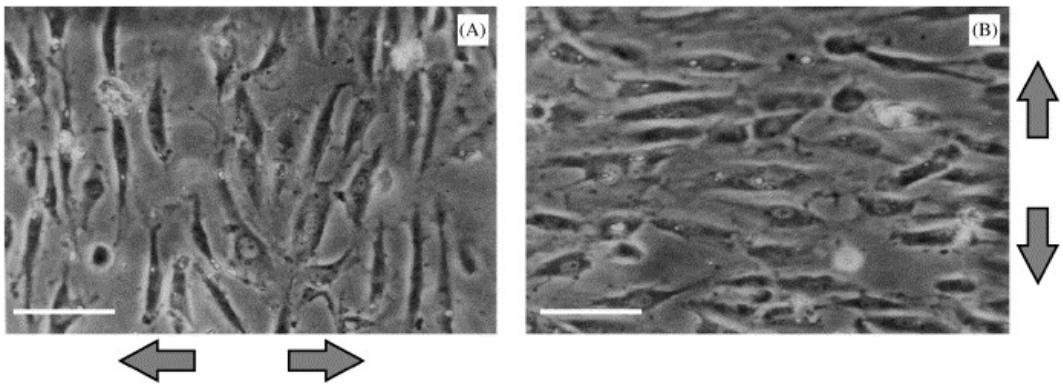

Figure 1.10 Human aortic endothelial cells are stretched in the direction of the arrows, resulting in a reorientation in the direction perpendicular to the direction of stretching. Scale bar is 100 µm. Figure adapted from [Wang et al., 2001].

experiment. ES cells are a very sensitive (both with respect to biochemical and mechanical cues) and dynamic cell type. Also, because they only adhere to substrates in particular conditions, they require a highly optimised system. Likely for this reason, little work has been carried out on the effects of stretching on embryonic stem cells.

1.3.3 The overall cellular response to stretching

The cellular response induced by stretching of the substrate involves multiple pathways, morphological changes, gene expression and protein translation. These are reflective of the profound changes in cell state that can be induced by this large-scale form of mechanical input [Neidlinger Wilke et al., 1994; Wang et al., 2005].

The first genes affected by stretch are members of a family of genes called 'Early and Immediate Genes' (IEGs), including Egr-1, Fos, Jun and Myc. These genes constitute a quick response system activated in response to a wide range of types of stress, for example after heat shock, exposure to UV radiation, and even behavioural training [Bahrami and Drabløs, 2016; Guzowski et al., 2001; Wisdom et al., 1999]. The baseline expression level in ES cells is typically very low, but they are upregulated rapidly after stretching [Gaut et al., 2016]. Egr-1, for example, can be upregulated 10 to 20-fold within minutes after stretching, while Jun and Fos respond on timescales of 1-2 hours [Dawes et al., 1996; Yamaguchi et al., 2002]. Interestingly, the precise dynamics of the response of the IEGs, both in terms of time-specificity, duration and magnitude, depend on the type (and potentially intensity) of the stress signal. Also cell type, strain magnitude (when stretching) and ECM appear to play a role; for example Morawietz et al. [1999] report that Fos expression is not induced in

vascular smooth muscle cells, while we do observe expression of Fos when stretching ES cells (see Section 5.2.1).

The dynamics leading to IEG expression are one of the most complex in the cell. Transcription of the IEGs is, among others, influenced by Erk. This member of the MAPK pathway is at the crossroads of global signalling within cells; as discussed, its activation is connected to the integrins through FAK-Ras-Sos signals [Bass et al., 2008; Yee et al., 2008], but this cascade is also influenced by EGF, meaning Erk is exposed to both mechanical and biochemical external cues [Sparta et al., 2015]. In addition to Gsk3, 2i culture media inhibits MEK, an activator of Erk, putting Erk and the MAPK pathway also on the front row of the regulation of pluripotency [Ying et al., 2008]. Its activation can lead to translocation into the nucleus, and incorporates multiple feedback loops. As such, the activation of Erk by mechanical inputs might have both wide-ranging effects and be mediated through complicated mechanisms [Kolch, 2000].

Erk has been shown to be active in the form of short repeated pulses [Aoki et al., 2013]. Recent evidence shows that the IEGs are regulated through a dynamic filtering of Erk signals, where only specific pulse frequencies of Erk activity are converted into sustained IEG transcription [Ryu et al., 2015]. For example, the continuous activation of Erk only results in a transient peak in Fos expression, while pulsing with a period of 32 min maximises its long-term transcription [Wilson et al., 2017]. While these dynamics are likely similar across different IEGs, additional levels of control not related to this mechanism regulate the specificity of the IEG response. For example Erk also influences IEG activity through phosphorylation, modulating the half-life of the IEG proteins [Murphy et al., 2002]. As such, high levels of IEG transcription do not necessarily result in high levels of downstream transcription.

For both Fos and Egr-1, the direct mechanism leading to their activation consists of the phosphorylation of Elk-1 and its subsequent binding to the SRE on the promoter of the Fos or Egr-1 gene [Babu et al., 2000]. The gene output of both genes is also dependent on Serum Response Factor, which is influenced by the presence of Serum, indicating a likely difference in the response of ES cells to stretching when grown in Serum+LIF conditions compared to the serum-free 2i+LIF [Gille et al., 1995]. The activation of Fos transcription by Erk can also be induced through an alternative mechanism within the MAPK pathway. In certain cases, Elk-1 has also been described to be activated also by the JNK, bypassing the activation of Elk-1 by Erk [Cavigelli et al., 1995; Silvers et al., 2003].

Another IEG, Jun, is also phosphorylated and activated by JNK, incorporating a positive feedback loop whereby Jun binds to its own promoter, together with ATF2 [Gregg and Fraizer, 2011; Herdegen et al., 1997]. And similar to the other IEGs, activated Erk affects

both the transcription and the activity of Jun. Considering the four IEGs discussed here are all (indirectly) transcription factors, their downstream effects consist mainly of the activation of additional genes and mediating the global cellular response to external stresses. One of these mechanisms involves the AP-1 complex, which is composed of Jun, Fos and/or ATF, and regulates transcription directly. It has been described to be involved in cell growth, differentiation and the mediation of apoptosis [Ameyar et al., 2003; Eckert et al., 2013; Sui et al., 2014]. The precise role of the AP-1 complex in the stretch response is still unclear, with different reports pointing towards either responses by specific proteins in the MAPK pathway or the AP-1 complex as the dominant method of activation and upregulation [Kito et al., 2000; Kushida et al., 2001; Nadruz et al., 2005].

Apart from the conventional mechanotransductive pathways discussed above, in cardiac myocytes, stretching (20%) was observed to induce an increase (within 24 - 48 h) in the expression of α-actinin and β-myosin heavy chain [Sadoshima et al., 1992]. While these cells were also observed not to remodel significantly upon stretching, these results indicate that stretching has a significant effect on the cytoskeleton on longer timescales. This is unlikely to hold in ES cells, which have short cell cycles and rapid cytoskeletal remodelling, allowing them to mitigate stretch quickly. In addition, although promotion of actin expression also occurs through the binding of activators to the SRE domain of the actin promoter, the mechanisms behind the activation of actin expression are likely to differ from those of Fos [Carson et al., 1995].[2]

Finally, stretching causes a number of separate, broader mechanosensitive responses. For example, stretching of cardiomyocites and osteoblasts induces intracellular Ca^{2+} accumulation by activating stress-sensitive calcium channels such as TRPV4, with additional downstream effects (e.g. to calcium-sensitive phospholipases such as PI3K), followed by a steady decrease after stretching [Matthews et al., 2010]. Stretching osteoblasts in Ca^{2+}-free medium reduces the calcium response to stretching, and this response appears to be entirely separate from the induction of the IEGs [Sadoshima and Izumo, 1997; Walker et al., 2000]. However, in neurons, a calcium influx can lead to Erk1/2 activation, indicating that calcium might feed into the same MAPK pathway that the IEGs can also activate [Dolmetsch et al., 2001]. Furthermore, the activation of JNK, a part of the MAPK pathway, in response to stretching in smooth muscle cells was dependent on extracellular calcium, stretch-activated ion channels and calmodulin (a messenger protein).

Stretching also induces the expression of a range of growth factors such as TCF-β and PDGF [Skutek et al., 2001], which might tie into the increase proliferative response described

[2]This is likely to be the case because, out of three SREs in the actin promoter, only an SRE bound by protein YY1 is essential for the activation of actin in response to stretching.

above. In addition, cells undergoing long-term (48 h) stretching (cyclic) exhibit an increased expression of extracellular matrix proteins such as collagen [Harter et al., 1995].

1.4 Mechanotransduction and pluripotency

The profound effect of the mechanical environment on cell state, morphology and organisation extends to pluripotency, as it induces, discourages or specifies differentiation [Sun et al., 2012a]. Tissue stiffness is one of the primary drivers of this process, both in vivo and in vitro. For example, in muscle stem cells, higher stiffness and lower fibronectin levels have been observed in aged tissues, pointing to the role of stiffness and ECM in regulating stemness and ageing [Gilbert et al., 2010; Lukjanenko et al., 2016]. In general, the influence of stiffness is mediated by external factors on one hand, such as type of ECM (see earlier), attachment level, and cell spreading, and by internal contractility and biochemical factors on the other.

Mesenchymal stem cells' lineage choice is partially dependent on the stiffness of their substrate, with soft substrates (0.1-1 kPa) inducing differentiation towards neurogenic lineages while rigid substrates (25 - 40 kPa) cause osteogenic differentiation [Engler et al., 2006]. This behaviour is dependent on non-muscle myosin II. Similarly, self-renewal of muscle stem cells in culture is enhanced on relatively soft (12 kPa) substrates but is rapidly lost on stiff substrates (10^6 kPa) [Gilbert et al., 2010]. Since the morphology of cells on these substrates, similarly to those shown in Fig. 1.9, is substantially different, cell shape and spreading might be an intermediate factor in the downstream effects on cell state. In mouse ES cells, preventing cell spreading by limiting substrate attachment inhibits differentiation, allowing cells to be cultured in Serum only (without LIF) [Murray et al., 2013]. While increasing the amount of substrate-bound fibronectin increases spreading, it is accompanied by a reduction in pluripotency markers. This mechanism is likely driven by direct cell-substrate attachment via the integrins, as a lack of fibronectin (including that produced by the cell itself) is detrimental to transitions in pluripotency [Hunt et al., 2012].

The effect of substrate stiffness, and thus of cell spreading, is modulated internally through cytoskeletal contractility. Generated by RhoA and ROCK, contractility is required for the differentiation of human mesenchymal stem cells into osteoblasts. Modulating spreading or contractility, by micro-patterning PDMS surfaces or by activating ROCK, influences lineage specification, as shown in Fig. 1.11 [McBeath et al., 2004]. This indicates that both the external physical environment as well as the internal downstream mechanotransductive pathways are important in modulating the effects of mechanics on differentiation.

Most evidence originates from later stages of differentiation, and less is known about the role of the mechanical environment in driving differentiation of ES cells. Findings from

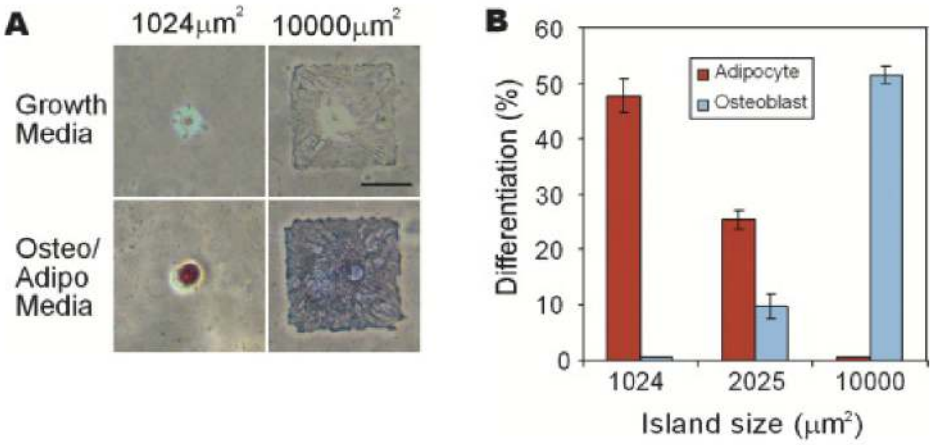

Figure 1.11 Growing human mesenchymal stem cells (hMSCs) on patterns with different sizes induces different lineage specification. A. hMSCs are grown in two types of culture medium on fibronectin islands with a surface area of 1024 μm^2 and 10000 μm^2, alkaline phosphatase staining in red. B. Differentiation into two types of lineages, after one week of culture in osteo/adipo medium. Figure adapted from [McBeath et al., 2004].

our lab indicate the impact on the pluripotent state of substrate stiffness [Chibeza Agley, Celine Labouesse, *personal communications*]. Pluripotency of ES cells is maintained even in difficult conditions containing only a single chemical inhibitor when they are cultured on soft substrates. These findings are confirmed by the observation that mouse embryonic stem cells grown in Serum+LIF medium remain largely undifferentiated and produced teratomas five days after LIF is removed, when grown on soft (600 Pa) substrates, but not when grown on stiff ($> 4 \times 10^6$ Pa) substrates (both coated with collagen) [Chowdhury et al., 2010a]. The two conditions also differ in the higher expression levels of Oct4 and alkaline phosphatase on soft substrates. Interestingly, growing human ES cells on stiff substrates has been observed to increase the maintenance of pluripotency, which is the reverse observed in mouse ES cells [Sun et al., 2012b].

Two important questions that remain unresolved, however, are at which stages of differentiation mechanical forces play a role, and how their magnitude compares with that of biochemical cues. For example, in the experiments of Engler et al. [2006], within the first week of differentiation inhibitors could reverse the lineage choice prompted by substrate stiffness, but not at later stages, indicating that mechanical cues can affect only early pathways to the extent that they induce a permanent switch. Similarly, mesenchymal stem cells on stiff substrates exhibit early soft muscle cell markers such as α-actin, but do not on soft substrates, a difference that can be amplified by the expression of TGF-β [Park et al., 2011].

In ES cells, the phenotypical differences between cells on stiff and soft gels are amplified by the addition of PD03 [Chibeza Agley, Celine Labouesse, *personal communications*]. It is not quite clear if growing cells on soft substrate induces a distinct pathway that 'nudges' cells more towards pluripotency, or whether it merely compliments or amplifies the signals of the inhibitors. This latter effect might not be sufficient to retain cells in the pluripotent states in certain situations, while the combination of the biophysical signals and the inhibitors could be [Chowdhury et al., 2010a].

Pluripotency is also influenced by the application of active forces on cells, both when targeted to specific areas of the cell or when applied globally. For example, in ES cells plated on collagen IV-coated substrates and undergoing differentiation, stretching increases the growth rate and increases markers of vascular smooth muscle cell differentiation in a PDGFRβ-dependent manner. Shear stress, on the other hand, increases markers of vascular endothelial cells [Shimizu et al., 2008; Yamamoto et al., 2004]. Another study proposes a role for reactive oxygen species in transducing mechanical signals in embryoid bodies, which were found to enhance cardiovascular differentiation [Schmelter et al., 2006]. Contrasting with these findings, differentiation of human ES cells was found to be reduced (but not abolished) in response to cyclic strain of 10% [Saha et al., 2006].

These effects also occur in response to targeted forces. Applying a cyclic force to embryonic stem cells using a 4 μm RGD-coated magnetic bead caused spreading, and applying a continuous stress of 17.5 Pa using this technique for 60 min induced a 50% downregulation of Oct4 after 72 h [Chowdhury et al., 2010b]. This observation indicates the relevance of even small forces to the system regulating pluripotency in ES cells, although an effect of this magnitude still is to be reproduced in other settings. In addition, the level of spreading after applying this local stretch was different for differentiated cells compared to ES cells. The response of cells to the localised stretching depends on the stiffness of the cells themselves, on actin levels within the cells and on ROCK expression and activity.

1.5 Auxeticity and granular system as a modelling approach

While cells respond biochemically to changes in the external physical environment, the reverse is also true; the material properties of cells can change significantly in response to internal biochemical changes. An example is the sixfold stiffening of the nucleus as cells undergo differentiation from ES cells into fibroblasts, which is largely explained by the appearance of the lamins during differentiation [Pajerowski et al., 2007]. The investigation of the mechanical characteristics of cellular components often requires the application of external forces. As such, both the device proposed in this study, as well as a computational

model to study the effect of external forces on granular systems, can provide potential means to further investigate the material properties of the cell and nucleus.

The significant structural changes that take place in the nucleus are also reflected in the physical response to stress. As discussed in Section 1.1, 24 h after initiating differentiation, by changing the medium from 2i to N2B27, ES cells occupy a transition state. At this point, the nuclei were discovered to exhibit a physical property called auxeticity, referring to the negative Poisson's ratio of a material under compressive or tensile stress [Pagliara et al., 2014]. In conditions of free deformation, a normal material expands in the transverse direction when compressed in the axial direction. For example, a rubber band narrows when stretched, corresponding to a positive Poisson's ratio ν:

$$\nu = -\frac{d\varepsilon_{trans}}{d\varepsilon_{axial}} \tag{1.1}$$

where ε_{trans} and ε_{axial} are the strains in the transverse and axial direction respectively. Equation 1.1 assumes that the material's deformation is caused by externally-applied forces in one of the directions, while the material is free to deform in the other direction. In practice, a test of the Poisson's ratio requires the absence of side walls and the application of a uniaxial compressive or tensile strain. In contrast to most materials, auxetic materials, contract (expand) in the transverse direction when compressed (stretched) in the axial direction. Examples of these materials include some types foams, single cadmium crystals and salamander skin [Alderson and Alderson, 2007; Grima et al., 2009].

A diagram of the auxetic phenotype in the nuclei of ES cells is shown in Fig. 1.12. In these experiments, cells are flowed through channels with a width smaller than the diameter of the cell but larger than the diameter of the nucleus. As a result, the cells expands in the axial direction (parallel to the channel), and the cytoskeleton exerts a pulling force on the nucleus, which therefore also expands. Since the elastic behaviour of the cytoskeleton is non-linear, i.e. its compressive strength is considerably lower than its tensile strength, the transverse boundaries of the nucleus are not fixed [Ofek et al., 2009]. As such, in transition state cells the expansion of the nucleus in both the axial and transverse directions is an accurate test of its negative Poisson's ratio.

The emergence of this feature requires large-scale changes to the structural components of the cell and the nucleus, as the overall nuclear response under stress changes from no change or a volume decrease to an overall volume increase. Surprisingly, since chromatin decondensation caused the nucleus to exhibit auxetic behaviour, even in naive cells, chromatin is likely the most important structural element involved in this process.

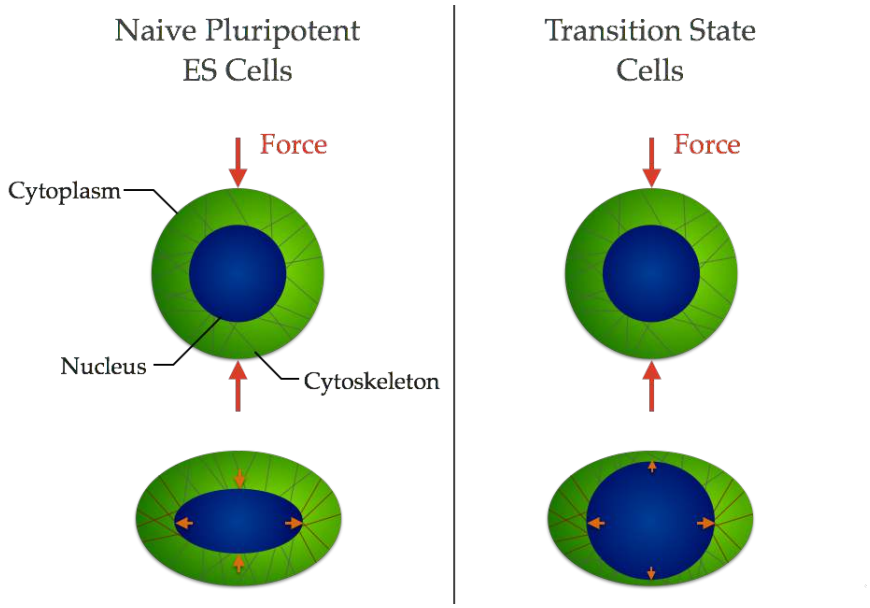

Figure 1.12 Compression of the naive cells in the vertical (transverse) direction causes the cytoskeleton to exert a force on the nucleus, which in turn expands in the horizontal (axial) direction. In naive cells, this is accompanied by a vertical contraction, while the nucleus in transition state cells expands in the vertical direction, indicative of auxeticity.

DNA is structured at several levels into chromatin domains, with increased interactions between genes within a domain, and few interactions between genes located between domains [Sexton and Cavalli, 2015]. One possible approach to connect the disordered (yet heavily regulated) structure of chromatin with its physical behaviour, is to model the nucleus as a granular system. For this purpose, the topological associated domains resemble grains connected to their neighbours at specific points, as shown in Fig. 1.13. They can expand and contract, but remain attached to their neighbours.

Using this abstraction, we propose a model in Chapter 6 to calculate the forces on individual domains and determine the associated movements. In this manner, the corresponding strains of the grains can be separated into expansive, translational and rotational components. This approach can be used to connect the local structure of the granular system and its associated microscopic and macroscopic displacements, and onwards to the chromatin organisation-driven changes in gene expression [Maharana et al., 2016].

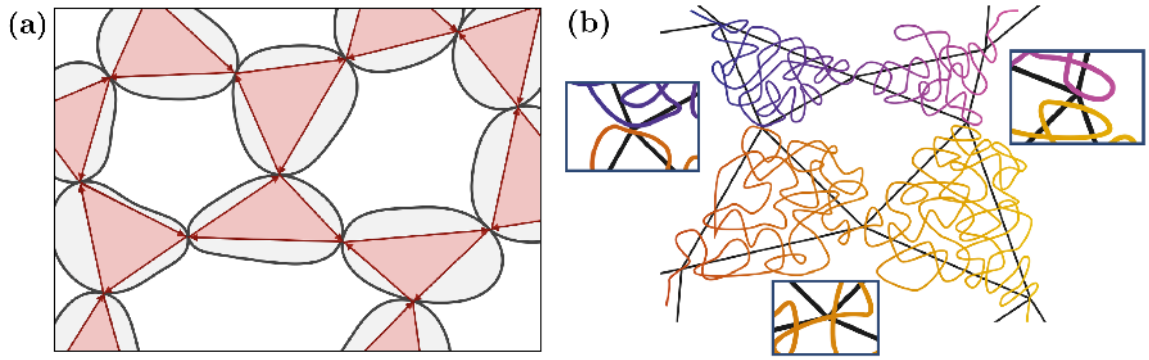

Figure 1.13 (a) Microscopic structure of a granular system. The contact points of individual grains (black outlines) can be connected by vectors (red arrows). If each grain has 3 contact points, the structure can be reduced to a system of connected triangles (red). (b) Simplified structure of DNA wrapped into chromatin domains (DNA coloured according to position along the polymer). Domains can be connected through physical links (e.g. DNA strand entering and exiting a domain), remodelling complexes or transcriptional complexes (e.g. promoter-transcriptional complexes). Again the contact points can be connected to convert the domains to triangles (black outlines).

Chapter 2

Objectives & hypotheses

In the previous chapter I presented the mechanisms that contribute to force sensing and transduction in cells, the types of experiments used to study these, and the effects on the overall cell state and, in particular, pluripotency and differentiation. There is broad support for the impact of external mechanics on cell state and behaviour. On the other hand, there is scant evidence of the effects of these influences in embryonic stem cells, even though they are a highly sensitive and dynamic cell type. Furthermore, most techniques induce a plethora of tissue-wide secondary effects, affecting morphology, signalling and attachment, which are difficult to disentangle from the impact of the forces themselves. In this study, we aimed to get more insight into the mechanisms through which direct forces affect ES cells, and how they are propagated through the complex disordered environment within a cell and its nucleus. We therefore put forward the following goals and hypotheses:

1. **Direct mechanical signals can be separated from wider biochemical cues** We hypothesised that forces influence ES cell behaviour even when not accompanied by changes to cell attachment, morphology, or cell-substrate versus cell-cell attachment preference. To test this, we developed a device to apply forces directly to cells by stretching their substrate. We optimised our set-up for embryonic stem cells and the biological study of their behaviour in response to stretching, including staining, live imaging, transcriptional measurements, and timecourses.

2. **Cells respond rapidly to direct forces** Considering that most cell types contain components that rapidly detect and respond to forces, we hypothesised that important mechanosensitive pathways are present also in ES cells, and that they are activated on short timescales when triggered by direct mechanical cues. To investigate this, we exposed cells to stretch and measured changes to intracellular calcium and the expression of genes (IEGs) involved in the rapid response to external stresses.

3. **Stretching affects pluripotency and differentiation in ES cells** As pluripotency was found to be affected by changes to substrate stiffness, we hypothesised that the impact of mechanical changes on pluripotency is a result of the forces themselves rather than of biological side-effects. To analyse this, we stretched ES cells in naive pluripotency and during differentiation. We then measured changes to transcription and a Rex1 reporter to study how stretching affects pluripotency.

4. **Forces induce characteristic changes to the transcriptome** Mechanotransduction involves specific pathways such as MAPK that influence downstream transcription and are connected to the pluripotency network. Therefore, we hypothesised that stretching is associated with characteristic transcriptional changes. We speculated that these are influenced by the biochemical signals provided by the culture media and by ES cells' pluripotent state. To test this, we performed RNA sequencing on stretched cells in multiple media conditions, and compared the susceptibility of the transcriptional network to stretch across conditions. We then used gene ontology techniques to identify which pathways were most affected.

5. **The force response of the nucleus depends on chromatin structure** Direct forces, such as stretching, can cause the nuclei of ES cells to exhibit a negative Poisson's ratio (auxeticity; see Section 1.5). We hypothesised that this feature is caused by a specific chromatin conformation. To test the relationship between a nucleus' macroscopic response and its microscopic structure, we developed a conceptual model of how forces propagate within a disordered system. We then used this computational model to study how the system's global response depends on its local structure.

Chapter 3

Materials & methods

3.1 Cell substrate stretcher set-up

3.1.1 Substrate stretcher

The original version of the device we report here was inspired by the device developed by the lab of Matthieu Piel, as reported by Fink et al. [2011]. Our devices were designed using Inventor 2015-2018 (Autodesk) and exported to the STL format. They were prepared for 3D printing using Slic3r 1.2.9 (developed by Alessandro Ranellucci), Simplify3D 3.1.0 (Simplify3D) when printing on a MakerGear printer, or using the Makerbot application 3.10 (Makerbot Industries) when printing on a Makerbot printer.

Devices were printed using fusion deposit modelling printers. Early versions of the single stretcher were printed on the Makerbot Replicator 2 (Makerbot Industries), while later versions and all other designs were printed on the MakerGear M2 Rev E. (MakerGear). On the MakerGear printer, models were printed using PLA plastic (orange: MP006051, Makerbot Industries) with an extruder temperature of 210ºC and a bed temperature of 75ºC, and using an extruder width of 0.25 mm, with an infill between 10% and 15% in a grid structure. Plastic scaffolding was manually removed after printing using tweezers and a scalpel.

The stretchers were automated using a 5 - 500 rpm DC 3 - 24 V high torque motor (fk-180SH-10400, Honda). One or two motors were connected using electric wires to a L293D motor driver chip (Texas Instruments). One or two chips were connected to the GPIO ports of a Raspberry Pi 3 Model B (Raspberry Pi Foundation) running the latest version of Raspbian (up to 4.9, released in March 2018, based on Debian Stretch and developed by the Raspberry Pi Foundation), and connected to a Raspberry Pi official 7" touch screen (Raspberry Pi Foundation). A graphical user interface was developed in Python 2.7 and Kivy.

3.1.2 PDMS membrane & functionalisation

To stretch the substrate of cells, an elastic membrane was clamped in the stretcher. The membranes were manufactured from polydimethylsiloxane, or PDMS (Sylgard 184, Dow Corning), which was produced by combining the elastomer and curing agent at a ratio of 1:20, except where mentioned differently, and mixing thoroughly. After degassing, PDMS was spincoated on silicon wafers with a diameter of 15 cm at 250 rpm. The coated wafers were then baked at 65ºC for 2.5 h. From the centre of the wafer, three rectangular membranes with dimensions of 27.5×54 mm were cut out of the PDMS to form thin membranes.

PDMS membranes were functionalised within two months after manufacture. At the start of the functionalisation protocol, scotch tape (Magic tape 810, Scotch) was used to cover the PDMS membrane such that an area of 23×29 mm in the middle of the membrane remained uncovered. The membranes were exposed to oxygen plasma at 100 W for 2 min (Diener Electronic). After removal from the plasma cleaner, the membranes were immediately washed in ethanol, facilitating the removal of the tape, followed by distilled water.

Sulfo-SANPAH-based functionalisation

After plasma treatment, 500 µm of 1 mg/ml sulfo-SANPAH in 50 mM HEPES buffer (H3375, Sigma) in anhydrous DMSO (D12345, Thermo Fisher) was added to the hydrophilised area of the membrane, and exposed for 8 min to 365 nm light from a UV lamp (UVLMS-38, fischer scientific). The membranes were washed threefold in HEPES, and then sulfo-SANPAH was again exposed to UV light for 8 min. After three more washes, 500 µl of ECM protein was added at a concentration of 100 µg / ml for Fibronectin (356008, Corning), Laminin (L2020, Sigma) or Collagen IV (356233, Corning). Membranes were incubated with ECM proteins overnight, then washed using DMEM before cells were added to the membrane.

BS^3-based functionalisation

To increase the roughness of the surface of the membrane and promote crosslinker attachment, the area of the membrane hydrophilised using plasma treatment was exposed to 500 µl of the following Bind Silane solution, for 3 h:

94%	Ethanol
0.5%	Acetic acid
0.1%	PlusOne Bind-Silane (GE Healthcare)

The membranes were washed in distilled water thrice for 5 min. Each membrane was incubated with 500 µl 1 mM BS^3 in H_2O during 30 min. The membranes were then again

washed three times with distilled water, and then the extracellular matrix protein of choice was added (see Section 3.1.2) at a concentration of 100 µg / ml and left to incubate overnight. The membranes were washed using DMEM and cells were added to the membrane.

3.1.3 General stretching protocol

On the first day, PDMS membranes were manufactured in a large batch according to the procedure outlined above, typically in triplicate for each condition. On the next day (or later), the membranes were functionalised, with the BS^3 protocol used for most experiments (except where outlined in the text). Where relevant, after the bind silane treatment the membranes were transferred on the holders and placed in the stretcher. Then the functionalisation protocol was continued.

After the membranes were incubated overnight with the ECM protein, the holder was removed such that the membranes were now in the stretcher in an unstretched state. The membranes were incubated with PBS containing 2.2% Penicillin Streptomycin (P0781, Sigma) for 30 min, then washed twice using DMEM. In the meantime cells were passaged and counted, and then plated on the membranes. The stretcher was held in a dish in a tissue culture incubator in normal culture conditions. The cells were left for at least 8 h before stretching.

In case of manual stretching, at each stretching timepoint the stretcher was removed from the incubators and stretched by turning the screw in the tissue culture hood, then placed back into the incubator. When cells were stretched using the automated protocol, the motor was connected to the controlling unit using thin wires that fit along the rubber sealing of the incubators without causing CO_2 or temperature leakage. A programme was started on our GUI on the Raspberry Pi. Throughout the programme, the actual level of stretch was verified.

3.1.4 Characterisation of the substrate stretcher

To study the relationship between the force and the membrane deformation, the clamp in the stretcher was connected to a spring balance (ME495-0003, Sinco). The membrane was stretched to the intended extent, and the applied force registered. This was repeated in quadruplicate. To measure the local strain in response to the stretch of the entire membrane, membranes were manufactured using PDMS mixed with a concentration of 1:1000 fluorescent beads (F8801, Invitrogen). ES cells were plated on the membrane and stretched. The positions of the beads before and after stretching were registered, and their displacement was related to the position of the closest cells, as described in the text. The deformation of cells

was measured by plotting a bounding rectangle around cells as they were undergoing stretch. Images of the cells were taken maximum 5 min after stretching.

3.1.5 Biological procedures

Cell & tissue culture

This study used wild type ES cells derived from 129/Sv strain mice, and were a kind gift from Jennifer Nichols's laboratory at the University of Cambridge. Cells were cultured at 37ºC and 7% CO_2. Media was replaced every 2 days and cells were split every 2-3 days. Splitting consisted of detaching cells from the dish using accutase (423201, Biolegend), mixing cells with PBS followed by centrifugation. The pellet was then resuspended in new media and added to a new gelatin-coated (G1890, Sigma) flask.

N2B27 Cells were differentiated in neuronal differentiation media, containing no LIF or differentiation inhibitors. 100 ml of N2B27 comprised the following ingredients [Ying et al., 2008]:

50 ml	Neurobasal Media (21103-049, Gibco)
50 ml	DMEM F-12 Ham (21331020, Gibco)
1.1 ml	200 nM L-glutamine (25030024, Invitrogen)
500 µl	N2 (SCM012, Millipore)
1 ml	B27 (17504044, Invitrogen)
110 µl	0.1 M 2-mercaptoethanol (21985023, Life Technologies)

N2B27 was stored at 4ºC and was used within 2 weeks from its preparation.

2i+LIF Cells were routinely cultured in 2i+LIF to keep them in a fully pluripotent state. 100 ml of 2i+LIF consisted of the following ingredients [Ying et al., 2008]:

100 ml	N2B27 (vide supra)
30 µl	4.65 mg/ml Chiron CHIR99021 (prepared by SCI tissue culture facility)
10 µl	4.5 mg/ml PD03 PD0325901 (supplied by SCI tissue culture facility)
200 µl	10 µg/ml murine LIF (CS204463, Millipore)

2i+LIF was stored at 4ºC and was always used within 7 days from its preparation, although it was usually prepared in smaller volumes and used within 3 days.

Serum+LIF Serum+LIF media was used for most routine culturing and experiments. It contained the following ingredients [Wakayama et al., 1999]:

500 ml	GMEM (G5154, Sigma)
55 ml	FBS (SV30180.03, GE Healthcare)
5.5 ml	MEM NEAA (M7145, Sigma)
5.5 ml	200 nM L-glutamine (25030024, Invitrogen)
5.5 ml	100 mM Sodium Pyruvate (S8636, Sigma)
605 µl	0.1 M 2-mercaptoethanol (M7522, Sigma)
1 ml	10 µg/ml murine LIF (CS204463, Millipore)

Serum+LIF was stored at 4ºC and was used within 2 weeks from its preparation. Depending on the experiment, 1.1 ml of Penicillin Streptomycin was added.

Immunofluorescence stainings

To visualise cell attachment and morphology, cells were fixed and stained. Cells on PDMS membranes were fixed for 15 min in 4% paraformaldehyde (158127, Sigma). The samples were then rinsed thrice in PBS and incubated with blocking & permeabilisation buffer (0.05% Serum (Goat: G9023, Donkey: D9663), 0.3% Triton X-100 (T8787, Sigma) in PBS) for 10 min. The H3K27 (9733 Cell Signaling Technology at 1:1200) or phospho-paxillin (2541 Cell Signaling Technology at 1:50) primary antibody was diluted in a buffer containing 0.3% Triton X-100 and 0.002% BSA (15620-037, Gibco) in PBS and incubated overnight at 4ºC. Samples were then washed thrice in PBS and incubated with secondary antibody (488 nm: A11008, 647 nm: A31573, Thermo Fisher) and phalloidin (CytoPainter ab176759, abcam at 1:800) at room temperature for 90 min. The samples were then incubated with Hoechst to stain the nucleus, washed in PBS 3 times for 5 min and sealed with antifade reagent (P36934, Life Technologies).

3.2 Effects of stretching on cell behaviour

3.2.1 RT-qPCR measurements

To obtain gene expression measurements, the stretchers were removed from the incubator at the correct time point, then washed twice with PBS to reduce the number of floating or weakly attached cells in the samples. Cells were then collected and their RNA extracted using

the RNeasy mini kit (74106, Qiagen) and treated with DNase (79254, Qiagen). RNA was quantified using a spectrophotometer (ND-1000, Nanodrop). Up to 8 µg of RNA was used in a reverse transcriptase step using SuperScript III, with the following reaction components:

4 µl	Reverse transcriptase buffer (Y02321, Invitrogen)
2 µl	50 mM $MgCl_2$ (AM9530G, Thermo Fisher)
2 µl	0.1 M DTT (Y00147, Invitrogen)
1 µl	Random hexamers (100026484, Invitrogen)
1 µl	10 mM dNTPs (55082-55085, Invitrogen)
1 µl	RNase Out (100000840, Invitrogen)
1 µl	Superscript III (18080093, Thermo Fisher)

The reverse PCR step consisted of the following steps, and was run on a Prime Full Size PCR machine (Techne):

10 min	25ºC
50 min	50ºC
5 min	85ºC

The PCR product was diluted 1:10 and stored at -20ºC. Gene expression was quantified using the TaqMan system. The TaqMan probes used in this study (all from Thermo Fisher) are shown in Table 3.1.

Table 3.1 TaqMan probes used in this study

Gene name	Fluorescent Dye	Assay ID
GAPDH	VIC	4352339E
Klf4	FAM	Mm00516104
Nanog	FAM	Mm02384862
Esrrb	FAM	Mm0044241
Acta2	FAM	Mm00725412
Myc	FAM	Mm00487804
Fos	FAM	Mm0487425
Jun	FAM	Mm00495062
Egr1	FAM	Mm00656724

Each well contained a 20 µl reaction, each with the following ingredients:

10 µl	TaqMan master mix (4352042, Thermo Fisher)
1 µl	Target probe, as above
1 µl	GAPDH probe, as above
3 µl	H_2O
5 µl	DNA

The reaction was run on a StepOne Plus RT-qPCR machine (Applied Biosystems) for 40 cycles. Only one qPCR replicate was run for each sample, but this was compensated for by a larger reaction volume, and three biological replicates were included. To verify the accuracy of this approach, stretching experiments were also run using multiple technical replicates, and the biological errors were always larger than the technical errors. The error bars in all figures correspond to the standard deviation of the expression of the replicates. Single, double or triple asterisks in figures indicate statistical significance at $p = 0.05$, $p = 0.01$ and $p = 0.001$ respectively.

3.2.2 Rex1-GFP experiments

To measure the effect of stretching on the rate of differentiation, we analysed the fluorescence intensity of ES cells with a mutant Rex1 locus, Rex1GFPd2, containing an unstable form of GFP with a half-life of 2 h, as developed and reported by Wray et al. [2011]. Rex1-GFP ES cells, kindly donated by the lab of Austin Smith at the University of Cambridge, were cultured in 2i media for at least two passages, then 200,000 cells were plated in N2B27 on PDMS membranes coated with laminin, in the stretcher. The media was partially replaced after 12 h and 24 h. Apart from the control membranes, which were left unstretched, the membranes were stretched at the 24 h timepoint according to the following protocol. First, membranes were stretched 35% for 90 min, then they were fully relaxed and left for 30 min. This cycle of stretching and relaxation was then repeated continuously. Then, after 2 h, 6 h and 12 h later cells were collected using accutase, spun down and resuspended in DMEM. The intensity of cells' fluorescence signal was then measured using the CyAn flow cytometer (Beckman Coulter). The resulting data was analysed using the FlowJo v8 software (FlowJo LLC).

3.2.3 Overall transcriptional characterisation

RNA sequencing

RNA was extracted from cells as described in Section 3.2.1. The concentration and amount of RNA was quantified, and RNA from the three biological replicates on each stretcher were combined at equal concentration into one RNA sample. Libraries were generated using ribosomal RNA depletion (Ribo-Zero rRNA Removal Kit MRZH11124, Illumina), and produced from rRNA-depleted RNA using NEXTflex Directional RNA-Seq Kit V2 (Bioo Scientific) with 12 cycles of PCR amplification. Libraries were sequenced using the illumina platform using single-end sequencing for the SL-type samples and using pair-end sequencing for the 2i-type samples.

The sequencing data was analysed using the DESeq2 package in R. Considering the importance of this methodology in the interpretation of the transcriptional data, I discuss here in some more detail the technical background of the technique as applied on our dataset, although this is not essential for the interpretation of the biological data.

DESeq2 background The DESeq2 package fits the counts K of each gene i in sample j as a binomial distribution $NB(\cdot)$, as developed by Love et al. [2014]:

$$K_{ij} = NB(\mu_{ij}, \alpha_i) \tag{3.1}$$

$$\mu_{ij} = s_j q_{ij} \tag{3.2}$$

$$log_2(q_{ij}) = x_j \beta_i \ , \tag{3.3}$$

using mean μ, gene dispersion parameter α_i. The mean is equal to a parameter proportional to the true concentration q_{ij} multiplied by a sample sizing factor s_j (often corresponding to differences in sample sequencing depth). Finally, q_{ij} depends on a design factor x_j, for example indicating whether a sample is a control sample or not, times the ratio of the experimental to control samples of gene j, β_j. The second variable of the binomial distribution is the dispersion parameter α_i, representing the variance in the counts of gene i across samples as follows:

$$Var(K_{ij}) = \mu_{ij} + \alpha_i \mu_{ij}^2 \ ,$$

hence the variability of a gene depends highly on its overall expression level as well as on the gene-specific parameter α_i. This expression relates how much the expected observed count is expected to differ from the mean (theoretical) value as a function of the expression and the dispersion parameter.

The procedure of DESeq2 consists of first estimating the size factors s_j, as the median, across all genes, of the ratio of the count of sample j to the geometric mean of all sample counts [Anders and Huber, 2010]:

$$s_j = median_i \left(\frac{k_{ij}}{(\prod_{v=1}^{m} k_{iv})^{1/m}} \right) .$$

This allows the calculation of the mean count for each each gene in each condition μ_{ij}, adjusted for different sequencing depths.

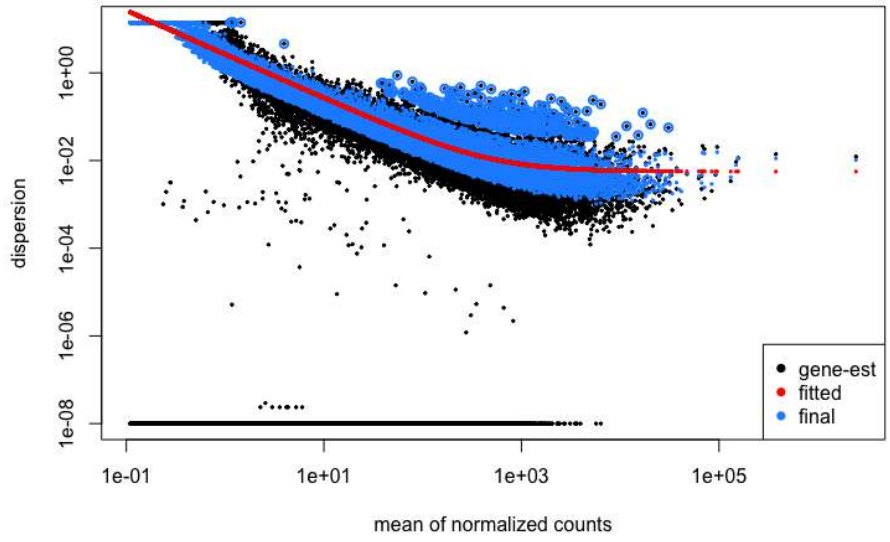

Figure 3.1 Dispersion of the counts of all genes in our experiment, as estimated using DESeq2, across all samples (black). A function of the form $y = \frac{a}{x} + b$ is fit to the data (red). The dispersions of all genes are scaled towards the trend (blue), except outliers (blue circles).

The advantage of using DESeq2 is its robustness in dealing with low sample replicates, in particular because in this study we sequenced only two replicates per sample. It does this by assuming a correlation between the mean count of a gene and its dispersion, allowing the entire sample to be used to estimate the global trend, which can be significantly more accurate due to the increase in sample size. This global fit can then be used to correct the dispersion of individual genes towards the trend: First the mean and variance of the counts of individual genes is calculated, without prior assumptions, and used to estimate the dispersion of the individual sample. The dispersion of all genes in our experiment, plotted as a function of the normalised counts, is shown in Fig. 3.1. The trend of the distribution of the dispersions

is fitted as the inverse of $\alpha_{tr}(\bar{\mu}) = \frac{a}{\bar{\mu}} + b$, where $\bar{\mu}$ is the mean count of the sample [Anders et al., 2012]. This procedure increases the accuracy of the dispersion measurements, which are used later to estimate statistical significance, by combining all genes across all conditions to estimate the relationship between count and dispersion (but excluding outliers above the trend). A Bayesian model is then used to shrink the dispersion estimates towards the trend. The effect of this to the $\log_2$-fold change (LFC) graphs is that the absolute value LFC of each gene is reduced, broadly in a count-dependent manner, depending on the dispersion of each gene. The shrinkage also depends on the number of samples, with experiments with a higher number of samples being shrunk less.

Counts are automatically filtered within the results function, as genes with very low mean counts typically have a high dispersion and hence a small probability of being differentially regulated at a statistically significant level. This reduces the computation and memory required by the algorithm, and (as long as the proportion of low-count samples with low p-values to those with high values is low) improves the discovery rate. Outliers are not discarded automatically because the number of samples we used is below three, but otherwise the algorithm would use the Cook's distance (the contribution of each individual sample to the overall coefficients) to detect and then remove outliers.

The shrunk mean and modified dispersion of the count of each gene serve as the mean and variance of a conceptual lognormal likelihood distribution. Considering each gene is now associated with an *experimental* and *control* distribution, they can be compared to establish statistical significance of the shift in distribution, i.e. of the $\log_2$-fold change. A Wald test is performed: the LFC estimate is divided by the standard error, and compared to a normal distribution, producing a p-value. These p-values can then be shrunk to produce adjusted p-values [Benjamini and Hochberg, 1995]. In essence, this test compares the number of positives expected from a random distribution (i.e. 5% when using a 5% significance level) to the actual level. A correction for the False Discovery Rate (FDR), as developed by Benjamini and Hochberg, takes into account the shape of the histogram of p-values for p-values smaller than the significance level. First it finds the p-value where $p = q = \frac{k\alpha}{m}$ with k, α and m being the ranked p-value, the significance level and the number of genes respectively. Then all genes with p-values below this level are statistically significantly regulated. The adjusted p-value is then $p_{adj,i} = \min_{k \in i,\ldots,m}(\min(\frac{m}{k} p_k, 1))$. As such, the procedure starts from the largest p-value, whose p_{adj} is the smallest of $\frac{m}{k} p_k$, or 1. The adjusted p-value of the element with the second largest p-value is then either $\frac{m}{k} p_k$, or the p_{adj} of the last element, depending on which is smaller, and so on. Following the convention in RNA-Seq analysis, we used an adjusted p-value of 10% as the threshold for statistical significance.

Gene ontology

An analysis of the differential enrichment of biological pathways was performed using a number of gene ontology tools. Again the different techniques are described concisely to allow the comparison of the underlying methodologies.

GOrilla: ranked & unranked We used the web-based GOrilla package for two purposes [Eden et al., 2009]. First, we compared a set of significantly regulated genes to a list of background genes, containing all genes in our dataset. This unranked approach uses the GO annotation system, which contains a database of all biological processes and their constituent gene components in mouse. This type of tool identifies the pathways that are significantly regulated based on the significant regulation of their gene members [Zeeberg et al., 2003]. The probability of a certain number of genes b (out of a total N, of which n are significantly upregulated) being part of the GO process (which contains B genes), can be modelled in the form of a hypergeometric distribution $HGT(\cdot)$, $Prob(X \geq b) = HGT(b;N,B,n)$ [Eden et al., 2009]. To compensate for the multiple comparison problem (see Section 3.2.3), we used the FDR q-value.

Second, we analysed a list of all genes in the dataset ranked by the p-value of the LFC. By analysing the enrichment of a pathway's constituent genes towards the top or bottom of this list, a ranked GOrilla analysis permits the identification of differentially regulated pathways even when none of its gene members are differentially up- or downregulated [Eden et al., 2007]. The algorithm extends the hypergeometric model. The ranked genes are associated with a binary vector λ with elements in $0,1$, indicating whether the gene is in the set associated with the GO term. GOrilla then calculates the minimum probability mHG that the observed number of genes are part of the pathway, as the partition size is gradually increased, starting with the lowest p-values:

$$mHG(\lambda) = \min_{1 \leq n < N} HGT(\sum_{i=1}^{n} \lambda_i; N, B, n) \ .$$

From this value, a p-value is calculated, as in [Eden et al., 2007], which is then adjusted using the Benjamini-Hochberg method [Benjamini and Hochberg, 1995].

goseq A potential problem with the unranked approach used in GOrilla is that biases are inherently present in the data. goseq addresses a major confounding issue in GO analysis, which is the influence of transcript length on statistical power, with genes with longer transcript having a higher read count and more statistical power [Oshlack and Wakefield, 2009]. This influences the probability of a gene being detected, and hence becomes relevant

if there is a difference in mean transcript length of gene members between pathways [Young et al., 2010]. To address this, first a monotonic function is fitted to the relation between gene length and the proportion of differentially regulated genes. In our analysis, we used the mm9 dataset using Ensemble IDs. Then, a probability distribution is produced through a repeated random reshuffling of the genes weighted by their gene length (in fact, this distribution is approximated using the Wallenius non-central hypergeometric distribution for computational reasons). This then allows p-values to be calculated for the over- and underrepresentation of the enrichment of GO categories. We used a p-value of 5% or less as indication of statistical significance. To produce the diagrams showing the contribution of seven large biological processes, we used only biological processes in the GO annotation system, and manually sorted the pathways into large categories.

GSEA The enrichment of pathways based on a ranking of the genes by p-value was estimated also using the Gene Set Enrichment Analysis or GSEA package (Broad Institute) [Mootha et al., 2003; Subramanian et al., 2005]. This analysis first calculates an enrichment score (ES) for each position in the list by increasing the score as it goes through the ranked list of all genes and encounters a gene in the pathway, and decreases otherwise. The magnitude of the increase or decrease depends on the correlation of the gene with the phenotype. The enrichment score of the entire list is defined as the maximum value of the score in the list. It is small in the case of an even distribution of the genes of pathway throughout the list, as increases in the ES while going through the list are balanced by decreases, but large if genes are non-uniformly distributed near the top or bottom of the list.

A disadvantage of this method, however, is that it does not provide an exact p-value, which is instead estimated using permutations. Indeed, in our analysis, after the ES of the list has been computed, 1000 random gene sets are computed from permutations of the genes, and their histogram corresponds to the null distribution of the ES. The p-value of the ES of the sample of interest is computed with respect to this distribution, and then the ES is normalised using the mean of the entire database. In addition, the FDR is calculated. We used an FDR of less than 0.25 as the criterion of statistical significance.

The c2.cp.v6.1.symbols database was used for the gene sets, which comprises data from a range of sources, including KEGG, Signaling Gateway, BioCarta, L2L database, and extracted from publications. The ENSEMBL mouse database was used as chip platform. The dataset was not collapsed to gene symbols, and was permutated by gene set. Genes were sorted the Signal2Noise metric, which uses $\frac{\mu_a - \mu_b}{\sigma_a - \sigma_b}$, of the count data, and other metrics did not substantially change the number of enriched pathways. Interestingly, considering this is an asymmetric measure, it allows the distinction between up- and downregulated pathways,

which is not possible when analysing only fold changes. The results of the analysis were visualised using Cytoscape (Cytoscape Consortium).

3.2.4 Measurement of intracellular calcium concentration

With the aim of measuring the intracellular calcium concentration in cells undergoing stretching, WT ES cells were plated in Serum+LIF media on PDMS membranes functionalised with fibronectin. 23.5 h later, they were incubated with 10 µM X-Rhod-1 dye (X14210, Thermo Fisher) for 30 min. Then the media was replaced with new Serum+LIF media containing 10 mM HEPES (H3375, Sigma) at pH 7.4 and containing 2 µM Hoechst 33342 for 30 min. Samples were then imaged on a Leica CTR7000 HS epifluorescence microscope using a 20x objective (HCX PL Fluotar L 20x/0.4, Leica). Images were analysed using Volocity (PerkinElmer) and Fiji [Schindelin et al., 2012]. We found that the X-Rhod-1 signal was largely homogeneous throughout the cell, and therefore the Hoechst signal was tracked during the entire image series, and was used as a mask for the channel containing the X-Rhod-1 signal. Abnormally small nuclei were discarded, and the intensity profile of each nucleus throughout the time series was plotted and analysed. Apoptosing cells were detected using the CellEvent Caspase-3/7 Green Detection Reagent (C10423, Thermo Fisher). Two drops were added to the media 30 min before the start of the experiment.

Chapter 4

The development of a technique to stretch ES cells on an elastic substrate

4.1 Introduction

As discussed in detail in Chapter 1, cells experience forces from their close environment which drive changes in morphology and behaviour. Techniques to apply forces to cells are useful to investigate the downstream biochemical impact (e.g. to study the effect of forces on gene expression and mechanosensitive pathways), or to perform a biophysical characterisation of the cell itself (e.g. to measure stiffness or Poisson ratio of cellular components). We developed a device to apply global forces to cells, designed to satisfy the technical specifications arising from these two main applications.

This chapter discusses the development process of the cell substrate stretcher. Starting with an overview of the technical requirements, we introduce a number of designs adapted for specific applications, and present a novel technique to functionalise the elastic membrane. We characterised the technical and biological capabilities and performance of the devices.

The resulting set-up is a 3D-printed device to stretch an elastic substrate which can be functionalised using two possible functionalisation methods. A graphical user interface can be used to drive an automated programme, consisting of applying static or cyclic stretch to cells. We found the local strain to be relatively homogeneous within the biofunctionalised region of the membrane, which cells experienced without adverse effects to cell viability. Overall, the results show that the cell substrate stretcher is a versatile and accurate device, which supports its application to characterise ES cells' biological response to stretch as discussed in Chapter 5.

4.2 Development of the cell substrate stretcher

A layout for a simple cell stretcher was developed by the Piel lab and described by Fink et al. [2011] and Carpi and Piel [2014]. It comprises two metal holders, one of which can slide on a track using a micrometric screw pushed against a barrier, as shown in Fig. 4.1. A PDMS membrane is clamped between the two metal holders. Cells are cultured in culture media in a PMDS well, placed on the membrane and sealed with vacuum grease. The set-up, while relatively easy to produce and use, has several disadvantages. The membrane's size means the number of cells harvested is not sufficient for most downstream biological analyses, that the device cannot be used for imaging using high magnification objectives, and cannot be automated. In addition, the sealing of the vacuum grease is often insufficient, often causing media leakage during stretching (terminating the experiment). Considering the application of this technique to exert forces directly on cells to influence the direction of spindle formation [Fink et al., 2011], we used this set-up as a general template to develop a device with improved specifications.

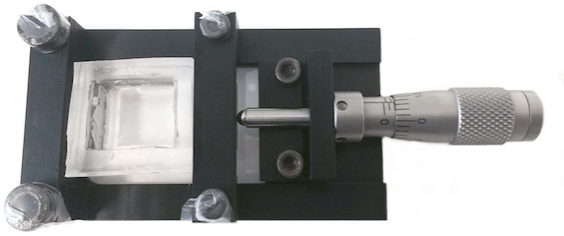

Figure 4.1 A cell stretcher developed by the Piel lab, as reported in [Fink et al., 2011] and [Carpi and Piel, 2014].

4.2.1 Design requirements

Applying the device in a broad biological investigation of the effect of direct forces on cells, introduced a number of design requirements. The major considerations were the following:

Structural requirements

- **Substrate** With the aim of developing a single-parametric model, cells should experiences forces directly. This is most easily achieved using a functionalised elastic substrate. When used for general microscopy, the membrane should be thin and trans-

parent. Ideally, the membrane should be reusable or replaceable. The incorporation of a PDMS membrane, as in the Piel lab stretcher, satisfies this criterion.

- **Durability** The stretcher has to be able to resist the tension of the membrane at 37ºC for multiple experiments without breaking or bending. The force applied by a PDMS membrane (of around 2 $\times$ 5 cm) would be in the order of 1 - 2 N, so the device should be able to resist a force of up to 5 N. The cross-sectional area of the elements which support the tension in the membrane would together, similar to the Piel device, be around 50 mm^2, which means the yield stress at 37ºC should be above 100 kPa. At the forces mentioned above, the device should have minimal deformation, since it is aimed at applying a fixed deformation to the membranes, implying that the device should have a stiffness above 10 MPa.
- **Accuracy** To assure experimental validity, the stretch applied to the membrane has to be reproducible on a macroscopic and microscopic scale. Since that the device applies a deformation to the cells, an accuracy on the strain of 10% would be acceptable. With a membrane length of around 4 cm, this translates to an accuracy of $\pm$ 3 mm. Similarly, the strain should have a precision of around 5%, or 1.5 mm, since any precision below this level would very likely be surpassed by any biological variability.

Biological requirements

- **Biocompatibility** The external components of the device are likely to be in close contact with cells or culture media (possibly accidentally); therefore the external casing should be entirely biocompatible and allow sterilisation.
- **Media** The device should be capable of holding tissue culture media without contact with non-sterile or toxic components, and without leaks at any time. Replacing media or harvesting cells should be convenient and fast. The media well should not deform the membrane or interfere with stretching.
- **Functionalisation** Because an elastic membrane will be used, the substrate should allow functionalisation using ECM proteins to which cells adhere stably. The functionalisation should be sufficiently strong to retain attachment of cells during and after stretching, and the method should be compatible with multiple ECM proteins to minimise the specific effect of one ECM protein on mechanosensitivity.
- **Replicates** For transcription measurements, the set-up should allow multiple replicates or sample types within a single experiment, with replicates possibly treated differently or harvested at different timepoints.

- **Flexibility** Different types of biological experiments have different technical requirements. For example, at least 1×10^6 cells are required for chromatin immunoprecipitation (ChIP) experiments, excluding replicates, while imaging experiments contain only around 1×10^4 cells. The system should be sufficiently flexible to adapt to these requirements.

Use requirements

- **Tissue culture** The device should be resistant to the warm, humid and highly corrosive environment of a cell culture incubator. As only small cables can enter the incubator, the set-up inside the incubator should be as self-sufficient as possible, while still easily removed and transferred to the culture hood for manipulation.

- **Microscopy** For use in a microscope, the device should be compatible with a heated microscopy stage. Ideally, imaging should be possible using a high numerical aperture objective; therefore, the membrane should be as thin as possible, and its refractive index similar to that of water or glass.

- **Immunofluorescence** To allow easy fixation and immunofluorescence (IF) stainings, the fixative (which touches similar surfaces as the culture medium) should not come into contact with the device, washing should be convenient, and the culture area should be kept small (so only low amounts of antibody are required).

- **Flexibility** The conflicting requirements regarding shape and size of the device can be addressed through the development of customised devices, each designed for specific purposes. Therefore the manufacturing process should be cheap and efficient. We identified 3D printing as a technique well-suited for this type of fast prototyping.

- **Automation** To maintain experimental accuracy and convenience even in large experiments, with multiple timepoints and replicates, the stretcher should be automated. The user should be able to determine the magnitude and duration of the stretch using a graphical user interface, which should support complex protocols involving both static and cyclic stretch.

- **Convenience** Assuring its continued future application, the device should be easy to use and to program. It should be possible for a cell biologist with no previous experience with the device to set up and run the experiment. The entire protocol, from device manufacture to membrane functionalisation, should be as short as possible.

4.2.2 Stretching devices

According to the technical specifications above we developed several specialised devices, each customised for one or multiple applications. The basic layout is largely similar across these devices: a large frame contains a holder on one side and a track along its length. A separate module, also containing a holder, can slide along the length of the device, and is connected to the outer frame by a long screw. When a knob is turned on the screw, the slider and the clamped PDMS membrane move away from the other clamp, and the membrane is stretched.

The devices were designed using CAD software and printed using fusion deposit modelling, which constructs a three-dimensional model by depositing melted plastic filament layer-by-layer, which hardens and binds to the previous layer as it cools. Polylactic acid (PLA) has low thermal expansion (limited bending upon cooling), prints at high resolutions (around 250 µm) and is fully biocompatible [Rosenzweig et al., 2015]. Compared to acrylonitrile butadiene styrene (ABS), PLA has a higher average tensile strength (PLA: 28.5 MPa, ABS: 56.6 MPa) and Young's modulus (PLA: 3368 MPa, ABS: 1807 MPa) [Tymrak et al., 2014], and was found to have a higher flexural modulus and strength (PLA: around 95 MPa, ABS: around 60 MPa) [MakerBot, 2014]. Since PLA offered the best combination of structural strength and printing convenience, we used this material to print the devices.

Single manual stretcher

Our design for a generic stretcher is shown in Fig. 4.2, containing a frame with one holder, a second holder capable of sliding back and forth, and two clamps. Originally all components apart from the nuts and bolts were 3D-printed, but after multiple experiments the clamps displayed minor bending, and were replaced by aluminium versions. The device has dimensions of 100 by 56 mm, and was designed to be used with a single membrane with size of 27.5 by 54.0 mm. Cells are cultured in a hydrophobic area of 21.0 by 30.0 mm, corresponding to a surface area of 6.3 cm^2 (the functionalisation protocol is discussed in Section 4.2.3). The device thus allowed a maximum cell number of at least 95,000 cells at a plating density of 15,000 cells per cm^2.

The single manual stretcher performed well in experimental tests and in the optimisation and characterisation of the protocol. However, the procedure to position the membrane in the stretcher is cumbersome and could be a potential source of variability. The membrane needs to be lifted, stretching the membrane before commencing the experiment and potentially causing the spillage of the liquid on the device. The device is also suboptimal for large biological experiments that requiring multiple replicates.

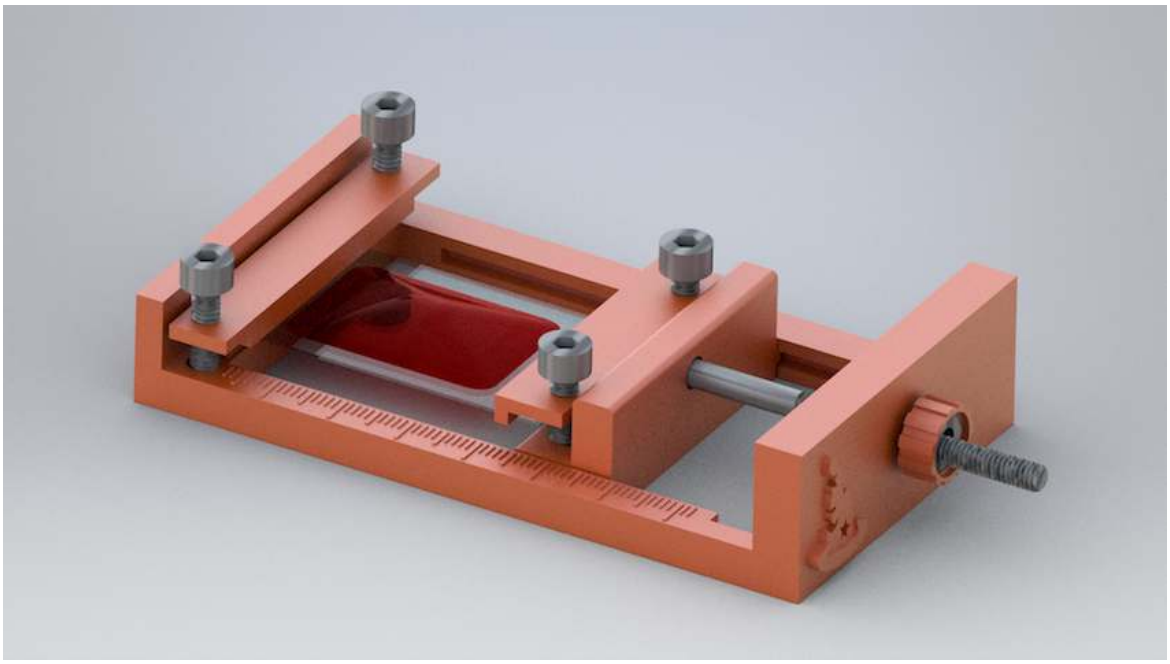

Figure 4.2 Diagram of the single manual stretcher with an elastic PDMS membrane, with the rectangular functional hydrophilised area containing media and cells in red.

Parallel manual stretcher

To address the shortcomings of the single stretcher, we developed an alternative device that could incorporate three separate membranes, as shown in Fig. 4.3. This allows experiments to be performed in triplicate, better matching the requirements for transcriptional measurements. Additional replicates remain necessary to account for the potential variability in actual stretch between devices, however.

We also added a stage (green element in Fig. 4.3) on which membranes can be placed immediately after plasma treatment, helping to reduce variability and eliminating the need to transfer membranes into the stretcher after functionalisation. The device contains six components: two parts of the frame, a slider, two clamps and a stage, and has dimensions of 100 by 150 mm. The stage can be slotted into the holders, the membranes clamped at both ends, and then the stage and holders can slide into the frame. Then, before the experiment, the stage can easily be removed. Because of this improved handling procedure, the biofunctionalised area could be increased to 24 by 32 mm, corresponding to a larger cell number of 120,000 cells, such that all replicates together yield a cell number of 360,000. By plating cells more densely, 1 million cells could be cultured, which makes this stretcher

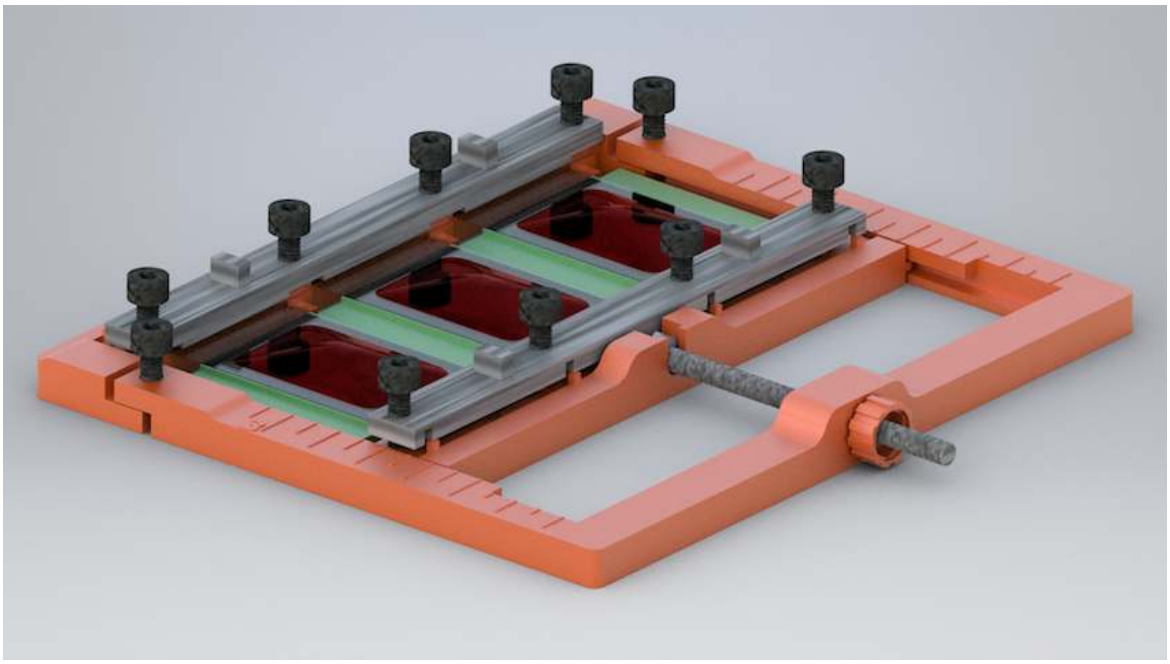

Figure 4.3 Diagram of the parallel manual stretcher.

suitable for ChIP experiments. A small tweak could also allow a single large membrane instead of three smaller membranes.

This device was easy to set up and highly reproducible, and was used for most gene expression studies in this project. However, due to its large size, the device is not suitable for live imaging or IF stainings, and is not automated.

Manual stretcher for immunofluorescence

Specifically modified for immunofluorescence applications, we designed another stretcher that is smaller to fit in the stage holders of most microscopes. The device, shown in Fig. 4.4, has a reduced height to accommodate the Z-axis travel limits of objectives, and can be flipped vertically to allow imaging directly through a coverslip without having to pass through the membrane (whose thickness might exceed the working distance of high-magnification objectives). The screw to increase or decrease the stretch can more easily be removed to prevent interference with the microscope stage.

Automated stretcher

A manual stretcher is impractical for long experiments or for protocols with repeated cycles of stretching. The recurrent removal of the stretcher from the incubator and its manipulation

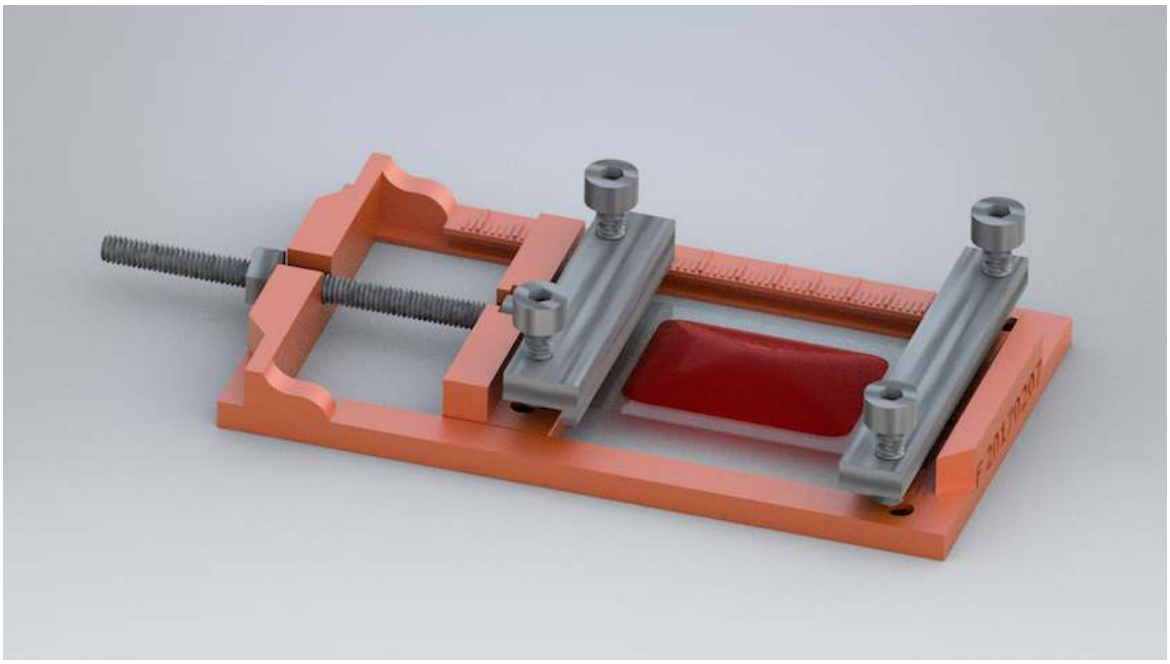

Figure 4.4 Diagram of a stretcher containing a single membrane and operated manually. The dimensions and shape of the device are adjusted to facilitate fixation protocols and imaging from cell-side of the membrane.

in the hood increases experimental variability, in an already very sensitive experiment. Therefore we developed a modified parallel stretcher that includes the stretching component, a motor, a control unit and a small computer.

A motor is incorporated in the stretcher itself. It is connected to a control unit and — beyond — to the I/O ports of a Raspberry Pi. The Raspberry Pi provides a constant voltage, such that the strain rate is approximately equal to 0.14 cm/s, although the setup could be adjusted to take varying voltages as input. We developed a custom-written graphical user interface (GUI) to set up and control the experiment. The user can adjust the stretch or visually add modules on a touchscreen to a protocol pane to assign the magnitude of the stretch (or release) and the duration between stretches. It is possible to apply an increasing stretch (using several steps in a specific time frame), or cycles of subsequent stretch and relaxation steps. On a control pane, the current status of the experiment can be tracked. Up to four separate parallel stretchers can be connected to a control unit, but multiple control units can be connected to the Raspberry Pi and controlled separately.

To run an experiment, the experimenter first calibrates the motor, to adjust for different strain rates as a result of different loads between experiments. They can then add steps to the protocol and start the experiment. During the experiment, the stretch can be increased or

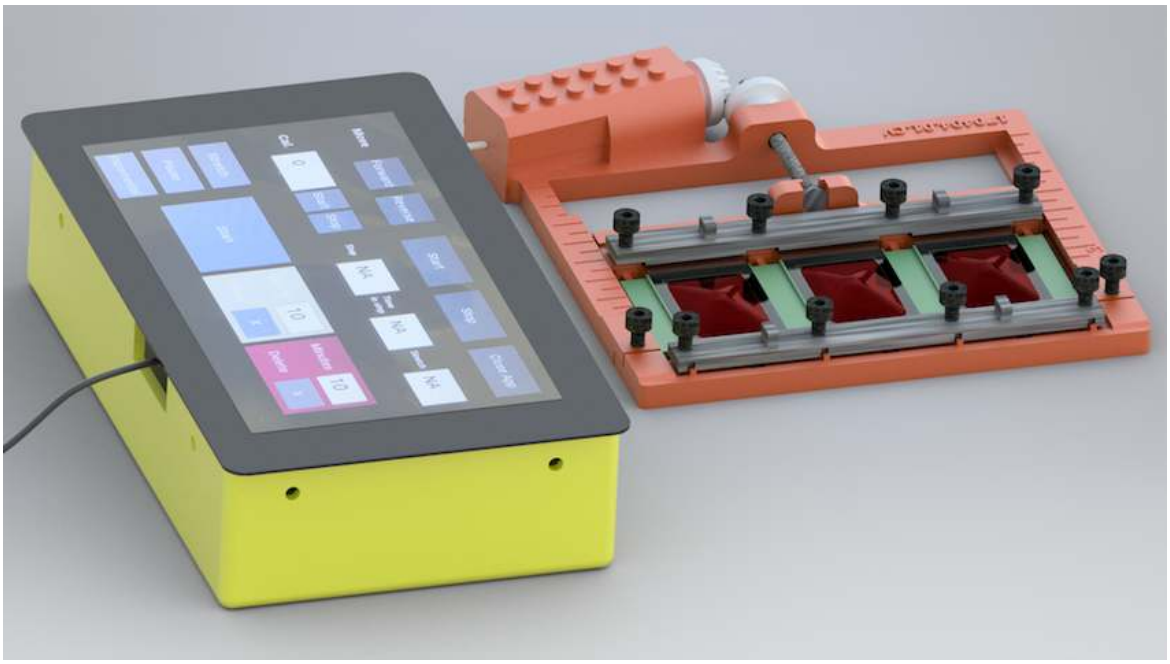

Figure 4.5 Set-up of the automated stretcher. The motor is connected to a Raspberry Pi (yellow box) and touchscreen that allow the user to control the protocol.

decreased if necessary without affecting the state of the experiment. Every stretcher can be unplugged easily, for example when harvesting multiple samples for gene expression analysis at different timepoints. We successfully used this device for all cyclic stretching experiments discussed in Chapter 5, including those that continued overnight. The device stretched the membranes with high fidelity. Future versions of the automated stretcher will incorporate an automated calibration mechanism, feedback regarding the actual stretch (which is currently derived from the calibration), and an internet-controlled system, so that the device can be controlled remotely.

4.2.3 PDMS membrane and functionalisation

To apply large-scale forces directly to cells, we used polydimethylsiloxane (PDMS) as elastic substrate. Here I discuss the manufacturing and chemical functionalisation of PDMS to allow the stable adherence of cells to the membranes. We propose two distinct techniques to attach ECM proteins to the membrane, using either a sulfo-SANPAH or BS^3 crosslinking protocol.

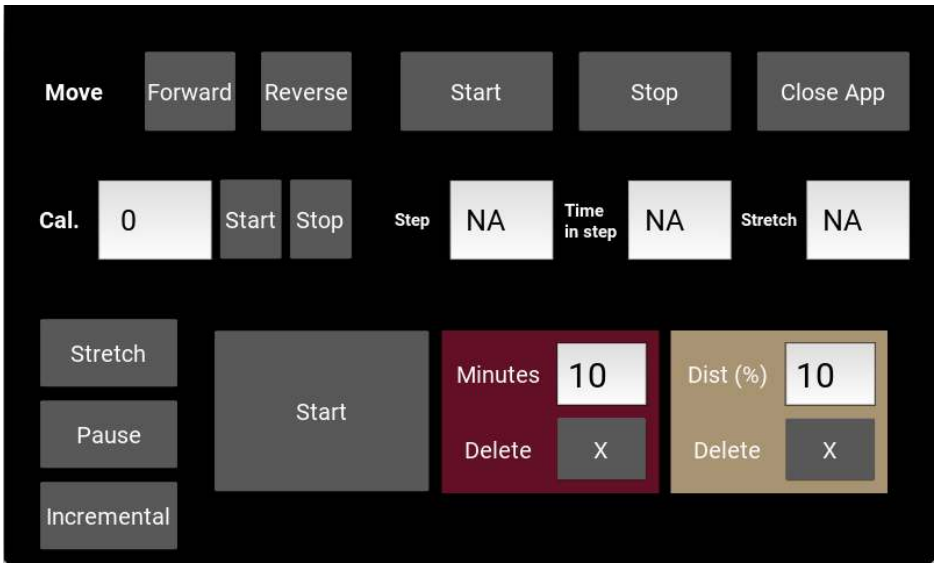

Figure 4.6 Screenshot of the graphical user interface, run on a touchscreen connected to a Raspberry Pi. The top half of the screen contains the experiment status. In the bottom half, steps can be added and removed to the protocol using the buttons on the left. When started, the experiment shown would first pause for 10 min, then execute a 10% stretch.

Manufacture of PDMS membranes

PDMS is a transparent and biocompatible elastic polymer that is produced by curing (baking) a mix of an elastomer and a crosslinker. The ratio of these two components controls the elasticity of the material, with the Young's modulus of the cured PDMS correlating linearly with the concentration of the crosslinker. In general, the extent of crosslinking causes the final membrane to consist of a single super-molecule [Fincan, 2015]. We mixed the two components at a ratio of 1:20 crosslinker to elastomer. This ratio has been described to translate to an elastic modulus of around 1 MPa, although thickness, curing temperature and duration, and environment temperature also play a role in determining the final stiffness and material properties [Wang et al., 2014a]. Our protocol should assure linear elastic behaviour within a range of 0 - 50% stretch (discussed in Section 4.3).

After degassing, we spincoated uncured PDMS onto a silicon wafer to produce a layer of 1 mm. Since PDMS features non-dimension-dependent behaviour at thicknesses above 200 µm, the spincoating procedure should not affect the material properties of the membrane.[1] After baking, oxygen plasma treatment induces the formation of silanol bonds on the surface

[1] Below a thickness of 200 µm, the random coils of polymer within the membrane reorient due to the shear stress at the higher angular velocities required to produce this lower thickness, inducing orientation that depends on the thickness of the PDMS layer.

of the PDMS, improving the hydrophilicity of the membrane [Hillborg et al., 2000]. We created a hydrophilic rectangle in the middle of the membrane by selectively covering the membrane with tape before plasma treatment, such that a bubble of liquid remained on the membrane, eliminating the need for a well for media and other liquids.

After plasma treatment, membranes were suspended in water to reduce hydrophobic recovery [Fritz and Owen, 1995; Murakami et al., 1998]. We found that membranes remain hydrophilic during at least the next 2 days when the samples are kept suspended in water before functionalisation, but we always proceeded with the next step of the functionalisation process within 5 hours after plasma treatment.

Membrane functionalisation using sulfo-SANPAH crosslinker

While some cell types are able to bind directly to the plasma-treated membranes, ES cells require the presence of integrin-binding ECM proteins such as fibronectin or laminin to assure stable binding. We first used an amine crosslinker to allow these ECM proteins to bind covalently to the membrane.

Sulfo-SANPAH has been used extensively as an amine crosslinker in previous studies, including to functionalise hydrogels [Sunyer et al., 2012] and PDMS [Li et al., 2006; Wen et al., 2014] and in applications such as the investigation of substrate stiffness [Yeung et al., 2005], the effect of cell surface area on behaviour [Carpi and Piel, 2014], and ECM tethering [Trappmann et al., 2012]. We modified the protocol to functionalise membranes suitable for stretching: After plasma treatment, sulfo-SANPAH was added to the membranes and exposed to ultraviolet light. As shown in Fig. 4.7, this induces the phenylazide group to interact with the silanol group of the PMDS membrane. After adding an ECM protein that contains an amine group, the N-hydroxysuccinimide (NHS) ester group is partially replaced by the ECM protein itself. This arrangement is stable for at least one week.

Although this protocol is a convenient and rapid method to functionalise PDMS for most cell types, we noticed a number of possible disadvantages. First, the binding of the crosslinker to the surface of the PDMS relies on hazardous UV wavelengths. While the associated hazards could be easily mitigated using protective equipment, it would be advantageous if this step could be avoided. Second, most importantly, ES cell attachment was substandard in a minority number of membranes, irrespective of medium type, as also observed in earlier studies [Farrukh et al., 2016; Huebsch et al., 2010; Wen et al., 2014]. Cells on these membranes, manufactured identically to successful membranes, did not adhere or displayed a round morphology characteristic of weak attachment (see Section 4.3). Adjusting the duration of UV exposure and introducing multiple washes reduced the occurrence of defective membranes to around 10-15%, but we failed to determine the exact cause of this

variability. Interestingly, we did not experience attachment issues when using other cell types such as smooth muscle cells, indicating the effect could possibly be exacerbated by the sensitive nature of ES cells' attachment [Granata et al., 2017].

Membrane functionalisation using BS^3 crosslinker

To address the variability of the sulfo-SANPAH-based functionalisation method, we developed a novel functionalisation technique (in collaboration with Dr C. C. Agley). This approach also relies on an amine-binding crosslinker to covalently attach fibronectin molecules to the PDMS surface, but does so in a more convenient way.

After plasma treatment, the PDMS membranes are treated with bind silane (3-(trimethoxysilyl)-propyl methacrylate), which links three oxygen molecules on the silica surface and a single silicon near the base of the bind silane molecule. Bind silane has previously been used to functionalise microfluidic devices [Zeng et al., 2006] and glass slides [Angenendt et al., 2002]. When adding BS^3, the amine group on one end of the molecule can interact with the carboxyl group, formed in neutral pH conditions, of the bind silane. Adding the amine-containing ECM protein automatically binds to the crosslinker, completing the functionalisation. Optionally, an ethanol amine wash can prevent further binding of other reagents to any remaining available amine groups on the crosslinker. However, we did not find this to be necessary, as the high concentration of fibronectin should assure that most groups are bound by fibronectin.

This protocol provides a convenient and reliable method to induce robust functionalisation of PDMS membranes with ECM proteins, with cells attaching well to the membranes, spreading similarly as on plastic (see Section 4.3), and remaining well-attached for at least five days. The technique we present here as two potential disadvantages. First, the duration of the protocol using BS^3 is longer than when using sulfo-SANPAH, involves additional washes, and a step involving additional reagents. Nevertheless, the reagents used in this protocol are easier to handle. For example, while sulfo-SANPAH is light-sensitive and has a very short half-life in water, BS^3 is water soluble and can be stored in the freezer for long time periods. Second, the spontaneous interaction of the NHS-ester in the BS^3 with the PDMS substrate could cause the BS^3 to connect multiple groups on the aminated silica surface. However, the effect is reduced due to the length of the 11.4 Å 8-carbon spacer, and does not appear to counteract good functionalisation and cell attachment [Mattson et al., 1993].

Using the PDMS membranes with the stretcher

When plating cells on single stretchers, the membranes were functionalised and then placed into the stretcher and clamped in place. In contrast, when plating cells on parallel stretchers,

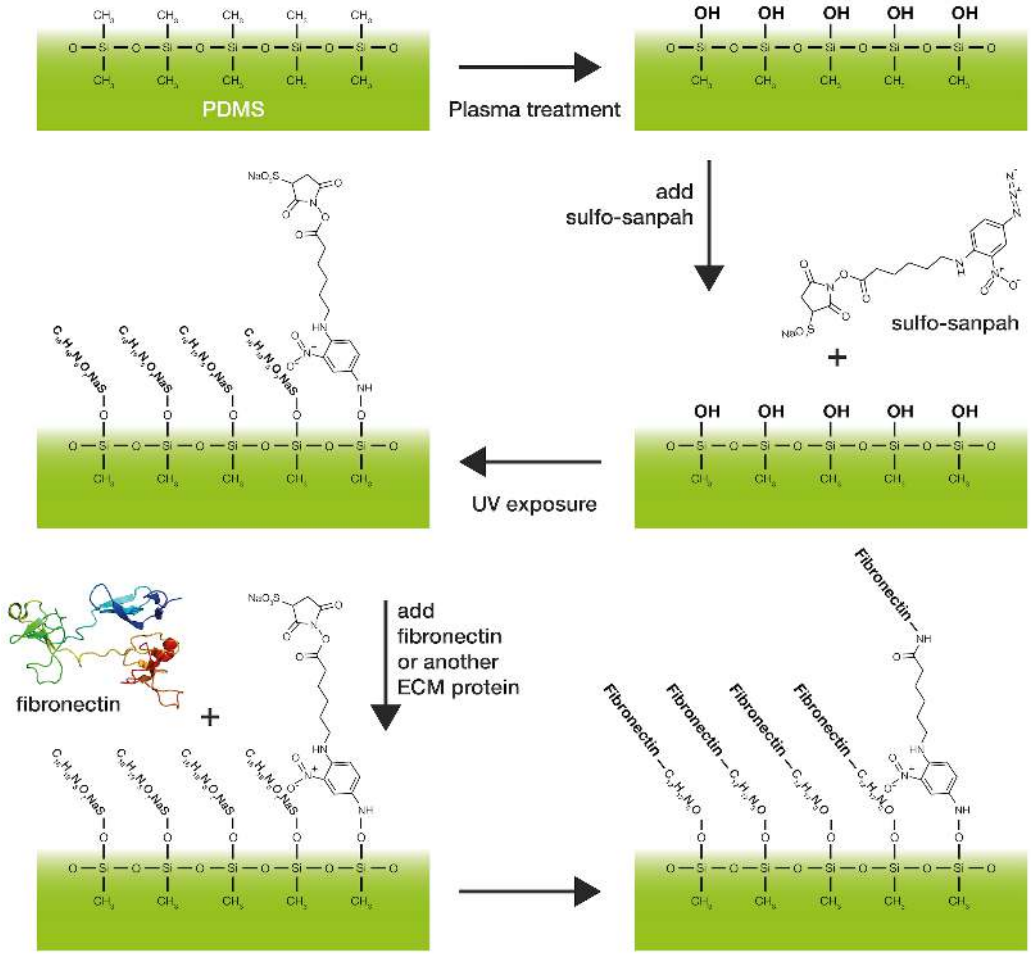

Figure 4.7 Functionalisation of PDMS membranes using a protocol based on the sulfo-SANPAH crosslinker. Plasma treatment exposes silanol groups on the PDMS membrane, to which a part of sulfo-SANPAH binds in response to UV exposure. In neutral pH conditions, the NHS ester is then replaced by an NH_2-containing ECM protein such as fibronectin.

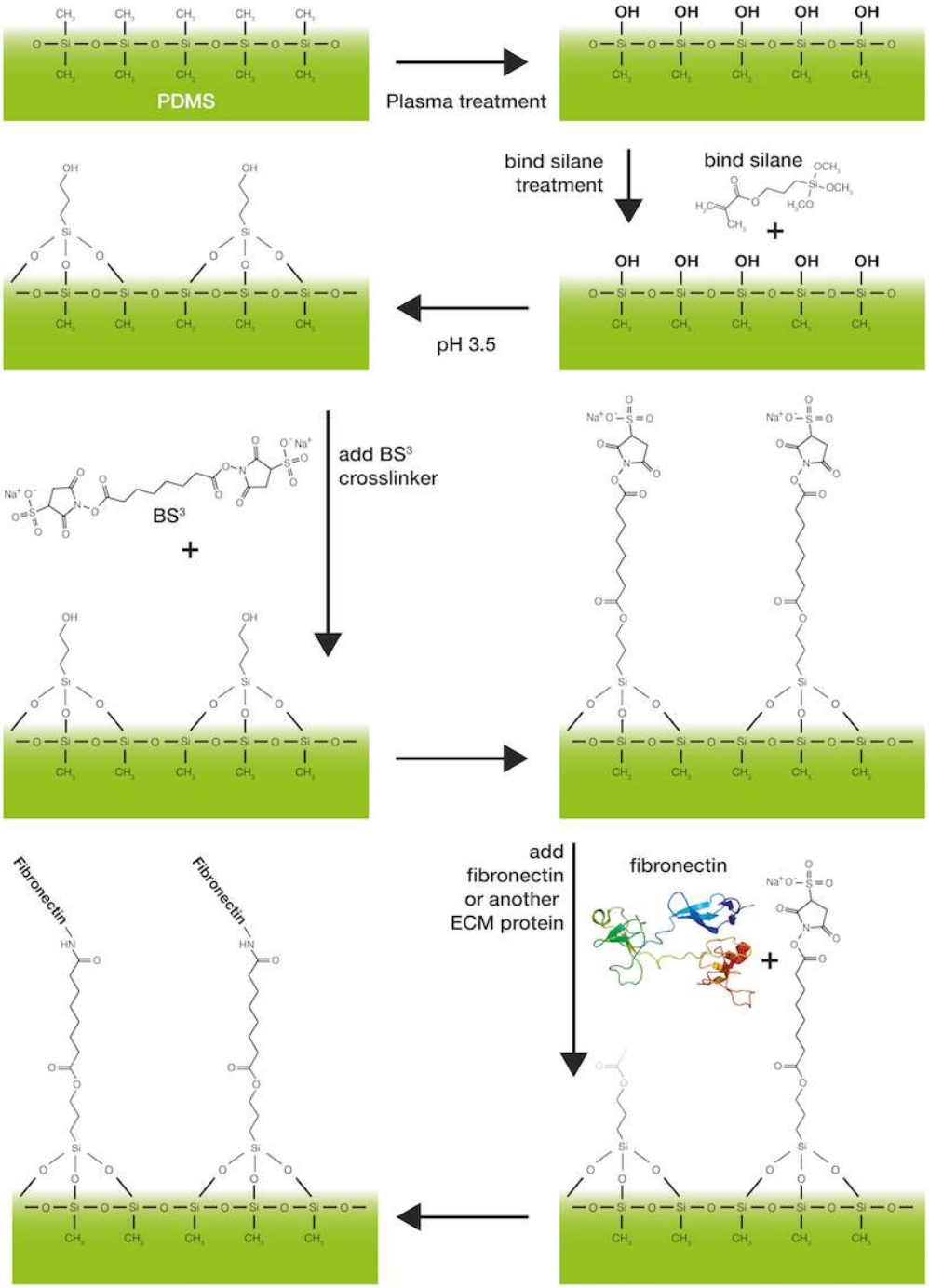

Figure 4.8 Functionalisation of PDMS membranes using a BS^3 crosslinker. After plasma treatment, which exposes the silanol groups, the membranes are incubated with a bind silane solution, which binds up to three hydroxyl groups on the PDMS surface. BS^3, a homobifunctional crosslinker, links these groups to fibronectin or other ECM proteins.

the membranes were first positioned on the stage and clamped in place. They remained on the stage during the functionalisation protocol and could then be slid into the stretcher, such that the functional area remained covered with liquid at all times during the procedure. After washes, cells in medium could be plated onto the membrane. Because the functional area was hydrophilised while the remainder of the membrane was highly hydrophobic, only this area remained covered with medium, usually up to 1 ml, even while cells were being stretched.

4.3 Mechanical and biological characterisation of the cell substrate stretching devices

To assure the accuracy of the devices in biological experiments, we carried out a number of characterisation and control experiments. First we studied the steps of the functionalisation protocol. We then estimated the stiffness of the membrane, and analysed the local strain in the functionalised area. Finally, we showed that cells attach stably to the substrate and remain well-attached during stretching.

Chemical and mechanical characterisation of the elastic substrates

Verifying the BS^3 functionalisation protocol Embryonic stem (ES) cells attach weakly to the hydrophilised PDMS membranes without attachment. Due to the weak nature of this attachment, they exhibit a round morphology and easily detach during washes. To verify that the functionalisation protocol was effective, we interrupted the protocol at different steps, as shown in Fig. 4.9, to check that attachment is suboptimal without completion of the protocol.

Plasma and bind silane treatment cause the exposure of hydroxyl groups on the surface of PDMS, similar to treatment only with oxygen plasma. Indeed, ES cells in Serum+LIF exhibited a round morphology and were weakly attached after both steps (Fig. 4.9a). Cells continued to be weakly attached even after the addition of BS^3 crosslinker (Fig. 4.9b), but attached well after completion of the functionalisation protocol (Fig. 4.9c). Ethanolamine incubation, which inhibits binding of proteins to BS^3, did not change the attachment level (Fig. 4.9d). Our results show that cells attach well to the functionalised membranes, and that all steps in the functionalisation protocol (apart from ethanolamine treatment) are essential. Only after fibronectin binding do cells flatten and stably attach.

Forces required for PDMS deformation, and estimate of PDMS stiffness To support the development of the automated stretcher, we estimated the forces required to stretch the membrane. This measurement could also be used to obtain a rough estimate of the stiffness

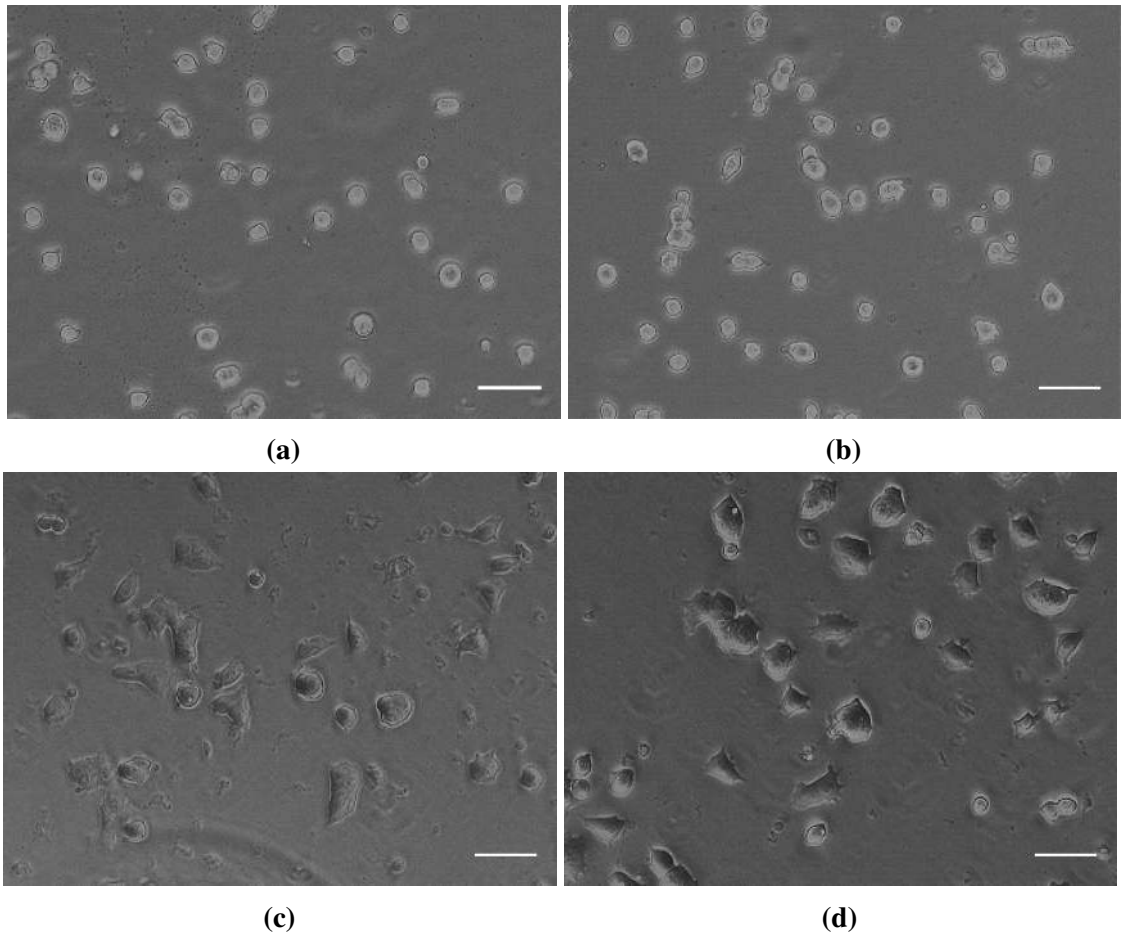

Figure 4.9 ES cells in Serum+LIF conditions, 4 hours after plating on PDMS membranes, treated with (a) plasma and bind silane (b) plasma, bind silane and BS^3 (c) plasma, bind silane, BS^3 and fibronectin and (d) plasma, bind silane, BS^3, fibronectin and ethanolamine, as described in the materials and methods. The scale bar is equal to 100 µm.

of the PDMS membrane. Therefore, we measured, using a calibrated spring, the forces required to stretch a membrane with original length of 40 mm between 0 and 50%, as shown in Fig 4.10a. The stretch is the added length of the membrane beyond the original 40 mm. The Cauchy stain is defined as

$$\varepsilon = \frac{\Delta L}{L}$$

where L is the original length (corresponding to 40 mm) and ΔL is the stretch. As ε varied between 0-50%, the force varied from 0-700 mN. This allowed us to calculate the Young's modulus of the PDMS membrane, since $E = \frac{\sigma}{\varepsilon} = \frac{F/A}{\Delta L/L}$, where σ is the stress, defined as the force divided by the cross-sectional area. While our method only provides a range of possible stiffnesses since it does not take into account the differences in the shape change

along the length of the membrane, it allows us to obtain a very rough estimate. Considering the cross-sectional area at a strain of 0% and 50% varied from 8.4 to 6.2 mm^2 respectively, we find that the stiffness of the membrane lies between 7 - 70 kPa. This values are lower than those described in the literature, but are the same order of magnitude. For example, Park et al. [2010b] find a stiffness of 280 kPa for 1:20 PDMS, while Wang et al. [2014b] mention a value of 600 kPa, although the curing times and temperatures in these studies are higher, which are both correlated with increasing PDMS stiffness Johnston et al. [2014]. Both for our values and those quoted in the literature, the stiffness of the PDMS membranes would be comparable to muscle tissue or cartilage, and significantly softer than plastic or bone [Cox and Erler, 2011].

As discussed, the stiffness of the PDMS membrane is influenced by the ratio of the two constituent components and the curing time during its preparation. We chose the ratio of crosslinker to elastomer ratio so the stretch applied remains within the linear range of the stress-strain curve, and away from the breaking point. The ease of handling the membranes, which decreases with lower stiffnesses, provided a lower limit on the stiffness. Across a range of elastomer-to-crosslinker ratios from 1:15 to 1:24, we found that cell attachment was not significantly affected by the stiffness of the PDMS membranes, as shown in Fig. 4.10c - d.

The local strain within the PDMS membrane We wanted to assure that the stretch exerted on the membrane on a macroscopic level is translated into homogeneous microscopic strains. Therefore, we embedded microscopic florescent beads in the PDMS membranes, then stretched the membranes up to 30%. We wanted to measure the ratio of the microscopic to macroscopic strain between beads at 9 points distributed throughout the functional area, for each 10% increase in the stretch of the membrane. Therefore we first calculated the microscopic Cauchy strain at each point i, parallel and perpendicular to the direction of the macroscopic stretch, corresponding to $\bar{\varepsilon}^i_{yy}$ and $\bar{\varepsilon}^i_{xx}$ respectively (stretch was applied along the y-axis). We then divided these values by the macroscopic strain parallel to stretching (i.e. $E_{yy} \in \{10\%, 20\%, 30\%\}$). The results for all points, $\varepsilon^i_{yy}/E^i_{yy}$ and $\varepsilon^i_{xx}/E^i_{yy}$, are shown in Fig. 4.10e - f. Overall, the strain in the direction parallel to stretch was homogeneous, with a mean equal to 0.88 ± 0.12. Since the device applies a deformation to the cells, rather than a specific force, the deviation of this value from unity is acceptible. As expected, in the direction perpendicular to the stretch, the ratio was negative, with a mean equal to -0.36 ± 0.04. The associated Poisson's ratio of the membrane, derived from the microscopic strains, was equal to 0.41 ± 0.08 in the functional area, with no strong deviations towards its edges. This value is slightly below the Poisson's ratios found in the literature, with [Johnston et al., 2014] quoting a value between 0.45 - 0.50, and Dogru et al. [2018] finding a Poisson's

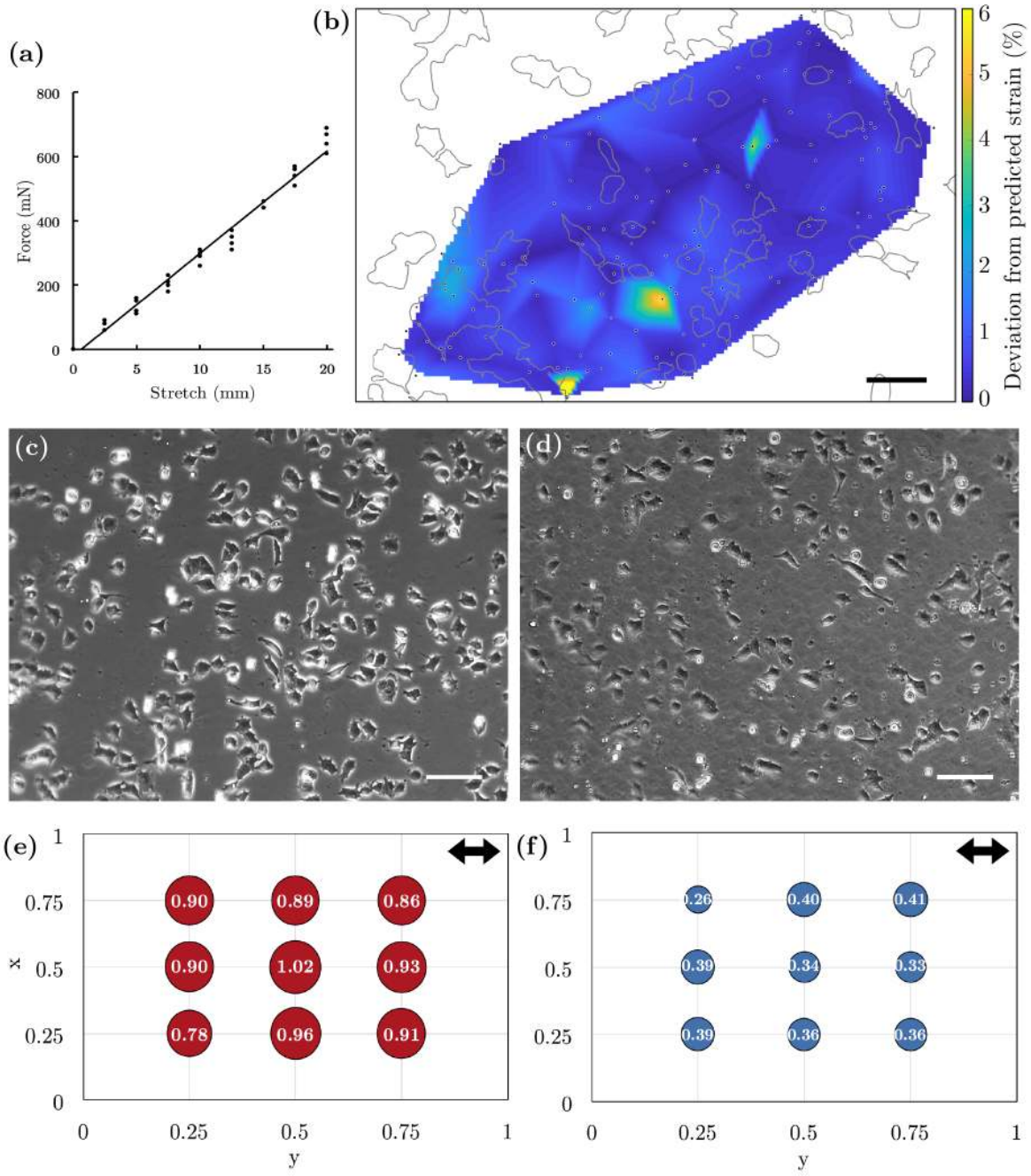

Figure 4.10 (a) Force required to stretch a membrane of 40 mm between 0 - 20 mm, fit well using $y = 32x + 21$. (b) Deviation of the displacement of 148 beads (black/white dots) as percentage of the global strain. Outlines of cells are shown in grey. The scale bar is 50 µm. (c) - (d) ES cell attachment in Serum+LIF on PDMS membranes with (c) 1:15 (d) 1:24 crosslinker to elastomer ratio, and functionalised using the BS^3 protocol. The scale bar is equal to 100 µm. (e) - (f) Ratio of local strain to the macroscopic stretch at 9 locations in the functional area of the membrane, (e) parallel and (f) perpendicular to stretching. The direction of stretch is indicated by the arrows.

ratio of 0.47 - 0.48 for thin PDMS films, which varies with different curing agent to elastomer ratios. Our values are, as expected, fully below 0.50, the upper limit for isotropic materials.

In the absence of large imperfections, the local strain of the membrane parallel to stretch should be homogeneously distributed along the length of the entire membrane. Our data shows that this was indeed the case, such that cells experienced a local strain in the direction of stretch ε_{yy} close to that applied to the macroscopic system. Because the membrane narrows with increasing stretch near the middle point along the x-axis, this does not hold for the strain perpendicular to the macroscopic stretch. However, as our data illustrates, these effects remained small throughout the functionalised area, and should not significantly affect the biological results.

Next, we wanted to check whether the local strain is affected by the presence of cells, to assure that colonies are not able to withstand the macroscopic stretch on a local level by exerting forces on the upper layers of the membrane to counteract its macroscopic deformation. This could also affect the optimal cell density, as large colonies of ES cells might be able to cooperatively resist the stretch, thus reducing its downstream biological effects. To test this, we measured the displacement of beads, embedded near the surface of the membrane, and subtracted what would be expected from the displacement on the macroscopic scale. This measure, divided by the actual displacement, is shown in Fig. 4.10b, and shows how much the actual displacement deviates from what would be expected from the global trend. The actual deviation of a point from the average displacement was below 2.5% for all but three points, which exhibited an unexpectedly higher deviation than their neighbours and could be disregarded as outliers. Moreover, the distance of beads to neighbouring cells or colonies did not influence the deviation of their displacement. This data indicates that cells are unable to resist the deformations of their substrates, and could therefore be expected to experience the stretch according to the predictions.

Attachment of cells to the stretcher and cellular behaviour

We first analysed the attachment of cells in different media types on unstretched membranes, functionalised using the different protocols. Using sulfo-SANPAH resulted in a good attachment for the majority of cells in Serum+LIF and on fibronectin, although colonies were interspersed with cells which maintained a round morphology characteristic of suboptimal attachment, as shown in Fig. 4.11. In contrast, ES cells in identical conditions on BS^3-functionalised membranes were attached better and displayed a more flattened morphology, both at 4 h after plating (see Fig. 4.12a), and at 26 h after plating (see Fig. 4.12b), when the morphology was very similar to plastic. We observed the same morphological similarity to

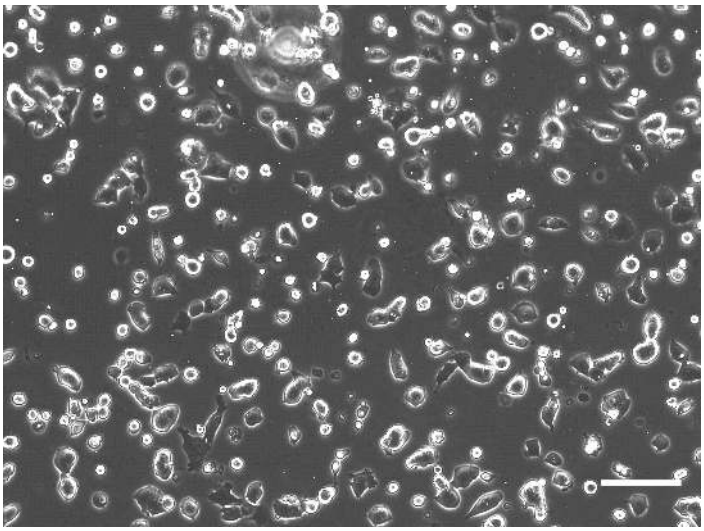

Figure 4.11 ES cells plated in Serum+LIF media conditions on PDMS membranes functionalised using the sulfo-SANPAH crosslinker and fibronectin, 8 h after plating. The scale bar is 100 μm.

plastic also for cells in other conditions, such as 2i+LIF or 2i on a fibronectin coating (not shown).

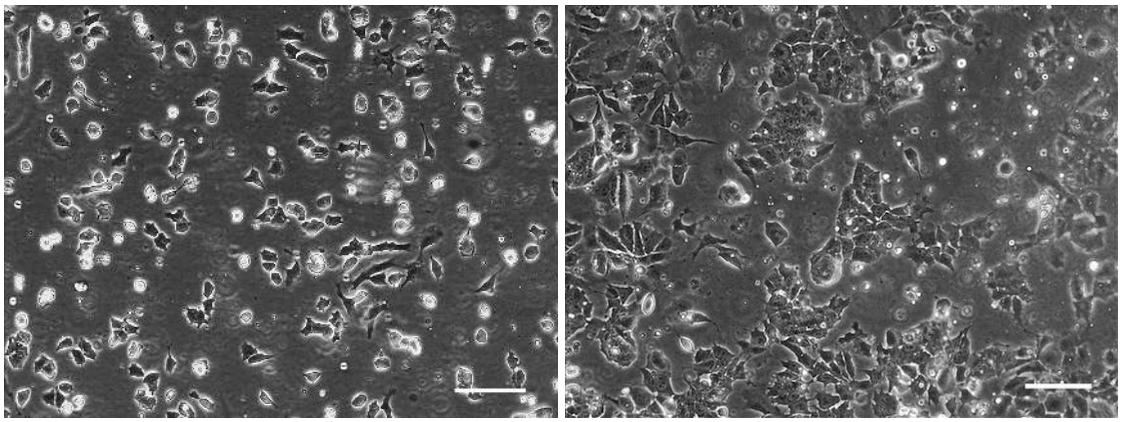

Figure 4.12 ES cells in Serum+LIF medium conditions plated on PDMS membranes, functionalised using the BS^3 crosslinker and fibronectin, after (a) 4 h and (b) 26 h. The scale bar is 100 μm.

Using the hydrophobicity of the membranes as a replacement for a well for culture media limits the amount of media that fits stably on the membrane. As such, the media should be replaced every 12 h to prevent the effect of a change in media acidity or nutritional content on the experiments. If so, cells remained well attached to the membranes for several days with a healthy morphology, and the maximum duration of culturing on a single membrane

was mainly determined by the membrane's confluence. In general, the morphology of cells did not indicate any visible differences to cells grown on plastic.

To test our stretching protocol, we stretched ES cells in Serum+LIF on fibronectin, as shown in Fig. 4.13. We then measured the cells' expansion parallel and perpendicular to the stretch as the membrane underwent a stretch of 20% and 40%. As shown in Fig. 4.14, the parallel extension of the cells was broadly equivalent to the macroscopic stretch. The actual strain, with a mean of $19.1 \pm 0.1\%$ and $38 \pm 1\%$ at a strain of 20% and 40% respectively, was slightly lower than the global stretch, matching the lower local strain of the membrane (as shown earlier in Fig. 4.10d - e). In the perpendicular direction, cells' withdrawal was larger than predicted from the local strain. As shown in Fig. 4.14, the strain of cells in this direction had a mean of $-11.2 \pm 0.3\%$ and $-21.8 \pm 0.3\%$ respectively. However, in both directions, while protrusions responded fully to the stretch level of their substrate, the surrounding membrane stretched somewhat less, and the cell surface area did not expand proportionally to the protrusions.

Our data demonstrates the following: First, the substrate was stretched as expected, and cells experienced this stretch. Second, cells remained well attached to the substrate, both before, during and after stretch. Third, during the first few minutes after stretching, cells did not remodel significantly and remained well-attached to the substrate. Antibody stainings for Y118 phospho-paxillin (pPax), shown in Fig. 4.15, mark focal adhesions, and the distribution remained similar before and after stretching. On longer timescales, however, the cytoskeleton did exhibit significant changes. Starting around 5 min after stretching, cells started to retract from their maximum extended position. During the next 30 min, substantial changes occurred as cells slowly returned to their original shape, as shown in Fig. 4.16. This retraction was not an indication of a decrease in cell health. Using caspase 3/7 we showed that the proportion of cells undergoing apoptosis did not increase significantly during this time frame (discussed in Section 5.5).

In summary, cells attached well to their substrate and remained so during and immediately after stretching, as evidenced by bright-field images and immunofluorescence stainings. This is true both for embryonic stem cells and muscle cells, on fibronectin, laminin and collagen. While cells do remodel significantly, starting minutes after stretching, they remain healthy during longer experiments and in the sub-ideal conditions of live imaging, as evidenced by the low proportion of cells undergoing apoptosis after having been stretched.

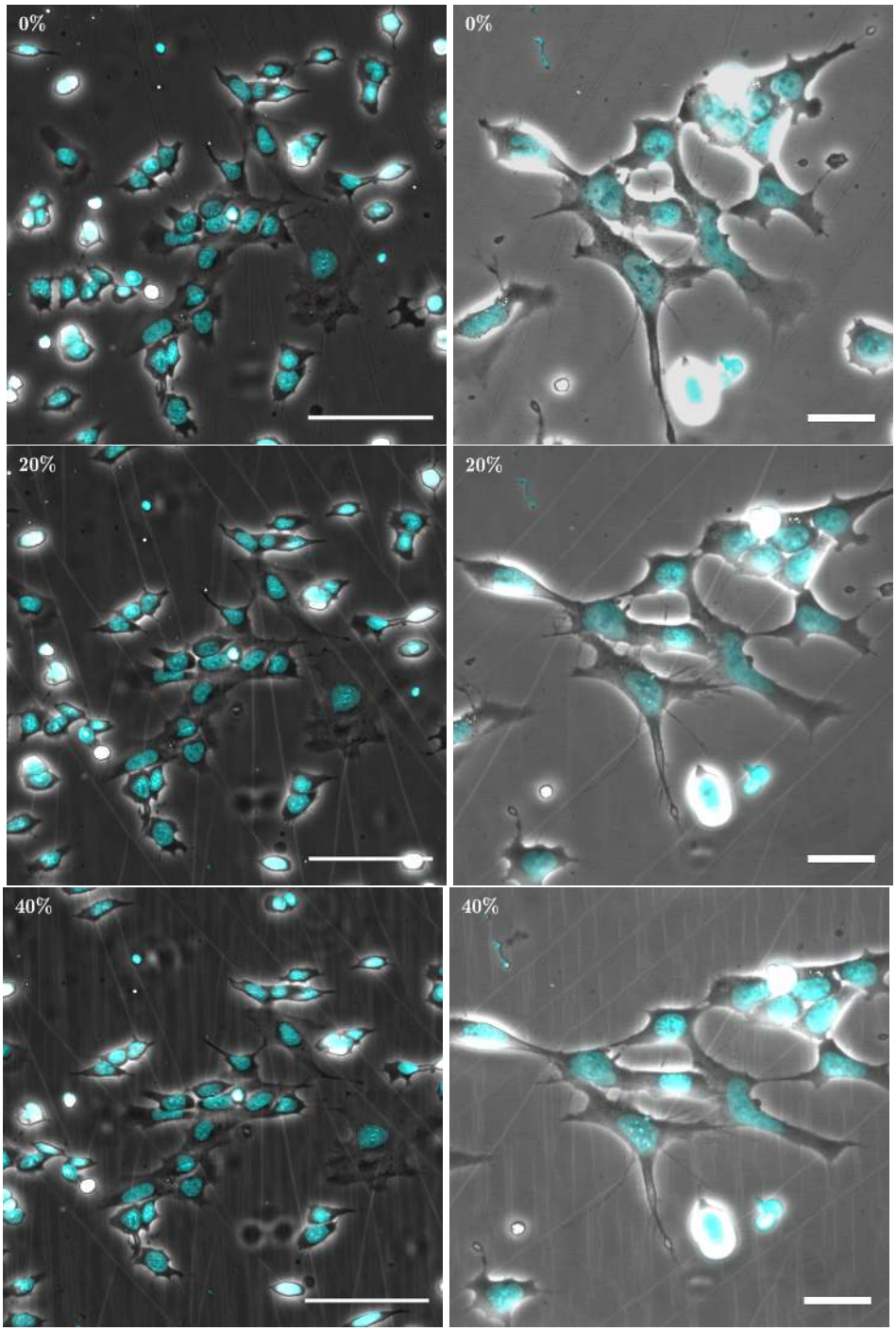

Figure 4.13 Examples of ES cells in Serum+LIF medium conditions undergoing stretching, including rest (top), 20% (middle) and 40% (bottom). Nuclei are stained using Hoechst (cyan). Images were taken within 5 min after stretching. The scale bars are 100 μm (left) and 25 μm (right).

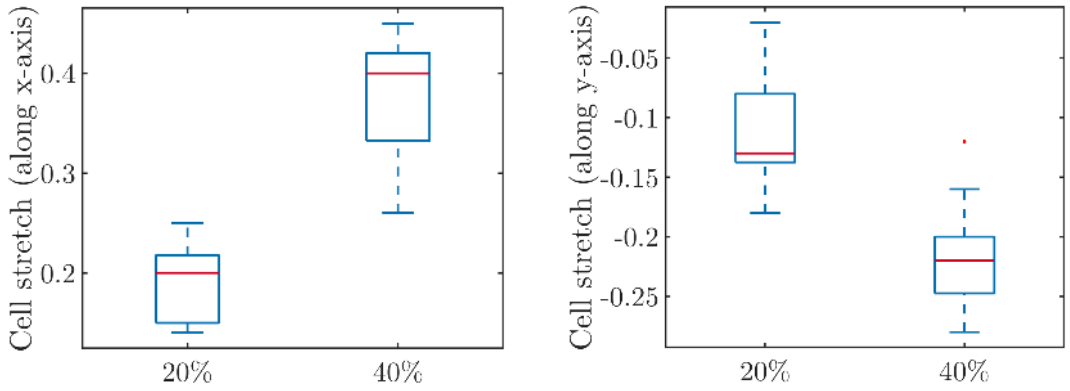

(a) **(b)**

Figure 4.14 Strain in the directions (a) parallel and (b) perpendicular to the applied stretch, as measured by fitting a bounding box to each cell, of cells ($n = 15$) exposed to a macroscopic stretch of 20% and 40%. Measurements were taken within 5 min after stretching.

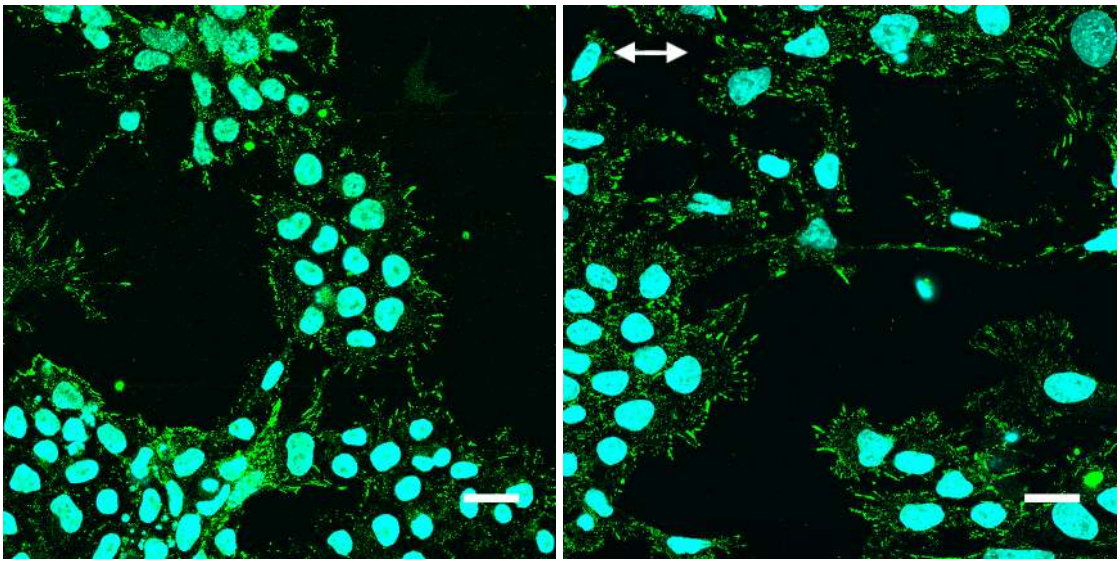

(a) **(b)**

Figure 4.15 ES cells in Serum+LIF medium conditions, stained for pPax antibody and DNA (Hoechst), fixed (a) before stretching and (b) 2 min after stretching. Arrows indicate the direction of stretching. The scale bar is 50 µm.

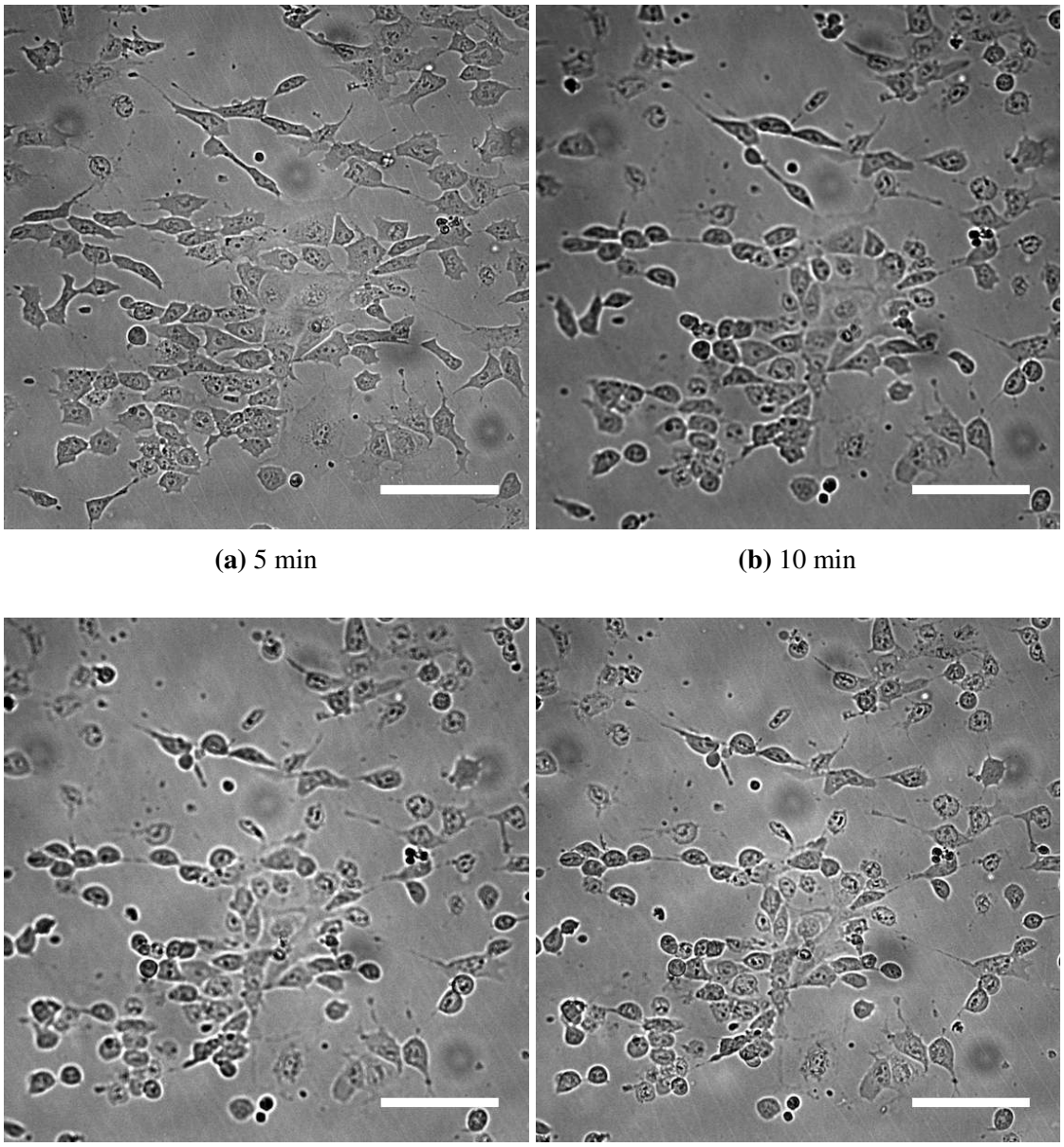

(a) 5 min **(b)** 10 min

(c) 20 min **(d)** 30 min

Figure 4.16 Cells retracting after stretching. Bright-field images of ES cells in Serum+LIF (a) 5 min, (b) 10 min (c) 20 min (d) 30 min after stretching. The scale bar is 100 μm.

4.4 Conclusion

In this chapter discussed the development of an apparatus aimed at stretching an elastic substrate. The device's specifications satisfy the requirements originating from its use in biological settings, such as easy automation and use for live imaging, fixation and immunofluorescence stainings. We measured the PDMS membranes used with the device to have a stiffness between 10^4 - 10^5 Pa, and found that the stretch propagates homogeneously throughout their surface, resulting in similar microscopic and macroscopic strain values. We presented two techniques to functionalise the membrane, and showed that cells remained attached to the substrate, were insensitive to the stiffness of the membrane, and were unable to measurably deform the membrane. The cells were stretched as expected but exhibit significant shape remodelling soon after stretching, while also remaining healthy. These results confirmed the validity of our methodology and practical approach, and justified its use to study the effects of stretching to ES cells and analyse their response, in the next chapter.

Chapter 5

Cell stretching affects cell behaviour but has limited effects on pluripotency

5.1 Introduction

In the previous chapter we presented a device to stretch cells through an elastic substrate, and characterised its technical and biological behaviour. This chapter focusses on the application of this device to embryonic stem (ES) cells, which are susceptible to a wide range of signals that can disturb the precarious balance between pluripotency-maintaining and differentiation-inducing cues. By perturbing the mechanical environment, we investigated ES cells' sensitivity to mechanical signals in various states of pluripotency, and studied how the magnitude of the effects induced by these signals compares to those of biochemical signals typically used to induce differentiation.

We tested the response to stretch in a range of experimental conditions. We first focused on gene expression, using the expression of the immediate and early genes as a readout of the early effects of stretching. Then, we studied the response of the pluripotency network using gene expression measurements and Rex1-GFP reporter intensity, and found that the impact of stretching on pluripotency and early differentiation was limited. To analyse the breadth of pathways affected, we performed transcriptome-wide sequencing, which highlighted the large impact of culture media on susceptibility to mechanical signals. Finally, we found that intracellular calcium concentration was highly influenced by stretching and likely constitutes one of the first responders to stretch.

For most experiments in this study, we stretched the PDMS membranes 35% to maximise the effect of the stretch on the cells. This amount, while considerably higher than physiological levels of stretch, was chosen because membranes still exhibited a homogeneous and

linear stretch-strain relationship and remained below the yield point. Since some membranes would break when attempting to stretch 40% or more, we considered 35% the upper limit to still obtain reliable membrane behaviour.

5.2 Investigating the effects on gene expression

5.2.1 Transcriptional changes to the immediate and early genes

One of the primary readouts of cell state is the transcriptional expression of the relevant genes. Considering the stress-related nature of stretching, we first analysed its effect on the expression of four members of the family of immediate an early genes (IEGs). One of the primary transcriptional responders to a variety of stresses (see Section 1.3.3), the IEGs were found to be affected by stretch in other cell types [Morawietz et al., 1999], and therefore constituted a likely candidate for mechanosensitive reporters in ES cells.

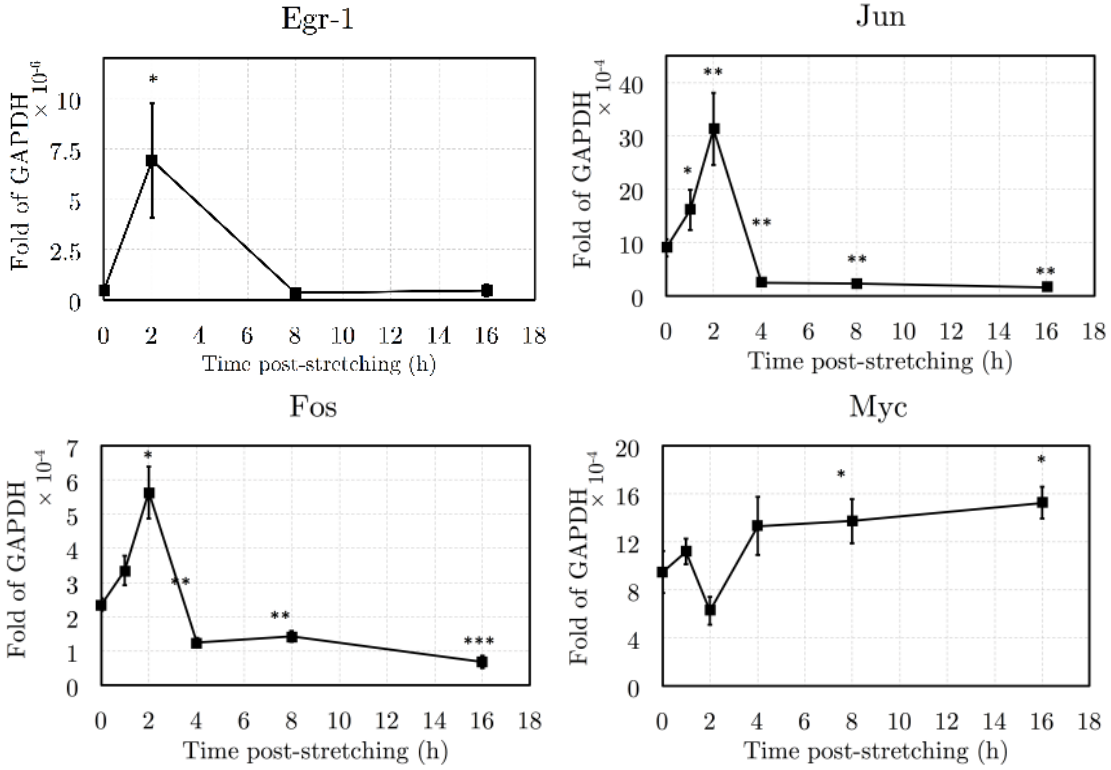

Figure 5.1 Gene expression changes to four immediate and early genes after stretching. Cells were plated in Serum+LIF on fibronectin-coated membranes, then stretched at t = 0 h, and collected as indicated. Samples at t=0 h were left unstretched. Error bars correspond to standard deviation.

To test the role of the immediate and early genes in the response of ES cells to stretch, we plated ES cells in Serum+LIF media conditions on fibronectin-functionalised PDMS membranes, as described in the previous chapter. For each sample, cells were left to attach for 8 h to a membrane within a stretcher. The membrane was then stretched 35% and cells were collected after 1 h, 2 h, 4 h, 8 h and 16 h. Unstretched samples were collected together with the 1 h timepoint, and were plotted at 0 h.

As shown in Fig. 5.1, stretching was followed by a strong increase in the transcription of three of the IEGs; Egr-1, Jun and Fos. The increase was strongest at two hours, at which point the increase was statistically significant across all three genes. By four hours the expression of Egr-1, Jun and Fos had returned to baseline levels.[1] Myc exhibited a remarkably different trend, showing a short-term decrease at 2 h, followed by a quick recovery. This divergent behaviour agrees with previous findings which describe the persistent upregulation of Myc, starting at 1 h after stretching [Alway, 1997; Hurley et al., 2010].

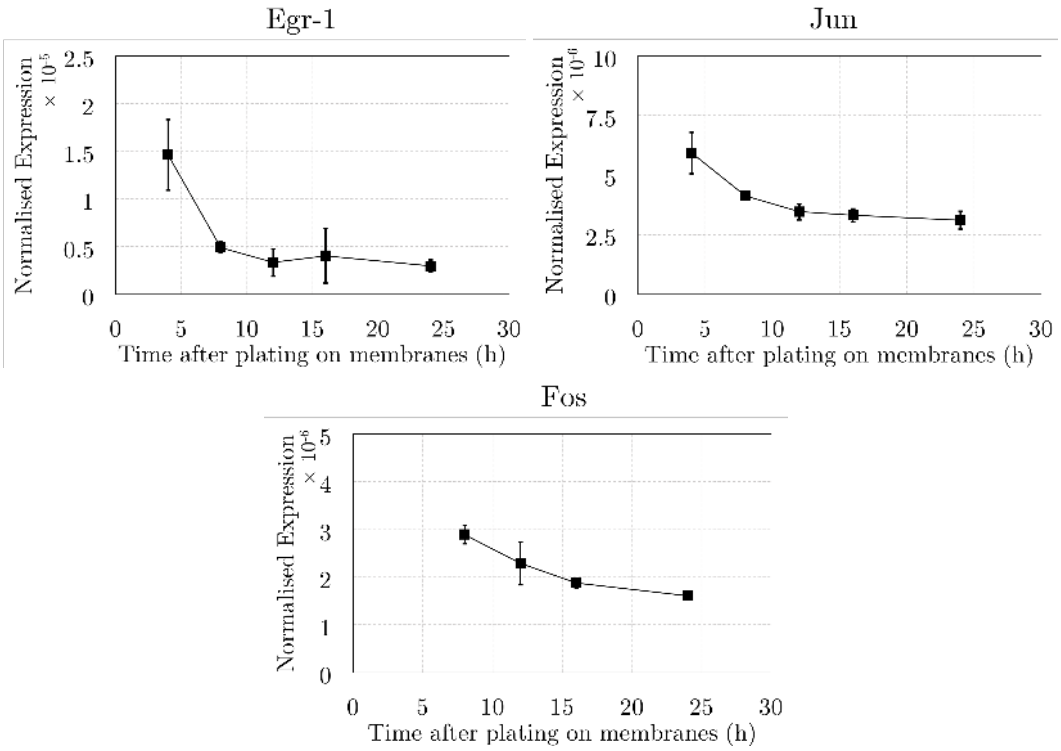

Figure 5.2 Gene expression of the IEGs after plating cells on PDMS membranes without stretching. Error bars correspond to standard deviation.

[1] We plated cells 8 h prior to the start of the experiment. Therefore the upregulation of the IEGs after plating could still persist at the start of the experiment, explaining the differences between the baseline expression levels at 0 h and after 4 h. This does not affect the main conclusion of this experiment, however.

To control for potential changes in the IEGs in unstretched samples, we plated cells on PDMS membranes without stretching and analysed the changes in the expression of the IEGs during the next 24 h. As shown in Fig. 5.2, Egr-1, Jun and Fos experienced a peak in transcription for 8 h after plating that slowly decreased during the next 16 h. Therefore, to reduce the effects of the changes in the IEG caused by plating on the increase prompted by stretching, we waited with stretching until 8 h after plating. Although significant changes still occur from 8 h to 24 h after plating, the shape of the short-term increases in the IEGs shown in Fig. 5.1 implies that the effect is small.

The three IEGs exhibiting transient transcriptional upregulation have all been described to be affected by the specifics of the type of external input, including magnitude and duration [Murphy et al., 2004; Thalhauser and Komarova, 2009]. In addition, their activation was recently found to be dependent on the characteristics of the upstream Erk signal, with persistent Erk activation resulting in an initial transcriptional peak, while repeated and interrupted Erk activation causes multiple peaks, provided the inactive interval is sufficiently long [Nakakuki et al., 2010; Ryu et al., 2015]. Using an optogenetic technique to activate Ras (upstream of Erk), Wilson et al. [2017] found the minimum required duration between activations to produce separate peaks in Fos expression to be around 25 min.

Before publication of these findings, we tested the mechanical response of ES cells to cyclic strain. We exposed cells to a protocol comprising a single cycle consisting of first applying a stretch of 35% for one hour, then relaxing and retaining the membrane fully for one hour, and then finally permanently re-applying 35% stretch. If IEG transcriptional induction is a direct function of the input signal, without hysteresis, the transcription profile would exhibit an additional increase at one and two hours after the second stretch, i.e. at the 3 h and 4 h timepoints. However, as shown in Fig. 5.3, the dynamics of the IEGs in this experiment were similar to those without the release and re-application of the stretch.

Our observation suggested that the regulatory system of the IEGs might have the ability to store past information, some sort of cellular memory, allowing the current state to capture any past gene inductions, thus preventing the immediate re-activation of the genes soon after the original signal. In the context of the role of Erk activation, this implied one of two possibilities. On the one hand, the Erk activating signal could be continuous after stretching, which would preclude the repeated activation of the IEGs, as previously described [Ryu et al., 2015]. As such, the early transcriptional effects of stretching on Erk would be either a reflection of the current state of the system (i.e. stretched versus relaxed) or incorporate a delayed decrease of the initial activation. On the other hand, stretching could induce a temporary increase in Erk. Considering the dynamic nature of the experiment, and the fact that we observed cellular remodelling even 30 min after stretching, this is perhaps the

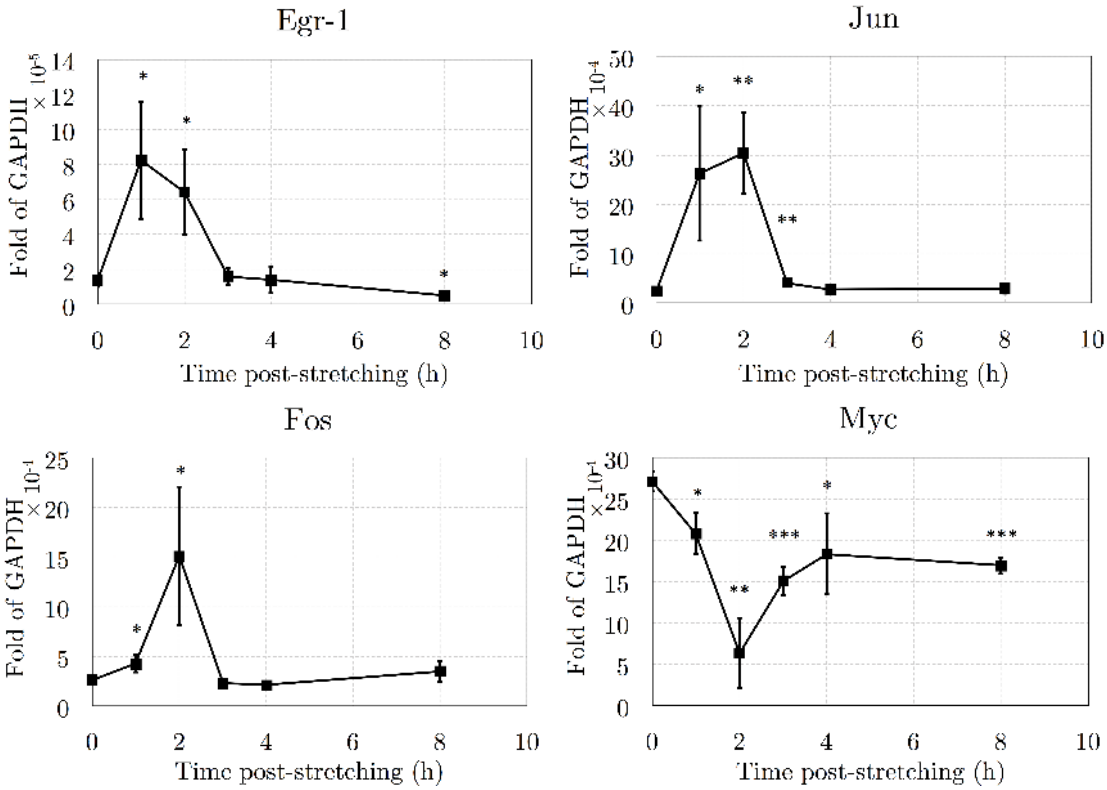

Figure 5.3 Gene expression changes of IEGs in response to a cycle of stretching (1 h), releasing (1 h) and stretching. Cells are plated in Serum+LIF on fibronectin, and collected at indicated times, including at timepoints when the stretch cycle was not yet completed (i.e. 1 h and 2 h). Error bars correspond to standard deviation.

most likely option. However, the lack in IEG activation after the second stretch would then imply that the gap between the repeated stretches (either 2 h if only stretching would matter or 1 h when including both stretching and relaxing steps) was shorter than that required for repeated re-activation, which contrasts with the earlier observation that even 32 min causes repeated Fos activation peaks [Wilson et al., 2017]. In either case, the nature of IEG activation in response to mechanical stretch would be different from that observed in biochemically-activated experiments. The duration of the recovery time of the IEGs in response to stretching can be explored further in future experiments by adjusting the duration of the stretch.

Note that the differential regulation of the IEGs in the stretch-and-release experiments exhibited an earlier upregulation than the previous experiment. Since the two protocols were still identical at the 1 h timepoint, the differences were indicative of the high experimental variability that was present across the different stretching experiments in this project (dis-

cussed further in Section 5.2.4). Considering this variability and the temporary nature of IEG activation, these experiments did not yet shed light on how the magnitude of the downstream effects of stretching on the cellular machinery compares to other experimental (possibly biochemical) variables.

5.2.2 Effects on the pluripotency network

We next wanted to get an initial understanding of the direct effects of stretching on the pluripotency network. Hence, we quantified the transcription of Nanog after stretching to a control sample at each timepoint, as shown in Fig. 5.4. We found Nanog to be downregulated in response to stretching at 8 h, but the fold change was small. In addition, there were no significant differences between the stretched and unstretched timepoints at 2 h or 16 h. This indicated that the effects of stretching, and particularly of the upregulation observed in the IEGs, remained limited, and involved a delay of several hours before reaching the pluripotency network.

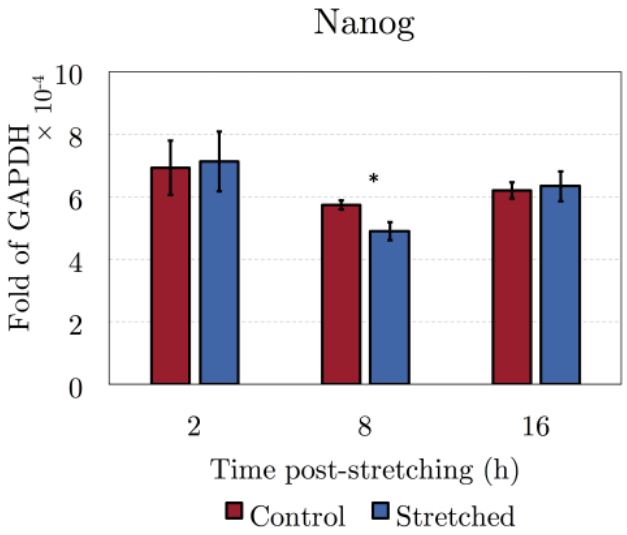

Figure 5.4 Expression level of Nanog in Serum+LIF media conditions on fibronectin, 2 h, 8 h and 16 h after stretching. Error bars correspond to standard deviation.

Next we tested and compared the effects of different types of experimental inputs. In particular, we wanted to establish the effect of stretching on differentiation, and compare its magnitude to chemical signals. Secondly, we intended to determine whether ES cells' mechanical sensitivity varies as they passed through the various states of the differentiation process. Our initial investigation focused on the Serum-based media types. Considering the

rounder morphology and less attached character of cells in 2i, and because of the inhibition of MEK by PD03, the effects of stretching would likely be diminished in 2i culture conditions [Ying et al., 2008].

To test this, we ran both control and stretched samples in parallel, each in triplicate. This implied a minimum of six samples per experiment, which increased exponentially by the number of samples and membranes in the experiment. A differentiation assay also requires the inclusion of naive (control and stretched) samples, adding another six membranes, multiplied by the number of timepoints. For this reason, we limited ourselves to one or two timepoints, resulting in a total number of samples of 18 or 24, which were each manufactured and functionalised individually.

We first plated ES cells grown in Serum+LIF media conditions into Serum-only media, thus removing the LIF media component, onto the PDMS membranes. This should induce cells to move slowly away from the naive pluripotent state towards an intermediate state, although the effect of differentiation would be limited at the timepoints we considered [Cherepkova et al., 2016]. As such, this experiment was aimed mainly at testing the effect of stretching when somewhat relaxing the 'forces' confining cells within their pluripotent state. First, cells were plated on fibronectin-coated membranes, then stretched 35% 24 h later, and collected after 8 h, 16 h and 24 h, corresponding to timepoints of 32 h, 40 h and 48 h from the start of differentiation in Serum-only media. We measured the expression level of Nanog, one of the earliest responders of differentiation [Kalkan et al., 2017], such that any differences in the rate of differentiation induced by stretching should be easily detectable in the expression of stretched to control samples. We also measured transcription of Klf4, which experiences regulation by the MAPK pathway, positioning it as a potential downstream marker of the changes in the expression of the IEGs [Riverso et al., 2017].

The resulting transcriptional profiles of Nanog and Klf4 are shown in Fig. 5.5. In contrast to the effect of stretching in Serum+LIF media conditions, the mean expression level for both genes actually increased, indicating that while stretching pushed cells towards differentiation in the heterogeneous naive conditions of Serum+LIF media, it could actually reduce the rate of differentiation in Serum-only media. However, the differences between stretched and control samples were not statistically significantly different from unity, so we could not draw this conclusion conclusively.

The transcriptional changes following LIF withdrawal from Serum+LIF are typically significantly slower than in N2B27 after the withdrawal of 2i/LIF [Smith, 1991]. As such, differentiation from Serum+LIF to Serum-only, originally selected because the Serum-containing media are more susceptible to mechanical signals than 2i+LIF, could be suboptimal to study the influence of mechanotransduction during differentiation. To further investigate

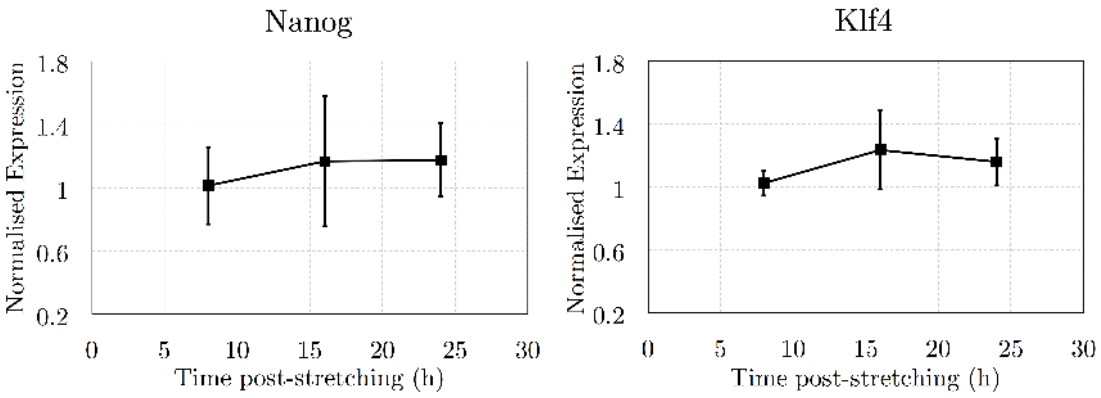

(a) Nanog **(b)** Klf4

Figure 5.5 Ratio of the expression level (as fold of GAPDH) of stretched to control samples, for Nanog and Klf4 in response to static stretching in Serum. Cells were plated on fibronectin-coated membranes in Serum, from Serum+LIF. The membrane was stretched 24 h later, and timepoints shown are 8 h, 16 h and 24 h after stretching. Error bars correspond to standard deviation.

the potential differential effects of stretching during the different stages of differentiation, we also stretched cells during differentiation from 2i media conditions. Naive cells in 2i media were plated onto laminin-coated membranes in N2B27 media, left to attach during 12 h, then stretched 35%. The associated gene expression profiles are shown in Fig. 5.6.

None of the changes were statistically significant. However, stretching caused an increase in the expression of the three pluripotency genes tested here at the 6 h timepoint, but induced a decrease in their expression at the 12 h timepoint. As such, the overall changes supported the hypothesis that the effect stretching might have on the pluripotency network depends on the stage of the differentiation process.

5.2.3 Comparing the effects of single and cyclic stretch

In Section 5.2.1 we showed that the effects of a protocol consisting of a single cycle of 1 h of stretching, relaxing and stretching, did not differ substantially from those caused by static stretch. To explore this difference further, we used the automated stretcher to apply a programme of cyclic stretching. The protocol involved repeated cycles, with each consisting of stretching cells 35% at $t = 0$ and maintaining this stretch for 60 min, then releasing the stretch completely and leaving the cells in a relaxed state during 60 min. Using the programme on the Raspberry Pi, we could execute this procedure for 12 h without requiring constant supervision or intervention.

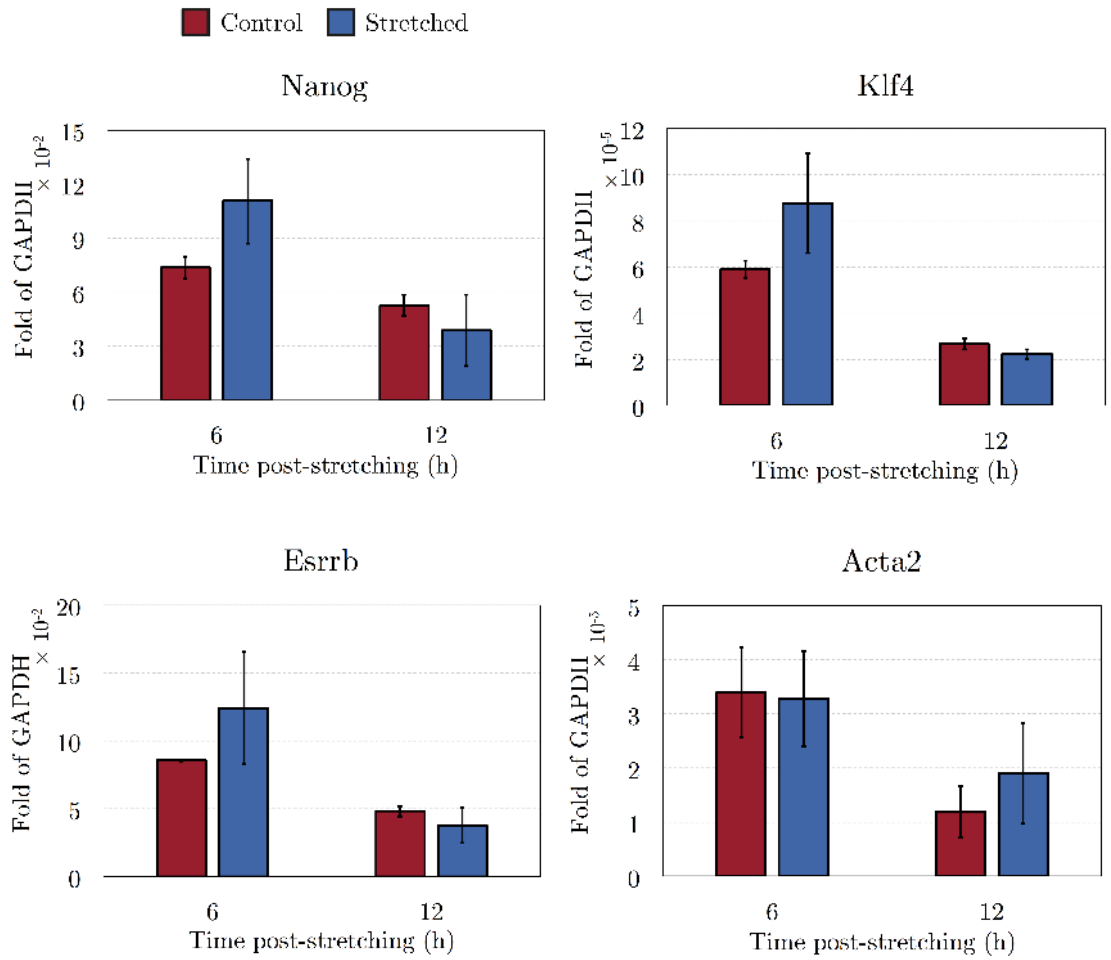

Figure 5.6 Expression levels of Nanog, Klf4, Essrb and Acta2 in response to single stretch in N2B27. Cells were plated from 2i into N2B27, then left to attach during 12 h, and stretched 35%. They were collected after 6 h and 12 h. The difference between control and stretched cells is not quite significant at 6 h for Nanog ($p = 0.058$) and Klf4 ($p = 0.086$), and at 12 h for Klf4 ($p = 0.081$). Acta2 expression is included to demonstrate that the trend in expression levels differs for other genes. Error bars correspond to standard deviation.

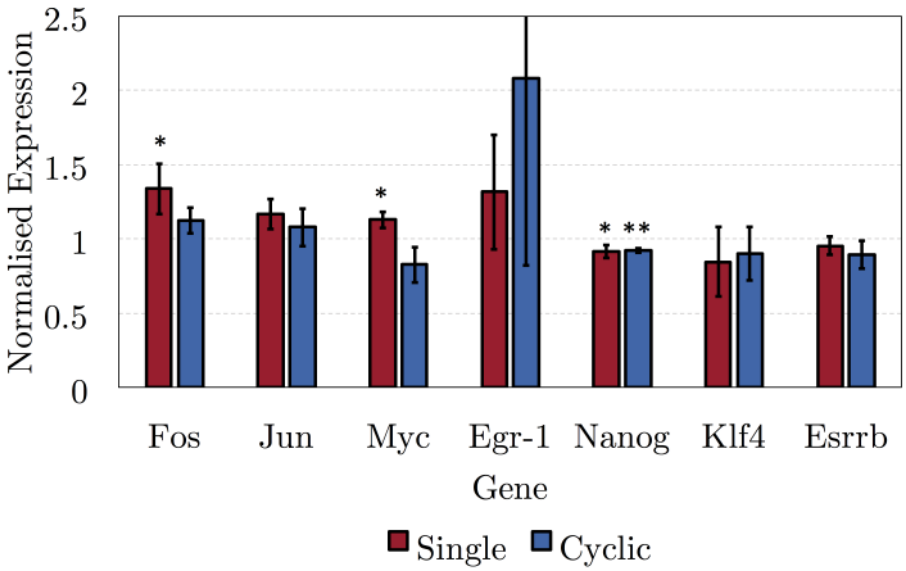

Figure 5.7 Ratio of gene expression of genes after 12 h of static or cyclic stretching. ES cells were plated into 2i. After 12 h, the media was changed to N2B27. 12 h later, cells were stretched 35% once (single), or underwent a cyclic programme of 1 h of stretching 35% followed by 1 h in a relaxed state (cyclic). The cells were collected after 12 h, having gone through six stretch-and-release cycles (cyclic), or having experienced continuous stretch for 12 h (single). Only for Myc were the differences between single and cyclic stretching significant. Error bars correspond to standard deviation.

We plated naive ES cells from 2i media onto laminin-coated PDMS membranes into 2i media. After 12 h the media was replaced with N2B27. Again 12 h later, cells were stretched once (single), exposed to six cycles of the cyclic stretch programme (cyclic), or left in a relaxed state (controls), and collected 12 h after the start of the stretching programme. The resulting ratios of gene expression in stretched (single or cyclic) to control samples are shown in Fig. 5.7.

The data fell into two different categories. First, the IEGs were mostly upregulated in response to stretching, with changes ranging from a 108% increase (Egr-1) to a 17% decrease (Myc). The impact of stretching on the IEGs was smaller (but not statistically significant) when exposing cells to cyclic stretch. In contrast, all pluripotency genes were downregulated, consistent with our earlier findings, with the change being significant only for Nanog. Second, there was no significant difference between cyclic and single stretch except for Myc, where the two approaches induced opposite effects. In addition, Egr-1 expression was heavily affected but simultaneously highly variable. Comparing the expression of Egr-1 and Myc with the time series in Fig. 5.3 on p. 75, we found similarities between the 12 h timepoint here and the 1 h or 2 h timepoint of that experiment, which could be an indication that the recovery period following the initial stretch is around 9 - 10 h, or a divisor of this. Future work would certainly include additional stretching experiments with varying durations between subsequent stretched, aimed at further studying the recovery rate of the IEGs and Erk response.

5.2.4 A note on experimental variability

The experiments shown here were characterised by a large variability in the intensity and direction of the transcriptional response of ES cells to stretch. Each experiment was performed on three membranes per stretcher, then executed using multiple stretchers on separate days. Nevertheless, when comparing results from one of these datasets to other datasets collected at different times, they occasionally contained large differences in the magnitude of the gene expression changes, particularly with respect to the IEGs. Here we discuss some of the implications of this observation, and how we have attempted to correct for this.

The large fluctuations, even between data originating from large experiments with multiple replicates, complicated any conclusions drawn from our findings. For example, note the difference between the magnitude and shape of the increases in Fos and Myc in Fig. 5.1 and Fig. 5.3, even though the 1 h timepoint was identical. Multiple factors could account for these differences:

First, if the true role of mechanotransduction in inducing transcriptional changes is small, our observations would largely constitute random fluctuations in gene expression or be a

side-effect of the experimental conditions. Indeed, we found the pluripotency genes to have a coefficient of variation of 62% even when plated on unstretched membranes (data not shown), illustrating the high level of variation, although the changes were a predictable function of the time after plating. In addition, while the magnitude of the response of most genes observed here was variable, the presence and direction was much more consistent.

Second, downstream effects of stretching might be highly dependent on the cells' biochemical state. The population in each experiment could occupy a slightly different position within the spectrum of cell states, which could be reflected in how the cells respond. Considering it would be unfeasible to verify or disprove this hypothesis, we did not specifically consider or address this beyond assuring before starting each experiment that cells were as similar as possible to those in earlier experiments (in terms of morphology, pluripotency and general health).

A third source of variability originated from the practical execution of the experiments. Throughout the development of the devices we worked extensively on identifying and eliminating potential sources of variability, from the chemical composition and manufacture of the membranes, to the execution of stretching experiments. Some of these efforts were highlighted in earlier sections (such as the different functionalisation techniques aimed at achieving perfect cell attachment and spreading), but we also focused on the careful practical execution of the experiments, from using only membranes that originated from the centre of the spin coated wafer (to prevent a thickness gradient within each membrane), to collecting samples within a single minute of their indicated time.

Cell density might affect reproducibility and magnitude of stretching. Extracellular matrix production is an important driver of many mechanical signals, including durotaxis [Hartman et al., 2016], and is heavily influenced by cell density. As we demonstrated by measuring the local strain in the membrane as a function of the distance to the closest colony (see Section 4.3), cells always experienced the imposed strain fully, even when part of a larger colony.

We tested the effect of cell density on the expression of two IEGs by plating cells in Serum+LIF conditions at a density of 100,000, 200,000 and 400,000 cells per membrane, corresponding to 14,700, 29,300 and 58,700 cells/cm^2 respectively. We stretched cells 35%, 24 h after plating and collected 2 h later. As shown in Fig. 5.8, cell density affected IEG expression, with 200,000 cells per membrane causing the largest increase in Egr-1 and Jun. Other genes, such as the pluripotency genes, were not significantly affected. These results could be interpreted as a likely result of the balancing act between the effect of the increase in extracellular matrix as cell number increases, on the one hand, and overconfluence, on the other. Therefore, the remaining experiments in this study were executed with a cell density of

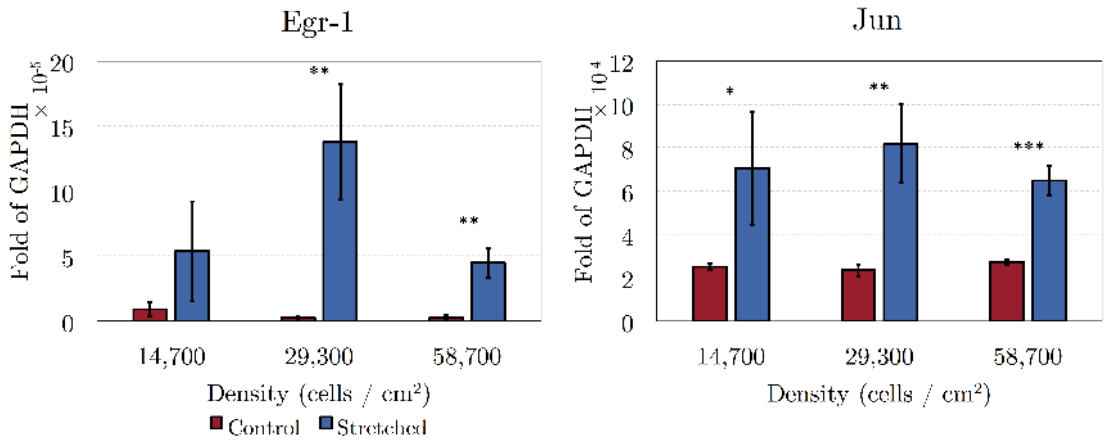

(a) Egr-1 **(b)** Jun

Figure 5.8 Expression levels of (a) Egr-1 en (b) Jun in cells on control and stretched membranes, in Serum+LIF media conditions. Cells were first left to attach during 24 h, then stretched 35% and collected 2 h later. There is a significant difference in the intensity of Egr-1 between a density of 29,300 vs 14,700 ($p < 0.05$), and for the stretched to control ratio between 29,300 and 58,700. Error bars correspond to standard deviation.

29,300 cells/cm^2, or an equivalent density when adjusting the plating time before stretching the density.

Finally, the results presented here are only a small subset of all the data gathered during the project. Whenever we observed that multiple sets of data, obtained in a similar experimental set-up, varied substantially between replicates, these data were excluded, with the exception of whenever the underlying trends and observations were consistent.

5.2.5 Conclusions

Applying our novel cell substrate stretcher, we investigated the effects of stretching on the transcription of a number of potential genes of interest. First, we found that stretching induced a quick transcriptional effect, influencing the IEGs Egr-1, Jun and Fos around 1 - 2 h after stretching. While this response was influenced by a range of experimental conditions such as cell number, density and stretch protocol, it showed that cells experience and react to stretch, through a response that involves the Erk pathway. It was not yet clear what the involvement of these biological processes implied for the broader gene expression network or for later timepoints, which is a question that is addressed in Section 5.4. Second, we performed an investigation of the effect of stretching on transcription related to pluripotency and differentiation, when transitioning from Serum+LIF into Serum-only and from 2i into

N2B27. The changes in both conditions were limited, but we always observed a consistent trend, although not always statistically significant, across genes. Interestingly, the effects of stretching varied between conditions and timepoints, with stretching increasing expression of pluripotency genes in Serum-only and at the 18 h timepoint in N2B27 (stretched for 6 h), while reducing their expression at the 24 h in N2B27 (stretched for 12 h).

5.3 Effect of stretching on differentiation

From the experiments in the previous section it was not clear whether the transcriptional changes cause a corresponding and substantial difference in the rate of differentiation in ES cells. Specifically, the dual nature of the transcriptional changes in N2B27 raised the possibility of stretching having a time-dependent effect on differentiation. In addition, previous studies have reported that cyclic stretching has a negative effect on differentiation of endothelial progenitor cells (EPCs) [Le et al., 2016]. Therefore we investigated the effect of stretching as cells underwent differentiation in N2B27 from 2i.

We used a Rex1-GFPd2 ES cell line in which the native Rex1 protein was connected to a destabilised version of GFP, with a half-life of two hours, as presented in Wray et al. [2011]. As discussed in Section 1.1, Rex1 is downregulated around 24-36 h after the initiation of differentiation; hence its fluorescence intensity provides a readout of the pluripotent state of cells. We plated cells from 2i into N2B27 on laminin-coated PDMS membranes. After 24 h we started a cyclic stretching protocol, as shown in Fig. 5.9a, consisting of a repeated cycle of 35% for 90 min followed by relaxation for 30 min. We then analysed the GFP signal 2 h, 6 h and 12 h later using flow cytometry.

Earlier experiments showed that, using the PDMS substrate and the density of 200,000 cells per membrane, the largest shift in the Rex1 profile occurs around 28-36 h after the start of differentiation, which was confirmed by Fig. 5.9b. Considering that the changes that occur before this time are relatively small (based on our own preparatory experiments and what was reported by Kalkan et al. [2017]), we hypothesised that the change between stretched and control samples would most strongly express itself around the 28-36 h timepoints, during the main leftward shift of the Rex1 expression.

However, the profiles of the stretched and control membranes were largely indistinguishable. Taking into account that Rex1 was found to be a good reporter of the state of cells along the differentiation process [Kalkan et al., 2017; Wray et al., 2011], it appeared that stretching did not have any influence on the rate of neuronal differentiation in N2B27. This, together with our earlier finding that stretching affected the pluripotency genes at 18 h and 24 h to an extent that was not statistically significant, allowed us to conclude that the effect of

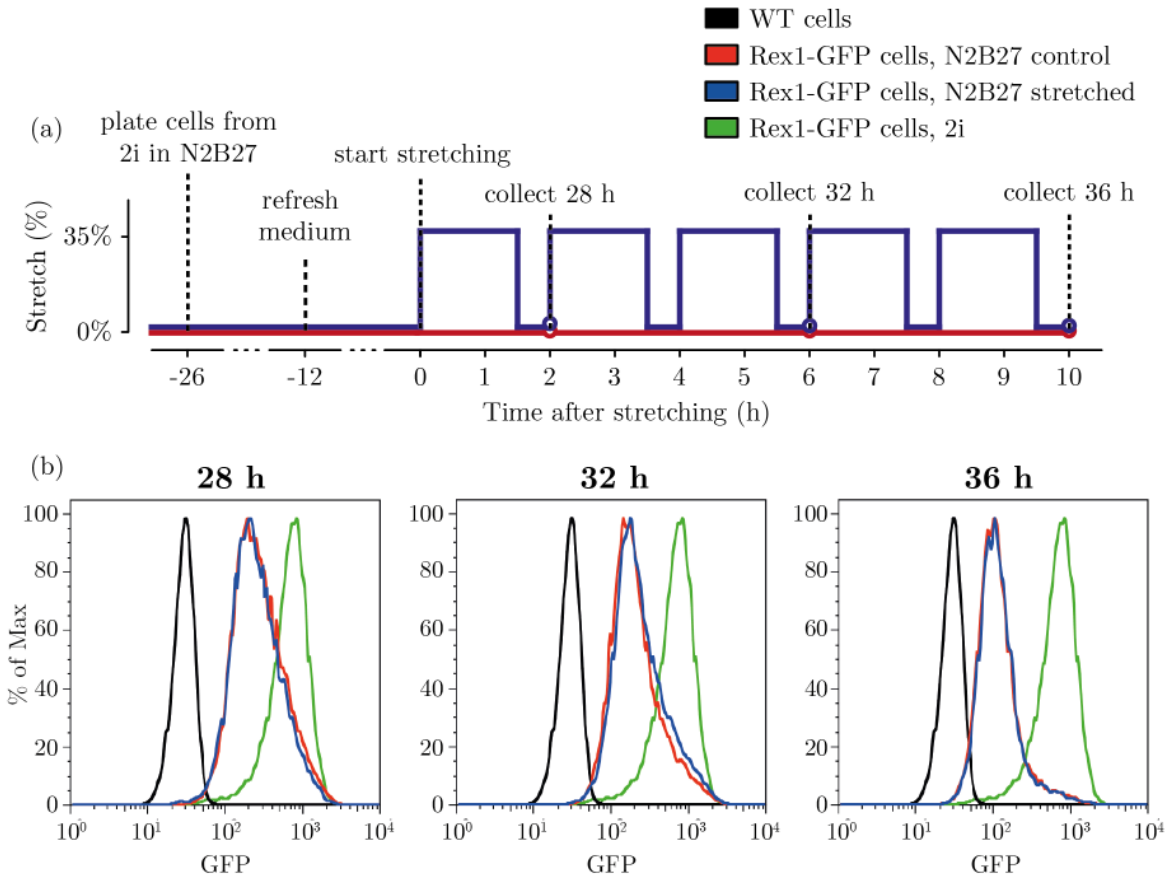

Figure 5.9 Intensity of Rex1-GFP during differentiation in N2B27, 28 h, 32 h and 36 h after initiation of differentiation after 2i removal, and 2 h, 6 h and 10 h after stretching. The positive and negative controls shown in each graph correspond to the respective profiles at 28 h only.

our stretching method on pluripotency and differentiation is limited, contrasting with earlier findings of stretching affecting differentiation in other experiments and cell types [Horiuchi et al., 2012; Saha et al., 2006; Teramura et al., 2012].

5.4 Overall transcriptional characterisation of cells during stretching

In the previous experiments we studied the results of stretching on a number of specific transcriptional targets. Considering the narrow range of our earlier investigation and the fact that cyclic stretch in other cell types has a general effect on the transcriptional activity [Le

et al., 2016], we decided to study the broader effect of stretching on the entire transcriptome. Therefore we conducted two separate experiments, covering two types of culture media; Serum-containing or N2B27-based media.

In particular, the design of the experiments was aimed at providing insight into a number of issues simultaneously. First, we analysed the time-dependence of cells' response by comparing the effect of stretching at 2 h and 12 h. Second, we studied the result of the stretch protocol by comparing singly versus cyclically stretched samples. Third, we tested the role of the media conditions, through the juxtaposition of Serum+LIF and Serum-only. Finally, we investigated the susceptibility of cells to stretching in conditions of naive pluripotency (SL and 2i), early differentiation (S) and intermediate differentiation (N2B27).

5.4.1 Overview of the experimental procedure

Samples in Serum+LIF and Serum media

To gain a better understanding of the broader transcriptional response in Serum-containing conditions, we plated cells from Serum+LIF media onto membranes functionalised with fibronectin, in either Serum+LIF and Serum, at a density of 200,000 cells per membrane. Starting 24 h later, we exposed the membranes to a cyclic stretching protocol (cyclic), as shown in Fig. 5.10, or to single stretch of 35% (single). Cells were collected either 2 h (cyclic stretching samples) or 12 h (static and cyclic stretching samples) after the start of the stretching protocol. This protocol was performed twice, on separate days, producing two replicates for the RNA sequencing dataset. For each replicate, to reduce the variability between samples, all three membranes on a single automated stretcher were pooled into one sample submitted for RNA sequencing. RNA from these timepoints was extracted and sequenced using single-end sequencing.

Samples in 2i and N2B27 media

We executed a similar protocol for cells in 2i and N2B27. Cells were plated from 2i into 2i or, to initiate differentiation, into N2B27, onto laminin-coated membranes. Then cells were exposed to a cyclic stretching protocol 24 h later, as shown in Fig. 5.11, and collected after 12 h. Due to our observations that few changes occur during early differentiation, this timing was chosen to capture the cell state after the initiation of the differentiation programme, in the primed state. This allowed us to investigate the cellular response to stretch during intermediate stages of differentiation, when the network supporting naive pluripotency was largely extinguished. Again, the cells from the three membranes on each automatic stretcher

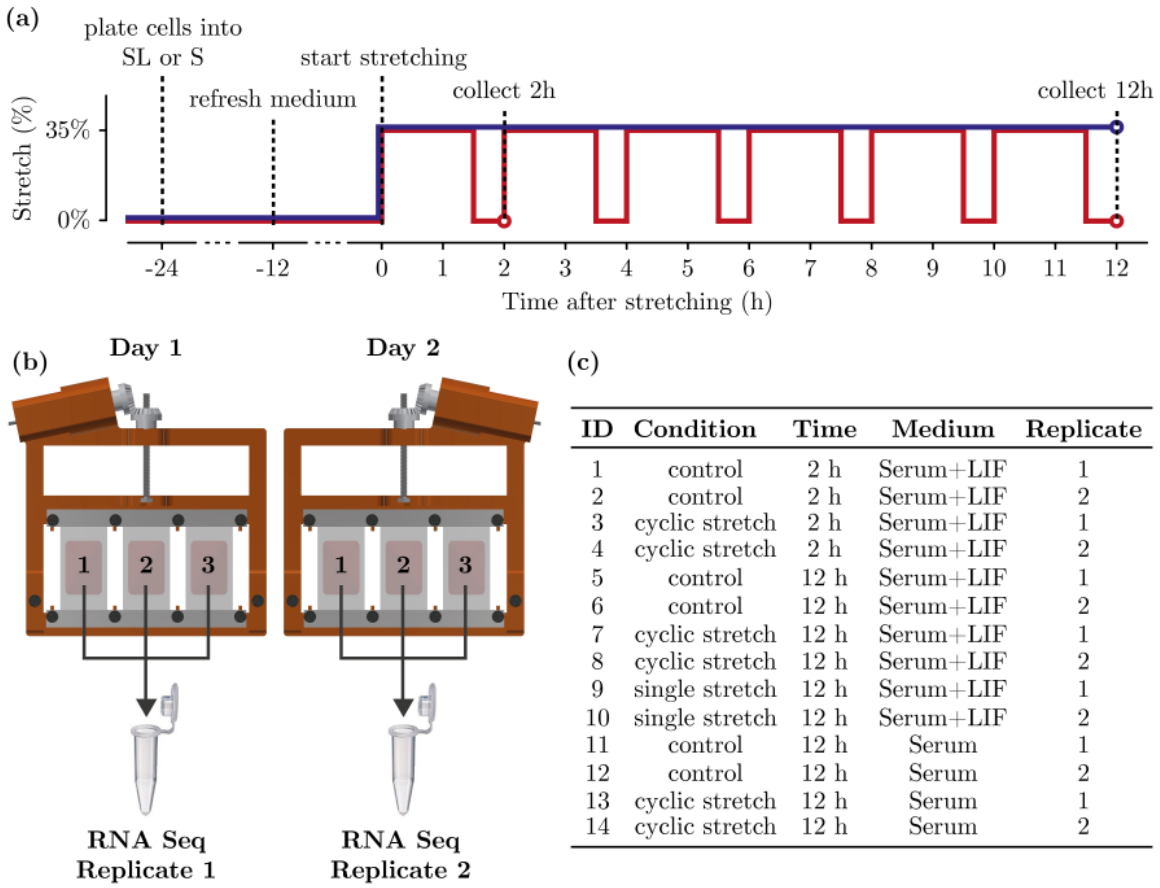

(c)

ID	Condition	Time	Medium	Replicate
1	control	2 h	Serum+LIF	1
2	control	2 h	Serum+LIF	2
3	cyclic stretch	2 h	Serum+LIF	1
4	cyclic stretch	2 h	Serum+LIF	2
5	control	12 h	Serum+LIF	1
6	control	12 h	Serum+LIF	2
7	cyclic stretch	12 h	Serum+LIF	1
8	cyclic stretch	12 h	Serum+LIF	2
9	single stretch	12 h	Serum+LIF	1
10	single stretch	12 h	Serum+LIF	2
11	control	12 h	Serum	1
12	control	12 h	Serum	2
13	cyclic stretch	12 h	Serum	1
14	cyclic stretch	12 h	Serum	2

Figure 5.10 (a) Protocol of stretching experiment to collect cells in Serum+LIF and Serum media conditions for RNA-Seq. (b) Cells from three membranes were pooled into one RNA-Seq replicate, and the experiment was repeated on another day to produce another replicate. (c) Overview of all samples in the dataset.

were pooled into one replicate, and the experiment was repeated on a separate day to produce a second replicate. RNA was sequencing using pair-end sequencing.

5.4.2 Transcriptional profile

After library preparation and sequencing, the expression of RNA in the two experiments was analysed (separately) using DESeq2 as detailed in Section 3.2.3. The adjusted p-value was used to correct for multiple comparisons, such that the remaining genes marked as significantly regulated would be more likely to reflect real changes (that is, with 95% confidence). The number and distribution of the counts did not shift significantly between the conditions.

(a)

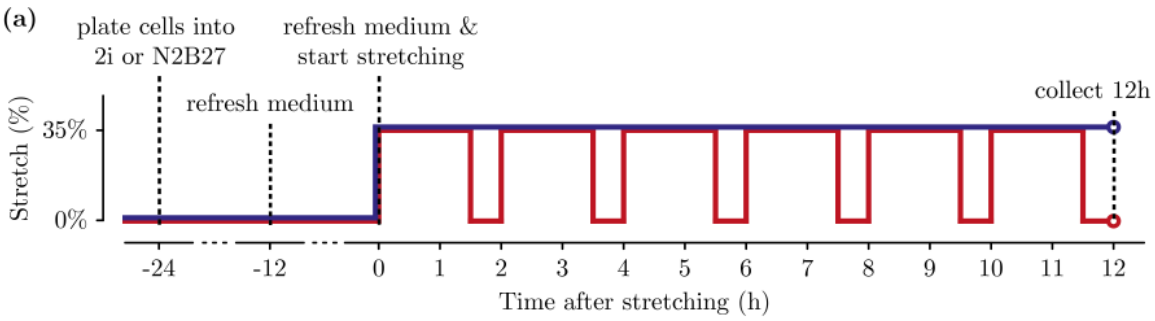

(b)

ID	Condition	Time	Medium	Replicate
1	control	12 h	2i	1
2	control	12 h	2i	2
3	cyclic stretch	12 h	2i	1
4	cyclic stretch	12 h	2i	2
5	control	12 h	N2B27	1
6	control	12 h	N2B27	2
7	cyclic stretch	12 h	N2B27	1
8	cyclic stretch	12 h	N2B27	2

Figure 5.11 (a) Protocol of stretching experiment to collect cells in 2i and N2B27 media conditions for RNA-Seq. (b) Overview of all samples in the dataset.

To get an initial understanding of the global transcriptional changes in the two conditions, we compared the expression levels of each stretching condition to the unstretched control at the same timepoint and media condition. The resulting number of significantly regulated genes in the Serum-containing conditions, shown in Table 5.1, reflected the time-dependence of cells' response to mechanical stimuli. 105 genes were significantly expressed at the 2 h timepoint in Serum+LIF (SL) conditions, and 73 of those genes (70%) were upregulated, while the remaining 32 (31%) were downregulated. At the later timepoint of 12 h, only a single gene was significantly regulated in SL conditions, Hspa1b. No genes at all were significantly regulated when cells experienced a single stretched or were cyclically stretched in Serum-only (S) conditions. When comparing stretched to control samples across all media types and times (that is, using media type, time and stretch as explanatory variables across all conditions), we found that 12 genes were significantly changed, 9 of which were upregulated. As such, mechanical signals appeared to lead to transient transcriptional changes that were highly media-dependent.

In contrast to the Serum-containing conditions, the samples in 2i and N2B27 conditions were included specifically to investigate the change in susceptibility to mechanical signals as cells exited the pluripotent state. As cells occupy a fully naive state when in 2i and have

Table 5.1 Overview of samples stretched in Serum-containing media conditions

Sample	Timepoint (h after stretching)	Differentially expressed genes (vs control)
SL Cyclic 2 h	2	105
SL Cyclic 12 h	12	1
SL Single 12 h	12	0
S Cyclic 12 h	12	0
Cyclic All	N/A	12

Table 5.2 Overview of samples stretched in 2i-type media conditions

Sample	Timepoint (h after stretching)	Differentially expressed genes (vs control)
2i Cyclic	12	1
N2B27 Cyclic	12	34
Cyclic All	12	65

entirely left the naive state by 36 h after the initiation of differentiation, this experiment really allowed us to test the effect of mechanical signals in differentiating cells [Kalkan et al., 2017]. Indeed, as shown in Table 5.2, we found that there was a substantial difference between the naive and differentiating samples. At the 12 h timepoint, directly comparable to the 12 h timepoint in the Serum-containing experiment, only 2 genes were significantly regulated in the naive 2i condition. In contrast, 34 genes were significantly regulated in differentiation conditions (of which 19, or 56%, were upregulated), highlighting that these differentiation conditions were more conducive to mechanical signals than the naive conditions. This was not entirely surprising, considering that we established that the Erk pathway plays a role in the activation of the IEGs, implying its involvement in modulating the response to stretch. Since 2i media contains PD03, which is an inhibitor of the Erk pathways, this might close off an important responder to mechanical signals.

An analysis of the principal components (PCA) displayed the heterogeneity between the samples and allowed us to assess the significance of stretching compared to other factors. In both experiments, the first component distinguished the two culture media, as illustrated in Fig. 5.12 for 2i and N2B27 (not shown for SL and S, where PC1 accounts for 67% of the variance). The second component, or the first component when calculating PCAs for individual culture media, contained the variability due to replicates. The second component (with only 1% of the variance) for individual media distinguished between the stretched

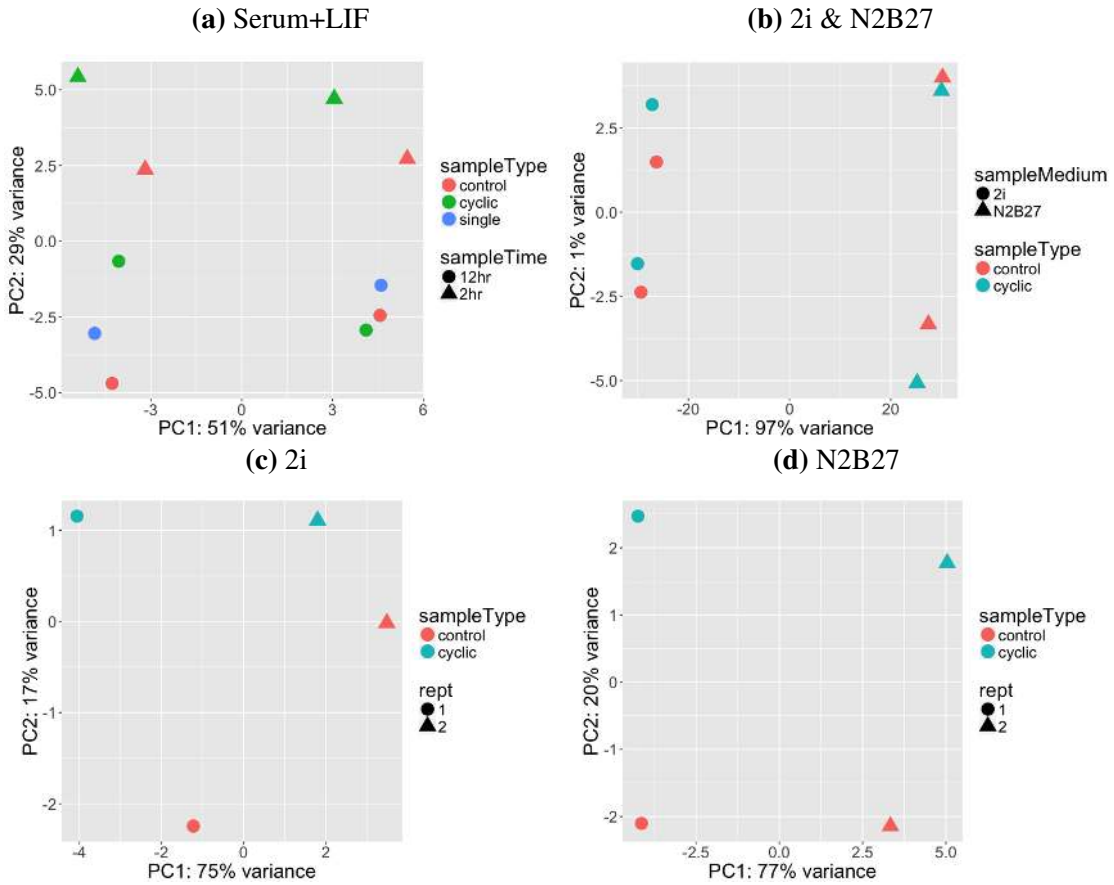

Figure 5.12 Position along the first two principal components of the different samples in (a) Serum+LIF, (b) 2i and N2B27, (c) 2i and (d) N2B27 media conditions.

and unstretched samples in the case of 2i and N2B27, where the differences induced by stretching were the largest. Only the fourth component of Serum+LIF (but incorporating different timepoints and stretch types) captured clearly the difference between stretched and control samples. From our observations we concluded that, compared to other variables such as media type and even random variability, the effect of the stretch was relatively weak. This observation was indicative of the high variability inherent in the stretching experiments, and decreased substantially the analytical power of our downstream analysis. However, mindful of this observation, we cautiously proceeded with our analysis, considering that this variability would automatically be incorporated in DESeq2 and other forms of quantitative analysis.

A subset of the significantly expressed genes is shown in Fig. 5.13a for the Serum-containing conditions. There were obvious differences in the magnitude of these genes across the different samples, with the Serum+LIF Cyclic 2 h sample containing all significantly

regulated genes across all Serum-containing conditions. Interestingly, the fold change of these genes was anti-correlated to the changes in Serum Cyclic 12 h, with a Pearson correlation of -0.18, while the fold change at the 2 h timepoint was positively correlated to the other 12 h samples, with a correlation of 0.47 and 0.17 for cyclic and single stretch respectively. Similarly, the correlation between the two 12 h cyclic samples in Serum+LIF and Serum was weak, with a coefficient of 0.17. These observations showed that stretching is associated with a highly time- and medium-dependent effect, and that cells likely responded in the opposite way on shorter than on longer timescales in Serum-only conditions. The fold changes in the 2i-type conditions, displayed in Fig. 5.13b, were much more closely correlated, with a coefficient of 0.85. Hence, although the magnitude of the effect of stretching at 12 h in a condition in which cells have left their pluripotent state (since cells have been in N2B27 for 36 h at that point), was larger, the direction of the effects on the most differentially regulated genes did not appear to change as substantially as in the Serum-containing conditions. Overall, the upregulation of the genes was not associated with one particular type of genes, with genes including those involved in biosynthesis, sterol metabolism, ER proteins, and, as predicted from the qPCRs, the IEG family members Egr-1 and Fos (Fosl1). The specificity of cells' transcriptional response is explored in more detail in the next section. However, in Section 5.2.4 I raised the possibility that our analysis of the effects of stretching could actually detect random fluctuations. The consistent character of these observations means that this possibility is less likely.

The variation in the number of significantly regulated genes across media types is a reflection of the different nature of the overall transcriptional response in those conditions. We wanted to get further insight into whether these differences are also associated with a corresponding difference in the internal transcriptional homogeneity of a sample. We measured the variation in gene expression of each condition by selecting 1,000 genes at random from each sample and calculating the coefficient of variation (defined as the standard deviation divided by the mean), then repeating this process 10,000 times. Plotting this measure should give us insight into how much the gene expression varied within each sample, with a high measure for a condition showing that its mechanosensitive response is less homogeneous. The result, shown in Fig. 5.14, shows that there were significant differences in the response of different media conditions. The heterogeneity of the response of Serum+LIF at 2 h was of a similar level as that of Serum at 12 h. The latter was significantly higher than the two Serum+LIF conditions at 12 h, which, as expected considering the limited effect of stretching, were not significantly different. The response of 2i was highly homogeneous, which matched the highly regulated state of cells in this condition. Overall, this analysis shows that stretching increased the expression variability within samples on

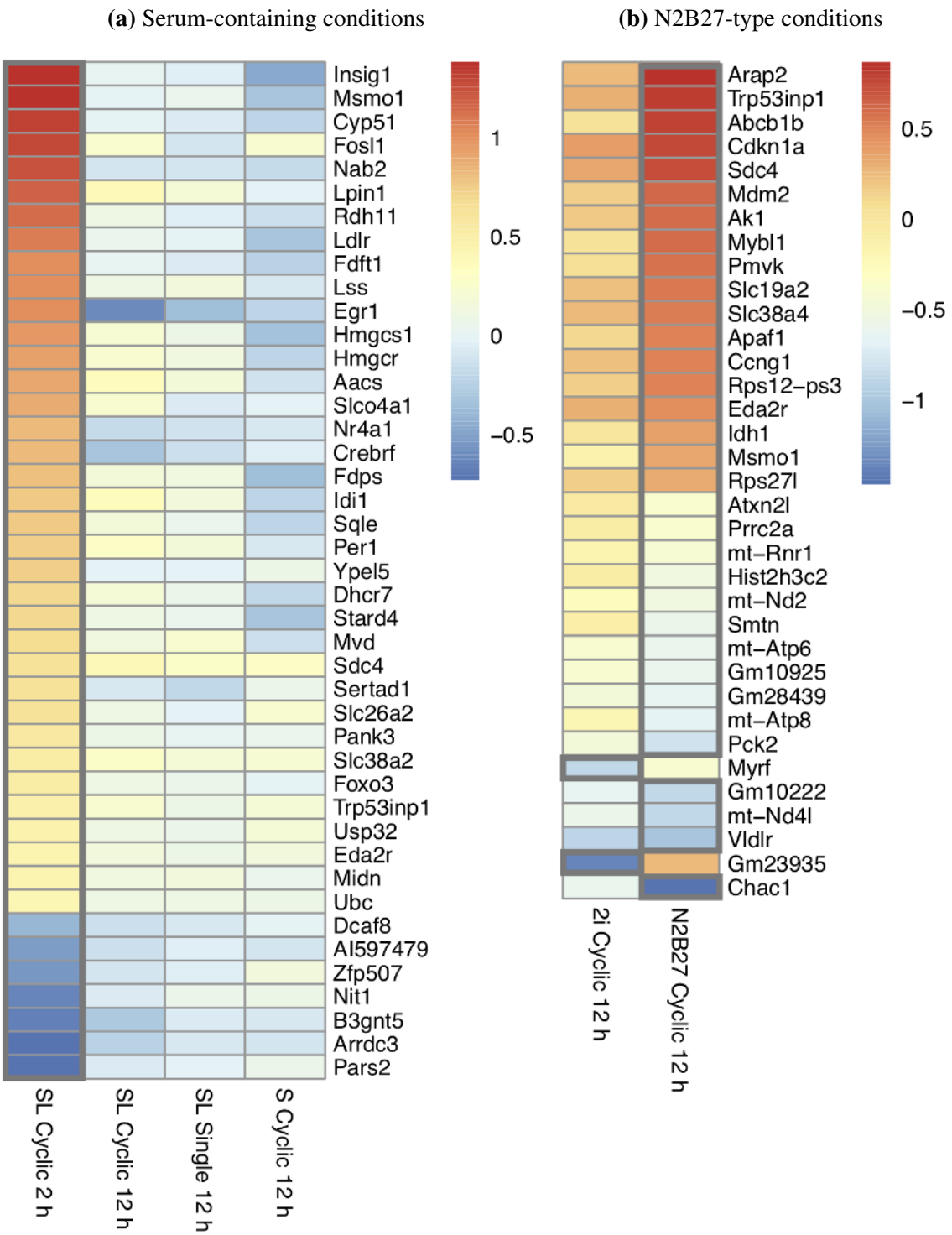

Figure 5.13 Log_2 fold change of the stretched to unstretched sample for each condition, labelled using a concatenation of culture media, stretch type and timepoint. Genes shown are those differentially regulated in any of the conditions with (a) $p_{adj} < 0.01$ or (b) $p_{adj} < 0.1$. A grey box indicates the sample in which the gene was found to be significantly regulated.

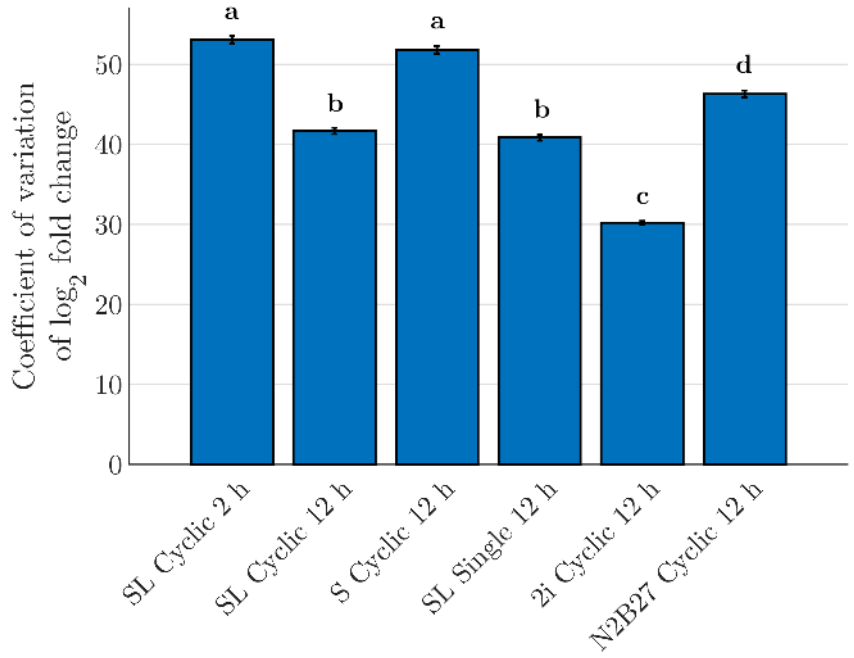

Figure 5.14 Coefficient of variation of the $\log_2$ fold change of stretched to control samples in different media conditions, with standard error of the mean plotted as the error bar. Different letters indicate that pairs are significant at the 5% level; pairs with the same letter are not statistically significantly different. Error bars correspond to standard error of the mean.

shorter timescales in Serum+LIF. This variability faded in Serum+LIF by the 12 h timepoint, with few differences between cyclic and single stretch. In contrast, the variability remained high in Serum-only conditions. The disparity in expression heterogeneity exhibited itself also in the comparison of 2i and N2B27 conditions. 2i was by far the most stringently controlled condition in the sample, but this control was released as these cells underwent differentiation. As such, we would expect from further gene ontology studies that the effect on specific pathways would be much larger in N2B27 than 2i.

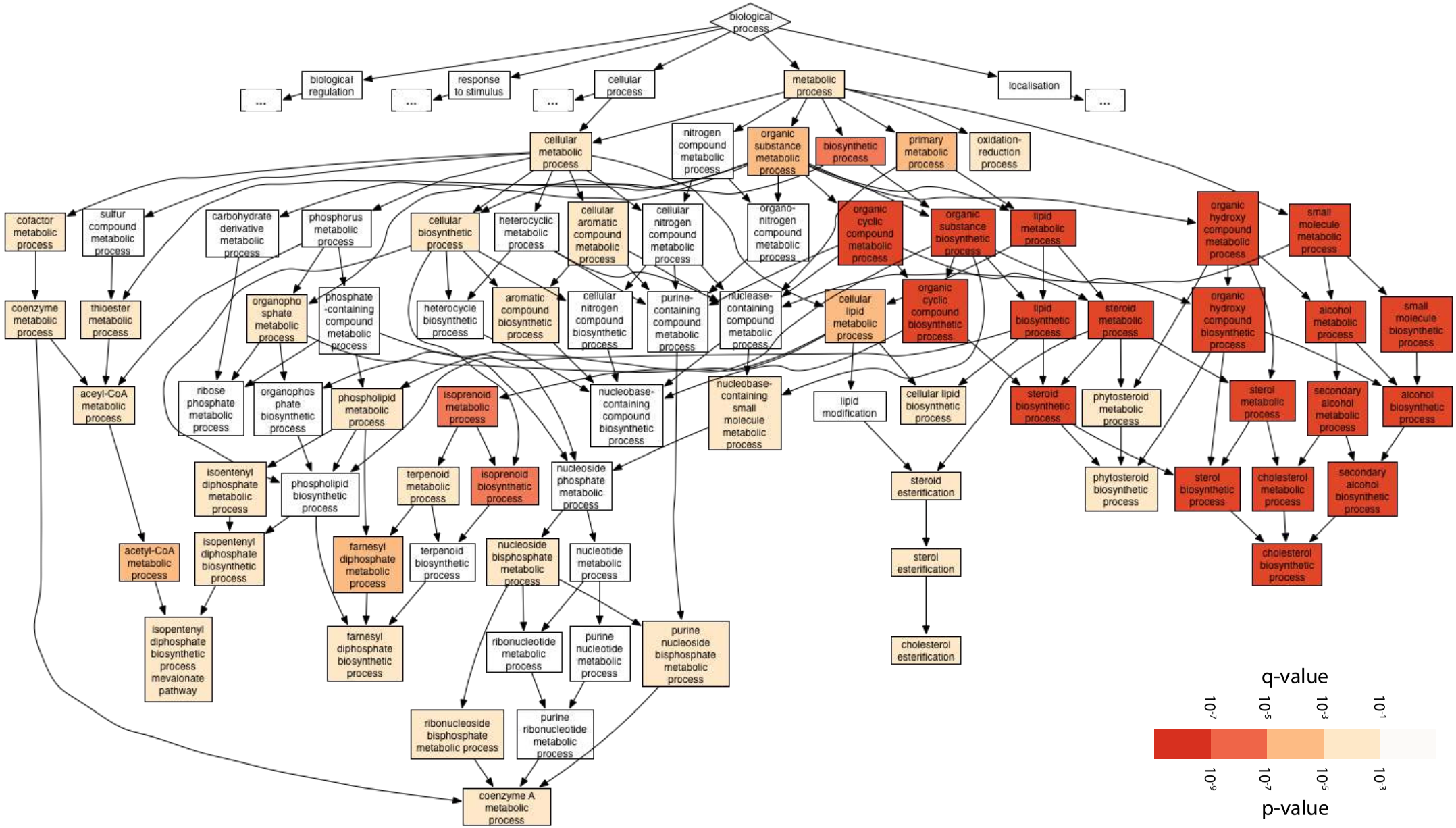
biological process
biological regulation
response to stimulus
cellular process
metabolic process
localisation
...
cellular metabolic process
nitrogen compound metabolic process
organic substance metabolic process
biosynthetic process
primary metabolic process
oxidation-reduction process
cofactor metabolic process
sulfur compound metabolic process
carbohydrate derivative metabolic process
phosphorus metabolic process
cellular biosynthetic process
heterocyclic metabolic process
cellular aromatic compound metabolic process
cellular nitrogen compound metabolic process
organo-nitrogen compound metabolic process
organic cyclic compound metabolic process
organic substance biosynthetic process
lipid metabolic process
organic hydroxy compound metabolic process
small molecule metabolic process
coenzyme metabolic process
thioester metabolic process
organophosphate metabolic process
phosphate-containing compound metabolic process
heterocycle biosynthetic process
aromatic compound biosynthetic process
cellular nitrogen compound biosynthetic process
purine-containing compound metabolic process
nuclease-containing compound metabolic process
cellular lipid metabolic process
organic cyclic compound biosynthetic process
lipid biosynthetic process
steroid metabolic process
organic hydroxy compound biosynthetic process
alcohol metabolic process
small molecule biosynthetic process
aceyl-CoA metabolic process
ribose phosphate metabolic process
organophosphate biosynthetic process
phospholipid metabolic process
isoprenoid metabolic process
nucleobase-containing compound biosynthetic process
nucleobase-containing small molecule metabolic process
lipid modification
cellular lipid biosynthetic process
steroid biosynthetic process
phytosteroid metabolic process
sterol metabolic process
secondary alcohol metabolic process
alcohol biosynthetic process
isoentenyl diphosphate metabolic process
phospholipid biosynthetic process
terpenoid metabolic process
isoprenoid biosynthetic process
nucleoside phosphate metabolic process
steroid esterification
phytosteroid biosynthetic process
sterol biosynthetic process
cholesterol metabolic process
secondary alcohol biosynthetic process
acetyl-CoA metabolic process
isopentenyl diphosphate biosynthetic process
farnesyl diphosphate metabolic process
terpenoid biosynthetic process
nucleoside bisphosphate metabolic process
nucleotide metabolic process
sterol esterification
cholesterol biosynthetic process
isopentenyl diphosphate biosynthetic process mevalonate pathway
farnesyl diphosphate biosynthetic process
ribonucleotide metabolic process
purine nucleotide metabolic process
purine nucleoside bisphosphate metabolic process
cholesterol esterification
ribonucleoside bisphosphate metabolic process
purine ribonucleotide metabolic process
coenzyme A metabolic process
q-value
10^{-7}
10^{-5}
10^{-3}
10^{-1}
10^{-9}
10^{-7}
10^{-5}
10^{-3}
p-value

5.4.3 Gene ontology

Figure 5.15 (previous page) Subset of GOrilla analysis of gene expression changes in response to stretching of Serum+LIF Cyclic 2 h samples. Pathways of which the subcomponents are not shown are indicated using ellipses. Individual pathways are coloured according to the magnitude of their q-value and p-value. For example, yellow indicates that simultaneously $10^{-3} < p < 10^{-5}$ and $10^{-1} < q < 10^{-3}$. This subset comprised all pathways in the analysis that were enriched with a p-value of 10^{-7}.

To understand the specificity of the response to stretch and to identify which were the pathways involved, even in those cases where no individual genes were significantly affected, we applied a number of gene ontology (GO) techniques. This allowed us to discern the involvement of an entire pathway based on the regulation or enrichment of its constituent genes. Since the Serum+LIF samples, which were stretched for 2 h, and the N2B27 samples, stretched for 12 h, both contained a number of significantly regulated genes, we could compare the set of differentially regulated genes to the background using conventional techniques. For the other samples, however, we relied on the reshuffling of gene expression across the population without imposing significance requirements. The combination of these two approaches allowed us to characterise common themes in the transcriptional response, and to highlight the difference between media conditions.

Initially we used the gene ontology package GOrilla to identify the enrichment of pathways under stretched conditions by calculating the probability that the observed number of upregulated genes would be associated with each GO-annotated pathway, based on a hypergeometric distribution (methodology discussed in further detail in Section 3.2.3) [Eden et al., 2009]. Comparing the set of significantly regulated genes (based on $p_{adj} < 0.1$) with the background set in the 2 h cyclically stretched Serum+LIF samples, we identified 79 pathways that were each enriched with a q-value below 0.10 and a p-value below 0.05. The predominant changes, shown in Fig. 5.15 and verified also using the PANTHER GO package, were concentrated within the metabolic and biosynthetic processes, including the synthesis of alcohols, sterols, cholesterols and lipids.[2] Other pathways affected included the acetyl-CoA synthesis ($q > 10^{-4}$), regulation of metabolism ($q > 10^{-3}$, driven by, inter alia, Sertad1, Per1, Foxo3, Egr-1, Insig1, Pot1a), and a number of pathways related to ionizing radiation ($q > 10^{-2}$, i.a. Egr-1, Fignl1, Bbc3) and p53 signalling ($q > 10^{-2}$, i.a. Foxo3,

[2]The enrichment of the metabolic and biosynthetic pathways were driven mainly by the differential regulation of the following common constituents: Hsd17b7, Cyp51, Mvd, Lss, Fdft1, Insig1, Hmgcr, Fdps, Pmvk, Nsdh1, Sqle, Dhcr7, Sc5d.

Sesn2, Mdm2). A ranking of the pathways with the lowest q-values is shown in Fig. 5.16. The increase in the biosynthesis of membrane-related molecules is likely a cytoskeletal response to stretch. Indeed, we visually observed a retraction of the membrane relative to the cytoskeletal protrusions, and it is possible this would be compensated for through an increase in membrane biosynthesis.

A similar analysis of the 12 h cyclically stretched samples in N2B27 revealed 12 enriched pathways, but with a different focus. The enriched processes comprised, on the one hand, cellular responses to external stimuli and stresses, including to hydroperoxide, light, radiation and UV. A second type of pathways involved the DNA damage response, internal stress pathways such as p53, and cell cycle transition. The general level of q-values was lower than in the SL Cyclic 2 h; a consequence of the lower number of significantly regulated genes in this condition. The effects on the cell cycle and the p53 pathway were driven in part by Cdkn1a (cell cycle regulator), Rps271 (ribosome component), Mdm2 (negative regulator of p53) and 4632434I11Rik (apoptosis suppressor). It should be noted that the enrichment of a pathway included genes involved in the positive as well as the negative regulation of that pathway. Interestingly, pluripotency was completely absent from this analysis in both conditions, and would appear not to be influenced by stretching at all.

The probability that a gene was detected and upregulated was influenced by its length, which biased the analysis if a pathway's constituent genes are not of the same length. Neither GOrilla nor PANTHER take these effects into account. We replicated our analysis using goseq, which includes this length bias in its calculations (methodology discussed in further detail in Section 3.2.3) [Young et al., 2010]. Using goseq, we identified 181 biological processes in the Serum+LIF sample exposed to cyclic stretch for 2 h, requiring that $p < 0.05$ and that a pathway constituted at least 5 genes of which minimum 3 were differentially expressed). In the N2B27 sample collected after 2 h of cyclic stretch, 93 biological processes were upregulated. We then manually sorted these genes into seven broad categories. As shown in Fig. 5.16, goseq identified metabolism and biosynthesis as the major type of pathways influenced by stretching in both conditions, while stress pathways and regulation of transcription and translation played a relatively larger role in N2B27 than in Serum+LIF. However, these observations indicated the broad effects of stretching on the overall transcriptome, with responses including metabolism, translation, oxidoreductase, apoptosis, and cell cycle. While the absence of strong targeted effects was surprising, the commonality of the types of activated pathways between the two conditions was encouraging, with the two primary overrepresented pathway groups involving stress and metabolic processes.

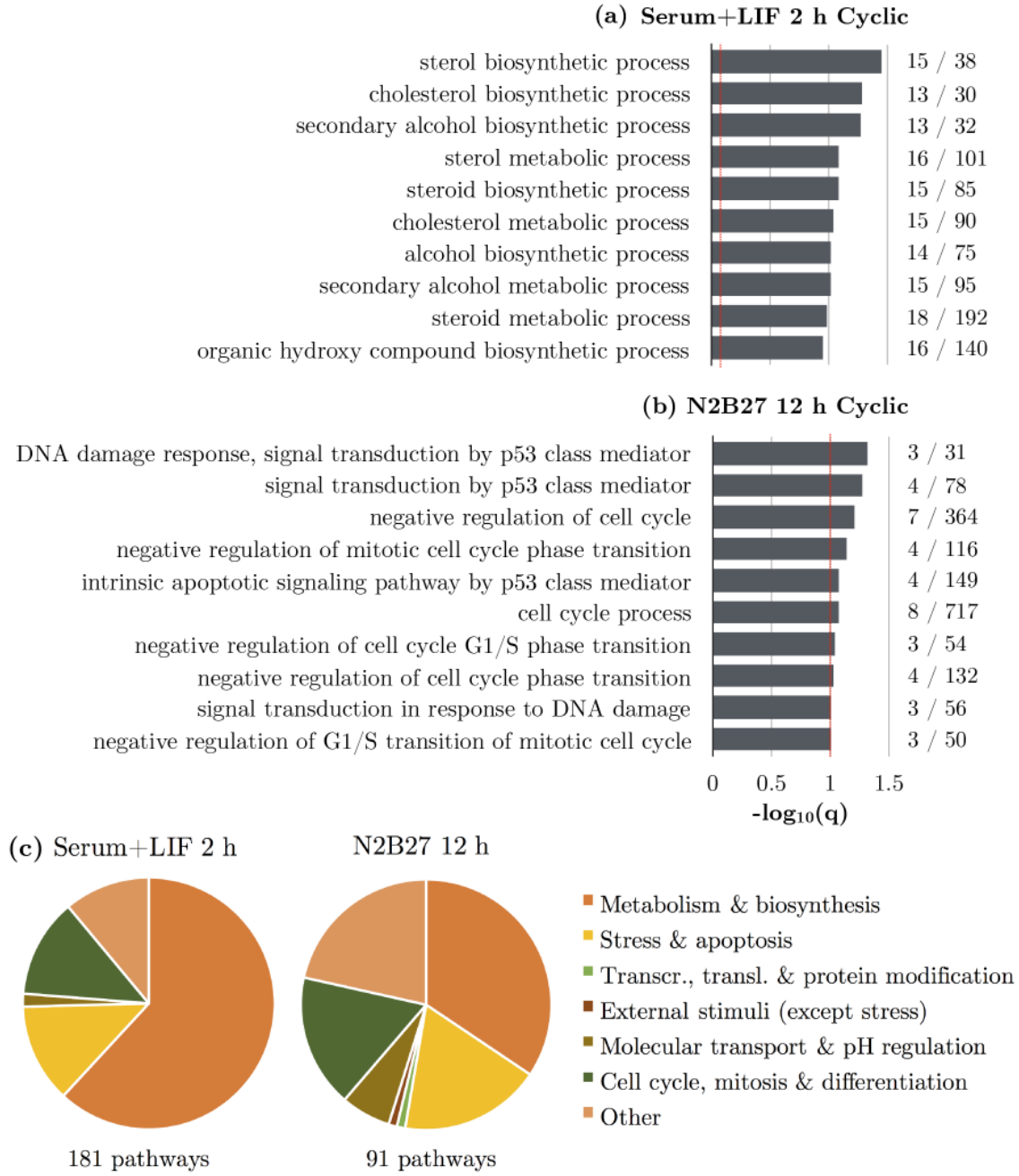

Figure 5.16 (a) & (b) Pathway enrichment analysis of samples in Serum+LIF, stretched cyclically for 2 h, and N2B27, stretched cyclically for 12 h. The ten biological processes with lowest q-values as identified using GOrilla are shown. The ratio of the number of differentially regulated genes to the total number of genes in each process is also indicated. (c) Enriched pathways in these samples, as identified using goseq, manually sorted into seven groups of types of biological role, with number of detected enriched pathways in each condition indicated below the chart.

Overall, our analysis of the effect of the transcriptome by comparing differentially regulated genes to the background set, indicated that the global response consisted of several steps. On short timescales, cells appeared to adjust their metabolic processes and initiate the production of a number of small molecules such as alcohols and sterols. On longer timescales, at 12 h, in N2B27, these processes played a much smaller role. However, the stress response, present even at 2 h in Serum+LIF in the form of the response to radiation and DNA damage, became the principal downstream effect of stretching at 12 h. It demonstrated that stretching and its biological impact were a significant source of stress to cells. And although we showed that there was no large increase in apoptosis after stretching (see Section 5.5), a number of pathways surrounding apoptosis and, more broadly, DNA damage and cell cycle arrest, were activated.

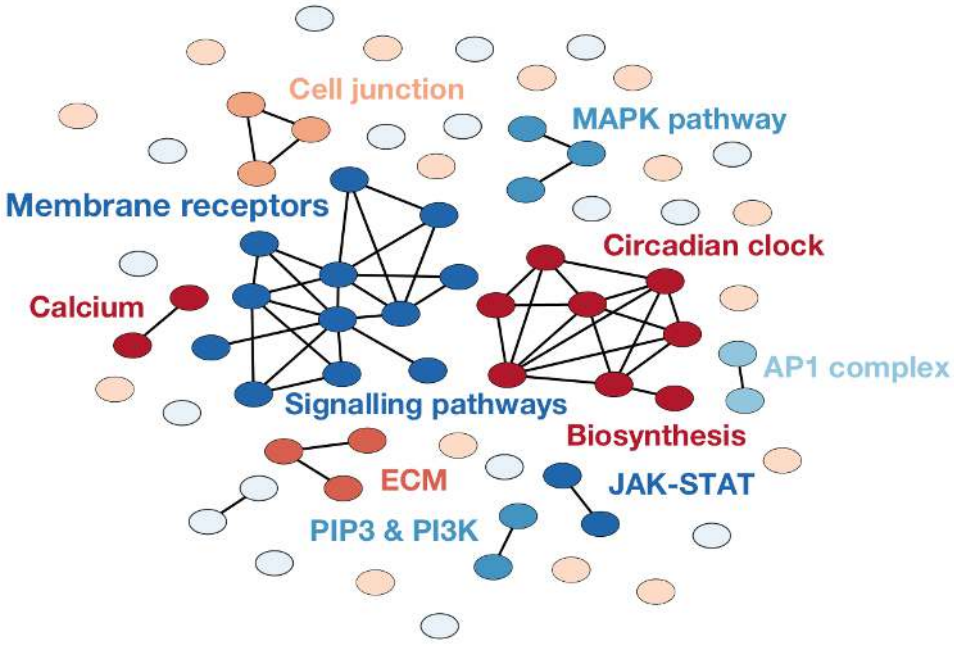

Figure 5.17 Interconnectivity map of pathways, identified using GSEA, enriched in SL Cyclic 2 h, with clusters labelled according to the general biological role. Connections between nodes indicate that pathways have genes in common.

The other samples in our RNA-Seq experiment did not contain sufficient differentially regulated genes (or none at all, see Table 5.1 & 5.2 on p. 89) to support conventional pathway enrichment analysis methods. The lack of significantly regulated individual genes did not preclude pathway or process-wide shifts, however. For example, if all constituent genes in a pathway exhibit a change in a particular direction, even when those individual changes are not statistically significant, this could constitute an interesting observation. We applied

two techniques to detect and statistically quantify these features; both rely on a list of genes ranked by significance of the fold change or by signal-to-noise ratio, and analyse the position of pathway members in the ranking. The distribution of genes is expected to be even in the case of a pathway that follows the trend of the entire sample. A skewed distribution, such as when most pathway members occur near the top of the list, indicates that that pathway is more likely to be differentially regulated (methodology discussed in further detail in Section 3.2.3).

To explore the comparability of two techniques, GOrilla (ranked) and GSEA, to the methods we applied earlier, we first used GOrilla (ranked) with the Serum+LIF Cyclic 2 h and N2B27 Cyclic 12 h samples. 201 Pathways were identified for Serum+LIF Cyclic 2 h, which largely overlapped with those identified by the unranked approach, with sterol, cholesterol and secondary alcohol biosynthetic processes having the lowest q-values. Similar pathways as in the unranked approach were also identified for N2B27 Cyclic 12 h, although GOrilla (ranked) selected more metabolic and biosynthetic processes than the previous method. We then used GSEA with $q < 0.25$ and $p < 0.05$, as recommended, such that the false discovery rate was below 25%, which was acceptable (only) considering the exploratory nature of our analysis. Applying this approach to Serum+LIF Cyclic 2 h, GSEA selected 69 significant genes, which again broadly agreed with the unranked approaches, although additional pathways were also identified, including those involving calcium, the IEGs (such as the AP-1 complex & ATF-2), JAK-STAT and ECM interaction. A connectivity map of enriched pathways in this condition, as discerned by GSEA, is shown in Fig. 5.17. The same analysis identified seven enriched pathways in N2B27, capturing limited overlap with our earlier method. The selection included three pathways involved in p53, the caspase pathway and amino acid metabolism, showing the stress-related effects of stretching. Across the different methods and samples, the breadth and overlap of the ranked and the unranked techniques confirmed their validity and supported their use on the other samples.

We thus first applied GOrilla (ranked) and GSEA to the other samples in the RNA-Seq data. For the samples in Serum+LIF, stretched cyclically for 12 h, GOrilla found 177 pathways to be significantly enriched. As shown in Fig. 5.18a, metabolism-related processes were again found to be affected, but stress pathways and pH regulation also showed changes. In contrast, GSEA only detected 17 pathways as being significantly *under*-represented, with a focus on translation (including ribosome assembly and peptide chain elongation), metabolism (including branched chain a.a. catabolism and arginine and proline metabolism) and respiration. Overall, this indicated that the response we observed at the 2 h timepoint persisted until 12 h at a lower level, possibly associated by a reduction in overall levels of translation.

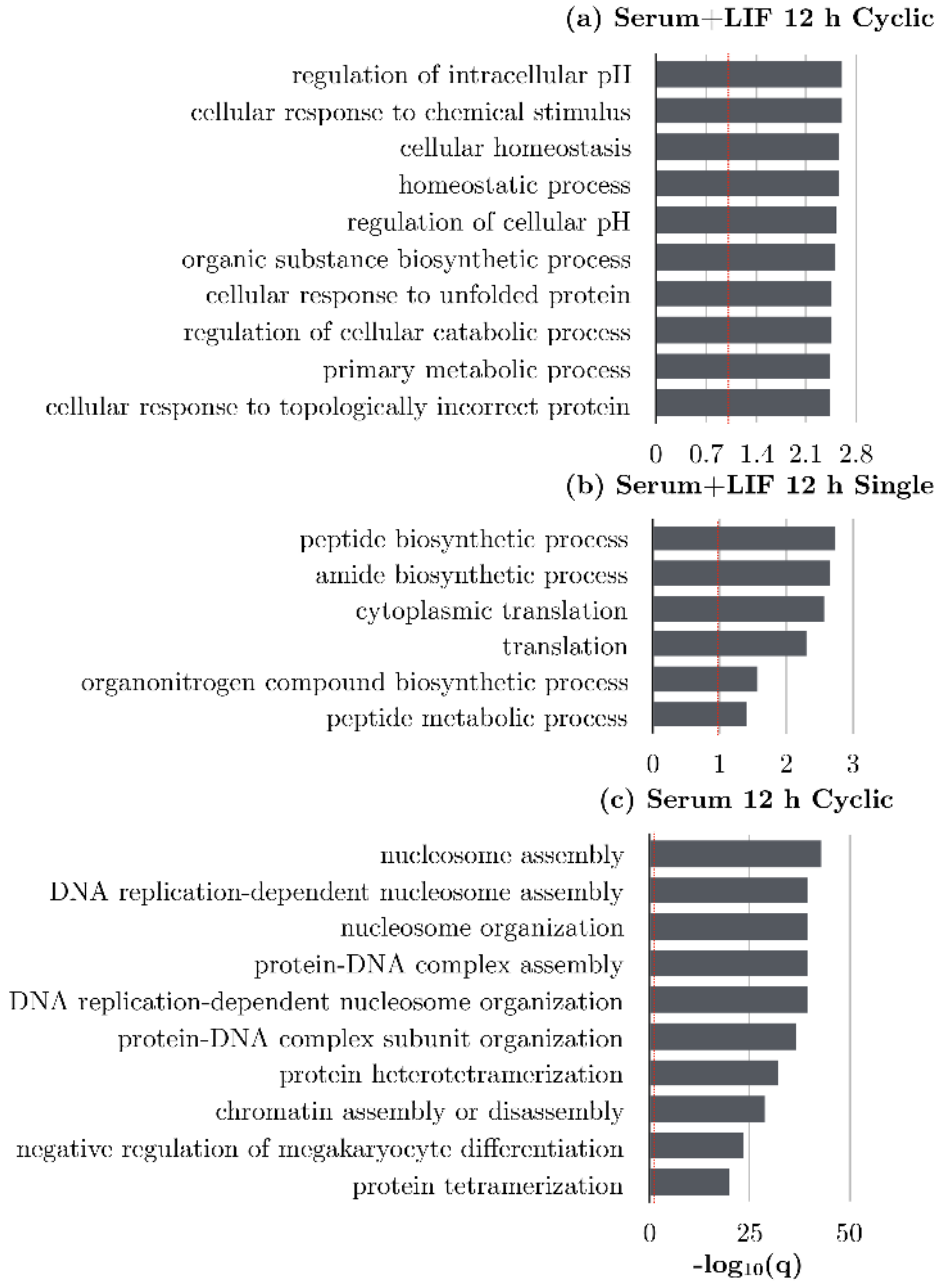

Figure 5.18 Ten most highly enriched pathways (or less if fewer pathways are significantly enriched with $q < 0.1$) using GOrilla with gene lists ranked by p-value, for (a) Serum+LIF 12 h Cyclic (b) Serum+LIF 12 h Single (c) Serum 12 h Cyclic stretch. The $q = 0.10$ limit is indicated using a red dashed line.

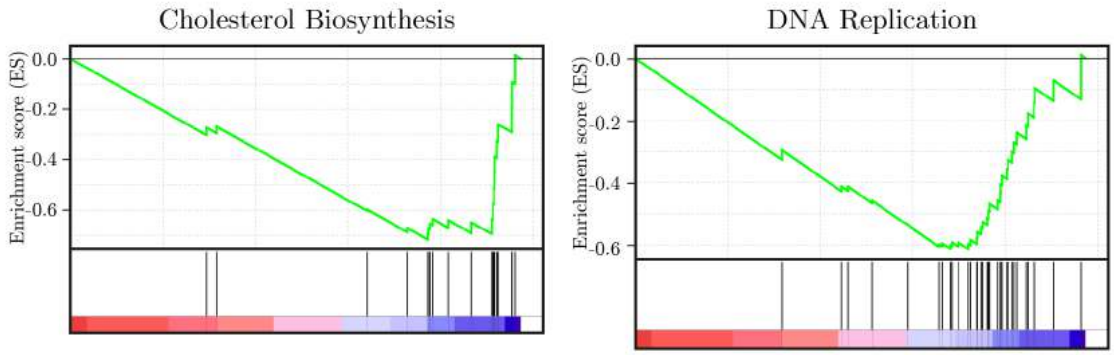

Figure 5.19 GSEA analysis of two pathways upregulated in S Cyclic 12 h stretched samples. The green line indicates the enrichment of the genes involved in the pathway among genes, ranked from left to right according to signal-to-noise ratio. The position of the genes in the pathways are indicated using black lines. Two pathways are related to metabolism and biosynthesis.

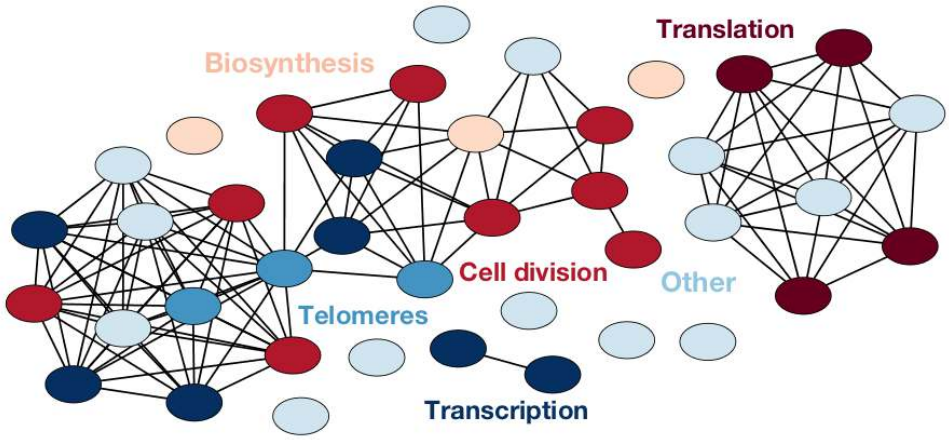

Figure 5.20 Interconnectivity map of pathways enriched in Serum Cyclic 12 h samples, with clusters labelled according to the general biological role. Connections between nodes indicate that pathways have genes in common. Map produced using GSEA package and Cytoscape.

Comparing the differences in pathways between the cyclic and single stretched 12 h samples in Serum+LIF allowed us to establish the effect of the stretch protocol. Interestingly, GOrilla identified only six enriched pathways in the single stretched samples, shown in Fig. 5.18b, which was an 93% reduction compared to cyclically stretched samples, with those detected exclusively involving metabolism, biosynthesis and translation, responses which were driven by the enrichment of a number of ribosomal proteins (which were not affected in the cyclic conditions). 39 Pathways were affected according to GSEA. The translational pathways overlapped well with those under-represented in cyclic conditions, while other pathways were much more general. As such, we concluded that a core set of effects was induced even by single stretch, while the wider response was somewhat diminished.

Similarly, we analysed the influence of media condition at the 12 h timepoint by comparing cyclic stretching in Serum to Serum+LIF. Interestingly, 82 pathways were detected as significantly upregulated by GOrilla, shown in Fig. 5.18c, with the main focus on pathways involved in the regulation of differentiation (including negative regulation of hemopoiesis and of myeloid cell differentiation, and regulation of megakaryocyte differentiation) and on DNA nucleosome assembly and chromatin organisation. Considering that the effects clustered into very specific responses, stretching did appear to have an influence on differentiation and chromatin organisation in this condition, but this effect was almost exclusively mediated through an enrichment of a series of histone cluster proteins. GSEA, in contrast, detected for these samples a reduction in 40 pathways involved in DNA replication, cell division and translation, with a connectivity map shown in Fig. 5.20 and two examples shown in Fig. 5.19. A decrease in proliferative activity is correlated to differentiation, and therefore the observed reduction could also indicate an increase in the rate of differentiation in response to stretching [Mehlen, 1997].

Finally, no pathways were identified in the 2i Cyclic 12 h sample using GOrilla (ranked) with $q < 0.1$, but relaxing this criterion yielded multiple pathways similar to the samples in N2B27, including biosynthesis, metabolism, signal transduction and molecular transport. The limited effect of mechanotransduction on 2i was confirmed also using GSEA, where only a single pathway was under-represented in the stretched samples. Of all samples, 2i was the condition least affected by stretching, confirming the strong impact of culture media. Considering the small overall response also in Serum+LIF conditions at 12 h, we attributed this effect at least partially to the naive pluripotency network.

In summary, we explored the differential effect of stretching on the overall transcriptome, and analysed the role of stretch programme, media condition and time after stretching. To improve the robustness of our analysis, we applied multiple gene ontology packages either on sets of differentially regulated genes, or on rankings of the impact of stretching on the

entire transcriptional programme. We noted a number of interesting features; first, stretching introduced specific effects that were common across different timepoints and media types. Specifically, we observed a consistent increase in pathways involved in metabolism and biosynthesis, particularly involving membrane components such as lipids, cholesterol and steroids, and in stress-related pathways, including those involving p53. Second, the effects of stretching on Serum+LIF strongly diminished from 2 h to 12 h, and the role of stress pathways appeared to increase at the later timepoint. The impact of stretching was diminished when exposing cells only to single stretch, although its influence on metabolic pathways persisted, potentially indicating that a core response to stretching was activated even in response to a single stretch. Third, stretching influenced differentiation in Serum-only conditions. Interestingly, stretching had no impact on differentiation pathways in N2B27, even though the latter was overall much more responsive to stretch. Finally, 2i was almost completely resistant to stretch, a likely consequence of its weaker cell-substrate attachment (see Fig. 1.3b on p. 5) and naive transcriptional state.

5.5 Calcium signalling

The effects of stretching on the transcription of specific genes and the changes to the overall transcriptome, although limited, raised further questions about the mechanisms involved in the detection, storage (cf. the *cellular memory* discussed in Section 5.2.1) and mechanical-to-biochemical translation of this signal. The next chapter discusses theoretically the role of the nucleus in this process, while this section is dedicated to calcium channels as a major component of the mechanotransduction network. Specific types of calcium channels can be activated by stretch, and might play a role in ES cells to connect the mechanical environment, in the form of stretch and substrate stiffness, on the one hand, and cell lineage choice, on the other [Pathak et al., 2014; Qi et al., 2015; Zhang et al., 2014]. This mechanism involves the TRP family, which is capable to convert physical signals into changes to intracellular calcium and, onwards, to neuronal development, differentiation and cytoskeletal organisation [Guilak et al., 2009].

The role of calcium channels in ES mechanotransduction is not fully understood, although calcium is involved in the regulation of a range of transcription factors and differentiation pathways [Apáti et al., 2012]. Considering their involvement in mechanotransduction in other systems, we hypothesised that they, together with stretch-activated components of the focal adhesions, are one of the front line mechanical sensors in ES cells. Changes in calcium concentration could then constitute an easy readout and additional biological verification of our technique and its short-term effects.

To this end, we used the calcium dye X-Rhod-1, a rhodamine intensity-based fluorescent marker of intracellular calcium concentration (an alternative dye, Fura-2, did not work when we tested it on ES cells). We analysed the intensity of X-Rhod-1 during live imaging, and found that the signal was moderately strong, stable, and exhibited low levels of bleaching when imaging every 5 min for 2 h. When exposing cells to a single stretch of 35%, similar to earlier experiments, we found that there was a significant increase in X-Rhod-1 intensity in response to stretching (166 cells, Welch's t-test $p = 0.01$), as shown in Fig. 5.22 and Fig. 5.21a. Considering we also observed an 8% increase in the signal strength of Hoechst, a part of the change in signal strength could be due to cells flattening and shrinking in response to stretch, thus increasing the amount of fluorescent signal within the plane of focus. However, this could not be the only cause, since the increase in X-Rhod-1 was significant even when normalising its signal by the change in Hoechst intensity.

Interestingly, within the first 30 min after stretching, a number of cells within each field of view exhibited sudden decreases in the intensity of X-Rhod-1 and, by extension, intracellular calcium. These 'calcium drops' were not accompanied by morphological changes closely before or after the event, or by similar changes in the intensities of nearby cells. An example of three cells exhibiting this behaviour is shown in Fig. 5.23a. The traces of mean X-Rhod-1 intensities in three cells with calcium drops, are shown in Fig. 5.23b, after fitting and subtracting an exponential from the entire 30 min time series to compensate for bleaching. Our images show that the rapid decreases in intracellular calcium had a duration of 30 - 60 s, and that X-Rhod-1 intensity was very stable outside of these events. Although we could start imaging only 60 s after stretching, the timeframe of the calcium drops was much longer than for the waves or peaks observed in neurons in response to changes in the external physical environment, which typically happen within 10 - 60 s after stretching [Bhattacharya et al., 2008; Lu et al., 2017].

We then quantified the proportion of cells which underwent a calcium drop, and found that the proportion of cells with a drop was significantly higher in samples which were stretched than in unstretched control samples over the course of 30 min, as shown in Fig. 5.23d. On stretched membranes, most drops occurred within the first 10 min after stretching, with the drops per min and the variance decreasing over time, with a mean of $18 \pm 7\%$ after 30 min. Unstretched samples contained a significantly lower number of cells with drops ($p = 0.007$), with a mean of $2 \pm 1\%$ by 30 min.

Interestingly, the proportion of cells with calcium drops increased somewhat in the last minutes of the experiments. We believe this could be related to the imaging conditions deteriorating in one of the repeats. The experiment was particularly sensitive to the humidity and CO_2 concentration due to the small culture volume, and adding additional culturing

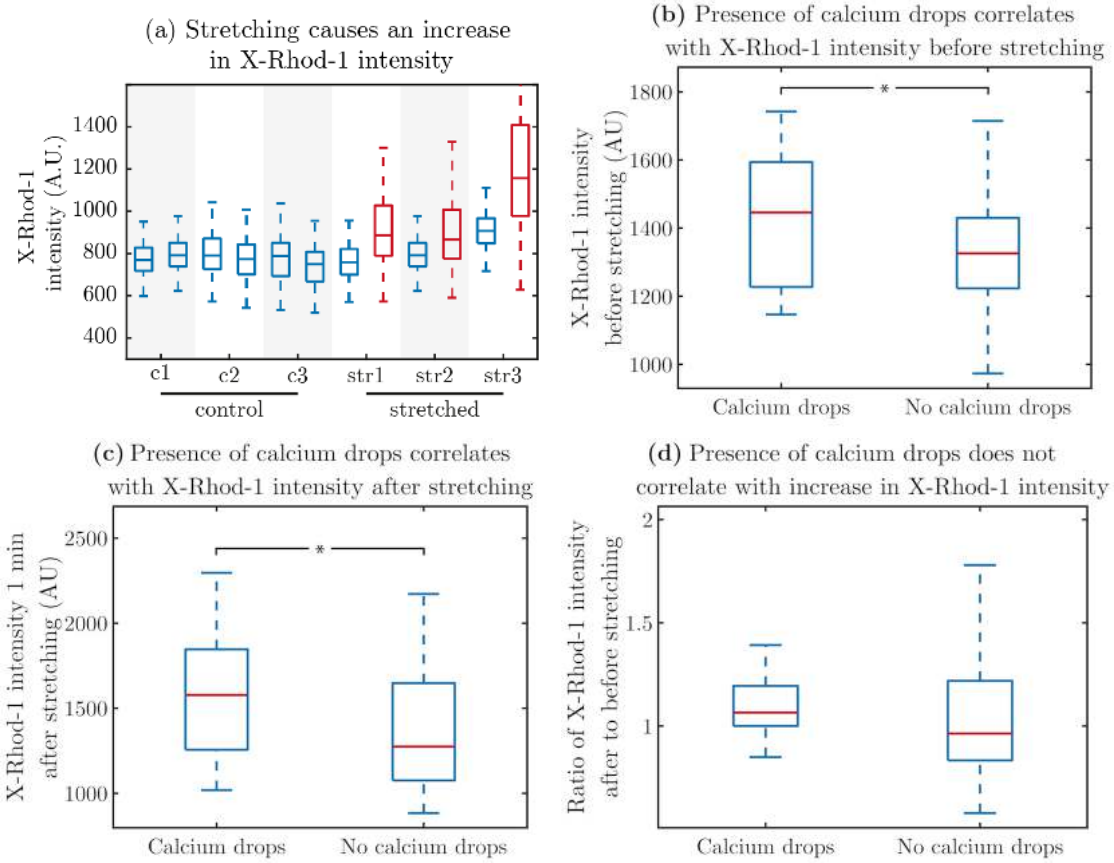

Figure 5.21 (a) The change in the mean X-Rhod-1 intensity of cells between two subsequent images (taken 3 min apart). Three membranes were left unstretched (c1-3), and three membranes were stretched 35% (str1-3). Boxplots correspond to around 400 unstretched (blue) and stretched (red) cells per experiment. (b)-(c) X-Rhod-1 intensity in the cells (b) before and (c) after stretching, and comparison between sub-populations which contain and do not containing a calcium drop. (d) Ratio of X-Rhod-1 intensities before and after stretching in the two sub-populations.

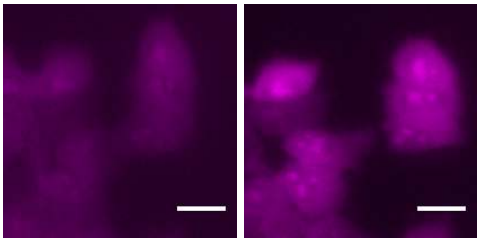

(a) Before **(b)** After

Figure 5.22 Intensity of X-Rhod-1 (a) before and (b) 3 min after stretching. Scale bar 20 µm.

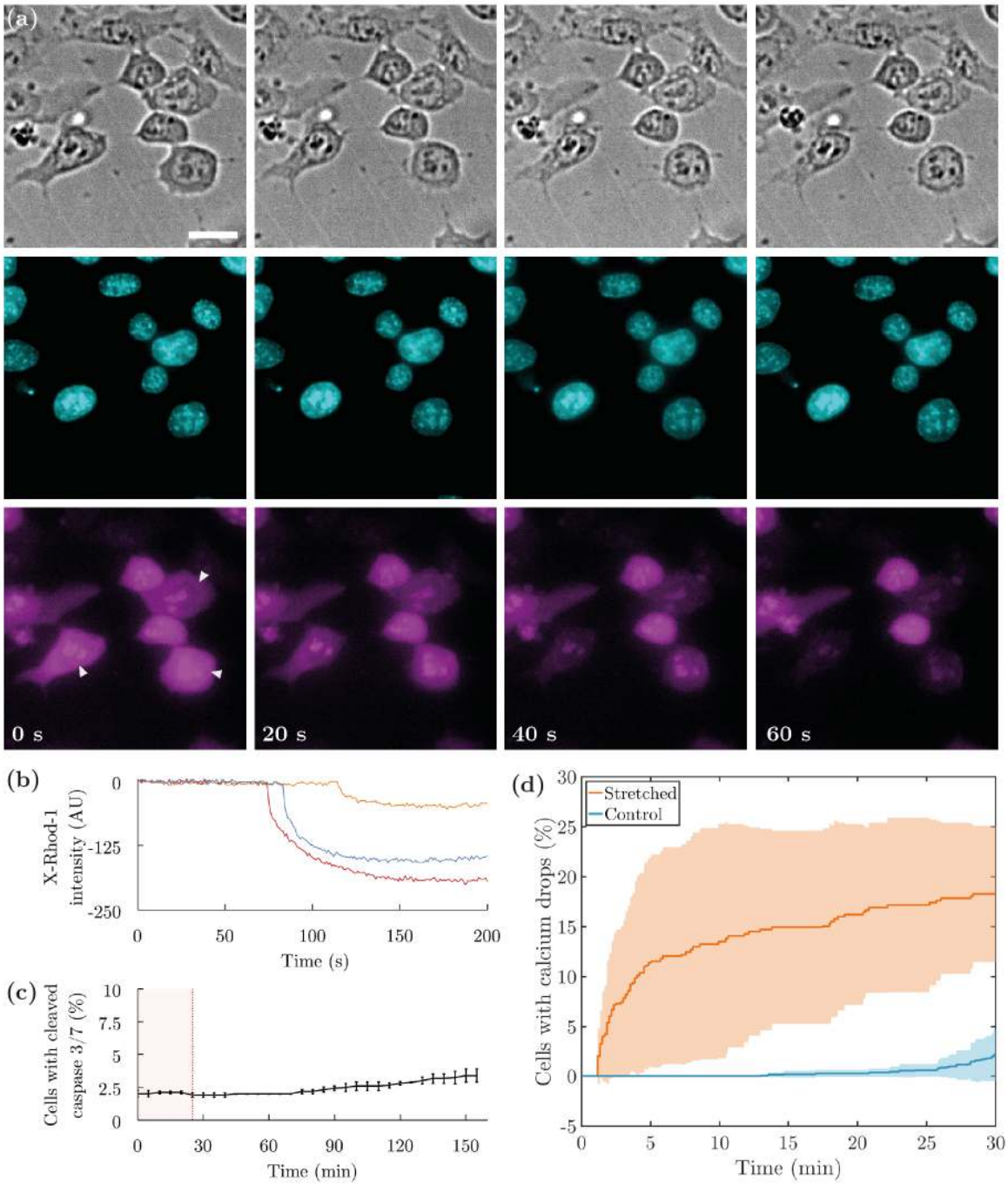

Figure 5.23 (a) Three cells (white arrows) undergoing a rapid decrease in intracellular calcium concentration. Brightfield, Hoechst (cyan) and X-Rhod-1 (magenta) images during 60 s, starting around 5 min after stretching. The scale in all images is identical; scale bar is 10 µm. (b) Traces of the mean intensity of three representative cells undergoing a calcium drop, images taken every 1.5 s. (c) Proportion of cells undergoing apoptosis, measured using caspase 3/7 cleavage, during 25 min before (red shaded area) and 130 min after stretching. Error bars correspond to standard deviation. (d) Proportion of cells with calcium drops in control (blue) and stretched (orange) conditions, starting 60 s after stretching. Standard deviation of 3 - 4 experiments shown as shaded area.

media during the experiment largely abrogated the late increase in calcium drops in the control cells. As such, we hypothesised that the calcium drops in either condition were a part of cells' early stress response, and that mechanotransduction and stress pathways are partly intertwined, both inducing an adaptive cellular response. Therefore, we wanted to verify that the sudden change to calcium concentration was not related to heavy cellular stress or apoptosis. To this aim we imaged cells with a dye for the cleavage of caspase 3/7, a marker of apoptosis, and quantified the number of cells undergoing apoptosis after stretching. As shown in Fig. 5.23c, there was no increase before or during the first 30 min after stretching in the number of cells with a measurable signal of the caspase marker. The proportion of apoptosing cells then increased slightly but remained very low, which showed that the calcium drops were not caused by an increase in apoptosis across the stretched or unstretched populations.

Considering that the average intracellular calcium concentration increased with stretching, we investigated whether a cell's calcium increase was predictive of the presence of a calcium drop after stretching. We observed a significant difference in the intensity of X-Rhod-1 between cells that contained a calcium drop and that did not ($p = 0.03$, no significant difference in the intensity of Hoechst), as shown in Fig. 5.21b, and a similar correlation with the intensity levels before stretching ($p = 0.03$, again no significant difference in the Hoechst signal), as shown in Fig. 5.21c. However, this could be an artefact of the analysis, with a drop in the intensity of X-Rhod-1 being more easily detected in cells that have a higher original intensity. Therefore we calculated the ratio of calcium intensity after to before stretching, shown in Fig. 5.21d, which did not display a significant difference ($p = 0.56$). Interestingly, there was a significant difference in the variance of the intensity ratios post vs pre-stretching, with cells exhibiting calcium drops after stretching having a narrower range of ratios (F-test $p = 1 \times 10^{-4}$). We did not observe a statistically significant correlation between the nuclear shape, size, nuclear Hoechst intensity or shape descriptors of cells that exhibited a drop in calcium and those that did not.

In conclusion, we observed a significant increase in the levels of intracellular calcium, as measured using the marker X-Rhod-1, in response to stretching. This was followed by sharp drops in calcium concentration in stretched cells, with a much lower proportion of unstretched cells exhibiting these drops. We interpreted these drops as early stress responses to stretch, which did not affect the viability or health of the cells in se. Our findings open the door to a range of other experiments to investigate this issue further. Considering we did not find a significant relationship between morphological parameters and calcium drops, we did not yet identify the underlying driver of the drops. In future experiments, we propose first varying the stretch, currently held constant at 35%, to study whether a correlation exists with

the amplitude of stretch, the size and the occurrence of the calcium drops. Second, with these drops as a direct readout of stretching, we would apply repeated stretches and investigate whether the increase in calcium concentration and the drops happen also after subsequent iterations.

5.6 Discussion

In this chapter we presented multiple observations that demonstrate the impact of stretching on cellular behaviour. We discussed multiple types of effects, from differences in the expression of individual genes, changes to the entire transcriptome, or the increase or decrease of the intracellular calcium concentration. Taken together, our results prove that stretching has a clear and measurable impact on cells, showing that direct forces influence cells even when not accompanied by larger changes to morphology, attachment and cell-cell interactions.

What is less clear, however, is how our different biological observations fit together into a coherent 'stretch-response strategy,' aimed at readying cells to adapt and respond to this substantial change in their physical environment, and possibly limit its detrimental effects. Time-wise, our results suggest that the components of this response are strongly sequential. Initially, stretching is associated with an instantaneous increase in intracellular calcium concentration. Then, within the range of a few minutes, there are sudden drops in the calcium levels of some cells, later followed by a strong upregulation of the immediate and early genes.

This pattern raises the question of how the calcium levels and transcriptional upregulation are related. It is likely that they are linked; that the drop in calcium sets in motion the positive loop that leads to the increase in IEG transcription. Chemically blocking the stretch-activated calcium channels could provide insight into both their role in the calcium increase, and test whether inactivating calcium would abrogate the changes to the IEGs. Whatever the exact mechanism might be, however, it is already clear that it is tightly regulated; we found that repeated stretching did not re-activate the IEGs and Fos in particular, contrasting with findings in earlier studies [Wilson et al., 2017], where repeated chemical cues did induce repeated transcription of Fos. Many other mechanisms leading to the activation of the IEGs also remain possible [Kopf et al., 2012]. For example, although not aimed at providing an answer to this question, in the next chapter we present a theoretical model of the disordered environment of the nucleus and its internal structure might play a role in responding to the direct forces induced by stretching.

The next element on the stretch-induced biological cascade is our observation of the effects on the entire transcriptome in Serum+LIF conditions, 2 h after stretching. We noticed that stretching had broad implications, inducing changes to metabolism, biosynthesis and p53 pathways, matching a recent report of the induction of senescence by p53 in non-ES cells in response to strain [Feng et al., 2018], and which are all likely a direct response to the stresses imposed on these cells two hours earlier. Surprisingly, however, these effects seem to persist for at least another ten hours. While the effects depend on the media condition and whether we stretch repeatedly, we continue to see a (weak) enrichment of the same type of pathways at 12 h even after a single stretch. At this timepoint the focus also seems to shift to stress- and cell cycle-related pathways.

We did not study whether these effects would persist this long even if the stretch would be released completely, but earlier work already suggested that there are effects even after the stretch has been suspended [Morawietz et al., 1999]. Since cytoskeletal reorganisation starts minutes after stretching, the presence of a stretch-induced tension is unlikely to be the sole driver of the long-lasting effects on the transcription scheme. How then does a cell preserve these signals long beyond the timeframe of the original input? This argues in favour of a 'differential-sensing mechanism,' which detects the change in strain, then preserves this in the form of a cellular memory, possibly involving fluctuations in Erk modulated by the IEGs. Testing the response to a stretch-and-release experiment could provide insight into this question.

The broad transcriptional effects are highly dependent on the culture conditions, and 2i, N2B27 and Serum-only samples responded remarkably different from Serum+LIF. The response in 2i was both the weakest and the most homogeneous (even adjusting for the magnitude of fold changes) of all conditions we tested, which is most likely a result of its restrictive transcriptional state and its insensitivity to mechanical signals [Martello and Smith, 2014]. In contrast, N2B27 was the second most permissive to stretching. There is an interesting equivalence in the increased susceptibility to stretch of cells in N2B27 after 36 h and the observation of nuclear auxeticity after 24 h, raising the possibility that auxeticity is an effect of the transition towards a nuclear state which is more sensitive to mechanics than cells in naive conditions. And while this was not widely reflected in the pluripotency network itself, it is possible that in Serum-only conditions stretching might also impact the differentiation process.

Chapter 6

Equally probable positive and negative Poisson's ratios in disordered planar systems

The results presented in this chapter were modified from an article published in the journal Soft Matter: Verstreken et al. [2018].

6.1 Context of this study

In parallel to the experimental work presented in the previous chapters, we developed a computational model of force propagation in disordered systems in collaboration with Dr Raphael Blumenfeld. The purpose of this project was to explain the role of the local structure of a material in explaining its auxetic behaviour (see Section 1.5). Earlier studies from our lab showed that nuclei of stem cells can exhibit auxetic behaviour as cells are undergoing differentiation, and that chromatin density and conformation play a role in causing this remarkable physical behaviour [Hodgson et al., 2017; Pagliara et al., 2014]. In this context, the types of disordered systems in this study functioned as a proxy of the chromatin organisation possibly present in the nucleus. Our physical observations in these simplified disordered systems could then serve as an initial avenue of exploration into the more complex and realistic environment of nuclei of real cells.

The results presented in this chapter are the first step of this larger study. We analysed the Poisson's ratio of a system on a global and a microscopic level, and correlated these parameters to the system's microstructure. Our current methodology, with adjustments, is well-suited to be applied to the biological context. Hence, we developed the experimental capabilities to apply forces directly to cells and their nuclei, as described in previous chapters.

In addition, we prepared a theoretical method to describe how these forces are propagated in the nucleus, and how global conformational changes depend on local chromatin structure. It is our ambition to in future work combine these two approaches to study nuclear force transduction and propagation, which would allow us to predict how chromatin conformation would change in response to forces from experimentally observed nuclear shape.

Even before these future developments, our present results are relevant to physics, material science and chemistry. For example, our analysis of which criteria allow systems to display negative Poisson's ratios on the system-wide or local level, could eventually influence technological applications in the form of the design of novel auxetic materials.

6.2 Introduction

Auxetic materials are characterised by a negative Poisson's ratio, which means that their horizontal and vertical strains are positively correlated such that they expand (contract) in both directions when stretched (compressed) [Lakes, 1987]. Most of the descriptions of materials that exhibit this feature, either observed in nature or artificially designed, have a highly ordered microscopic structure [Alderson and Alderson, 2007; Grima et al., 2009]. As discussed in Section 1.5, the observation of Pagliara et al. [2014] and Hodgson et al. [2017] of auxeticity in the nuclei of ES cells, is one of the exception to this.

In fact, auxeticity in disordered materials is quite common and reproducible. For example, any crumpled sheet of paper behaves auxetically when stretched between two fingers. Because of the lack of focus on these materials, however, there is still a lack of understanding of this behaviour in disordered systems. A recent study concluded that connectivity between microscopic elements plays a role in explaining auxeticity in disordered systems, but did not consider other structural parameters [Reid et al., 2018]. Before the release of this finding, we decided to simulate the displacements in disordered systems in response to external forces, to study which elements play a role in causing auxeticity.

6.3 Theoretical framework

Stresses on a local level can be modelled particularly conveniently in isostatic materials, which are systems where the forces applied by elements on their neighbours can be calculated from static interactions alone, similarly to the forces exerted by a ladder leaning on a wall [Ball and Blumenfeld, 2002; Blumenfeld and Edwards, 2012; Edwards and Grinev, 2001]. This eliminates the need to rely on the elasticity of elements on a microscopic level, which is typically associated with inexact or computationally intensive solutions.

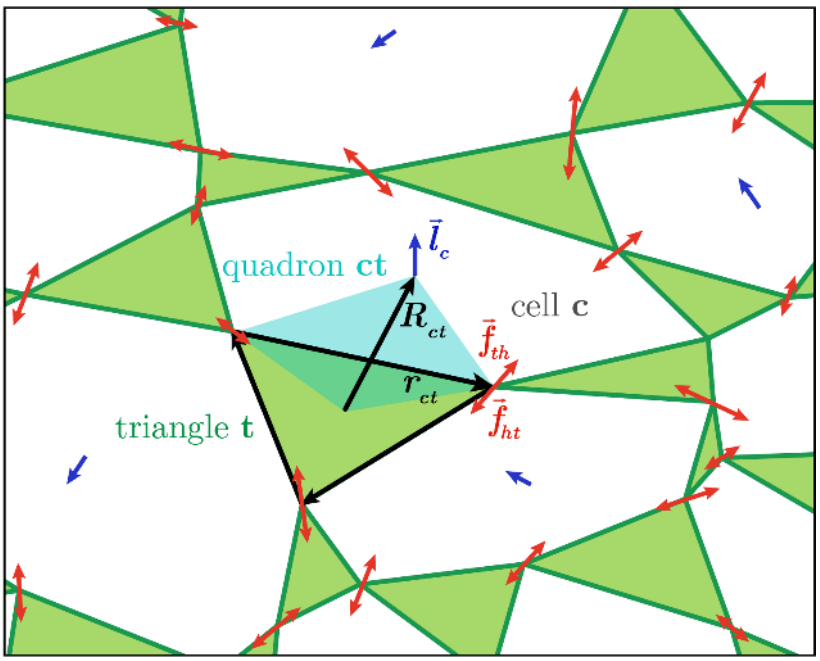

Figure 6.1 Close-up view of individual elements in our system. The edges of element t are made into vectors, $\vec{r}_{ct}$, that circulate the element clockwise. These vectors make a disordered graph of randomly shaped triangles, connected to their nearest neighbours at the vertices. The vector $\vec{R}_{ct}$ extends between the centroid of triangle t and that of its neighbouring cell, c. The vectors $\vec{r}_{ct}$ and $\vec{R}_{ct}$ are the diagonals of a quadrilateral volume element, which is called quadron [Blumenfeld and Edwards, 2006]. Intertriangular forces (red) are calculated as the difference between the loop forces $\vec{l}_c$ (blue) of neighbouring cells.

To be statically determinate, the mean number of force-carrying inter-element contacts (coordination number) per element should have a specific value z_c. This means that, in two dimensions, an isostatic system should consists of triangles, each connected to three other triangles. This critical coordination number of three is determined by equating the number of force and torque balance conditions to the number of unknown contact force components [Maxwell, 1864]. In two dimensions, with N grains, there are $\bar{z}N$ contacts and $2\bar{z}N$ force components are unknown. This compares to $\bar{z}N$ equations from action-reaction, $2N$ from force balance, and N from torque balance. Balancing the unknown force components and the known equations, means the system is determine with $\bar{z} = z_c = 3$ [Ball and Grinev, 2001; Camisasca, 2013]. Because of their static determinacy, we choose to study generic planar systems of interconnected triangles, illustrated in Fig. 6.1.

Ball and Blumenfeld developed a framework to solve the inter-element forces in response to external forces [Ball and Blumenfeld, 2002; Blumenfeld, 2004]. In their model, the open spaces surrounded by triangles are called ‘cells’ or ‘loops’. The edges of each triangle t

connect the hinges between the triangle and its neighbours, and are assigned a direction, which turns each edge into a vector $\vec{r}_{ct}$, with c referring to the cell that the edge borders. These vectors circulate clockwise around the triangles [Ball and Blumenfeld, 2002]. In addition, for each $\vec{r}_{ct}$, we define a vector $\vec{R}_{ct}$, extending from the centroid of element t to the centroid of loop c. These two vectors form the diagonals of a quadrilateral, known as a quadron [Blumenfeld and Edwards, 2003]. The quadrons are fundamental volume elements that tessellate the system space perfectly. These features make them well-suited for quantitative analysis of the local structure [Ball and Blumenfeld, 2002; Blumenfeld and Edwards, 2003, 2006].

Then, for each loop, it is possible to sum all inter-triangle forces (ITFs) along the loop, corresponding to a parametrised *loop force*. Then, the force that triangle t exerts on its neighbour t' is the difference between the loop forces of the two cells, c and c', straddling the common joint of these triangles [Ball and Blumenfeld, 2002] (see Fig. 6.1):

$$\vec{f}_{tt'} = \vec{l}_{c'} - \vec{l}_c \tag{6.1}$$

We use this description because, by construction, the loop forces automatically satisfy force balance on each triangle, leaving only the torque balance conditions. This cuts by two thirds the number of equations to solve, considerably reducing the computational effort.

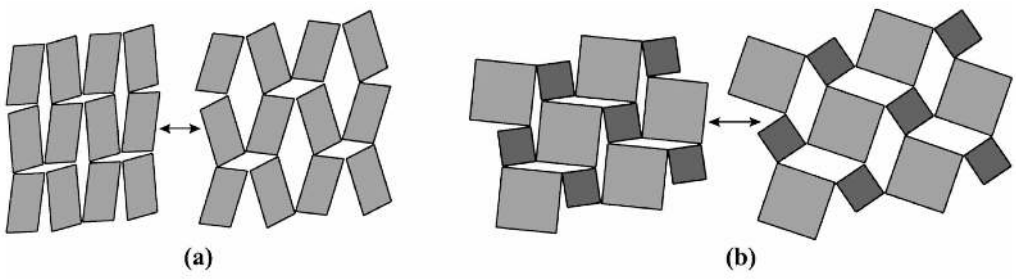

Figure 6.2 Diagram of the dynamics of two ordered auxetic systems. Image adapted from [Grima and Evans, 2006].

This method allows us to exactly calculate the forces with a large system of triangles with random shapes and sizes. The framework also provides a scalable quantitative description of the local structure, with the quadrons fully covering the total area of the entire system. In addition, we can define the structure of the quadrons as fabric or structure tensor, which corresponds to $\vec{r}_{ct} \otimes \vec{R}_{ct}$ and provides a measure of the isotropy of the local structure that can be scaled to the entire system [Ball and Blumenfeld, 2002; Blumenfeld, 2004; Gerritsen et al., 2008].

Rotation is a major driver of auxeticity in ordered systems. For example, in a system consisting of connected rectangle, as shown in Fig. 6.2, the elements rotate with respect to each other, thereby moving outwards in both directions. Using the framework we applied, it is possible to mathematically connect the local rotational strain to the rotation of the quadrons (see below) [Ball and Blumenfeld, 2003; Blumenfeld, 2005; Blumenfeld and Edwards, 2012]. This allows us to link rotation to the local structure on one hand, and to the Poisson's ratio on the other.

6.4 Theoretical model

In the previous section we established that, at a contact level of three, it is possible to write a set of equations such that all forces applied by elements on their neighbours are determined by statics alone. I now discuss the exact procedure of how to find those forces, and how this calculation relies on the boundary conditions of the system.

As discussed, in our model we consider a disordered planar system of $N(\gg 1)$ triangles. The contours of the triangles form a graph consisting of N_v connected vertices, N_e edges, and N_f faces. Identifying the N_b boundary triangles in this structure, it is convenient for the purpose of our analysis to enclose this graph within a frame to which the boundary triangles are connected by one of their vertices.

For such a graph, Euler's topological relation for two-dimensional graphs in the plane follows directly from the geometry of the system and corresponds to [Coxeter, 1973],

$$N_v - N_e + N_f = 1 \ , \tag{6.2}$$

where N_v, N_e and N_f are the numbers of the graph's vertices, edges and faces, respectively.

In our graph, the vertices are the contact points. The edges are the triangle edges and the additional N_b edges formed by the frame on the boundary of the system. The faces consist of the triangle faces and the internal elementary voids (called cells or loops here), which include the additional N_b voids formed by the frame. Considering there are N_c internal cells, the N loops around each triangle and the N_b boundary cells, the total number of faces is $N_f = N_c + N + N_b$. The edges around a loop on the boundary of the system consist of the edges of the triangles that made up that loop, on one hand, and one edge that is a part of the frame enclosing the whole system. As such, the total number of edges in the system is the sum of all edges of the triangles (equal to $3N$) and a single contribution to each boundary loop from the outer frame (equal to N_b), such that $N_e = 3N + N_b$. Finally, the number of vertices in the system is a function of the number of triangles. Each vertex is shared by two

triangles, except at the boundary. therefore, $N_v = (3N + N_b)/2$. Substituting these equations into Euler's relation (6.2), we have

$$N_c = 1 + \frac{N - N_b}{2} \, . \tag{6.3}$$

With a loop force associated with each cell, there are $N_c + N_b$ loop forces altogether, which yield, using (6.3), $2 + N + N_b$ unknowns.

Hence, to solve for these forces, we require $2 + N + N_b$ equations. Considering that, in steady state, the torque on each triangle should be equal to zero, there are exactly N torque balance conditions. We can then fix $N_b/2$ boundary forces on the vertices connected to the bounding frame, which in two dimensions provides N_b equations. This means we still require two additional equations. However, since each ITF is defined as the difference between two loop forces we are free to fix one of the loop forces at will [Ball and Blumenfeld, 2002]. This also reflects the nature of the loop forces field as a potential field, of which the local ITF is the gradient [Ball and Blumenfeld, 2002]. This leaves an exact set of equations to solve for the loop forces. Using this formalism, we then solve for the internal $N/2$ loop forces, from which we determine the ITFs.

Specifically, we can define the following $N \times N$ matrix $\mathbf{A}$, loop forces vector $\mathbf{X}$, and boundary forces vector $\mathbf{B}$, with $M = \frac{2+N+N_b}{2}$ [Camisasca, 2013],

$$\mathbf{A} = \begin{pmatrix}
0 & 0 & 0 & \cdots & -r^x_{1,10} & r^y_{1,10} & 0 & \cdots & -r^x_{1,N} & r^y_{1,N} \\
0 & \cdots & -r^x_{2,6} & -r^y_{2,6} & 0 & \cdots & -r^x_{2,14} & r^y_{2,14} & \cdots & 0 \\
\vdots & \vdots & \vdots & \vdots & \vdots & \vdots & \vdots & \vdots & \vdots & \vdots \\
-r^x_{N,1} & -r^y_{N,1} & 0 & \cdots & 0 & \cdots & -r^x_{N,21} & r^y_{N,21} & \cdots & 0 \\
0 & 0 & \cdots & 1 & 0 & \cdots & -1 & 0 & \cdots & 0 \\
\vdots & \vdots & \vdots & \vdots & \vdots & \vdots & \vdots & \vdots & \vdots & \vdots \\
0 & 1 & \cdots & 0 & -1 & \cdots & 0 & 0 & \cdots & 0 \\
1 & 0 & 0 & 0 & \cdots & 0 & 0 & 0 & 0 & 0 \\
0 & 1 & 0 & 0 & \cdots & 0 & 0 & 0 & 0 & 0
\end{pmatrix} \tag{6.4}$$

$$\mathbf{x} = \begin{pmatrix} f_1^x \\ f_1^y \\ \vdots \\ f_{10}^x \\ f_{10}^y \\ \vdots \\ f_{M-1}^y \\ f_M^x \\ f_M^y \end{pmatrix} \tag{6.5}$$

and

$$\mathbf{B} = \begin{pmatrix} 0 \\ 0 \\ \vdots \\ 0 \\ \\ b_1^x \\ \vdots \\ b_{N_b/2}^y \\ \\ 1 \\ 1 \end{pmatrix} . \tag{6.6}$$

These matrices correspond exactly to the set of equations described above. The first N rows of $\mathbf{A}$ and $\mathbf{B}$ correspond to setting the torque on each triangle equal to zero. The next N_b rows set the forces (in x- and y-directions) on the boundary vertices equal to a chosen boundary force, with those inter-triangular forces written as differences of the neighbouring loop forces. And the final two rows set the first two forces equal to one. As such, we have $\mathbf{Ax} = \mathbf{B}$, and we can solve for the loop forces by Gaussian elimination.

To study the potential auxetic behaviour of disordered systems, we generate numerically $15,000$ disordered planar assemblies of triangles. The procedure to generate these is as follows. First, we distribute around 200 points randomly and evenly in the plane, and apply a Voronoi tessellation on the set of points. The tessellation gives rise to a graph of polygonal cells, with each node of the graph of degree three, that is, each node is connected to exactly

three edges. Connecting the midpoints of these three edges produces a disordered network of 300 triangles connected at their vertices. We studied whether these isostatic systems are auxetic (referred to as iso-auxetic) [Blumenfeld and Edwards, 2012].

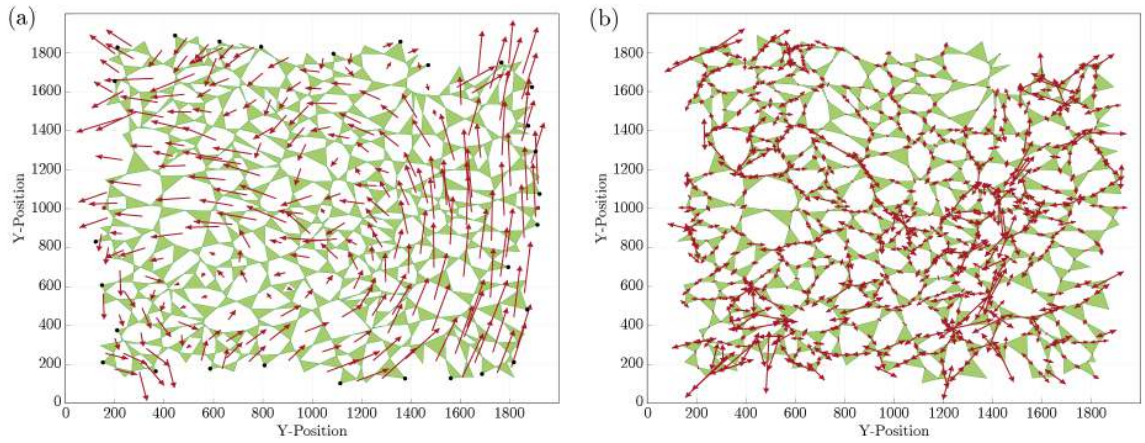

Figure 6.3 The response of a disordered system to the application of two antipodal forces on boundary vertices (marked by red dots): (a) loop forces, $\vec{l}_c$, (b) the corresponding ITFs, $\vec{f}$.

For each such a system, we calculated all the loop forces, illustrated in Fig. 6.3a, by applying two outward tensile boundary forces near the middle of the left and right boundaries. A typical solution for the inter-triangular forces (ITFs) is shown in Fig. 6.3b. Often the solutions consist of regions in which the loop forces have smoothly-changing directional orientation, separated by sharp breaks in the directional order. These boundaries correspond to localised force chains [Ball and Blumenfeld, 2002; Blumenfeld, 2004, 2007; Bouchaud et al., 2001].

We first used these solutions to determine the ITFs, as outlined above, and then analysed the quasi-static deformations of the systems under these forces. The triangle vertices are deemed to be connected by hinges. As such a triangle's displacement and deformation could be via rotation, translation, or expansion (compression), as long as their edges remain straight. This means that triangles are fully flexible; they can expand, contract or deform fully depending on the forces of their neighbours.

To determine the displacements of the vertices of the triangles, starting from the determined equilibrium state, we apply two small tensile sources on two vertices along the x-axis near the middle of the system, pulling those points outward. We then recalculate the change in the equilibrium ITFs, $\vec{\delta} f_{ij} \ll \vec{f}_{ij}$. This produces new ITFs for the entire system. We assume that the vertex displacements are expected to be proportional to the forces acting on them. This is a reasonable assumption, considering that, being statically determinate and in

the absence of inertial effects, the vertices can only displace owing to the compliance of the triangles. However, since the ITFs are determined from balance conditions, two equal and opposite forces act on each vertex. We determine the force, which induces displacement by the vertex's proximity to the one of the external loads, with the vertex displacing towards the external tensile force it is closest to. This divides the system naturally into two halves with an imaginary half-line at $x = 0$. The magnitude of the vertex's displacement is the absolute value of the x-component of the force on it, scaled down by a factor ζ that is proportional to its proximity to the load: $\zeta = 0$ and 1 on the half-line and on the corresponding boundary, respectively. A typical example of a displacement field is shown in Fig. 6.4a. We then collect the displacements data for later analysis, increase magnitudes of the boundary loads, calculate the new ITFs and repeat the process. The accumulated displacement resulting from 100 successive repetitions of the process is shown in Fig. 6.4b.

6.5 Results

Here we refer to the gradient of the displacement as strain, for short, although this term is normally reserved for its symmetric part. The strain can be defined for individual triangles and can be separated into a translational, an expansive and a rotational component:

$$\varepsilon_t = \varepsilon_t^{trans} + \varepsilon_t^{exp} + \varepsilon_t^{rot}. \tag{6.7}$$

In our system of non-rigid elements, all these components are relevant [Blumenfeld and Edwards, 2012], while in systems consisting of rigid elements, only the translational and rotational components contribute to the total strain [Ball and Blumenfeld, 2002].

The translational strain captures the displacements of the triangles' centres of mass. It represents the displacement of all three vertices in parallel with an equal magnitude, thus moving the triangle while maintaining its shape and size constant. It is defined as

$$\varepsilon_{t,\alpha\beta}^{trans} = \frac{\langle \delta\vec{R} \rangle_\alpha}{(\vec{R}_t - \vec{R}_0)_\beta}\ , \tag{6.8}$$

where $\vec{R}_t$ is the vector from the origin to the centroid of triangle t, $\vec{R}_0$ is the position of the entire system's centre of mass, and $\delta\vec{R}$ is the mean displacement of the vertices of t.

The expansive component of the strain depends on the displacement of an individual vertex inward or outward along the vector from the centre of mass of the triangle to that

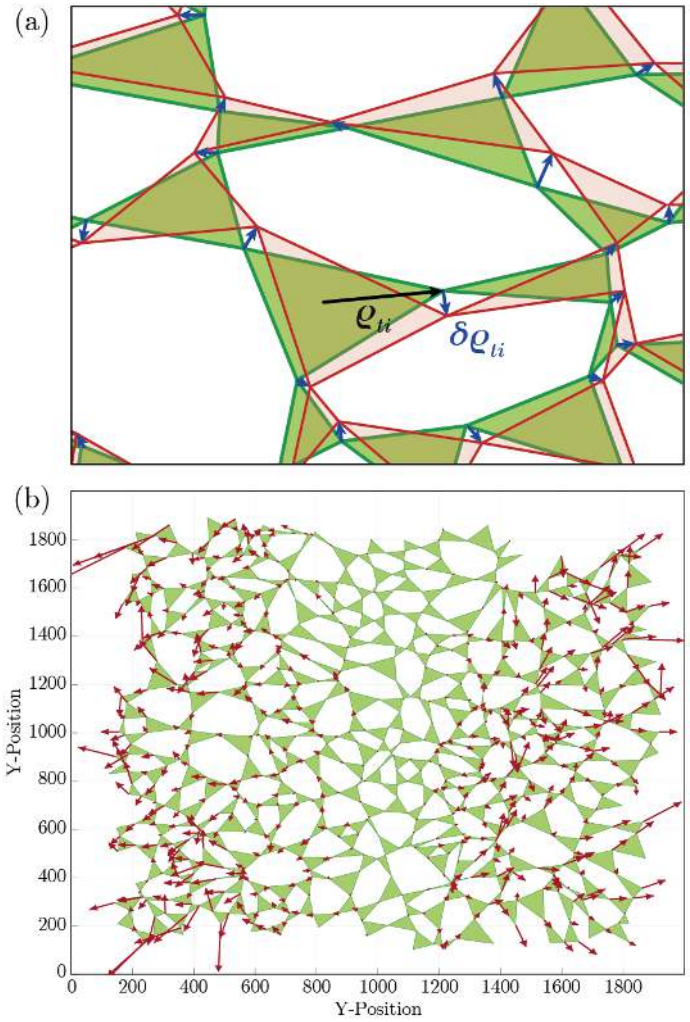

Figure 6.4 (a) Vector $\vec{\rho}_{ti}$ points from the centroid of triangle t to its vertex i, and this vertex is displaced by $\vec{\delta\rho}_{ti}$. (b) Displacement of vertices in response to 100 small increments of the boundary forces.

vertex, i.e. the vertex's displacement projected on the vector ρ_{ti}

$$\delta R_i^{exp} = \frac{(\vec{\delta\rho}_i - \langle\vec{\delta\rho}\rangle)\cdot\vec{\rho}_i}{|\,\rho_i\,|}\cdot\frac{\vec{\rho}_i}{|\,\rho_i\,|}\,, \tag{6.9}$$

where $i = 1,2,3$ are the three vertices of the triangle. For each vertex, this is the normalised projection of the displacement on ρ_{ti}, multiplied by the unit vector of ρ_{ti}. The expansive strain is then

$$\varepsilon_{t,\alpha\beta}^{exp} = \sum_i \varepsilon_{i,\alpha\beta}^{exp} = \frac{\delta R_{ti,\alpha}}{\rho_{i,\beta}}\,. \tag{6.10}$$

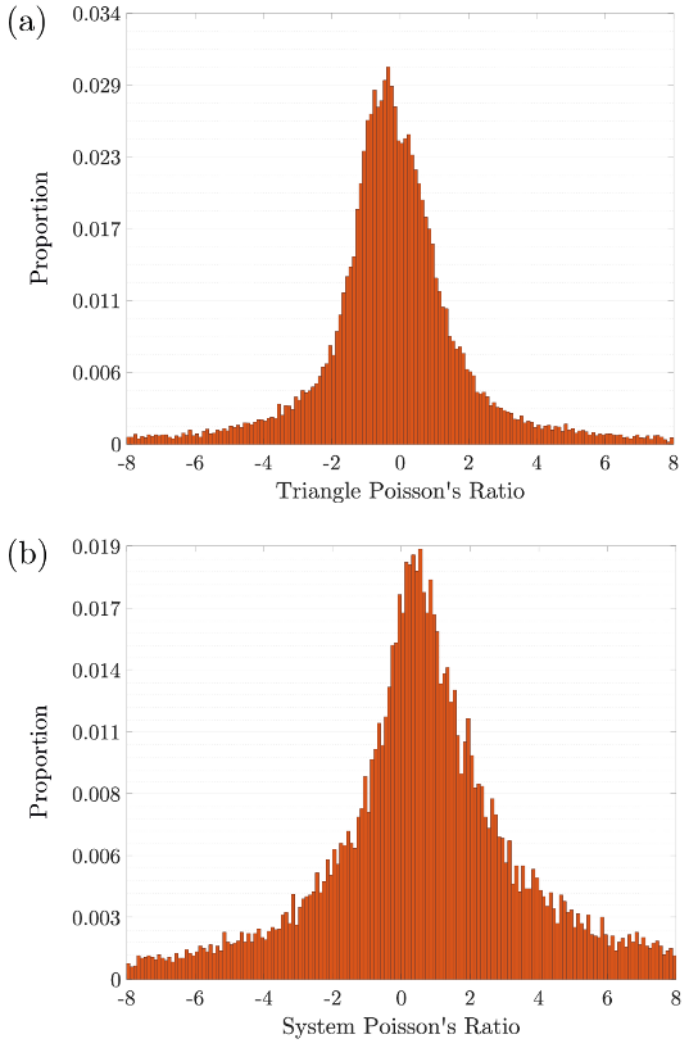

Figure 6.5 (a) Histogram of the PR ν_t of individual triangles, calculated from over 40,000 elements over 100 simulated systems. (b) Histogram of the PR of global systems, calculated from over 15,000 systems of 300 triangles each.

As discussed, each triangle hosts exactly three quadrons, as shown in Figure 6.1, each described by a structure tensor $\mathbf{C}_{ct} = \vec{r}_{ct} \otimes \vec{R}_{ct}$ [Blumenfeld and Edwards, 2003]. The triangle's structure tensor is the sum of the structure tensors of its three quadrons:

$$\mathbf{C}_t = \sum_{c=1}^{3} \mathbf{C}_{ct} \ . \tag{6.11}$$

The antisymmetric part of this tensor gives the area associated with the triangle's three quadrons, A_t,

$$\frac{1}{2}\left[\mathbf{C}_t - \mathbf{C}_t^T\right] = A_t \Theta \ , \tag{6.12}$$

where $\mathbf{C}_t^T$ is the transpose of $\mathbf{C}_t$ and Θ is the two-dimensional $\pi/2$ rotation matrix (the Levi-Civita operator). The symmetric part of $\mathbf{C}_t$,

$$\mathbf{Q}_t \equiv \frac{1}{2}\left[\mathbf{C}_t + \mathbf{C}_t^T\right] \ , \tag{6.13}$$

describes the local rotation of the element relative to the global mean [Ball and Blumenfeld, 2002; Blumenfeld, 2004]. It has also been shown [Ball and Blumenfeld, 2003] that the rotational strain satisfies

$$\varepsilon_t^{rot} = \frac{\theta_t}{A_t}\mathbf{Q}_t \ . \tag{6.14}$$

In terms of the triangle variables, the rotational component of the displacement is the displacement perpendicular to the direction of the expansion

$$\delta R_i^{rot} = \frac{(\vec{\delta\rho}_i - \langle\vec{\delta\rho}\rangle) \times \vec{\rho}_i}{\mid \rho_i \mid} \cdot \hat{r} \ . \tag{6.15}$$

Therefore, the rotation angle of vertex i is

$$\theta_i = tan^{-1} \frac{\mid \vec{\delta R}_i \mid}{\mid \vec{\rho}_i \mid} \ , \tag{6.16}$$

and the rotational strain of the entire triangle is

$$\varepsilon_{t,\alpha\beta}^{rot} = \frac{\frac{1}{3}\sum_i \theta_i \cdot Q_t}{A_t} \ . \tag{6.17}$$

We define the PR of triangle t as

$$\nu_t = \varepsilon_{t,yy}/\varepsilon_{t,xx} \ . \tag{6.18}$$

This provides a local definition of the PR and makes it possible to study the spatial distribution of this property across the system. We also computed the global PR of each system, defined as

$$\nu_{sys} = \frac{\Delta L_y / L_y}{\Delta L_x / L_x} \, . \tag{6.19}$$

Here, L_α is the system extension in the α direction, defined as the difference between the mean positions of the vertices at opposite boundaries, and ΔL_α is the mean change in that distance.

We impose deformations on the system on a local and a global scale using forces in both directions. On a global scale, we set a boundary force on every other vertex on the vertical and horizontal sides of the system. As such, the system would not be able to expand infinitely in the direction perpendicular to the disturbance forces. On a local scale, triangles can experience forces from neighbouring triangles on all sides and in all directions. Therefore the deformation space for the system's constituent elements is restricted by neighbouring triangles, preventing triangles from freely expanding or contracting. As discussed in Section 1.5, this means that the boundary conditions required to measure the Poisson's ratio, i.e. allowing deformation in the direction perpendicular to the direction of the externally-applied force, are not entirely respected. Keeping this in mind, we continued our analysis, which might be able to provide us with an approximation of the Poisson's ratio and allow us to distinguish between the different types of deformation: translation, expansion or rotation.

In Figure 6.5a, we plot a histogram of the local PRs for data collected from over $40,000$ triangles from 100 different system realisations. It is symmetric, with the mean and standard deviation being -0.2 and 1.8, respectively, demonstrating that there is hardly any sign preference for the local PRs. In Figure 6.5b we show the histogram of ν_{sys} across $15,000$ systems of 300 triangles each. This histogram is also symmetric, with its mean and standard deviation 0.9 and 7.0, respectively. Interestingly, this histogram's standard deviation is much larger than for the individual triangles, which is a result of its tails falling slower than exponential, although faster than algebraically, as shown in Fig. 6.6.

To examine the dependence of these results on system size, we repeated the simulations for systems of sizes ranging from N = 150 to N = 1050 triangles each, as shown in Fig. 6.7. We find that the distributions' standard deviations are an order of magnitude larger than their means and are broadly symmetric around 0, as can be observed in Figures 4. Zooming in on the means and standard deviations of the global PR distributions over the 7-fold size variation, we observe that the mean decreases slightly with N, from 0.82 to 0.66. This decrease is not statistically significant and is also consistent with no change within 95% confidence. In contrast, the standard deviation increases significantly with size by about 53%, from 6.31 to

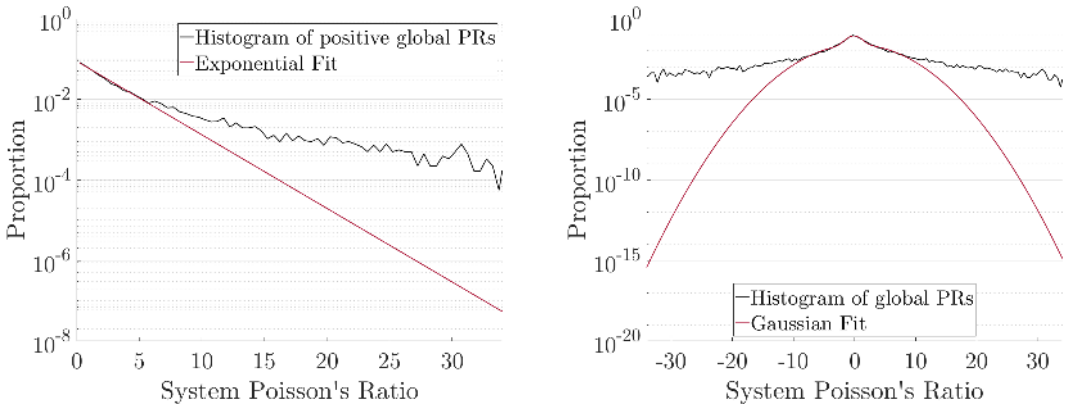

(a) **(b)**

Figure 6.6 Attempted (a) exponential and (b) Gaussian fits of the histogram of global PRs, as plotted on a semi-log scale, using (a) only the positive or (b) both positive and negative PRs.

9.70, indicating, with 95% confidence, that the width of the PR value distribution increases proportionally to N .

To understand the emergence of this feature as a function of the structural components, we investigated the local correlations between structural, elastic and strain properties, with the structural characteristics quantified using the above quadron description. To this end, we first express the stress on triangle t in terms of the loop forces of the cells surrounding it [Ball and Blumenfeld, 2002]. The increase in the boundary forces gives rise to the following change in the stress

$$\delta\sigma_t = \frac{1}{A_t}\sum_c \vec{\delta} f_c \otimes \vec{r}_{ct} \ . \tag{6.20}$$

Given a triangle's stress and strain, we also calculated its compliance matrix, $\mathbf{S}_t$, using $\sigma_t = \mathbf{S}_t \varepsilon_t$.

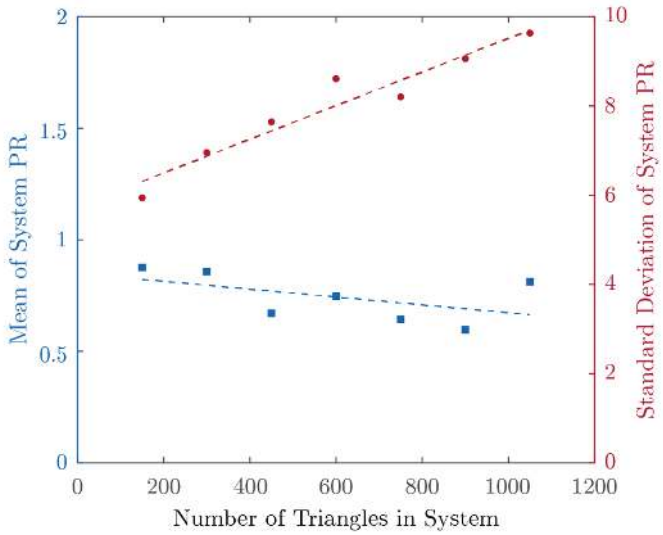

Figure 6.7 Mean (blue; left axis) and standard deviation (red; right axis) of system of 150 to 1050 triangles each. The mean is fitted well by $PR = -1.8 \times 10^{-4} N + 0.8$ and the standard deviation by $\bar{\sigma}_{PR} = 3.8 \times 10^{-3} N + 5.7$, with N the number of triangles.

In particular, we correlated the traces of the different strain components of individual triangles with the trace of that triangle's total strain, for 100 systems and 3×10^4 elements. Irrelevant outliers, within the 2% highest and lowest strains, were disregarded. We find that the expansive component is the dominant contributor to the symmetric part of the strain, with a correlation of $\gamma = 0.93$ between $Tr\{\varepsilon_t^{exp}\}$ and $Tr\{\varepsilon_t^{tot}\}$ (Figure 6.8a). The second largest contributor is the translational strain, with a correlation of $\gamma = 0.24$ between $Tr\{\varepsilon_t^{trans}\}$ and $Tr\{\varepsilon_t^{tot}\}$ (Figure 6.8b). In contrast, there is hardly any correlation between the rotational

component and the total strain, $\gamma = 0.03$ (Figure 6.8c). As expected, the importance of expansion in the overall strain of individual triangles causes a negative correlation of $\gamma = -0.10$ between the expansive strains of neighbouring triangles (Figure 6.8d). The translational strains of neighbours are positively correlated, with $\gamma = 0.67$, which is induced by our method of determining vortex displacements. Interestingly, while the rotational strain does not correlate well between nearest neighbours, with $\gamma = -0.06$, the rotation angle of neighbours is anti-correlated, with $\gamma = -0.35$, which is an aspect of the 'anti-ferromagnetic'-like rotational nature of such systems [Ball and Blumenfeld, 2003; Baram et al., 2004; Blumenfeld and Edwards, 2009; Blumenfeld et al., 2010; Grima and Evans, 2006].

We also investigated the correlations between the one-triangle PR and local structural characteristics, including the triangle: size, shape, quadron sizes, displacement, and any of the strain contributors. We found no significant correlation between any of these quantities.

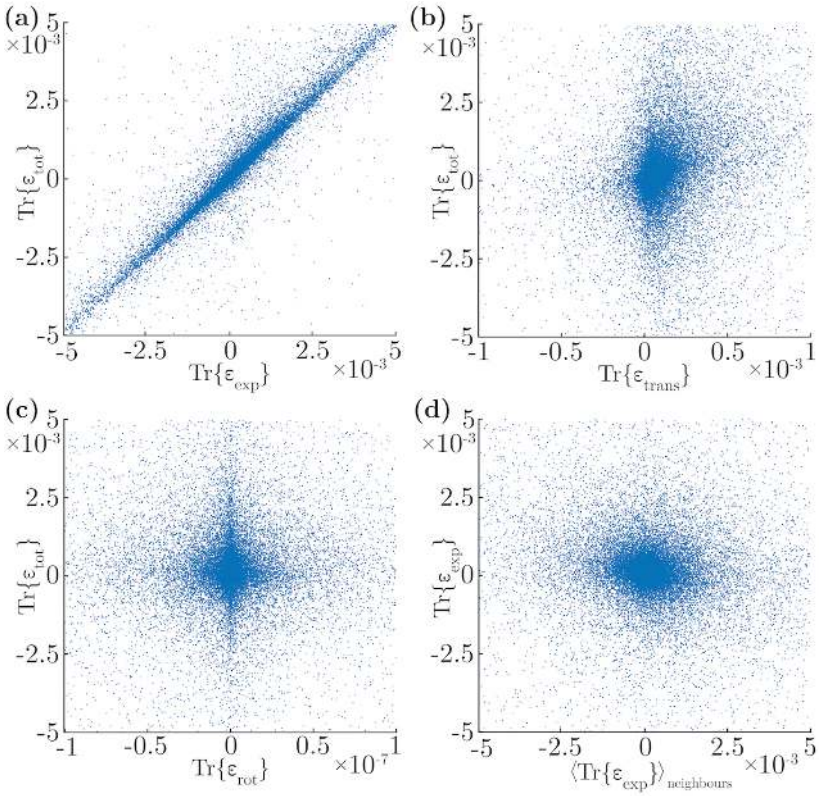

Figure 6.8 The relative contribution of strain components to the total strain of individual triangles. We show the correlation between the traces of a triangle's: (a) expansive and total strain; (b) translational and total strain; (c) rotational and total strain. In (d) we show correlation between the trace of a triangle's expansive strain and the average of the trace of the expansive strain components of the element's neighbours.

6.6 Discussion

We studied the auxetic behaviour in disordered structures, modelled here as planar statically determinate, or isostatic, systems of triangular elements. We investigated whether a negative Poisson ratio (PR) can emerge spontaneously without design or whether a positive PR is more common, as its dominance in the macroscopic world might suggest.

We simulated $15,000$ planar systems, each containing 300 randomly-shaped compliant triangles, connected by joints at the vertices, determined the equilibrium stress state of each system by fixing the force on every other boundary point to zero, and then applied small additional equal and opposite tensile forces antipodally along a line that passes through the centre of the system. The force response to these loads was translated into triangle vertex displacements, from which we computed the local triangle strains, as well as the global system-wide strain. From these we derived the PR both locally and globally.

Our main finding is that, in completely randomly generated systems, positive and negative PRs are almost equally likely to occur. This is true both on the element scale (Figure 6.5a) and for the entire system (Figure 6.5b). This suggests that large-scale systems with this layout would be almost PR-neutral, displaying a behaviour that is neither conventionally elastic nor fully auxetic. This result may seem counter-intuitive in view of the prevalence of positive PRs in macroscopic structures. However, it reinforces that: (i) these are not conventional elastic systems, (ii) that PR should be regarded as a strain-based, rather than a stress-based, quantity, and (iii) the PR is at least as sensitive to the microscopic structural characteristics as it is to the local elastic moduli.

The mean contributions of the translational, expansive and rotational strains to the one-element total strain were $23.2 \pm 0.05\%$, $77.3 \pm 0.05\%$ and $0.0 \pm 0.05\%$, respectively. The corresponding correlations between those and the one-element total strain were 0.24 ± 0.005, 0.93 ± 0.005, and 0.03 ± 0.005, respectively. We also found a significant anti-correlation of -0.10 between the expansive strains of neighbouring triangles, as well as a considerable anti-correlation of -0.35 between their rotations. The latter is directly related to anti-ferromagnetic-like rotational dynamics in such systems [Ball and Blumenfeld, 2003; Baram et al., 2004; Blumenfeld and Edwards, 2009; Blumenfeld et al., 2010]. It should be emphasised that, by imposing static determinacy, we constrained movement in our systems. To achieve static determinacy, we imposed a boundary load every second boundary vertex. With such boundary conditions, rigid triangles would not displace as they cannot expand. Indeed, the displacements we observe arise mainly from triangle expansions and contractions, which explains the correlations we observe.

We also searched for correlations between the sign of the PR and local micro-structural descriptors. Such correlations, if found, could lead to informed design of auxetic disordered

structures. However, we found none in this study. It is possible that such correlations have been washed out by the strong anti-correlation between nearest-neighbour expansive strains. To study this issue in more depth, a similar study should be carried out on systems of fully rigid triangles [Grima et al., 2005]. We conjecture that such systems would show stronger correlations between the local PR and the translational and rotational strains. Since the latter is directly related to the local structural rotational disorder (as defined in [Ball and Blumenfeld, 2002; Blumenfeld, 2004]) which is a function of the symmetric part of the local tensor $\Theta_t(\vec{r})$, we expect such systems to give rise to local correlations between the disordered structure and the PR. To allow systems of rigid triangles to deform, one must reduce the number of boundary loads in order to free internal translational and rotational degrees of freedom. This might then better correlate the global PR with the distribution of the local structure tensors.

Chapter 7

Discussion & future directions

The relevance and the effects of mechanotransduction in biology have been studied in great depth in previous studies [Wang, 2017], through multiple systems and various cell types, with examples ranging from how substrate stiffness influences neuronal activity [Zhang et al., 2014], to how stretching can distinguish healthy from diseased muscle cells [Granata et al., 2017]. But while biophysical parameters have been shown to play a role in differentiation [Engler et al., 2006; Sun et al., 2012a; Trappmann et al., 2012], the understanding of the impact of mechanics on pluripotent stem cells and early differentiation is limited [Chowdhury et al., 2010a; D'Angelo et al., 2011].

We argue that embryonic stem cells are a valuable system to study mechanotransduction. Because of the connection between mechanotransduction and transcription, external changes can result in clear and measurable changes to differentiation and cell fate. In addition, due to low levels of lamin A/C, the stiffness of the nuclear lamina is lower, simplifying the link between cytoskeleton and transcription [Constantinescu et al., 2006].

In this project we have attempted to characterise the influence of external physical signals on ES cells, with the following objectives: First, we set out to develop a device to apply forces to ES cells while limiting the secondary effects that might interfere with a thorough investigation of the mechanical pathways. Second, we studied cell state changes in response to external forces and investigate whether this 'disturbance' is sufficient to perturb the signalling balance in pluripotent cells. The magnitude of the resulting changes to the pluripotency network could then be compared to the biological effects of other physical and chemical signals, and provide insight into the mechanical susceptibility of the different cell states. Third, we aimed to dissect the intracellular mechanotransduction pathways, connecting front line mechanosensitive components to changes in nuclear organisation and linking extracellular signals to gene expression.

We approached these goals by designing a cell substrate stretcher and developing a new functionalisation protocol to attach ECM proteins to an elastic substrate, as presented in Chapter 4. We applied this set-up to characterise the effects on cells in Chapter 5. Our findings suggest that stretching has a significant impact on ES cells on short timescales, including initial changes to intracellular calcium concentration, a rapid gene expression response, and a broader long-term impact on the transcriptome in some media conditions. Finally, we investigated the reliance of the physical response of disordered systems, such as a cell's nucleus, on its structural configurations using a computational model, as discussed in Chapter 6.

In short, the main novel contributions of this study are the following: We present a convenient and versatile single-parametric method that can be used to stretch ES cells. We also applied our set-up for other purposes, including to study the alignment of defective muscle cells (see [Granata et al., 2017]), to investigate pattern formation in zebrafish embryos, and to stretch mouse oesophagi. Second, we report an increase in intracellular calcium due to stretching, followed by sudden decreases, which is a response not previously observed in ES cells. Third, we confirmed that in ES cells stretching introduces a strong upregulation of the IEGs on short timescales, matching behaviour observed in other cell types [Morawietz et al., 1999] and proposed that the recovery period of the IEGs in response to mechanical signals is significantly longer than when induced chemically [Wilson et al., 2017]. In addition, we showed that the effect of stretching depends highly on culture media, with Serum+LIF being most affected on short timescales, and N2B27 on long timescales. Furthermore, we presented multiple observations to support the hypothesis that forces, without associated morphological and biochemical secondary effects, have limited effects on pluripotency, except in Serum. Finally, we presented a novel theoretical approach to model forces in disordered systems, showed that negative Poisson's ratios in these systems are much more common than previously assumed, and investigated correlations between the local structure and the local and global PR.

These findings are now discussed in more detail. The set-up we present here allowed us to exert forces directly on ES cells. Manufacturing the device is easy: it can be 3D printed from biocompatible plastic and uses a functionalised PDMS membrane. The device is highly versatile; it was designed for use in molecular biology but can easily be modified for other uses by any researcher with access to a 3D printer. And due to the optional integration of an actuator and graphical user interface, the device can be used with complex protocols. As such, while other devices have been presented that are capable of exerting forces on cells (see for example [Fink et al., 2011; Quinlan et al., 2011; Shao et al., 2013]), to our knowledge none exist that exhibit a similar combination of biological accuracy with this level of experimental

versatility. We intend to release our current device as a platform to allow other investigators to print the device themselves, or to modify and adapt the set-up according to their own requirements.

Our device is complemented by a novel technique to functionalise PDMS by covalently attaching ECM proteins to the surface. Our method resulted in a level of cell attachment and morphology that was similar to or better than tissue culture plastic, with similar cytoskeletal features, which assured that cells experienced the stretch fully. In the future we hope to expand the possibilities of the stretcher by attaching a hydrogel to the PDMS membrane, which our functionalisation technique is well-suited for, allowing us to investigate the combined effect of stretching and substrate stiffness.

From a biological point of view, a key advantage of our set-up is the possibility to stretch multiple conditions and replicates at the same time, simplifying experiments and reducing potential inter-experiment variability that arises from a combination of experimental errors. Most importantly, however, stretching cells directly using the method that we proposed is a single-parametric technique; that is, the impact of stretching on cell density and cell-cell vs. cell-substrate attachment preference remains limited. This is not the case when modifying substrate stiffness, for example. As a consequence, any secondary changes to chemical cell-to-cell signalling remain small, and therefore the effects on the biological phenotype should be primarily a direct result of stretching. On the other hand, a number of disadvantages are associated with our method; its uses are limited to stretching or compression, it is not well-suited to apply other types of mechanical inputs, and it is dynamic, providing a time-varying and time-limited signal rather than durably changing the overall biophysical environment (as is the case for substrate stiffness).

When stretched on the PDMS membrane, cells elongated proportionally along the direction of stretch. However, minutes after stretching, cells slowly started to return to their original shape by releasing bonds at their extremities, which was accompanied by visible rounding, demonstrating the dynamic and temporal character of our technique. To maximise the potential downstream effects, we stretched cells repeatedly with intervals of 60-90 min, such that they were able to remodel after every stretch. It remained possible, however, that internal mechanisms might prevent subsequent stretches from inducing similar intracellular effects. Indeed, repeated stretching did not result in the repeated upregulation of the IEGs, contrasting with the timeline of other studies [Aoki et al., 2013; Wilson et al., 2017]. Our results do not yet contribute to identifying the duration or mechanism of this recovery period. In the future, varying the duration between subsequent stretches could help further explore this feature.

Even a single stretch induced a sharp increase after two hours in the transcription of the IEGs, similar to what has been described by Morawietz et al. [1999] in vascular smooth muscle cells. However, they observed that Fos was not upregulated and that Jun transcription increased already by 30 min (compared to 2 h). This discrepancy demonstrates the high variability of IEG expression and the transcriptional dependence on the experimental conditions [Kletsas et al., 2002; Komuro and Yazaki, 1993; Nadruz et al., 2005]. We found that a high variability was present also in the other qPCR and the RNA-Seq experiments. And while it constituted a major confounding effect throughout our experiments, we have not yet been able to confidently pinpoint its precise cause. However, after extensive optimisation, our findings suggest that the main source of experimental variability is not caused by the practical execution of the protocol (that is, not caused by the experimenter). Instead, it is most likely an inherent feature of how cells respond to the type of mechanical input we apply to them. This again supports the dominance of morphology over mechanics, as plating conditions would supersede the effects generated by stretching itself. However, we have only explored a fraction of the continuum of the experimental parameters (including genes, timepoints, media conditions, stretching amplitude and stretching type), and studying this mix in more detail might unveil an ideal set of 'ingredients' that maximise the effect of stretch.

Our observations are sufficient to conclude confidently that stretching of cells' substrate affects their behaviour. However, our transcriptional experiments did not shed light onto whether increases in the IEGs translate into durable downstream effects and long-term biological changes. Although these might be reflected in the broader MAPK and pluripotency network [Chappell et al., 2013; Gregg and Fraizer, 2011; Ying et al., 2008], it is likely that cells' cytoskeletal reorganisation has at least some inhibitory impact on genes' long-term susceptibility to stretching. The single-parametric character of our approach should allow us to, in future experiments, analyse further how stretching modifies transcription, particularly for the IEGs.

RNA sequencing of cyclically stretched cells showed that few genes were significantly regulated in Serum, Serum+LIF and 2i after 12 h. In contrast, there was a broad transcriptional response in Serum+LIF at 2 h and in N2B27 at 12 h. Both conditions expressed similar pathways, but N2B27 displayed a larger emphasis on stress pathways. All genes taken together, we conclude that the media condition has a large effect on susceptibility to stretching. However, we also propose that there is a core set of stretching responses that is common across the different conditions. It would consist primarily of pathways related to metabolism and biosynthesis of membrane components, and secondarily of pathways reacting to stress induced by extracellular signals. It is possible that these responses assist cells in adjusting to a larger surface footprint, as their membrane adapts to the stretch in the cytoskeleton,

even though cells already partially relaxed the additional cytoskeletal tension induced by stretching.

Our transcriptional results show that the effect of stretching on pluripotency is limited in most media conditions, including Serum+LIF and Serum. In N2B27, single stretching had a positive effect on Nanog, Klf4 and Esrrb initially, but a negative effect later (although the changes were not significant). However, RNA-Seq data of cyclically stretched cells in N2B27 detected no effects on the pluripotency network. Surprisingly, limited evidence from gene ontology techniques suggested that stretching might affect differentiation of cells in Serum. Overall, our findings in this respect deviate substantially from the trend observed in earlier studies (see Chapter 1, including Chowdhury et al. [2010a]; Engler et al. [2006]). While our system and methods are different from these investigations, when also including findings from our lab, our results suggest that the effect of forces on the pluripotency network is mainly conveyed through changes in morphology, cell-cell vs. cell-substrate preference, and cell density. This would imply that the factors indicated in this text as 'secondary effects' really are the main drivers of changes in pluripotency in response to substrate-mediated forces.

Earlier studies have proposed a link between calcium levels and Egr-1 transcription, relying (among others) on Ca^{2+}-channels and Erk [Thiel et al., 2010]. Using the marker X-Rhod-1, we detected a significant increase in intracellular calcium concentration in response to stretching. Furthermore, up to 20% of stretched cells exhibited a sudden drop in their calcium concentration, the presence of which was uncorrelated to the earlier increase. Although still unsubstantiated in our study, but supported by earlier findings (see Section 1.3.3) the level of calcium might be a front line response to mechanical signals, initiating a positive feedback loop that would then lead (via Erk) to IEG transcription. Our observation could be one of the first observations of the importance of calcium in the mechanotransduction processes of ES cells.

Furthermore, we hypothesise that the calcium level is anti-correlated to a cell's susceptibility to subsequent mechanical signals. A heightened calcium level might then be associated with mechanical recovery and an insensitivity to additional mechanical inputs. Then, as cells switch off their high calcium state, they would again 'reactivate' their mechanical sensitivity. Important initial experiments to study this further might include the analysis of the dependence of calcium intensities to the levels of stretch, or of the presence of calcium drops even after subsequent stretches, which could directly link an absence of calcium drops to the lack of response in the IEGs. It would also be interesting to investigate further which are the underlying morphological drivers that distinguish the presence, intensity and timing of the decrease in intracellular calcium concentration. We could analyse this by applying the

functionalisation in geometric patterns, to test the role of cells' shape and whether they are more susceptible to stretch when oriented in the direction of or perpendicular to the stretch.

We complemented our biological analysis with a physical analysis of the structural requirements for the nucleus to exhibit the physical behaviour that we observed experimentally. Modelling the nucleus as a disordered cluster of random domains, we used a theory of isostatic materials to calculate the exact forces within the system in response to global stresses. We found that the systems exhibit positive and negative Poisson's ratios with close to equal probability, and that the local structure is not predictive of the microscopic or macroscopic PR. Rotation of domains appeared to play a role in driving their local behaviour, which is consistent with the typical behaviour of artificially designed macroscopic auxetic materials.

The premises in our model restrict its direct practical (biological) implications [Reid et al., 2018]. Concretely, our findings appear to suggest that the sign of the PR of a material on a macroscopic level is primarily a function of the larger-scale structures embedded in the material. Again keeping in mind that important assumptions were made, this might imply that chromatin structure alone is not sufficient to predict the presence of auxeticity in ES cells. We will modify the model to remove the reliance on these assumptions, including the ability of domains to expand indefinitely. We could then study the responses of rigid domains to external forces both theoretically and experimentally. In addition, the theory is valid even in three dimensions, and we would like to adjust our model for these settings. Overall, the changes should make our theory more relevant for biological application such that it can be used to verify and complement our experimental observations.

In conclusion, our analysis of the broad impact of stretching on cellular behaviour allows us to propose a hypothetical model, coherent with our observations, of the cellular response to external forces:

The front line response to stretching consists of an upregulation of intracellular concentration, possibly using stretch-activated calcium channels. We hypothesise that this is the initial step in the translation of external mechanical into internal biochemical cues. These signals would then enter the positive feedback loop that promotes IEG expression for as long as the calcium concentration is increased. It has been proposed that IEG expression results in long-term changes depending on the input's magnitude and duration [Murphy et al., 2002]. We hypothesise that the prolonged increased intracellular calcium concentrations is a regulatory mechanism that temporarily turns cells insensitive to further mechanical signals, reducing the effect of cyclic stretching on cells. This might be complemented by a second regulatory system downstream of the IEGs to regulate the long-term impact of stretching. It would be heavily mediated by the biochemical environment, which is influenced by the culture media. This would explain why the long-term effects of stretching are relatively

limited. However, they include a core response across different conditions, consisting of the enrichment of pathways related to metabolism, biosynthesis and stress, which might prepare cells to adapt to the cytoskeletal changes forcibly induced by stretching. The specific changes would depend on culture condition; naive pluripotency is not conducive for mechanical signals, while N2B27 is strongly affected, raising the possibility that differentiation in N2B27 increases cells' mechanical susceptibility. Our computational model indeed suggests that the physical behaviour of the nucleus during differentiation is not caused by chromatin conformation, supporting the possibility that this transition is caused by changes in the large-scale structural components of the nucleus. Curiosity permitting, our overall findings could serve as a basis to test this model and further explore how forces and mechanical signals are modulated in cells and random systems.

Chapter 8

Appendix

The following paper (Hodgson et al. [2017]) was submitted as co-first author during this PhD project, but did not form an essential part of the main results. It has therefore been included here, as an appendix, with permission from The Royal Society of Chemistry.

Lab on a Chip

PAPER

View Article Online
View Journal | View Issue

Cite this: *Lab Chip*, 2017, **17**, 805

A microfluidic device for characterizing nuclear deformations

Andrew C. Hodgson,†[a] Christophe M. Verstreken,†[ab] Cynthia L. Fisher,[b] Ulrich F. Keyser,[a] Stefano Pagliara*[c] and Kevin J. Chalut*[ab]

Received 21st October 2016,
Accepted 13th January 2017

DOI: 10.1039/c6lc01308b

www.rsc.org/loc

Cell nuclei experience and respond to a wide range of forces, both *in vivo* and *in vitro*. In order to characterize the nuclear response to physical stress, we developed a microfluidic chip and used it to apply mechanical stress to live cells and measure their nuclear deformability. The device design is optimized for the detection of both nucleus and cytoplasm, which can then be conveniently quantified using a custom-written Matlab program. We measured nuclear sizes and strains of embryonic stem cells, for which we observed negative Poisson ratios in the nuclei. In addition, we were able to detect changes in the nuclear response after treatment with actin depolymerizing and chromatin decondensing agents. Finally, we showed that the device can be used for biologically relevant high-resolution confocal imaging of cells under compression. Thus, the device presented here allows for accurate physical phenotyping at high throughput and has the potential to be applied to a range of cell types.

Introduction

Cells experience a wide range of chemical and physical cues from their microenvironment, but the biological and physical relevance of these signals are not well understood. On the one hand, the external physical environment has been shown to affect cell fate and development, for example by influencing lineage commitment of ES cells upon differentiation.[1,2] On the other hand, the phenotype of the cell, such as cell type and differentiation state, can drive changes in cell mechanics. For example, large changes in nuclear organization and stiffness during key developmental stages have been observed.[3,4] Given the precision with which the physical and chemical environment can be controlled, and the capability for high throughput measurements, microfluidic devices are an ideal platform to explore the effects of external stresses on the biological and biophysical processes occurring in single cells.[5]

The prevalence and sophistication of microfluidic devices in the study of cellular biophysics has increased in recent years.[6,7] A wide range of assays now exist to modify the environment of a variety of cells, including controlling chemical gradients,[8] rapid cell sorting[9] and high throughput phenotyping.[10,11] The scale of microfluidic devices allows for parallelized measurements at the single-cell level, while simultaneously greatly reducing reagent usage compared to traditional techniques.[12] For example, microfluidic devices have recently been used to uncover the physical behavior of embryonic stem (ES) cells in response to external signals, providing physiologically relevant information for *in vitro* investigations.[13]

In this paper we introduce a microfluidic platform for the high-throughput measurement of cellular and nuclear deformability of ES cells whose mechanics have been shown to alter as the cells exit pluripotency and initiate lineage choice.[14] The device consists of a chip made of polydimethylsiloxane (PDMS), prepared in advance of the experiment day and finalized using a 30 minute procedure. This permits short setup times and straightforward use by a cell biologist with little or no experience with microfluidics, while assuring repeatability in terms of the physical and chemical environment inside the chip as to minimize the impact on cell viability and culture quality.

Before the experiment, cells are labelled with SYTO 13 (Invitrogen), a fluorescent nucleic acid marker to illuminate the nucleus with an intensity that is 3–4 times higher than the cytoplasm.[15] This allows easy visualization and detection of the nucleus and the surrounding cytoplasm inside the chip. The cells, when loaded into the chip, are flowed in suspension and a compression force is applied by confining them in a channel slightly smaller than their cross-sectional

[a] *Cavendish Laboratory, Department of Physics, University of Cambridge, Cambridge CB3 0HE, UK. E-mail: kc370@cam.ac.uk*
[b] *Wellcome Trust/Medical Research Council Cambridge Stem Cell Institute and Department of Clinical Neurosciences, University of Cambridge, Cambridge CB3 0ES, UK*
[c] *Department of Biosciences, College of Life and Environmental Sciences, University of Exeter, Exeter, Devon EX4, UK. E-mail: s.pagliara@exeter.ac.uk*
† These authors contributed equally.

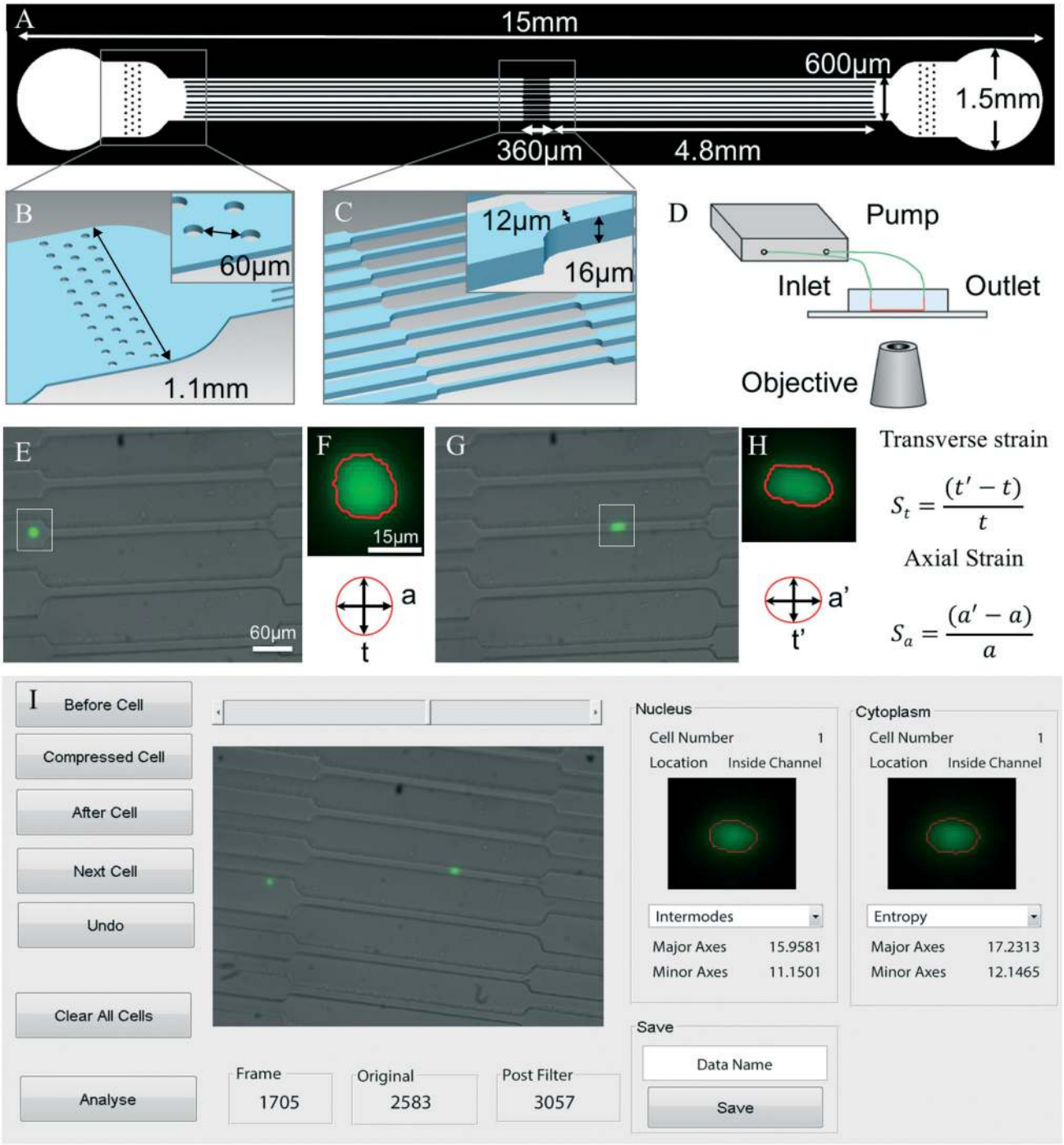

Fig. 1 Chip design and experimental setup. (A) Photomask design. The inlet and outlet are situated at the large circular extremes of the design. (B) Expanded view of the inlet. An array of pillars acts as a filter for any object substantially larger than the cells, thus decreasing channel blockages. (C) Cells are guided through separate large channels to the compression channels, where they experience a one-dimensional compression. (D) Experimental set-up: a pressure pump is connected to the chip inlet and outlet *via* FEP tubing containing cells and media. The pump drives the cells from the inlet to the outlet across the constriction region. (E) Fluorescent image overlaid on bright field image of an ES cell before compression. (F) A region of interest is selected by the user on the GUI for thresholding and measurement. *a* and *t* are the axial and transverse dimensions respectively. (G) The ES cell is compressed within a 12 μm constriction channel. (H) A second region of interest is selected to re-threshold the cell under compression. *a'* and *t'* are the compressed axial and transverse measurements respectively. The transverse and axial strains are determined using the formulas shown. (I) Screenshot of the MATLAB analysis GUI. The GUI displays the fluorescence image of the cells superimposed on the bright field image of the chip. The user can then see the cells move frame-by-frame towards and through the constriction channels. A box is drawn around the cell of interest by the user, after which the GUI displays the thresholded and measured image in the 'selected cell' section of the GUI.

area. The cells are imaged before, during and after compression. A custom Matlab GUI analyzes such images and calculates cellular and nuclear strain, or deformability, allowing the assessment of the cellular and nuclear response to physical stress. Deformability is a proxy for cell and nuclear mechanics, which correlates with cell states in development and disease.[16–18] In this manner, the device can be used for accurate mechanical phenotyping and identifying various stages of development while simultaneously providing valuable data on the physical biology of cells at those stages.

Experimental

Design and production of the molds

The mask was designed using AutoCAD (Autodesk). The designs were translated into a photomask (Photodata) and printed onto an emulsion film with a resolution of 128 000 dpi to be used for photolithography. The 16 μm structures, serving as a template to produce reservoirs and compression channels in the subsequent step (see below) were deposited onto a silicon wafer using a single lithography step as follows. SU-8 2015 (Microchem) was spin-coated onto the wafer at 3000 rpm for 60 s after a ramp of 300 rpm per second. A UV lamp (365–405 nm, 20 mW cm^{-2}) was used to expose the mask onto the deposited photoresist for 6 s. After post-baking for 5 min and developing in propylene glycol monomethyl ether acetate (PGMEA) (Sigma-Aldrich), the wafer contained SU-8 structures with a height of 16 μm as verified using a stylus profilometer (Dektak). The dimensions of this device are reported in Fig. 1.

Production of microfluidic chip & experimental procedure

A device negative replica was produced by placing the patterned silicon wafer into an open container with base surface area slightly larger than the wafer itself. The wafer was then covered with degassed 9 : 1 (base : curing agent) polydimethylsiloxane (PDMS) and cured at 70 °C for 60 min, before the area around the features was cut with a scalpel to remove the microfluidic chip from the mold. A 1.5 mm biopsy punch (Kai Medical) was used to create fluidic accesses to the chip at the outer ends of both reservoirs. Oxygen plasma treatment (10 s exposure at 100 W, Diener) was used to bond the patterned surface of the PDMS chip to a glass slide (24 × 50 mm, 0.13–0.16 mm, Menzel-Gläser). This treatment temporarily renders PDMS and glass hydrophilic, so within 5 min after bonding the chips were filled with the cell culture medium that would be used during imaging. FEP tubing (1/16 in × 0.03 in, outer and inner diameters respectively, Gilson) was used to connect the reservoirs to a pressurized microfluidic flow control system (MFCS-4C, Fluigent). The inlet tube was filled with a cell suspension while the outlet tube was filled with cell culture media pre-equilibrated to culture conditions by incubating it at 37 °C and 7% CO_2. The flow across the constriction channels was controlled using the MFCS-4C's computer software (MAESFLO, Fluigent). Imaging was performed on a Leica SP5 in epifluorescence mode, using a 20×/0.5 N.A. objective and 2 × 2 binning. For translocation measurements, the microfluidic chip was connected to a syringe pump (Nemesys, Cetoni) to supply a constant flow of 100 μl min^{-1} for each of the samples. Translocation measurements were performed by only imaging the region of interest and using 4 × 4 binning on an Olympus IX73 epifluorescence microscope using a 20×/0.5 N.A. Olympus objective and an optiMos sCMOS camera. 3D imaging on Lifeact-tagRFP cells was performed using a 40×/1.30 N.A. objective on a Nikon Eclipse Ti spinning disk confocal microscope. 3D images were reconstructed using Volocity (PerkinElmer). For each data set, a new microfluidic chip casted out of the same mold was used. The measurement error was estimated using (9.9 ± 0.12) μm green-yellow fluorescently labelled beads (10 μm Fluorospheres, Thermo Fisher).

Preparation of cells for microfluidic analysis

This study used wild type ES cells derived from 129/Sv strain mice, and cells of the same type but transfected with a Lifeact-tagRFP plasmid (ibidi). We received the ES cell as a kind gift from Jennifer Nichols's laboratory at the University of Cambridge. The cells were cultured at 37 °C and 7% CO_2 in medium based on Glasgow Eagle's Minimal Essential Medium (Merck), supplemented with 10% HyClone Fetal Bovine Serum (GE), L-glutamine (Invitrogen), MEM Non-Essential Amino Acids (PAA), sodium pyruvate (Invitrogen), ß-mercaptoethanol (Sigma) and LIF (Millipore).[19] For routine culture, cells were incubated at 37 °C in 7% CO_2 and split every 2 days. Splitting involved dissociation of cells from tissue culture plastic by incubation in Accutase for 5 min and subsequent dilution into PBS. Cells were then centrifuged for 3 min at 1400 rpm, resuspended in new medium and plated onto tissue culture flasks coated with 0.1% gelatin. Cells used in microfluidic experiments were first split into suspension and incubated with 2 μM SYTO 13 (Invitrogen) for 30 min, which stains the nucleus at an intensity 3 to 4 times higher than the cytoplasm, allowing us to detect both nuclear and cytoplasmic signals. The solution was then spun down and resuspended into medium at concentrations of 3 × 10^6 cells per ml. For Cytochalasin D treatment, this drug was added 10 min before the experiment at a concentration of 2 μM.[20] For Trichostatin A (TSA) treatment, cells were spun down and resuspended in medium containing 5 μM TSA (Sigma). They were then incubated for 5 h, after which SYTO 13 was added and the procedure above was followed.

Image analysis

We used the following protocol to investigate the cellular and nuclear response to external physical stress. We imaged cells incubated with SYTO 13 before, during and after the constriction. From the fluorescent images we then extracted the cellular and nuclear areas in Matlab using the *MaxEntropy* and *Intermodes* algorithms respectively, which were adapted from the ImageJ software suite.[21] These were chosen as somewhat conservative thresholding methods that yielded size results

similar to those deduced from high resolution microscopy measurements of ES cells and their nuclei in the media condition used in this study.[4] Increasing the sensitivity of thresholding, for example with the *Minimum* thresholding technique, made the thresholding sensitive to small intracellular features such as nucleoli. With major and minor axes of length a and t before compression respectively, and a' and t' during compression (Fig. 1), the axial strain is given by:

$$S_a = \frac{(a' - a)}{a},$$

while transverse strain is given by:

$$S_t = \frac{(t' - t)}{t}.$$

Statistical analysis

For the investigation into cell translocation time alteration due to Cytochalasin D treatment, statistical significance was calculated using an n-way ANOVA for the explanatory variables 'cell sample' & 'drug treatment'. Each cell sample was divided equally into a treated and untreated sample. In total 4 samples were used, to produce 4 treated and 4 control samples. ANOVA was also performed to analyze the statistical significance of the strain measurements and standard error of the mean where appropriate.

Results and discussion

The mechanics of ES cells has been shown to be influenced by their pluripotent state. During differentiation, mechanical changes occur both on a cellular[1,3] and a nuclear level.[4,14] In this paper we present a device that allows rapid mechanical phenotyping of cells and their nuclei. We characterize its capabilities by investigating the response of ES cells to compression in a variety of conditions and chemical treatments.

To optimize performance, the microfluidic device was designed with a focus on two major capabilities: compression throughput and run-time before clogging. As ES cells in serum+LIF medium conditions naturally adhere to substrates, cell aggregates will inevitably form after a certain time.[22] Furthermore, debris, apoptotic cells and aggregates can block the channels as these were designed specifically to apply a small compression to single cells. To alleviate this possibility, the device design first incorporates chip filters around the inlets to filter out objects larger than a single cell (Fig. 1A–C). Second, the inlet reservoir is split into large channels leading to isolated constriction regions. Hence, if adhering apoptotic cells cause a blockage, this occurs in a single constriction region, so the remaining channels continue to be fully operational.

We optimized the fabrication process and experimental protocol for users who might not be familiar with the technical aspects of microfluidics and might not want to set up high-end dedicated equipment. First, we choose to apply a one-dimensional compression to the ES cells using only the lateral walls but not the top and bottom ones. This allowed for the mold to be produced as a single height layer and to be fabricated in a single step without the use of dedicated photolithography equipment. Also, the one-dimensional approach avoids sharp corners and allows accurate control over the shape of the entrance to the constriction channel, enabling a streamlined approach and passage of cells through the channel without a shift in focal plane intrinsic to the two-dimensional designs. Second, we designed an algorithm to employ different thresholds to isolate the nuclear and cytoplasmic signal. The algorithm has been incorporated into a bespoke Matlab GUI to facilitate rapid semi-automated analysis of all images. As a large number of frames may be recorded during the course of a single experiment, the program first selects only those frames in which cells are detected (Fig. 1E–H). Then, for these frames the user draws a box around a cell, which is automatically thresholded to highlight the nucleus (or whole cell). This creates a boundary of the nucleus (cell), whose size is measured across the transverse and axial dimensions. Finally, the MATLAB program (Fig. 1I) calculates the strain of the nucleus (cell) in both dimensions. If more than one cell is present in a frame, the user has the option of drawing a box for each cell to obtain multiple measurements for a single frame. The GUI will be made available, complete with instructions for use, on http://www.stemcells.cam.ac.uk/researchers/principal-investigators/kevin-chalut.

We initially characterized our microfluidic chip by measuring the throughput of cells through the constriction channels as a function of flow rate from 10 to 80 μl h^{-1}. As expected, the relationship was linear at low flow rates, but the number of detected cells was largely constant for values above 40 μl h^{-1} (Fig. 2A). This is primarily due to the fact that at high flow rates cells translocate the channels very quickly and some of them might not be detected. Therefore, for a flow rate of 40 μl h^{-1}, the upper limit of the linear response of cell throughput, we varied the cell concentration from 1–5 million cells per ml (Fig. 2B). As expected, the throughput increased linearly with the concentration of cells in the medium. For the experiments below we used a concentration of 3.5 million cells per ml. The maximum flow rate was primarily limited by the frame rate of a typical microscope camera (between 30 and 100 fps). To estimate the accuracy of our size measurements, we flowed fluorescently labelled beads with a mean size of (9.9 ± 0.12) μm through the compression channels. By thresholding the images of the beads (n = 19) outside and inside the compression channels, we measured the diameter of the beads to be (9.98 ± 0.16) μm and (10.07 ± 0.19) μm respectively. This shows that the measurements obtained within this microfluidic device are accurate, and remain consistent while beads pass through the compression channels.

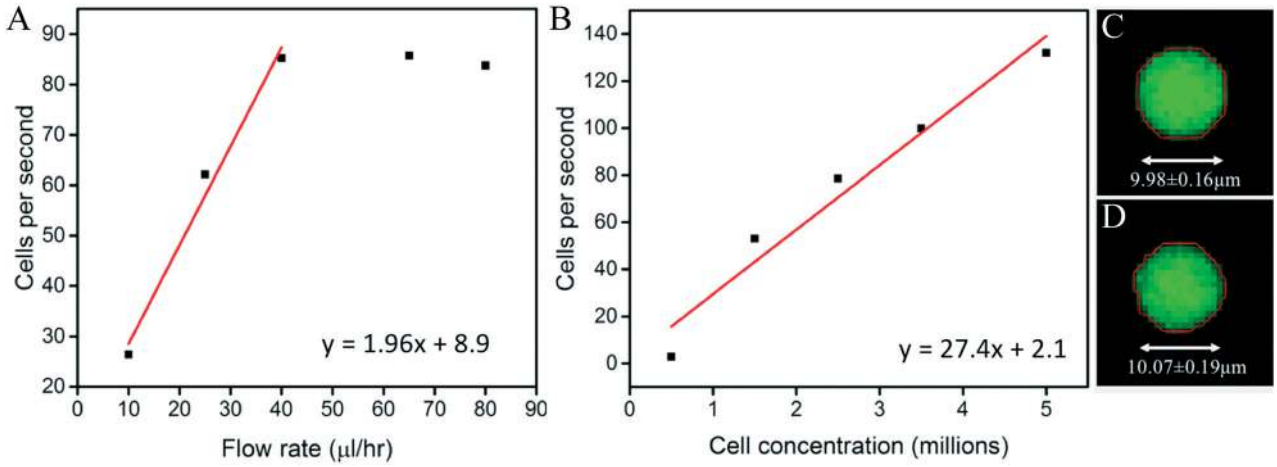

Fig. 2 Cell concentration, flow rate and accuracy of size measurements. Cell throughput, measured as number of cells per second, as a function of (A) the flow rate and (B) the initial cell concentration (ROI: 620 × 1100 μm, frame rate: 110 fps). A linear fit has been applied to both plots, however just the first three points of (A) have been utilized. (C & D) Thresholding of (9.9 ± 0.12) μm fluorescently labelled beads (red outline). The mean diameter was measured to be (C) (9.98 ± 0.16) μm outside and (D) (10.07 ± 0.19) μm inside the compression channel (n = 19), illustrating the consistency of our measurement technique.

To analyze both strain and recovery of the nuclear and cytoplasmic surface area, we imaged cells before, during and after compression. As expected, the major axis of both the nucleus and cytoplasm increased significantly during compression. However, we did not find evident correlation between axial strain and cell size, and no indication that larger cells (*i.e.* >16 μm, the channel height) have a different mechanical response than smaller cells (<16 μm). Importantly, we also found that cells, even those treated with TSA, a histone deacetylase inhibitor which decondenses chromatin, fully returned to their original values after compression (Fig. 3A & B). The fact that nuclei, even when treated with a chromatin decondensing agent, return to their original sizes, indicates that this technique probes the instantaneous mechanical response of the nucleus without permanently modifying the nuclear structure.

We examined whether the nuclei exhibited a delayed response to the compression as they translocate through the channel, which could be indicative of viscoelastic behavior. To test this, we imaged cells (n = 20) at multiple locations along the length of the channel. Each cell can be observed for multiple frames, or instances, across the channel. For each instance i of cell j we calculated a χ^2-value of the axial strain, defined as

$$\chi_{\mathrm{ij,ax}}^{\ 2} = \frac{\left(a_{\mathrm{ij,ax}} - \bar{a}_{\mathrm{j,ax}}\right)^2}{\bar{a}_{\mathrm{j,ax}}}$$

where $a_{\mathrm{ij,ax}}$ is the axial strain of the nucleus of cell j at the instance i, and $\bar{a}_{\mathrm{j,ax}}$ is the average axial strain of all the instances of cell j. Binning the instances according to their position in the first (n = 57), middle (n = 65) or final (n = 69) third of the channel, we found very small χ^2 values with no significant differences between channel positions, indicating that there is negligible influence of viscoelastic response on our measurements (Fig. 3C).

Next we treated ES cells with Cytochalasin D, which is an inhibitor of actin polymerization.[20] As cells are more easily deformed due to their lack of polymerized actin filaments, we expected a decrease in translocation time through the constriction channels after treatment with Cytochalasin D. Although there was a high variability between samples, we found that translocation time was indeed significantly shorter for samples treated with Cytochalasin D compared to control samples (Fig. 3D). These measurements confirmed that this microfluidic device is a high throughput method that can be used for mechanical phenotyping.

To analyze the differential effect of strain on cell nuclei, we set the channel width at 12 μm, larger than the median diameter of the nucleus (11.6 ± 0.2) μm yet smaller than the median cell size (14.3 ± 0.2) μm. Hence, nuclei larger than the approximate diameter of the channel experience compression directly from the sides of the channel. Nuclei smaller than the channel, however, experience this stress to an increasingly smaller extent (decreasing approximately as the inverse of the distance squared due to fluid stress). The cytoplasmic strain resulting from the compression in turn is propagated through the cytoskeleton to the nucleus (Fig. 4A) as an axial stress. Therefore, we expect the smallest nuclei to primarily experience uniaxial stress along the channel axis, while the largest nuclei would primarily experience uniaxial compression from the channels. Nuclei in the middle of the size distribution would experience a largely biaxial stress.

To distinguish the effects of compression on the cytoplasm and the nucleus while accounting for the size effect, we split the sample for analysis into two subpopulations of cells with large and small nuclei and calculated the strain (Fig. 4B & C). As expected, cells with nuclei larger than the median had a negative transverse cytoplasmic (−0.021 ±

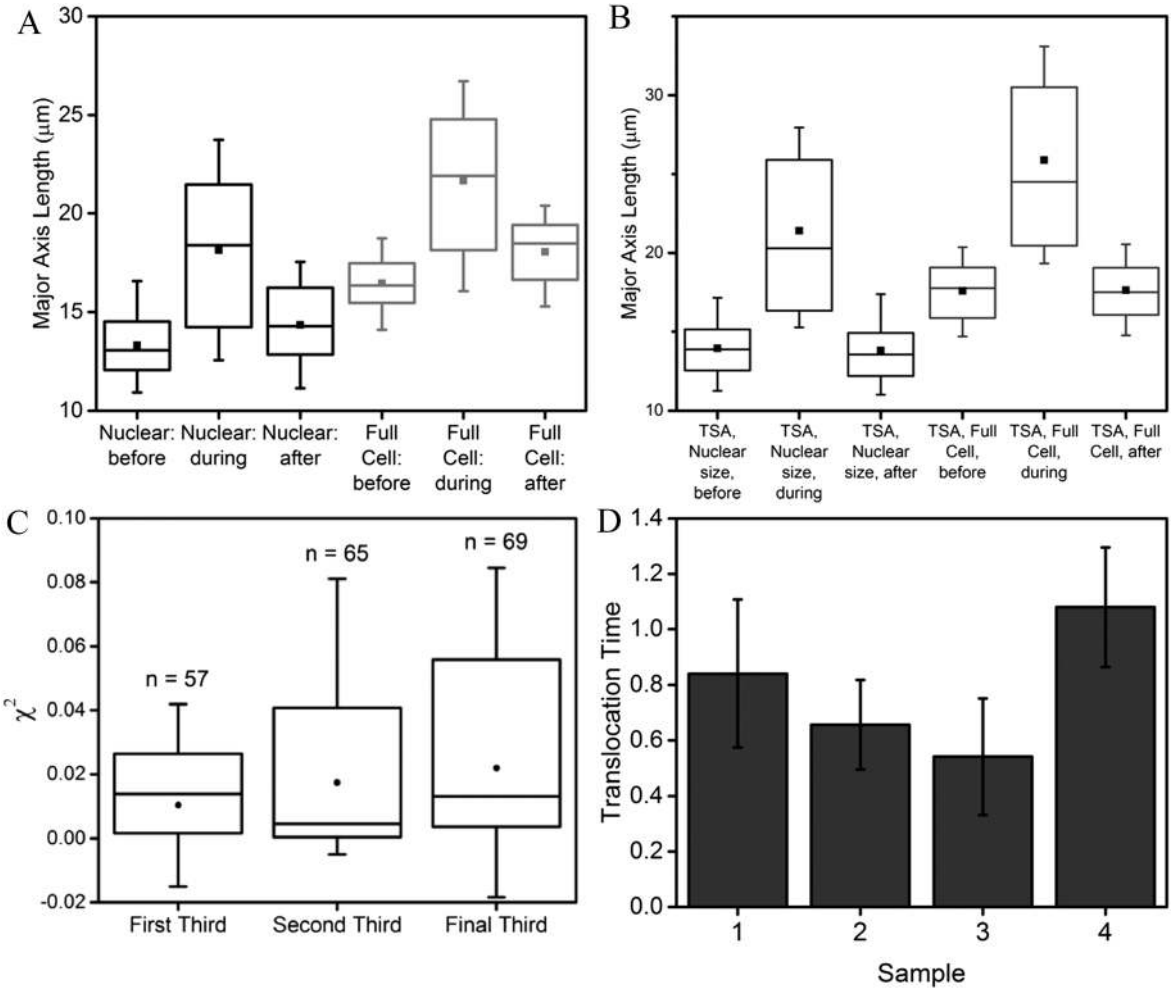

Fig. 3 Mechanical phenotyping of ES cells. Length of the nuclear and cellular major axis measured before, during and after compression for (A) control cells (n = 117) and (B) cells treated with TSA (n = 162). For both the whole cell and the nucleus, the major axial length returned to its approximate original size post-compression. (C) χ^2-value of the cells along the length of the channel. The distributions of χ^2-value of nuclei in the first, middle and final third of the channel are not significantly different. (D) The device was used to characterize cell mechanics by measuring changes in translocation time with cytoskeletal perturbation. Images were captured at 234 fps to record the translocation time, quantified by number of frames elapsed while the cell is in the channel. Cells treated with Cytochalasin D were compared to untreated control cells. Treatment with Cytochalasin D significantly decreased the translocation time ($P \ll 10^{-4}$, $n > 200$ cells for each dataset).

0.008) and nuclear (−0.06 ± 0.01) strain. Both the cytoplasm (0.24 ± 0.02) and the nucleus (0.26 ± 0.03) expanded in the axial direction during compression. However, the axial strain was significantly larger for cells with small nuclei ($P < 1 \times 10^{-4}$) which featured cellular and nuclear axial strain of (0.38 ± 0.04) and (0.46 ± 0.04) respectively. Interestingly, for those cells the transverse nuclear strain was positive yet very close to zero (0.02 ± 0.02), suggesting that some nuclei were auxetic in these conditions, as reported in (Pagliara 2014).[14]

To further explore this observation, we compared the relationship between axial and transverse strain (Fig. 4D). For small strains, the Poisson's ratio can be approximated by the negative of the transverse over axial strain. Thus, for axial strains smaller than 0.5, we approximated the Poisson's ratio by fitting the nuclear transverse strain *versus* nuclear axial strain data to a linear function. We aimed to analyse only cells that were experiencing primarily uniaxial stress (either tensile or compressive for small and large nuclei, respectively); therefore, we used only the smallest 25% and largest 25% of nuclei for the analysis. For cells with smaller nuclei, we found a line-fit gradient of 0.30 ± 0.09, compared to 0.15 ± 0.05 for cells with larger nuclei. Given the errors arising from the approximations made, these numbers are in relatively good agreement with one another. The finding indicates a negative Poisson's ratio in the nuclei of these cells, *i.e.* that these nuclei are exhibiting auxeticity. This can be compared with (Pagliara 2014), in which ES cells at the early stages of differentiation possess auxetic nuclei. In this paper, we are using serum+LIF conditions, which differ from (Pagliara 2014). Serum+LIF conditions should be much more heterogeneous, containing a combination of all three states described in (Pagliara 2014).[14] This method provides a way forward for approximations of Poisson's ratio in cell nuclei.

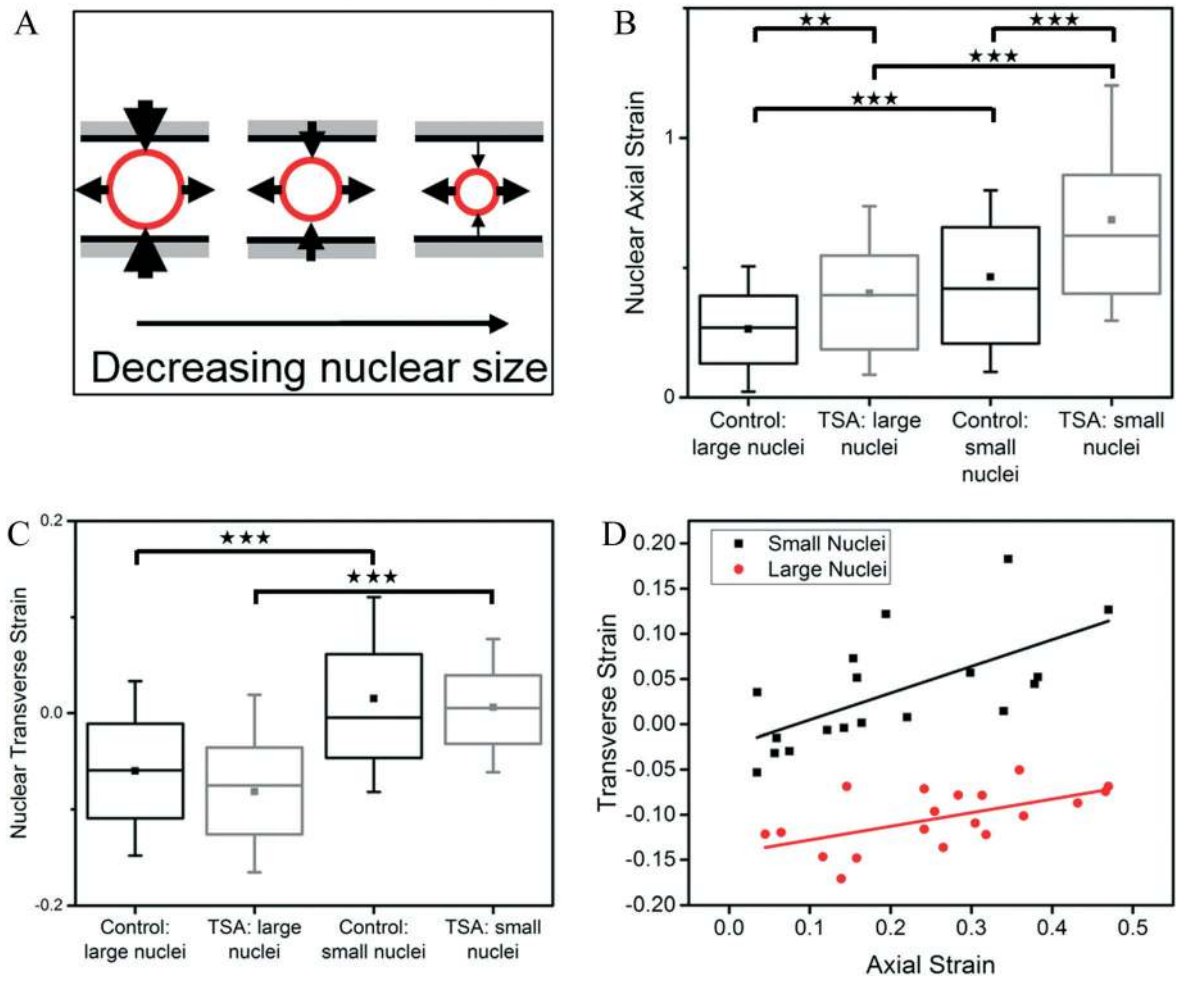

Fig. 4 Nuclear mechanics of ES cells. (A) Diagram of forces on the nucleus in response to confinement of cells in the channel. Large cells primarily experience compression forces from the walls of the channel in the transverse direction. As the nuclear size decreases, the compression forces decrease and become more comparable to the tensile forces arising from the elongation of the cell and resulting cytoskeletal stress. With smaller nuclei, the tensile cytoskeletal forces would dominate the compression forces. (B and C) Quantification of nuclear deformability in the (B) axial and (C) transverse direction for control and TSA-treated cells (n = 159 treated, n = 117 control). The nuclei of cells treated with TSA are more deformable, as evidenced by an increase in the magnitude of the axial strains, while the transverse strains are not significantly different. (D) Axial and transverse strain of control ES cell with the smallest nuclei (bottom 25% of size distribution) in black and largest nuclei (largest 25% of the size distribution), with the rationale that these nuclei would be primarily experiencing a uniaxial stress. In the case of uniaxial stress, there is a linear relationship between axial and transverse strain for small strains. Therefore, only axial strains smaller than 0.5 have been plotted. A line of best-fit have been plotted for both small nuclei and large nuclei. Each line has a positive linear relationship between transverse and axial strain (slope of 0.30 ± 0.09 for cells with small nuclei and 0.15 ± 0.05 for cells with large nuclei). The slope in the linear equation is the negative of the Poisson's ration; therefore, both subpopulations exhibit a negative Poisson's ratio.

We tested whether treatment of cells with TSA affected the relationship between compression and strain by modifying the material properties or average size of the nucleus. As chromatin is a primary structural component in the nucleus of ES cells, its decondensation could have a considerable effect on the nuclear response to compression.[2,3] Hence we examined whether the increase in nuclear deformability due to chromatin decondensation (as observed in both Chalut 2012, Krause 2013)[4,23] would increase the magnitude of the axial strain. The proposed device was ideal to investigate this question further. We first observed that TSA treatment had a modest enlarging effect on the median initial nuclear size (11.8 ± 0.2) μm. Second, the nuclear axial strain significantly increased ($P < 0.001$) across the whole population. This could potentially be explained by the larger average nuclear size leading to greater transverse strain. Nonetheless, for cells with nuclei smaller than the median, the mean transverse strain remained stable at 0.006 ± 0.006, while the axial strain increased significantly to 0.68 ± 0.04 ($P < 0.001$). This indicated that small nuclei become more deformable as evidenced by the increase in the axial strain, confirming previous observations but with much higher throughput.

The effect of cell confinement on cellular organization and structure has not yet been extensively studied. As the microfluidic chip presented here, with its single height throughout the chip, allows high-resolution microscopy without a shift in focal plane, we wanted to illustrate the opportunity to apply it to studies of the biological effects of external

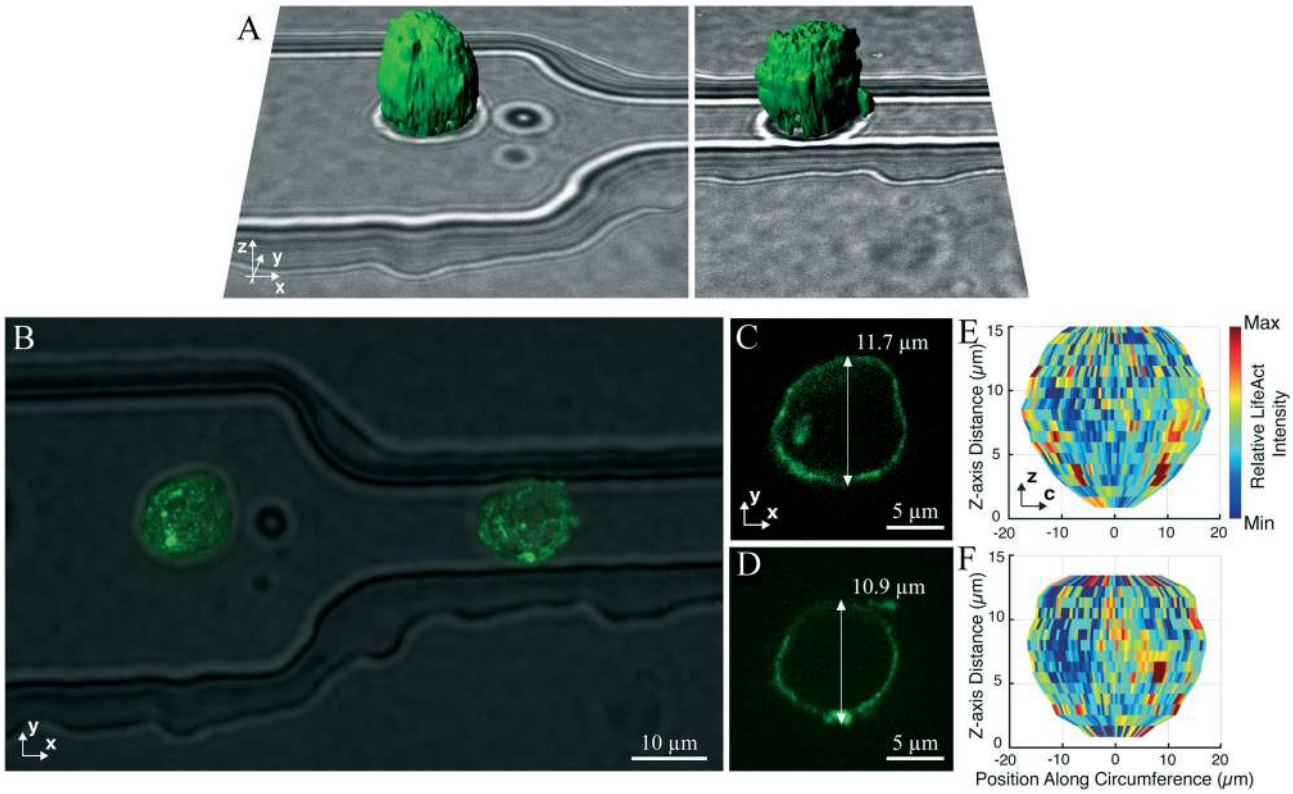

Fig. 5 3D reconstruction of ES cells in confinement. The microfluidic device can be used for confocal microscopy at high numerical aperture of cells containing biological markers to study the intracellular changes that take place in response to confinement. To demonstrate the image quality and level of positional control over the cells within the chip, as well as the possibilities for further analysis, we imaged cells that were transfected with the actin-marker Lifeact within the microfluidic device before and during compression. (A) Composite of two images showing three-dimensional reconstruction of the actin cytoskeleton (green) of a cell before (left) and inside (right) the channel overlaid on the corresponding bright-field images. (B) Maximum projection of the image from the actin network. A slice in the *xy*-plane through the middle of the cell (C) before and (D) inside the channel. (E and F) Two-dimensional projection of the Lifeact intensity in the cortex of the cell (E) before and (F) inside the channel, with the circumference of the cortex along the horizontal direction.

compression. To demonstrate the potential of the chip, we imaged the actin cortex of a cell line that was stably transfected with a Lifeact-tagRFP plasmid, an actin marker that binds preferentially to F-actin (Fig. 5). We imaged these cells outside and inside the channels using a spinning disk confocal microscope, and performed a three-dimensional reconstruction of the cellular actin cortex, which showed the presence of the actin cytoskeleton around the edge of the cell at high resolution. In addition, we converted these images to a two-dimensional heatmap of the intensity of the Lifeact signal along the cortex of the whole cell before and during compression, illustrating that the image quality and dimensions are sufficient for further analysis. Hence, the use of this technique, combining high resolution with high throughput microscopy, could be of great utility for future studies investigating structural intracellular changes with compression in single cells.

Conclusions

We have developed a high-throughput microfluidic chip for mechanically phenotyping ES cells. The PDMS chip can easily be produced and used for biological experiments, even by those unfamiliar with microfluidics. We designed a MATLAB GUI to allow swift and easy quantitative analysis of images obtained during experiments. Users can apply thresholding of the images *via* the GUI, visually assess the automatic detection of the boundary of the nucleus, and obtain size and strain measurements. We showed that the chip is capable of identifying differences in the cellular and nuclear deformability under compression within a sample of ES cells. We found that, in the investigated medium conditions, the nuclei of small cells exhibited a negative Poisson's ratio in response to compression. Furthermore, the device was able to detect changes to the mechanical phenotype of cells after treatment with chemical agents such as Cytochalasin D, which decreased the translocation time of the cells through the constrictions. In addition, nuclei of cells treated with TSA were found to have a greater axial strain, indicating greater nuclear deformability, to applied tensile stress than untreated cells. Finally, as a proof-of-principle of the further potential of the device, we showed that it can be used for high-resolution imaging. Thus the chip could in the future be used to investigate, using fluorescent markers, intracellular structural changes in response to compression.

The methodology presented here allows for the identification of mechanical phenotypes of cell compression, with either high throughput or high resolution. These capabilities are particularly relevant when considering the mechanical changes that take place in ES cells as they exit pluripotency and undergo lineage commitment. This feature is not limited to ES cells, however, and this device is well-suited to analyze the mechanical phenotype of other cell types, such as oncogenic cell types, which are heavily influenced by their mechanical environment. In addition, with the aim of promoting or inhibiting growth conditions for culture conditions or cancer treatment, the device can be used to characterize the influence of culture medium on the mechanical responsiveness to stress.

Acknowledgements

This work was supported by the Engineering and Physical Sciences Research Council (A. C. H. and C. M. V.), the Royal Society, Biotechnology and Biological Sciences Research Council, UK Medical Research Council and Wellcome Trust (K. J. C.), a European Research Council consolidator grant (U. F. K.), Leverhulme Early Career Fellowship (S. P.), the Wellcome Trust and the University of Cambridge (C. L. F.).

Notes and references

1 F. Chowdhury, S. Na, D. Li, Y.-C. Poh T. S. Tanaka, F. Wang and N. Wang, *Nat. Mater.*, 2010, **9**, 82–88.
2 M. J. Dalby, N. Gadegaard and R. O. C. Oreffo, *Nat. Mater.*, 2014, **13**, 558–569.
3 J. D. Pajerowski, K. N. Dahl, F. L. Zhong, P. J. Sammak and D. E. Discher, *Proc. Natl. Acad. Sci. U. S. A.*, 2007, **104**(40), 15619–15624.
4 K. J. Chalut, M. Höpfler, F. Lautenschläger, L. Boyde, C. J. Chan, A. Ekpenyong, A. Martine-Arias and J. Guck, *Biophys. J.*, 2012, **103**(10), 2060–2070.
5 V. Lecault, M. VanInsberghe, S. Sekulovic, D. J. H. F. Knapp, S. Wohrer, W. Bowden, F. Viel, T. McLaughlin, A. Jarandehei, M. Miller, D. Falconnet, A. K. White, D. G. Kent, M. R. Copley, F. Tahipour, C. J. Eaves, R. K. Humphries, J. M. Piret and C. L. Hansen, *Nat. Mater.*, 2011, **8**, 581–586.
6 G. Velve-Casquillas, M. Le Berre, M. Piel and P. T. Tran, *Nano Today*, 2010, **5**(1), 28–47.
7 E. K. Sackmann, A. L. Fulton and D. J. Beebe, *Nature*, 2014, **507**, 181–189.
8 W. J. Polacheck, R. Li, S. G. M. Uzel and R. D. Kamm, *Lab Chip*, 2013, **13**, 2252–2267.
9 D. R. Gossett, W. M. Weaver, A. J. Mach, S. C. Hur, H. T. Kwong Tse, W. Lee, H. Amini and D. Di Carlo, *Anal. Bioanal. Chem.*, 2010, **397**(8), 3249–3267.
10 K. Chung, M. M. Crane and H. Lu, *Nat. Methods*, 2008, **5**, 637–643.
11 O. Otto, P. Rosendahl, A. Mietke, S. Golfier, C. Herold, D. Klaue, S. Girardo, S. Pagliara, A. Ekpenyong, A. Jacobi, M. Wobus, N. Töpfner, U. F. Keyser, J. Mansfeld, E. Fischer-Friedrich and J. Guck, *Nat. Methods*, 2015, **12**, 199–202.
12 P. J. Hung, P. J. Lee, P. Sabounchi, R. Lin and L. P. Lee, *Biotechnol. Bioeng.*, 2005, **89**(1), 1–8.
13 Y. Zheng, J. Nguyen, Y. Weig and Y. Sun, *Lab Chip*, 2013, **13**, 2464–2483.
14 S. Pagliara, K. Franze, C. R. McClain, G. W. Wylde, C. L. Fisher, R. J. Franklin, A. J. Kabla, U. F. Keyser and K. J. Chalut, *Nat. Mater.*, 2014, **13**(6), 638–644.
15 M. A. van Zandvoort, C. J. de Grauw, H. C. Gerritsen, J. L. Broers, M. G. Oude Egbrink, F. C. Ramaekers and D. W. Slaaf, *Cytometry*, 2002, **47**(4), 226–235.
16 S. Talwar, N. Jain and G. V. Shivashankar, *Biomaterials*, 2014, **35**(8), 2411–2419.
17 K. N. Dahl, P. Scaffidi, M. F. Islan, A. G. Yodh, K. L. Wilson and T. Misteli, *Proc. Natl. Acad. Sci. U. S. A.*, 2006, **103**(27), 10271–10276.
18 M. Zwerger, C. Y. Hoo and J. Lammerding, *Annu. Rev. Biomed. Eng.*, 2011, **13**, 397–428.
19 T. Wakayama, I. Rodriguez, A. C. F. Perry, R. Yanagimachi and P. Mombaerts, *Proc. Natl. Acad. Sci. U. S. A.*, 1999, **96**(26), 14984–14989.
20 J. F. Casella, M. D. Flanagan and S. Lin, *Nature*, 1981, **293**, 302–305.
21 W. S. Rasband, *ImageJ*, US National Institute of Health, http://imagej.nih.gov/ij/, 1997–2015.
22 P. Cartwright, C. McLean, A. Sheppard, D. Rivett, K. Jones and S. Dalton, *Development*, 2005, **132**(5), 885–896.
23 M. Krause, J. Te Riet and K. Wolf, *Phys. Biol.*, 2013, **10**(6), 065002.

Bibliography

Akiyama, S. K. and Yamada, K. M. (1985). Synthetic peptides competitively inhibit both direct binding to fibroblasts and functional biological assays for the purified cell-binding domain of fibronectin. *The Journal of biological chemistry*, 260(19):10402–5.

Alberts, B., Johnson, A., Lewis, J., Raff, M., Roberts, K., and Walter, P. (2002). *Molecular Biology of the Cell*. Routledge.

Alderson, A. and Alderson, K. L. (2007). Auxetic materials. *Proceedings of the Institution of Mechanical Engineers, Part G: Journal of Aerospace Engineering*, 221(4):565–575.

Alway, S. E. (1997). Overload-induced C-Myc oncoprotein is reduced in aged skeletal muscle. *The journals of gerontology. Series A, Biological sciences and medical sciences*, 52(4):B203–11.

Ameyar, M., Wisniewska, M., and Weitzman, J. B. (2003). A role for AP-1 in apoptosis: The case for and against. *Biochimie*, 85(8):747–752.

Anders, S. and Huber, W. (2010). Differential expression analysis for sequence count data. *Genome Biology*, 11(10).

Anders, S., Reyes, A., and Huber, W. (2012). Detecting differential usage of exons from RNA-seq data. *Genome Research*, 22(10):2008–2017.

Angenendt, P., Glökler, J., Murphy, D., Lehrach, H., and Cahill, D. J. (2002). Toward optimized antibody microarrays: a comparison of current microarray support materials. *Analytical Biochemistry*, 309(2):253–260.

Aoki, K., Kumagai, Y., Sakurai, A., Komatsu, N., Fujita, Y., Shionyu, C., and Matsuda, M. (2013). Stochastic ERK activation induced by noise and cell-to-cell propagation regulates cell density-dependent proliferation. *Molecular Cell*, 52(4):529–540.

Apáti, Á., Pászty, K., Erdei, Z., Szebényi, K., Homolya, L., and Sarkadi, B. (2012). Calcium signaling in pluripotent stem cells. *Molecular and Cellular Endocrinology*, 353(1-2):57–67.

Babu, G. J., Lalli, J. M., Sussman, M. A., ichi Sadoshima, J., and Periasamy, M. (2000). Phosphorylation of Elk-1 by MEK/ERK pathway is necessary for c-fos gene activation during cardiac myocyte hypertrophy. *Journal of Molecular and Cellular Cardiology*, 32(8):1447–1457.

Bahrami, S. and Drabløs, F. (2016). Gene regulation in the immediate-early response process. *Advances in Biological Regulation*, 62:37–49.

Bain, J., Plater, L., Elliott, M., Shpiro, N., Hastie, C. J., McLauchlan, H., Klevernic, I., Arthur, J. S. C., Alessi, D. R., and Cohen, P. (2007). The selectivity of protein kinase inhibitors: a further update. *The Biochemical journal*, 408(3):297–315.

Ball, R. C. and Blumenfeld, R. (2002). Stress Field in Granular Systems: Loop Forces and Potential Formulation. *Physical Review Letters*, 88(11):115505.

Ball, R. C. and Blumenfeld, R. (2003). From plasticity to a renormalization group. *Philosophical Transactions of the Royal Society of London A: Mathematical, Physical and Engineering Sciences*, 361(1805).

Ball, R. C. and Grinev, D. V. (2001). The Stress Transmission Universality Classes of Periodic Granular Arrays. *Physica A: Statistical Mechanics and its Applications*, 292(1-4):167–174.

Baram, R. M., Herrmann, H. J., and Rivier, N. (2004). Space-Filling Bearings in Three Dimensions. *Physical Review Letters*, 92(4):4.

Bartalena, G., Loosli, Y., Zambelli, T., and Snedeker, J. G. (2012). Biomaterial surface modifications can dominate cell–substrate mechanics: the impact of PDMS plasma treatment on a quantitative assay of cell stiffness. *Soft Matter*, 8(3):673–681.

Bass, M. D., Morgan, M. R., Roach, K. A., Settleman, J., Goryachev, A. B., and Humphries, M. J. (2008). p190RhoGAP is the convergence point of adhesion signals from $\alpha 5 \beta 1$ integrin and syndecan-4. *Journal of Cell Biology*, 181(6):1013–1026.

Benjamini, Y. and Hochberg, Y. (1995). Controlling the false discovery rate: a practical and powerful approach to multiple testing.

Bershadsky, A. D., Balaban, N. Q., and Geiger, B. (2003). Adhesion-Dependent Cell Mechanosensitivity. *Annual Review of Cell and Developmental Biology*, 19(1):677–695.

Bhattacharya, M. R. C., Bautista, D. M., Wu, K., Haeberle, H., Lumpkin, E. A., and Julius, D. (2008). Radial stretch reveals distinct populations of mechanosensitive mammalian somatosensory neurons. *Proc. Natl. Acad. Sci.*, 105(50):20015–20020.

Blumenfeld, R. (2004). Stresses in isostatic granular systems and emergence of force chains. *Physical Review Letters*, 93(10).

Blumenfeld, R. (2005). Auxetic strains—insight from iso-auxetic materials. *Molecular Simulation*, 31(13):867–871.

Blumenfeld, R. (2007). Stresses in two-dimensional isostatic granular systems: exact solutions. *New Journal of Physics*, 9(6):160–160.

Blumenfeld, R. and Edwards, S. F. (2003). Granular entropy: Explicit calculations for planar assemblies. *Physical Review Letters*, 90(11):114303.

Blumenfeld, R. and Edwards, S. F. (2006). Geometric partition functions of cellular systems: Explicit calculation of the entropy in two and three dimensions. *The European Physical Journal E*, 19(1):23–30.

Blumenfeld, R. and Edwards, S. F. (2009). On granular stress statistics: Compactivity, angoricity, and some open issues. *Journal of Physical Chemistry B*, 113(12):3981–3987.

Blumenfeld, R. and Edwards, S. F. (2012). Theory of Strains in Auxetic Materials. *Journal of Superconductivity and Novel Magnetism*, 25(3):565–571.

Blumenfeld, R., Edwards, S. F., and Schwartz, M. (2010). Da Vinci fluids, catch-up dynamics and dense granular flow. *European Physical Journal E*, 32(4):333–338.

Boettiger, D. (2007). Quantitative Measurements of Integrin-Mediated Adhesion to Extracellular Matrix. *Methods in Enzymology*, 426:1–25.

Boroviak, T., Loos, R., Bertone, P., Smith, A., and Nichols, J. (2014). The ability of inner-cell-mass cells to self-renew as embryonic stem cells is acquired following epiblast specification. *Nature cell biology*, 16(6):516–28.

Bouchaud, J.-P., Claudin, P., Levine, D., and Otto, M. (2001). Force chain splitting in granular materials: A mechanism for large-scale pseudo-elastic behaviour. *The European Physical Journal E*, 4(4):451–457.

Brown, X. Q., Ookawa, K., and Wong, J. Y. (2005). Evaluation of polydimethylsiloxane scaffolds with physiologically-relevant elastic moduli: Interplay of substrate mechanics and surface chemistry effects on vascular smooth muscle cell response. *Biomaterials*, 26(16):3123–3129.

Burridge, K. and Chrzanowska-Wodnicka, M. (1996). Focal adhesions, contractility, and signaling. *Annual Review of Cell and Developmental Biology*, 12(1):463–519.

Buxboim, A., Swift, J., Irianto, J., Spinler, K., Dingal, P., Athirasala, A., Kao, Y.-R., Cho, S., Harada, T., Shin, J.-W., and Discher, D. (2014). Matrix Elasticity Regulates Lamin-A,C Phosphorylation and Turnover with Feedback to Actomyosin. *Current Biology*, 24(16):1909–1917.

Caille, N., Thoumine, O., Tardy, Y., and Meister, J.-J. (2002). Contribution of the nucleus to the mechanical properties of endothelial cells. *Journal of Biomechanics*, 35(2):177–187.

Camisasca, G. (2013). *Loop Forces & Mechanical Equilibrium of 2D Granular Structures*. Master's thesis, University of Cambridge.

Carpi, N. and Piel, M. (2014). Stretching Micropatterned Cells on a PDMS Membrane. *Journal of Visualized Experiments*, 1(83):e51193.

Carson, J. A., Yan, Z., Booth, F. W., Coleman, M. E., Schwartz, R. J., and Stump, C. S. (1995). Regulation of skeletal alpha-actin promoter in young chickens during hypertrophy caused by stretch overload. *The American journal of physiology*, 268(4 Pt 1):C918–24.

Cavigelli, M., Dolfi, F., Claret, F. X., and Karin, M. (1995). Induction of c-fos expression through JNK-mediated TCF/Elk-1 phosphorylation. *The EMBO journal*, 14(23):5957–64.

Chambers, I., Colby, D., Robertson, M., Nichols, J., Lee, S., Tweedie, S., and Smith, A. (2003). Functional expression cloning of Nanog, a pluripotency sustaining factor in embryonic stem cells. *Cell*, 113(5):643–655.

Chambers, I. and Smith, A. (2004). Self-renewal of teratocarcinoma and embryonic stem cells [review]. *Oncogene*, 23(43):7150–60.

Chappell, J., Sun, Y., Singh, A., and Dalton, S. (2013). MYC/MAX control ERK signaling and pluripotency by regulation of dual-specificity phosphatases 2 and 7. *Genes & development*, 27(7):725–33.

Chen, C. S., Tan, J., and Tien, J. (2004). Mechanotransduction at Cell-Matrix and Cell-Cell Contacts. *Annual Review of Biomedical Engineering*, 6(1):275–302.

Cherepkova, M. Y., Sineva, G. S., and Pospelov, V. A. (2016). Leukemia inhibitory factor (LIF) withdrawal activates mTOR signaling pathway in mouse embryonic stem cells through the MEK/ERK/TSC2 pathway. *Cell Death and Disease*, 7(1):e2050.

Choquet, D., Felsenfeld, D. P., and Sheetz, M. P. (1997). Extracellular matrix rigidity causes strengthening of integrin- cytoskeleton linkages. *Cell*, 88(1):39–48.

Chowdhury, F., Li, Y., Poh, Y. C., Yokohama-Tamaki, T., Wang, N., and Tanaka, T. S. (2010a). Soft substrates promote homogeneous self-renewal of embryonic stem cells via downregulating cell-matrix tractions. *PLoS ONE*, 5(12):e15655.

Chowdhury, F., Na, S., Li, D., Poh, Y. C., Tanaka, T. S., Wang, F., and Wang, N. (2010b). Material properties of the cell dictate stress-induced spreading and differentiation in embryonic stemcells. *Nature Materials*, 9(1):82–88.

Chrzanowska-Wodnicka, M. and Burridge, K. (1996). Rho-stimulated contractility drives the formation of stress fibers and focal adhesions. *Journal of Cell Biology*, 133(6):1403–1415.

Clark, K., Langeslag, M., Figdor, C. G., and van Leeuwen, F. N. (2007). Myosin II and mechanotransduction: a balancing act. *Trends in Cell Biology*, 17(4):178–186.

Constantinescu, D., Gray, H. L., Sammak, P. J., Schatten, G. P., and Csoka, A. B. (2006). Lamin A/C Expression Is a Marker of Mouse and Human Embryonic Stem Cell Differentiation. *Stem Cells*, 24(1):177–185.

Conti, M. A., Even-Ram, S., Liu, C., Yamada, K. M., and Adelstein, R. S. (2004). Defects in cell adhesion and the visceral endoderm following ablation of nonmuscle myosin heavy chain II-A in mice. *Journal of Biological Chemistry*, 279(40):41263–41266.

Cox, T. R. and Erler, J. T. (2011). Remodeling and homeostasis of the extracellular matrix: implications for fibrotic diseases and cancer. *Disease Models & Mechanisms*, 4(2):165–178.

Coxeter, H. S. M. (1973). *Regular Polytopes*. Dover Publications, New York, 3rd editio edition.

Crisp, M., Liu, Q., Roux, K., Rattner, J. B., Shanahan, C., Burke, B., Stahl, P. D., and Hodzic, D. (2006). Coupling of the nucleus and cytoplasm: role of the LINC complex. *The Journal of cell biology*, 172(1):41–53.

Critchley, D. R. (2000). Focal adhesions - The cytoskeletal connection. *Current Opinion in Cell Biology*, 12(1):133–139.

Cunningham, J. J., Nikolovski, J., Linderman, J. J., and Mooney, D. J. (2002). Quantification of fibronectin adsorption to silicone-rubber cell culture substrates. *BioTechniques*, 32(4):876–887.

Dahl, K. N., Ribeiro, A. J. S., and Lammerding, J. (2008). Nuclear shape, mechanics, and mechanotransduction. *Circulation research*, 102(11):1307–18.

Dalton, S. L., Marcantonio, E. E., and Assoian, R. K. (1992). Cell attachment controls fibronectin and $\alpha 5\beta 1$ integrin levels in fibroblasts. Implications for anchorage-dependent and -independent growth. *Journal of Biological Chemistry*, 267(12):8186–8191.

Danen, E. H. J., Sonneveld, P., Brakebusch, C., Fässler, R., and Sonnenberg, A. (2002). The fibronectin-binding integrins $\alpha 5\beta 1$ and $\alpha v\beta 3$ differentially modulate RhoA-GTP loading, organization of cell matrix adhesions, and fibronectin fibrillogenesis. *Journal of Cell Biology*, 159(6):1071–1086.

D'Angelo, F., Tiribuzi, R., Armentano, I., Kenny, J. M., Martino, S., and Orlacchio, A. (2011). Mechanotransduction: Tuning Stem Cells Fate. *Journal of Functional Biomaterials*, 2(4):67–87.

Dawes, N. J., Cox, V. M., Park, K. S., Nga, H., and Goldspink, D. F. (1996). The induction of c-fos and c-jun in the stretched latissimus dorsi muscle of the rabbit: responses to duration, degree and re-application of the stretch stimulus. *Experimental physiology*, 81(3):329–39.

De, R., Zemel, A., and Safran, S. A. (2007). Dynamics of cell orientation. *Nature Physics*, 3(9):655–659.

Discher, D. E., Janmey, P., and Wang, Y. L. (2005). Tissue cells feel and respond to the stiffness of their substrate. *Science*, 310(5751):1139–1143.

Dogru, S., Aksoy, B., Bayraktar, H., and Alaca, B. E. (2018). Poisson's ratio of PDMS thin films. *Polymer Testing*, 69:375–384.

Dolmetsch, R. E., Pajvani, U., Fife, K., Spotts, J. M., and Greenberg, M. E. (2001). Signaling to the nucleus by an L-type calcium channel- calmodulin complex through the MAP kinase pathway. *Science*, 294(5541):333–339.

Dovas, A., Yoneda, A., and Couchman, J. R. (2006). PKCbeta-dependent activation of RhoA by syndecan-4 during focal adhesion formation. *Journal of cell science*, 119(Pt 13):2837–46.

Dumbauld, D. W., Shin, H., Gallant, N. D., Michael, K. E., Radhakrishna, H., and García, A. J. (2010). Contractility modulates cell adhesion strengthening through focal adhesion kinase and assembly of vinculin-containing focal adhesions. *Journal of Cellular Physiology*, 223(3):746–756.

Dunn, S.-J., Martello, G., Yordanov, B., Emmott, S., and Smith, A. G. (2014). Defining an essential transcription factor program for naive pluripotency. *Science*, 344(6188):1156–1160.

Durbeej, M. (2010). Laminins. *Cell and Tissue Research*, 339(1):259–268.

Eckert, R. L., Adhikary, G., Young, C. A., Jans, R., Crish, J. F., Xu, W., and Rorke, E. A. (2013). AP1 transcription factors in epidermal differentiation and skin cancer. *Journal of skin cancer*, 2013:537028.

Eden, E., Lipson, D., Yogev, S., and Yakhini, Z. (2007). Discovering Motifs in Ranked Lists of DNA Sequences. *PLoS Computational Biology*, 3(3):e39.

Eden, E., Navon, R., Steinfeld, I., Lipson, D., and Yakhini, Z. (2009). GOrilla: A tool for discovery and visualization of enriched GO terms in ranked gene lists. *BMC Bioinformatics*, 10.

Edwards, S. F. and Grinev, D. V. (2001). Transmission of stress in granular materials as a problem of statistical mechanics. *Physica A: Statistical Mechanics and its Applications*, 302(1-4):162–186.

Engler, A. J., Sen, S., Sweeney, H. L., and Discher, D. E. (2006). Matrix Elasticity Directs Stem Cell Lineage Specification. *Cell*, 126(4):677–689.

Evans, M. J. and Kaufman, M. H. (1981). Establishment in culture of pluripotential cells from mouse embryos. *Nature*, 292(5819):154–156.

Farrukh, A., Paez, J. I., Salierno, M., and DelCampo, A. (2016). Bioconjugating thiols to poly(acrylamide) gels for cell culture using methylsulfonyl co-monomers. *Angewandte Chemie - International Edition*, 55(6):2092–2096.

Feng, C., Yang, M., Zhang, Y., Lan, M., Huang, B., Liu, H., and Zhou, Y. (2018). Cyclic mechanical tension reinforces DNA damage and activates the p53-p21-Rb pathway to induce premature senescence of nucleus pulposus cells. *International Journal of Molecular Medicine*.

Fincan, M. (2015). *Assessing Viscoelastic Properties of Polydimethylsiloxane (PDMS) Using Loading and Unloading of the Macroscopic Compression Test*. PhD thesis, University of South Florida.

Fink, J., Carpi, N., Betz, T., Bétard, A., Chebah, M., Azioune, A., Bornens, M., Sykes, C., Fetler, L., Cuvelier, D., and Piel, M. (2011). External forces control mitotic spindle positioning. *Nature cell biology*, 13(7):771–8.

Fritz, J. L. and Owen, M. J. (1995). Hydrophobic Recovery of Plasma-Treated Polydimethylsiloxane. *The Journal of Adhesion*, 54(1-4):33–45.

Fuhrmann, A. and Engler, A. J. (2015). The Cytoskeleton Regulates Cell Attachment Strength. *Biophysical Journal*, 109(1):57–65.

Gallant, N. D. (2005). Cell Adhesion Strengthening: Contributions of Adhesive Area, Integrin Binding, and Focal Adhesion Assembly. *Molecular Biology of the Cell*, 16(9):4329–4340.

Gaut, L., Robert, N., Delalande, A., Bonnin, M. A., Pichon, C., and Duprez, D. (2016). EGR1 regulates transcription downstream of mechanical signals during tendon formation and healing. *PLoS ONE*, 11(11):e0166237.

Gerritsen, M., Kreiss, G., and Blumenfeld, R. (2008). Stress Chain Solutions in Two-Dimensional Isostatic Granular Systems: Fabric-Dependent Paths, Leakage, and Branching. *Physical Review Letters*, 101(9):098001.

Gilbert, P. M., Havenstrite, K. L., Magnusson, K. E. G., Sacco, A., Leonardi, N. A., Kraft, P., Nguyen, N. K., Thrun, S., Lutolf, M. P., and Blau, H. M. (2010). Substrate Elasticity Regulates Skeletal Muscle Stem Cell Self-Renewal in Culture. *Science*, 329(5995):1078–1081.

Gille, H., Strahl, T., and Shaw, P. E. (1995). Activation of ternary complex factor Elk-1 by stress-activated protein kinases. *Current Biology*, 5(10):1191–1200.

Gittes, F., Mickey, B., Nettleton, J., and Howard, J. (1993). Flexural rigidity of microtubules and actin filaments measured from thermal fluctuations in shape. *Journal of Cell Biology*, 120(4):923–934.

Glogauer, M., Arora, P., Yao, G., Sokholov, I., Ferrier, J., and McCulloch, C. A. (1997). Calcium ions and tyrosine phosphorylation interact coordinately with actin to regulate cytoprotective responses to stretching. *Journal of cell science*, 110(1):11–21.

Goldyn, A. M., Rioja, B. A., Spatz, J. P., Ballestrem, C., and Kemkemer, R. (2009). Force-induced cell polarisation is linked to RhoA-driven microtubule-independent focal-adhesion sliding. *Journal of Cell Science*, 122(20):3644–3651.

Gorfien, S. F., Winston, F. K., Thibault, L. E., and Macarak, E. J. (1989). Effects of biaxial deformation on pulmonary artery endothelial cells. *Journal of Cellular Physiology*, 139(3):492–500.

Granata, A., Serrano, F., Bernard, W. G., McNamara, M., Low, L., Sastry, P., and Sinha, S. (2017). An iPSC-derived vascular model of Marfan syndrome identifies key mediators of smooth muscle cell death. *Nature Genetics*, 49(1):97–109.

Grashoff, C., Hoffman, B. D., Brenner, M. D., Zhou, R., Parsons, M., Yang, M. T., McLean, M. A., Sligar, S. G., Chen, C. S., Ha, T., and Schwartz, M. A. (2010). Measuring mechanical tension across vinculin reveals regulation of focal adhesion dynamics. *Nature*, 466(7303):263–266.

Gregg, J. and Fraizer, G. (2011). Transcriptional Regulation of EGR1 by EGF and the ERK Signaling Pathway in Prostate Cancer Cells. *Genes & Cancer*, 2(9):900–909.

Grima, J. N., Alderson, A., and Evans, K. E. (2005). Auxetic behaviour from rotating rigid units. *physica status solidi (b)*, 242(3):561–575.

Grima, J. N., Attard, D., Gaff, R., and Cassar, R. N. (2009). A novel process for the manufacture of auxetic foams and for their re-conversion to conventional form. *Advanced Engineering Materials*, 11(7):533–535.

Grima, J. N. and Evans, K. E. (2006). Auxetic behavior from rotating triangles. *Journal of Materials Science*, 41(10):3193–3196.

Gruenbaum, Y., Margalit, A., Goldman, R. D., Shumaker, D. K., and Wilson, K. L. (2005). The nuclear lamina comes of age. *Nat Rev Mol Cell Biol*, 6(1):21–31.

Guilak, F., Cohen, D. M., Estes, B. T., Gimble, J. M., Liedtke, W., and Chen, C. S. (2009). Control of Stem Cell Fate by Physical Interactions with the Extracellular Matrix. *Cell Stem Cell*, 5(1):17–26.

Guilluy, C., Osborne, L. D., Van Landeghem, L., Sharek, L., Superfine, R., Garcia-Mata, R., and Burridge, K. (2014). Isolated nuclei adapt to force and reveal a mechanotransduction pathway in the nucleus. *Nature Cell Biology*, 16(4):376–381.

Guzowski, J. F., Setlow, B., Wagner, E. K., and McGaugh, J. L. (2001). Experience-Dependent Gene Expression in the Rat Hippocampus after Spatial Learning: A Comparison of the Immediate-Early GenesArc, c-fos, and zif268. *The Journal of Neuroscience*, 21(14):5089–5098.

Harter, L. V., Hruska, K. A., and Duncan, R. L. (1995). Human osteoblast-like cells respond to mechanical strain with increased bone matrix protein production independent of hormonal regulation. *Endocrinology*, 136(2):528–535.

Hartman, C. D., Isenberg, B. C., Chua, S. G., and Wong, J. Y. (2016). Vascular smooth muscle cell durotaxis depends on extracellular matrix composition. *Proc. Natl. Acad. Sci.*, 113(40):11190–11195.

Haston, W. S., Shields, J. M., and Wilkinson, P. C. (1983). The orientation of fibroblasts and neutrophils on elastic substrata. *Experimental Cell Research*, 146(1):117–126.

Henry, M. D. and Campbell, K. P. (1998). A role for dystroglycan in basement membrane assembly. *Cell*, 95(6):859–870.

Herdegen, T., Skene, P., and Bahr, M. (1997). The c-Jun transcription factor–bipotential mediator of neuronal death, survival and regeneration. *Trends Neurosci*, 20(5):227–231.

Hillborg, H., Ankner, J., Gedde, U., Smith, G., Yasuda, H., and Wikström, K. (2000). Crosslinked polydimethylsiloxane exposed to oxygen plasma studied by neutron reflectometry and other surface specific techniques. *Polymer*, 41(18):6851–6863.

Hirata, H., Tatsumi, H., Lim, C. T., and Sokabe, M. (2014). Force-dependent vinculin binding to talin in live cells: a crucial step in anchoring the actin cytoskeleton to focal adhesions. *AJP: Cell Physiology*, 306(6):C607–C620.

Hodgson, A., Verstreken, C., Fisher, C., Keyser, U., Pagliara, S., and Chalut, K. (2017). A microfluidic device for characterizing nuclear deformations. *Lab on a Chip - Miniaturisation for Chemistry and Biology*, 17(5).

Hoffman, L. M., Jensen, C. C., Chaturvedi, A., Yoshigi, M., and Beckerle, M. C. (2012). Stretch-induced actin remodeling requires targeting of zyxin to stress fibers and recruitment of actin regulators. *Molecular Biology of the Cell*, 23(10):1846–1859.

Honda, H., Motosugi, N., Nagai, T., Tanemura, M., and Hiiragi, T. (2008). Computer simulation of emerging asymmetry in the mouse blastocyst. *Development*, 135(8):1407–1414.

Howard, J. (2001). *Mechanics of Motor Proteins and the Cytoskeleton*. Oxford University Press.

Hsieh, C. F., Chang, B. J., Pai, C. H., Chen, H. Y., Tsaia, J. W., Yi, Y. H., Chiang, Y. T., Wang, D. W., Chi, S., Hsu, L., and Lin, C. H. (2006). Stepped changes of monovalent ligand-binding force during ligand-induced clustering of integrin αIIBβ3. *Journal of Biological Chemistry*, 281(35):25466–25474.

Hsu, H. J., Lee, C. F., Locke, A., Vanderzyl, S. Q., and Kaunas, R. (2010). Stretch-induced stress fiber remodeling and the activations of JNK and ERK depend on mechanical strain rate, but not FAK. *PLoS ONE*, 5(8):e12470.

Huebsch, N., Arany, P. R., Mao, A. S., Shvartsman, D., Ali, O. A., Bencherif, S. A., Rivera-Feliciano, J., and Mooney, D. J. (2010). Harnessing traction-mediated manipulation of the cell/matrix interface to control stem-cell fate. *Nature Materials*, 9(6):518–526.

Humphries, J. D., Wang, P., Streuli, C., Geiger, B., Humphries, M. J., and Ballestrem, C. (2007). Vinculin controls focal adhesion formation by direct interactions with talin and actin. *Journal of Cell Biology*, 179(5):1043–1057.

Humphries, M. J. (1996). Integrin activation: The link between ligand binding and signal transduction. *Current Opinion in Cell Biology*, 8(5):632–640.

Hunt, G. C., Singh, P., and Schwarzbauer, J. E. (2012). Endogenous production of fibronectin is required for self-renewal of cultured mouse embryonic stem cells. *Experimental cell research*, 318(15):1820–31.

Hurley, N. E., Schildmeyer, L. A., Bosworth, K. A., Sakurai, Y., Eskin, S. G., Hurley, L. H., and McIntire, L. V. (2010). Modulating the functional contributions of c-Myc to the human endothelial cell cyclic strain response. *Journal of vascular research*, 47(1):80–90.

Isambert, H., Venier, P., Maggs, A. C., Fattoum, A., Kassab, R., Pantaloni, D., and Carlier, M. F. (1995). Flexibility of actin filaments derived from thermal fluctuations. Effect of bound nucleotide, phalloidin, and muscle regulatory proteins. *Journal of Biological Chemistry*, 270(19):11437–11444.

Janoštiak, R., Pataki, A. C., Brábek, J., and Rösel, D. (2014). Mechanosensors in integrin signaling: The emerging role of p130Cas. *European Journal of Cell Biology*, 93(10-12):445–454.

Jiang, G., Giannone, G., Critchley, D. R., Fukumoto, E., and Sheet, M. P. (2003). Two-piconewton slip bond between fibronectin and the cytoskeleton depends on talin. *Nature*, 424(6946):334–337.

Johansson, S., Svineng, G., Wennerberg, K., Armulik, A., and Lohikangas, L. (1997). Fibronectin-integrin interactions. *Frontiers in bioscience : a journal and virtual library*, 2(11):d126–46.

Johnston, I. D., McCluskey, D. K., Tan, C. K., and Tracey, M. C. (2014). Mechanical characterization of bulk Sylgard 184 for microfluidics and microengineering. *Journal of Micromechanics and Microengineering*, 24(3).

Kadler, K. E., Hill, A., and Canty-Laird, E. G. (2008). Collagen fibrillogenesis: fibronectin, integrins, and minor collagens as organizers and nucleators. *Current Opinion in Cell Biology*, 20(5):495–501.

Kalkan, T., Olova, N., Roode, M., Mulas, C., Lee, H. J., Nett, I., Marks, H., Walker, R., Stunnenberg, H. G., Lilley, K. S., Nichols, J., Reik, W., Bertone, P., and Smith, A. (2017). Tracking the embryonic stem cell transition from ground state pluripotency. *Development*, 144(7):1221–1234.

Kalmar, T., Lim, C., Hayward, P., Muñoz-Descalzo, S., Nichols, J., Garcia-Ojalvo, J., and Arias, A. M. (2009). Regulated fluctuations in Nanog expression mediate cell fate decisions in embryonic stem cells. *PLoS Biology*, 7(7):e1000149.

Kamble, H., Barton, M. J., Jun, M., Park, S., and Nguyen, N.-T. (2016). Cell stretching devices as research tools: engineering and biological considerations. *Lab Chip*, 16(17):3193–3203.

Katsumi, A., Milanini, J., Kiosses, W. B., del Pozo, M. A., Kaunas, R., Chien, S., Hahn, K. M., and Schwartz, M. A. (2002). Effects of cell tension on the small GTPase Rac. *The Journal of cell biology*, 158(1):153–64.

Katsumi, A., Naoe, T., Matsushita, T., Kaibuchi, K., and Schwartz, M. A. (2005). Integrin activation and matrix binding mediate cellular responses to mechanical stretch. *Journal of Biological Chemistry*, 280(17):16546–16549.

Keller, R. (2005). Cell migration during gastrulation. *Current Opinion in Cell Biology*, 17(5 SPEC. ISS.):533–541.

Kind, J., Pagie, L., De Vries, S. S., Nahidiazar, L., Dey, S. S., Bienko, M., Zhan, Y., Lajoie, B., De Graaf, C. A., Amendola, M., Fudenberg, G., Imakaev, M., Mirny, L. A., Jalink, K., Dekker, J., Van Oudenaarden, A., and Van Steensel, B. (2015). Genome-wide Maps of Nuclear Lamina Interactions in Single Human Cells. *Cell*, 163(1):134–147.

Kishino, A. and Yanagida, T. (1988). Force measurements by micromanipulation of a single actin filament by glass needles. *Nature*, 334(6177):74–76.

Kito, H., Chen, E. L., Wang, X., Ikeda, M., Azuma, N., Nakajima, N., Gahtan, V., and Sumpio, B. E. (2000). Role of mitogen-activated protein kinases in pulmonary endothelial cells exposed to cyclic strain. *Journal of applied physiology (Bethesda, Md. : 1985)*, 89(6):2391–400.

Kletsas, D., Basdra, E. K., and Papavassiliou, A. G. (2002). Effect of protein kinase inhibitors on the stretch-elicited c-Fos and c-Jun up-regulation in human PDL osteoblast-like cells. *Journal of Cellular Physiology*, 190(3):313–321.

Kolch, W. (2000). Meaningful relationships: the regulation of the Ras/Raf/MEK/ERK pathway by protein interactions. *Biochemical Journal*, 351(2):289–305.

Komuro, I. and Yazaki, Y. (1993). Control of cardiac gene expression by mechanical stress. *Annual review of physiology*, 55:55–75.

Kona, S., Chellamuthu, P., Xu, H., Hills, S. R., and Nguyen, K. T. (2009). Effects of cyclic strain and growth factors on vascular smooth muscle cell responses. *The open biomedical engineering journal*, 3:28–38.

Kopf, J., Petersen, A., Duda, G. N., and Knaus, P. (2012). BMP2 and mechanical loading cooperatively regulate immediate early signalling events in the BMP pathway. *BMC Biology*, 10(1):37.

Kubitschke, H., Schnauss, J., Nnetu, K. D., Warmt, E., Stange, R., and Kaes, J. (2017). Actin and microtubule networks contribute differently to cell response for small and large strains. *New Journal of Physics*, 19(9):093003.

Kushida, N., Kabuyama, Y., Yamaguchi, O., and Homma, Y. (2001). Essential role for extracellular Ca2+ in JNK activation by mechanical stretch in bladder smooth muscle cells. *Am J Physiol Cell Physiol*, 281(4):C1165–72.

Lakes, R. S. (1987). Foam Structures with a Negative Poisson's Ratio. *Science*, 235(4792):1038–1040.

Le, H. Q., Ghatak, S., Yeung, C. Y. C., Tellkamp, F., Günschmann, C., Dieterich, C., Yeroslaviz, A., Habermann, B., Pombo, A., Niessen, C. M., and Wickström, S. A. (2016). Mechanical regulation of transcription controls Polycomb-mediated gene silencing during lineage commitment. *Nature Cell Biology*, 18(8):864–875.

Lee, H., Adams, W. J., Alford, P. W., McCain, M. L., Feinberg, A. W., Sheehy, S. P., Goss, J. A., and Parker, K. K. (2015). Cytoskeletal prestress regulates nuclear shape and stiffness in cardiac myocytes. *Experimental Biology and Medicine*, 240(11):1543–1554.

Li, B., Chen, J., and Wang, J. H.-C. (2006). RGD peptide-conjugated poly(dimethylsiloxane) promotes adhesion, proliferation, and collagen secretion of human fibroblasts. *Journal of Biomedical Materials Research Part A*, 79A(4):989–998.

Litvinov, R. I., Shuman, H., Bennett, J. S., and Weisel, J. W. (2002). Binding strength and activation state of single fibrinogen-integrin pairs on living cells. *Proc. Natl. Acad. Sci.*, 99(11):7426–7431.

Lo, C. M., Wang, H. B., Dembo, M., and Wang, Y. L. (2000). Cell movement is guided by the rigidity of the substrate. *Biophysical Journal*, 79(1):144–152.

Loh, K. M. and Lim, B. (2011). A precarious balance: Pluripotency factors as lineage specifiers.

Love, M. I., Huber, W., and Anders, S. (2014). Moderated estimation of fold change and dispersion for RNA-seq data with DESeq2. *Genome Biology*, 15(12).

Lovett, D. B., Shekhar, N., Nickerson, J. A., Roux, K. J., and Lele, T. P. (2013). Modulation of Nuclear Shape by Substrate Rigidity. *Cellular and molecular bioengineering*, 6(2):230–238.

Lu, J., Lee, Y.-K., Ran, X., Lai, W.-H., Li, R. A., Keung, W., Tse, K., Tse, H.-F., and Yao, X. (2017). An abnormal TRPV4-related cytosolic Ca 2+ rise in response to uniaxial stretch in induced pluripotent stem cells-derived cardiomyocytes from dilated cardiomyopathy patients. *Biochimica et Biophysica Acta (BBA) - Molecular Basis of Disease*, 1863(11):2964–2972.

Lukjanenko, L., Jung, M. J., Hegde, N., Perruisseau-Carrier, C., Migliavacca, E., Rozo, M., Karaz, S., Jacot, G., Schmidt, M., Li, L., Metairon, S., Raymond, F., Lee, U., Sizzano, F., Wilson, D. H., Dumont, N. A., Palini, A., Fässler, R., Steiner, P., Descombes, P., Rudnicki, M. A., Fan, C.-M., von Maltzahn, J., Feige, J. N., and Bentzinger, C. F. (2016). Loss of fibronectin from the aged stem cell niche affects the regenerative capacity of skeletal muscle in mice. *Nature Medicine*, 22(8):897–905.

MacKenna, D. A., Dolfi, F., Vuori, K., and Ruoslahti, E. (1998). Extracellular signal-regulated kinase and c-Jun NH2-terminal kinase activation by mechanical stretch is integrin-dependent and matrix-specific in rat cardiac fibroblasts. *Journal of Clinical Investigation*, 101(2):301–310.

Maharana, S., Iyer, K. V., Jain, N., Nagarajan, M., Wang, Y., and Shivashankar, G. V. (2016). Chromosome intermingling - The physical basis of chromosome organization in differentiated cells. *Nucleic Acids Research*, 44(11):5148–5160.

MakerBot (2014). PLA and ABS Strength Data.

Mammoto, A., Mammoto, T., and Ingber, D. E. (2012). Mechanosensitive mechanisms in transcriptional regulation. *Journal of cell science*, 125(Pt 13):3061–73.

Martello, G. and Smith, A. (2014). The Nature of Embryonic Stem Cells. *Annual Review of Cell and Developmental Biology*, 30(1):647–675.

Martin, G. R. (1981). Isolation of a pluripotent cell line from early mouse embryos cultured in medium conditioned by teratocarcinoma stem cells. *Proc. Natl. Acad. Sci.*, 78(12):7634–7638.

Matsui, T., Amano, M., Yamamoto, T., Chihara, K., Nakafuku, M., Ito, M., Nakano, T., Okawa, K., Iwamatsu, A., and Kaibuchi, K. (1996). Rho-associated kinase, a novel serine/threonine kinase, as a putative target for small GTP binding protein Rho. *The EMBO journal*, 15(9):2208–16.

Matthews, B. D., Thodeti, C. K., Tytell, J. D., Mammoto, A., Overby, D. R., and Ingber, D. E. (2010). Ultra-rapid activation of TRPV4 ion channels by mechanical forces applied to cell surface $\beta 1$ integrins. *Integrative Biology*, 2(9):435.

Mattson, G., Conklin, E., Desai, S., Nielander, G., Savage, M. D., and Morgensen, S. (1993). A practical approach to crosslinking. *Molecular Biology Reports*, 17(3):167–183.

Maxwell, J. C. (1864). On the calculation of the equilibrium and stiffness of frames. *Philosophical Magazine*, 27:294–299.

McBeath, R., Pirone, D. M., Nelson, C. M., Bhadriraju, K., and Chen, C. S. (2004). Cell shape, cytoskeletal tension, and RhoA regulate stem cell lineage commitment. *Developmental cell*, 6(4):483–95.

McCullough, B. R., Blanchoin, L., Martiel, J. L., and De La Cruz, E. M. (2008). Cofilin Increases the Bending Flexibility of Actin Filaments: Implications for Severing and Cell Mechanics. *Journal of Molecular Biology*, 381(3):550–558.

Mehlen, P. (1997). hsp27 as a Switch between Differentiation and Apoptosis in Murine Embryonic Stem Cells. *Journal of Biological Chemistry*, 272(50):31657–31665.

Mootha, V. K., Lindgren, C. M., Eriksson, K.-F., Subramanian, A., Sihag, S., Lehar, J., Puigserver, P., Carlsson, E., Ridderstråle, M., Laurila, E., Houstis, N., Daly, M. J., Patterson, N., Mesirov, J. P., Golub, T. R., Tamayo, P., Spiegelman, B., Lander, E. S., Hirschhorn, J. N., Altshuler, D., and Groop, L. C. (2003). PGC-1α-responsive genes involved in oxidative phosphorylation are coordinately downregulated in human diabetes. *Nature Genetics*, 34(3):267–273.

Morawietz, H., Ma, Y. H., Vives, F., Wilson, E., Sukhatme, V. P., Holtz, J., and Ives, H. E. (1999). Rapid induction and translocation of Egr-1 in response to mechanical strain in vascular smooth muscle cells. *Circulation research*, 84(6):678–87.

Moretti, M., Prina-Mello, A., Reid, A. J., Barron, V., and Prendergast, P. J. (2004). Endothelial cell alignment on cyclically-stretched silicone surfaces. *Journal of Materials Science: Materials in Medicine*, 15(10):1159–1164.

Murakami, T., Kuroda, S.-i., and Osawa, Z. (1998). Dynamics of Polymeric Solid Surfaces Treated with Oxygen Plasma: Effect of Aging Media after Plasma Treatment. *Journal of Colloid and Interface Science*, 202(1):37–44.

Murphy, L. O., MacKeigan, J. P., and Blenis, J. (2004). A network of immediate early gene products propagates subtle differences in mitogen-activated protein kinase signal amplitude and duration. *Molecular and cellular biology*, 24(1):144–53.

Murphy, L. O., Smith, S., Chen, R. H., Fingar, D. C., and Blenis, J. (2002). Molecular, interpretation of ERK signal duration by immediate early gene products. *Nature Cell Biology*, 4(8):556–564.

Murray, P., Prewitz, M., Hopp, I., Wells, N., Zhang, H., Cooper, A., Parry, K. L., Short, R., Antoine, D. J., and Edgar, D. (2013). The self-renewal of mouse embryonic stem cells is regulated by cell-substratum adhesion and cell spreading. *International Journal of Biochemistry and Cell Biology*, 45(11):2698–2705.

Nadruz, W., Corat, M. A. F., Marin, T. M., Guimarães Pereira, G. A., and Franchini, K. G. (2005). Focal adhesion kinase mediates MEF2 and c-Jun activation by stretch: Role in the activation of the cardiac hypertrophic genetic program. *Cardiovascular Research*, 68(1):87–97.

Nagy, A., Rossant, J., Nagy, R., Abramow-Newerly, W., and Roder, J. C. (1993). Derivation of completely cell culture-derived mice from early-passage embryonic stem cells. *Proc. Natl. Acad. Sci.*, 90(18):8424–8.

Nakakuki, T., Birtwistle, M. R., Saeki, Y., Yumoto, N., Ide, K., Nagashima, T., Brusch, L., Ogunnaike, B. A., Okada-Hatakeyama, M., and Kholodenko, B. N. (2010). Ligand-specific c-Fos expression emerges from the spatiotemporal control of ErbB network dynamics. *Cell*, 141(5):884–96.

Neidlinger Wilke, C., Wilke, H. J. J., and Claes, L. (1994). Cyclic stretching of human osteoblasts affects proliferation and metabolism: A new experimental method and its application. *Journal of Orthopaedic Research*, 12(1):70–78.

Niakan, K. K., Schrode, N., Cho, L. T. Y., and Hadjantonakis, A.-K. (2013). Derivation of extraembryonic endoderm stem (XEN) cells from mouse embryos and embryonic stem cells. *Nature protocols*, 8(6):1028–41.

Nichols, J. (2001). Introducing embryonic stem cells. *Current Biology*, 11(13):R503–R505.

Nichols, J., Evans, E., and Smith, A. (1990). Establishment of germ-line-competent embryonic stem (ES) cells using differentiation inhibiting activity. *Development*, 110(4).

Nichols, J., Silva, J., Roode, M., and Smith, A. (2009). Suppression of Erk signalling promotes ground state pluripotency in the mouse embryo. *Development (Cambridge, England)*, 136(19):3215–22.

Nichols, J. and Smith, A. (2009). Naive and Primed Pluripotent States. *Cell Stem Cell*, 4(6):487–492.

Nishiuchi, R., Takagi, J., Hayashi, M., Ido, H., Yagi, Y., Sanzen, N., Tsuji, T., Yamada, M., and Sekiguchi, K. (2006). Ligand-binding specificities of laminin-binding integrins: A comprehensive survey of laminin-integrin interactions using recombinant a3b1, a6b1, a7b1 and a6b4 integrins. *Matrix Biology*, 25(3):189–197.

Niwa, H., Burdon, T., Chambers, I., and Smith, A. (1998). Self-renewal of pluripotent embryonic stem cells is mediated via activation of STAT3. *Genes and Development*, 12(13):2048–2060.

Niwa, H., Miyazaki, J. I., and Smith, A. G. (2000). Quantitative expression of Oct-3/4 defines differentiation, dedifferentiation or self-renewal of ES cells. *Nature Genetics*, 24(4):372–376.

Nonaka, S., Shiratori, H., Saijoh, Y., and Hamada, H. (2002). Determination of left-right patterning of the mouse embryo by artificial nodal flow. *Nature*, 418(6893):96–9.

Ofek, G., Wiltz, D. C., and Athanasiou, K. A. (2009). Contribution of the cytoskeleton to the compressive properties and recovery behavior of single cells. *Biophysical Journal*, 97(7):1873–1882.

Oshlack, A. and Wakefield, M. J. (2009). Transcript length bias in RNA-seq data confounds systems biology. *Biology Direct*, 4(1):14.

Pagliara, S., Franze, K., McClain, C. R., Wylde, G. W., Fisher, C. L., Franklin, R. J. M., Kabla, A. J., Keyser, U. F., and Chalut, K. J. (2014). Auxetic nuclei in embryonic stem cells exiting pluripotency. *Nature materials*, 13(6):638–44.

Pajerowski, J. D., Dahl, K. N., Zhong, F. L., Sammak, P. J., and Discher, D. E. (2007). Physical plasticity of the nucleus in stem cell differentiation. *Proc. Natl. Acad. Sci.*, 104(40):15619–24.

Park, C. Y., Tambe, D., Alencar, A. M., Trepat, X., Zhou, E. H., Millet, E., Butler, J. P., and Fredberg, J. J. (2010a). Mapping the cytoskeletal prestress. *AJP: Cell Physiology*, 298(5):C1245–C1252.

Park, J. S., Chu, J. S., Tsou, A. D., Diop, R., Tang, Z., Wang, A., and Li, S. (2011). The effect of matrix stiffness on the differentiation of mesenchymal stem cells in response to TGF-beta. *Biomaterials*, 32(16):3921–3930.

Park, J. Y., Yoo, S. J., Lee, E. J., Lee, D. H., Kim, J. Y., and Lee, S. H. (2010b). Increased poly(dimethylsiloxane) stiffness improves viability and morphology of mouse fibroblast cells. *Biochip Journal*, 4(3):230–236.

Pathak, M. M., Nourse, J. L., Tran, T., Hwe, J., Arulmoli, J., Le, D. T. T., Bernardis, E., Flanagan, L. A., and Tombola, F. (2014). Stretch-activated ion channel Piezo1 directs lineage choice in human neural stem cells. *Proc. Natl. Acad. Sci.*, 111(45):16148–16153.

Pelham, R. J. J. and Wang, Y.-l. (1997). Cell locomotion and focal adhesions are regulated by. *Proc. Natl. Acad. Sci.*, 94(December):13661–13665.

Poh, Y.-C., Chowdhury, F., Tanaka, T. S., and Wang, N. (2010). Embryonic Stem Cells Do Not Stiffen on Rigid Substrates. *Biophysical Journal*, 99(2):L19–L21.

Qi, Y., Li, Z., Kong, C.-W., Tang, N. L., Huang, Y., Li, R. A., and Yao, X. (2015). Uniaxial cyclic stretch stimulates TRPV4 to induce realignment of human embryonic stem cell-derived cardiomyocytes. *Journal of Molecular and Cellular Cardiology*, 87:65–73.

Quinlan, A. M., Sierad, L. N., Capulli, A. K., Firstenberg, L. E., and Billiar, K. L. (2011). Combining dynamic stretch and tunable stiffness to probe cell mechanobiology in vitro. *PLoS ONE*, 6(8).

Reddy, K. L., Zullo, J. M., Bertolino, E., and Singh, H. (2008). Transcriptional repression mediated by repositioning of genes to the nuclear lamina. *Nature*, 452(7184):243–247.

Reid, D. R., Pashine, N., Wozniak, J. M., Jaeger, H. M., Liu, A. J., Nagel, S. R., and de Pablo, J. J. (2018). Auxetic metamaterials from disordered networks. *Proc. Natl. Acad. Sci.*, 115(7):E1384–E1390.

Reyes-Reyes, M., Mora, N., Gonzalez, G., and Rosales, C. (2002). Beta1 and Beta2 Integrins Activate Different Signalling Pathways in Monocytes. *The Biochemical journal*, 363(Pt 2):273–80.

Riverso, M., Montagnani, V., and Stecca, B. (2017). KLF4 is regulated by RAS/RAF/MEK/ERK signaling through E2F1 and promotes melanoma cell growth. *Oncogene*, 36(23):3322–3333.

Romet-Lemonne, G. and Jégou, A. (2013). Mechanotransduction down to individual actin filaments. *European Journal of Cell Biology*, 92(10-11):333–338.

Rosenzweig, D., Carelli, E., Steffen, T., Jarzem, P., and Haglund, L. (2015). 3D-Printed ABS and PLA Scaffolds for Cartilage and Nucleus Pulposus Tissue Regeneration. *International Journal of Molecular Sciences*, 16(7):15118–15135.

Ryu, H., Chung, M., Dobrzynski, M., Fey, D., Blum, Y., Lee, S. S., Peter, M., Kholodenko, B. N., Jeon, N. L., and Pertz, O. (2015). Frequency modulation of ERK activation dynamics rewires cell fate. *Molecular Systems Biology*, 11(11):838–838.

Sadoshima, J. and Izumo, S. (1997). The Cellular and Molecular Response of Cardiac Myocytes to Mechanical Stress. *Annual Review of Physiology*, 59(1):551–571.

Sadoshima, J. I., Jahn, L., Takahashi, T., Kulik, T. J., and Izumo, S. (1992). Molecular characterization of the stretch-induced adaptation of cultured cardiac cells: An in vitro model of load-induced cardiac hypertrophy. *Journal of Biological Chemistry*, 267(15):10551–10560.

Saha, S., Ji, L., De Pablo, J. J., and Palecek, S. P. (2006). Inhibition of human embryonic stem cell differentiation by mechanical strain. *Journal of Cellular Physiology*, 206(1):126–137.

Schaffer, J. L., Rizen, M., L'Italien, G. J., Benbrahim, A., Megerman, J., Gerstenfeld, L. C., and Gray, M. L. (1994). Device for the application of a dynamic biaxially uniform and isotropic strain to a flexible cell culture membrane. *Journal of Orthopaedic Research*, 12(5):709–719.

Schindelin, J., Arganda-Carreras, I., Frise, E., Kaynig, V., Longair, M., Pietzsch, T., Preibisch, S., Rueden, C., Saalfeld, S., Schmid, B., Tinevez, J. Y., White, D. J., Hartenstein, V., Eliceiri, K., Tomancak, P., and Cardona, A. (2012). Fiji: An open-source platform for biological-image analysis. *Nature Methods*, 9(7):676–682.

Schlaepfer, D. D., Hanks, S. K., Hunter, T., and van der Geer, P. (1994). Integrin-mediated signal transduction linked to Ras pathway by GRB2 binding to focal adhesion kinase. *Nature*, 372(6508):786–791.

Schmelter, M., Ateghang, B., Helmig, S., Wartenberg, M., and Sauer, H. (2006). Embryonic stem cells utilize reactive oxygen species as transducers of mechanical strain-induced cardiovascular differentiation. *FASEB journal : official publication of the Federation of American Societies for Experimental Biology*, 20(8):1182–4.

Schwartz, M. A. and DeSimone, D. W. (2008). Cell adhesion receptors in mechanotransduction. *Current Opinion in Cell Biology*, 20(5):551–556.

Sexton, T. and Cavalli, G. (2015). The role of chromosome domains in shaping the functional genome. *Cell*, 160(6):1049–1059.

Shao, Y., Tan, X., Novitski, R., Muqaddam, M., List, P., Williamson, L., Fu, J., and Liu, A. P. (2013). Uniaxial cell stretching device for live-cell imaging of mechanosensitive cellular functions. *Review of Scientific Instruments*, 84(11).

Shimizu, N., Yamamoto, K., Obi, S., Kumagaya, S., Masumura, T., Shimano, Y., Naruse, K., Yamashita, J. K., Igarashi, T., and Ando, J. (2008). Cyclic strain induces mouse embryonic stem cell differentiation into vascular smooth muscle cells by activating PDGF receptor beta. *Journal of applied physiology*, 104(3):766–772.

Shirayoshi, Y., Okada, T. S., and Takeichi, M. (1983). The calcium-dependent cell-cell adhesion system regulates inner cell mass formation and cell surface polarization in early mouse development. *Cell*, 35(3 Part 2):631–638.

Silva, J., Nichols, J., Theunissen, T. W., Guo, G., van Oosten, A. L., Barrandon, O., Wray, J., Yamanaka, S., Chambers, I., and Smith, A. (2009). Nanog Is the Gateway to the Pluripotent Ground State. *Cell*, 138(4):722–737.

Silvers, A. L., Bachelor, M. A., and Bowden, G. T. (2003). The Role of JNK and p38 MAPK Activities in UVA-Induced Signaling Pathways Leading to AP-1 Activation and c-Fos Expression. *Neoplasia*, 5(4):319–329.

Sitterley, G. (2008). Laminin. *BioFiles*, 3.8(11).

Skutek, M., van Griensven, M., Zeichen, J., Brauer, N., Bosch, U., and Zeichen, G. J. (2001). Cyclic mechanical stretching modulates secretion pattern of growth factors in human tendon fibroblasts. *European journal of applied physiology*, 86(1):48–52.

Smith, A. G. (1991). Culture and differentiation of embryonic stem cells. *Journal of Tissue Culture Methods*, 13(2):89–94.

Sparta, B., Pargett, M., Minguet, M., Distor, K., Bell, G., and Albeck, J. G. (2015). Receptor level mechanisms are required for epidermal growth factor (EGF)-stimulated extracellular signal-regulated kinase (ERK) activity pulses. *Journal of Biological Chemistry*, 290(41):24784–24792.

Srinivas, S. (2004). Active cell migration drives the unilateral movements of the anterior visceral endoderm. *Development*, 131(5):1157–1164.

Storey, J. D. and Tibshirani, R. (2003). Statistical significance for genomewide studies. *Proc. Natl. Acad. Sci.*, 100(16):9440–9445.

Subramanian, A., Tamayo, P., Mootha, V. K., Mukherjee, S., Ebert, B. L., Gillette, M. A., Paulovich, A., Pomeroy, S. L., Golub, T. R., Lander, E. S., and Mesirov, J. P. (2005). Gene set enrichment analysis: a knowledge-based approach for interpreting genome-wide expression profiles. *Proc. Natl. Acad. Sci.*, 102(43):15545–50.

Suetsugu, S., Miki, H., and Takenawa, T. (1999). Identification of two human WAVE/SCAR homologues as general actin regulatory molecules which associate with the Arp2/3 complex. *Biochemical and biophysical research communications*, 260(1):296–302.

Sui, X., Kong, N., Ye, L., Han, W., Zhou, J., Zhang, Q., He, C., and Pan, H. (2014). P38 and JNK MAPK pathways control the balance of apoptosis and autophagy in response to chemotherapeutic agents. *Cancer Letters*, 344(2):174–179.

Sun, Y., Chen, C. S., and Fu, J. (2012a). Forcing Stem Cells to Behave: A Biophysical Perspective of the Cellular Microenvironment. *Annual Review of Biophysics*, 41(1):519–542.

Sun, Y., Villa-Diaz, L. G., Lam, R. H. W., Chen, W., Krebsbach, P. H., and Fu, J. (2012b). Mechanics Regulates Fate Decisions of Human Embryonic Stem Cells. *PLoS ONE*, 7(5):e37178.

Sunyer, R., Jin, A. J., Nossal, R., and Sackett, D. L. (2012). Fabrication of Hydrogels with Steep Stiffness Gradients for Studying Cell Mechanical Response. *PLoS ONE*, 7(10):e46107.

Swift, J., Ivanovska, I. L., Buxboim, A., Harada, T., Dingal, P. C. D. P., Pinter, J., Pajerowski, J. D., Spinler, K. R., Shin, J.-W., Tewari, M., Rehfeldt, F., Speicher, D. W., and Discher, D. E. (2013). Nuclear Lamin-A Scales with Tissue Stiffness and Enhances Matrix-Directed Differentiation. *Science*, 341(6149):1240104–1240104.

Tajik, A., Zhang, Y., Wei, F., Sun, J., Jia, Q., Zhou, W., Singh, R., Khanna, N., Belmont, A. S., and Wang, N. (2016). Transcription upregulation via force-induced direct stretching of chromatin. *Nature Materials*, 15(12):1287–1296.

Tee, S. Y., Fu, J., Chen, C. S., and Janmey, P. A. (2011). Cell shape and substrate rigidity both regulate cell stiffness. *Biophysical Journal*, 100(5):L25–L27.

Thalhauser, C. J. and Komarova, N. L. (2009). Specificity and Robustness of the Mammalian MAPK-IEG Network. *Biophysical Journal*, 96(9):3471–3482.

Thiel, G., Mayer, S. I., Müller, I., Stefano, L., and Rössler, O. G. (2010). Egr-1-A Ca2+-regulated transcription factor.

Trappmann, B., Gautrot, J. E., Connelly, J. T., Strange, D. G., Li, Y., Oyen, M. L., Cohen Stuart, M. A., Boehm, H., Li, B., Vogel, V., Spatz, J. P., Watt, F. M., and Huck, W. T. (2012). Extracellular-matrix tethering regulates stem-cell fate. *Nature Materials*, 11(7):642–649.

Tremblay, D., Chagnon-Lessard, S., Mirzaei, M., Pelling, A. E., and Godin, M. (2014). A microscale anisotropic biaxial cell stretching device for applications in mechanobiology. *Biotechnology Letters*, 36(3):657–665.

Tymrak, B., Kreiger, M., and Pearce, J. (2014). Mechanical properties of components fabricated with open-source 3-D printers under realistic environmental conditions. *Materials & Design*, 58:242–246.

Vallier, L., Mendjan, S., Brown, S., Chng, Z., Teo, A., Smithers, L. E., Trotter, M. W. B., Cho, C. H.-H., Martinez, A., Rugg-Gunn, P., Brons, G., and Pedersen, R. A. (2009). Activin/Nodal signalling maintains pluripotency by controlling Nanog expression. *Development*, 136(8):1339–1349.

Versaevel, M., Riaz, M., Corne, T., Grevesse, T., Lantoine, J., Mohammed, D., Bruyère, C., Alaimo, L., De Vos, W. H., and Gabriele, S. (2017). Probing cytoskeletal pre-stress and nuclear mechanics in endothelial cells with spatiotemporally controlled (de-)adhesion kinetics on micropatterned substrates. *Cell Adhesion and Migration*, 11(1):98–109.

Verstreken, C. M., Chalut, K. J., and Blumenfeld, R. (2018). Equally probable positive and negative Poisson's ratios in disordered planar systems. *Soft Matter*.

Vicente-Manzanares, M., Ma, X., Adelstein, R. S., and Horwitz, A. R. (2009). Non-muscle myosin II takes centre stage in cell adhesion and migration. *Nature Reviews Molecular Cell Biology*, 10(11):778–790.

Wakayama, T., Rodriguez, I., Perry, A. C., Yanagimachi, R., and Mombaerts, P. (1999). Mice cloned from embryonic stem cells. *Proc. Natl. Acad. Sci.*, 96(26):14984–9.

Walker, L. M., Publicover, S. J., Preston, M. R., Said Ahmed, M. A., and El Haj, A. J. (2000). Calcium-channel activation and matrix protein upregulation in bone cells in response to mechanical strain. *Journal of cellular biochemistry*, 79(4):648–661.

Wang, J. G., Miyazu, M., Xiang, P., Li, S. N., Sokabe, M., and Naruse, K. (2005). Stretch-induced cell proliferation is mediated by FAK-MAPK pathway. *Life Sciences*, 76(24):2817–2825.

Wang, J. H. C., Goldschmidt-Clermont, P., Wille, J., and Yin, F. C. P. (2001). Specificity of endothelial cell reorientation in response to cyclic mechanical stretching. *Journal of Biomechanics*, 34(12):1563–1572.

Wang, N. (2017). Review of cellular mechanotransduction. *J. Phys. D: Appl. Phys.*, 50(23):233002.

Wang, N., Butler, J., and Ingber, D. (1993). Mechanotransduction across the cell surface and through the cytoskeleton. *Science*, 260(5111):1124–1127.

Wang, N., Tytell, J. D., and Ingber, D. E. (2009). Mechanotransduction at a distance: mechanically coupling the extracellular matrix with the nucleus. *Nature reviews. Molecular cell biology*, 10(1):75–82.

Wang, Z., Volinsky, A. A., and Gallant, N. D. (2014a). Crosslinking effect on polydimethylsiloxane elastic modulus measured by custom-built compression instrument. *Journal of Applied Polymer Science*, 131(22).

Wang, Z., Volinsky, A. A., and Gallant, N. D. (2014b). Crosslinking effect on polydimethylsiloxane elastic modulus measured by custom-built compression instrument. *Journal of Applied Polymer Science*, 131(22).

Wells, R. G. (2008). The role of matrix stiffness in regulating cell behavior. *Hepatology*, 47(4):1394–1400.

Wen, J. H., Vincent, L. G., Fuhrmann, A., Choi, Y. S., Hribar, K. C., Taylor-Weiner, H., Chen, S., and Engler, A. J. (2014). Interplay of matrix stiffness and protein tethering in stem cell differentiation. *Nature materials*, 13(10):979–87.

Williams, R. L., Hilton, D. J., Pease, S., Willson, T. A., Stewart, C. L., Gearing, D. P., Wagner, E. F., Metcalf, D., Nicola, N. A., and Gough, N. M. (1988). Myeloid leukaemia inhibitory factor maintains the developmental potential of embryonic stem cells. *Nature*, 336(6200):684–7.

Wilson, M. Z., Ravindran, P. T., Lim, W. A., and Toettcher, J. E. (2017). Tracing Information Flow from Erk to Target Gene Induction Reveals Mechanisms of Dynamic and Combinatorial Control. *Molecular Cell*, 67(5):757–769.e5.

Winston, F. K., Macarak, E. J., Gorfien, S. F., and Thibault, L. E. (1989). A system to reproduce and quantify the biomechanical environment of the cell. *Journal of applied physiology*, 67(1):397–405.

Wipff, P. J., Majd, H., Acharya, C., Buscemi, L., Meister, J. J., and Hinz, B. (2009). The covalent attachment of adhesion molecules to silicone membranes for cell stretching applications. *Biomaterials*, 30(9):1781–1789.

Wisdom, R., Johnson, R. S., and Moore, C. (1999). c-Jun regulates cell cycle progression and apoptosis by distinct mechanisms. *The EMBO journal*, 18(1):188–97.

Wozniak, M. A. and Chen, C. S. (2009). Mechanotransduction in development: a growing role for contractility. *Nature reviews. Molecular cell biology*, 10(1):34–43.

Wray, J., Kalkan, T., Gomez-Lopez, S., Eckardt, D., Cook, A., Kemler, R., and Smith, A. (2011). Inhibition of glycogen synthase kinase-3 alleviates Tcf3 repression of the pluripotency network and increases embryonic stem cell resistance to differentiation. *Nature Cell Biology*, 13(7):838–845.

Wu, C., Bauer, J. S., Juliano, R. L., and McDonald, J. A. (1993). The alpha 5 beta 1 integrin fibronectin receptor, but not the alpha 5 cytoplasmic domain, functions in an early and essential step in fibronectin matrix assembly. *The Journal of biological chemistry*, 268(29):21883–8.

Yamaguchi, S., Yamaguchi, M., Yatsuyanagi, E., Yun, S.-S., Nakajima, N., Madri, J. A., and Sumpio, B. E. (2002). Cyclic strain stimulates early growth response gene product 1-mediated expression of membrane type 1 matrix metalloproteinase in endothelium. *Laboratory investigation; a journal of technical methods and pathology*, 82(7):949–956.

Yamamoto, K., Sokabe, T., Watabe, T., Miyazono, K., Yamashita, J., Obi, S., Ohura, N., Matsushita, A., Kamiya, A., and Ando, J. (2004). Fluid shear stress induces differentiation of Flk-1-positive embryonic stem cells into vascular endothelial cells in vitro. *AJP: Heart and Circulatory Physiology*, 288(4):H1915–H1924.

Yang, N., Higuchi, O., Ohashi, K., Nagata, K., Wada, A., Kangawa, K., Nishida, E., and Mizuno, K. (1998). Cofilin phosphorylation by LIM-kinase 1 and its role in Rac-mediated actin reorganization. *Nature*, 393(6687):809–812.

Yee, K., Weaver, V., and Hammer, D. (2008). Integrin-mediated signalling through the MAP-kinase pathway. *IET Systems Biology*, 2(1):8–15.

Yeh, Y. C., Ling, J. Y., Chen, W. C., Lin, H. H., and Tang, M. J. (2017). Mechanotransduction of matrix stiffness in regulation of focal adhesion size and number: Reciprocal regulation of caveolin-1 and β1 integrin. *Scientific Reports*, 7(1).

Yeung, T., Georges, P. C., Flanagan, L. A., Marg, B., Ortiz, M., Funaki, M., Zahir, N., Ming, W., Weaver, V., and Janmey, P. A. (2005). Effects of substrate stiffness on cell morphology, cytoskeletal structure, and adhesion. *Cell Motility and the Cytoskeleton*, 60(1):24–34.

Ying, Q.-L., Wray, J., Nichols, J., Batlle-Morera, L., Doble, B., Woodgett, J., Cohen, P., and Smith, A. (2008). The ground state of embryonic stem cell self-renewal. *Nature*, 453(7194):519–23.

Yoshigi, M., Hoffman, L. M., Jensen, C. C., Yost, H. J., and Beckerle, M. C. (2005). Mechanical force mobilizes zyxin from focal adhesions to actin filaments and regulates cytoskeletal reinforcement. *Journal of Cell Biology*, 171(2):209–215.

Young, M. D., Wakefield, M. J., Smyth, G. K., and Oshlack, A. (2010). Gene ontology analysis for RNA-seq: accounting for selection bias. *Genome Biology*, 11(2).

Zaidel-Bar, R. (2003). Early molecular events in the assembly of matrix adhesions at the leading edge of migrating cells. *Journal of Cell Science*, 116(22):4605–4613.

Zaman, M. H., Trapani, L. M., Sieminski, A. L., MacKellar, D., Gong, H., Kamm, R. D., Wells, A., Lauffenburger, D. A., and Matsudaira, P. (2006). Migration of tumor cells in 3D matrices is governed by matrix stiffness along with cell-matrix adhesion and proteolysis. *Proc. Natl. Acad. Sci.*, 103(29):10889–10894.

Zamir, E., Katz, B. Z., Aota, S., Yamada, K. M., Geiger, B., and Kam, Z. (1999). Molecular diversity of cell-matrix adhesions. *Journal of cell science*, 112 (pt11)(11):1655–1669.

Zeeberg, B. R., Feng, W., Wang, G., Wang, M. D., Fojo, A. T., Sunshine, M., Narasimhan, S., Kane, D. W., Reinhold, W. C., Lababidi, S., Bussey, K. J., Riss, J., Barrett, J. C., and Weinstein, J. N. (2003). GoMiner: a resource for biological interpretation of genomic and proteomic data. *Genome biology*, 4(4):R28.

Zeng, H.-L., Li, H.-F., Wang, X., and Lin, J.-M. (2006). Development of a gel monolithic column polydimethylsiloxane microfluidic device for rapid electrophoresis separation. *Talanta*, 69(1):226–231.

Zhang, Q. Y., Zhang, Y. Y., Xie, J., Li, C. X., Chen, W. Y., Liu, B. L., Wu, X. A., Li, S. N., Huo, B., Jiang, L. H., and Zhao, H. C. (2014). Stiff substrates enhance cultured neuronal network activity. *Scientific Reports*, 4.